Analysis and Comparison of Experimental Tests of Barrier-Deck Slab Overhang Structures Using Steel and GFRP Reinforcement

by

Juan Alberto Torres Acosta

A thesis submitted in partial fulfillment of the requirements for the degree of

Master of Science

in

Structural Engineering

Department of Civil and Environmental Engineering

University of Alberta

Abstract

Glass Fibre Reinforced Polymers (GFRP) have been commonly used as external or internal reinforcement of repaired or sound structures for some time in North America. GFRP-reinforced concrete (RC) technology has been implemented in bridge components like decks and barriers whose exposure to harsh environmental conditions is constant, given its non-corrosive nature. Despite their frequent use, some transportation ministries and contractors still see this technology as experimental and related to gaps in code provisions for repairs. For bridge barriers repairs, little to no provisions are offer in current codes; moreover, few studies conducted on bridge barriers using GFRPs have limited scopes, leaving out some critical aspects to assess bridge barrier-deck overhangs. This study was divided into an experimental and analytical phase. Experimental work included the fabrication of four concrete barrier-deck overhangs. Two served as controls by mimicking as-built structures using steel and GFRP reinforcement, while remaining ones simulated a repaired barrier-deck connection through bars doweled into deck. One of these specimens was fully reinforced with GFRPs and the other one was a hybrid structure (steel and GFRP bars). Structures were composed of a 1500×2500×250 mm deck and a single-sloped Alberta Transportation TL-4 bridge barrier connected at the tip of a 1500 mm-long overhang. Monostatic lateral load was applied until failure. Data gathered was used to analyze and compare response of specimens. RILEM beam-bond tests were also conducted to calibrate bond-slip models of GFRP bars embedded into concrete and bars with a surrounding epoxy resin embedded into concrete. For barrier-deck overhangs, one-way action weakened the barrier-deck joint which was able to be simulated using strut-and-tie models. By using this methodology, test-to-predicted ratios attained ranged between 1.15 to 0.99, showing good agreement to predict peak load.

All specimens, regardless of reinforcement material or if doweled showed the same failure mechanisms. Furthermore, structures' response was governed by the stiffness of reinforcement materials used in each specimen with steel-reinforced one showing the strongest and stiffest response of all and those reinforced with GFRPs showing the weakest; interestingly, hybrid structure did not achieve an intermediate response as expected but reported an early failure which was attributed by large tensile strains in the joint and poor confinement of this region. This latter aspect seemed to have contributed to low peak loads attained in all structures, except in steel-RC's. In a second phase, an analytical model was developed to analyze same structures as tested ones under same monotonic setup. Program was able to predict with good accuracy peak load and failure mode as real structures with test-to-predicted ratios lingering unity; deflection calculations, however, underestimated real specimens' response. This was attributed to model assumptions and limitations that limited its precision. Regarding RILEM beam-bond tests, bond-slip curves showed that the bond strength of a bar surrounded by epoxy resin will be 7.4% less to that of a bar in direct contact with concrete. Furthermore, both curves exhibit same trends with no other relevant aspects to highlight.

Preface

Elements of Chapter 3 were published with some formatting and content edits as: Torres Acosta, J. and Tomlinson, D. “Evaluation of Repair Technique Effectiveness for Bridge Barrier/Deck Systems with Glass-Fibre Reinforced Polymer Bars using Mechanics Based Modelling” in the proceedings of the 2023 Canadian Society for Civil Engineering Conference held in Moncton, New Brunswick. I was responsible for development of the MATLAB script, its idealization, and validation. The analysis of results along the parametric study proposed was of my authorship. D. Tomlinson was the supervisory author and was involved with concept formation and manuscript composition.

Content from Chapter 4 has been accepted as an ACI Special Publication as: Torres Acosta, J. and Tomlinson, D. “Effectiveness of Using Dowelled GFRP Bars to Repair Reinforced Concrete Bridge Barriers”. I was responsible for the development of the content of the chapter, execution of experimental program, data collecting, and analysis of it. D. Tomlinson was the supervisory author and was involved with concept formation, manuscript composition and edition.

Acknowledgements

The support of family, friends, and colleagues made this work possible. My deepest gratitude goes to all of you whose support added to this project that is now a reality.

Quisiera primero que todo agradecer a mis padres, **Germán y María Beatriz**. Ustedes son quienes me han impulsado a embarcarme en esta aventura desde mucho antes de que empezara. Sus sacrificios y cariño incondicional han hecho que este logro sea posible. Todo lo que soy es gracias a ustedes. A mi hermano, **Santiago y su familia** por apoyarme en este camino y ser una voz de aliento cuando más lo necesité. Su cariño y apoyo se refleja en este logro que hoy comparto con ustedes. A **mis abuelos y tíos**, quienes siempre creyeron en mí e hicieron posible este sueño. A ti especialmente, **querido abuelo**, quien me introdujo a la ingeniería… Me honra poder compartir este logro contigo. A mis amigos y todos los que formaron parte de esta experiencia, *gracias*… no me queda más que decirles que *lo logré.*

To my **friends** who I met during this experience, especially to **Avash, Camilo, Francisco, Jennifer, and Vanessa**: *thank you.* I cherish all those late study nights, early coffees, workout sessions, laughs, and motivating words we shared. I am honoured to call each one of you a friend.

My gratitude goes to all **TRG members** who helped me with specimens' fabrication and ancillary tests; to our structural lab technicians, **Greg Miller and Cameron West** who made the experimental program of this thesis possible. Also, to **Waleed and Norbert**, who came to help us when it was most needed. I appreciate all the hard work you folks put on to make this project a reality. Finally, to **Abdullah**, who installed strain gauges in reinforcement bars used in our specimens. That surely saved us a lot of time.

To my supervisor, **Dr. Douglas Tomlinson**. I'm grateful for the confidence you invested in me to do this project. Your passion for concrete is only exceeded by your knowledge in structural engineering. You have given me one of the most important gifts an engineer could ask for: love for the job. Thank you for your advice and expertise during all project phases. *My fond admiration goes to you.*

Lastly, this research was largely funded by The Natural Sciences and Engineering Research Council (NSERC) Discovery Grants Program and Faculty of Engineering of the University of Alberta. TUF-BAR donated GFRP bars used in specimens. All These are

gratefully acknowledged and appreciated in the aims of contributing to academia and knowledge on this field.

Table of Contents

1. Introduction ... 1
    1.1. Background ... 1
    1.2. Research Objective ... 3
    1.3. Research Scope ... 4
    1.4. Thesis Organization ... 4
2. Literature Review ... 6
    2.1. Introduction ... 6
    2.2. Bridge Barriers ... 6
    2.3. Fibre-Reinforced Polymers (FRPs) ... 10
    2.4. Fibre-Reinforced Polymer Reinforced Concrete (FRP-RC) ... 13
        2.4.1. Strength Requirements ... 13
        2.4.2. Serviceability Requirements ... 14
        2.4.3. FRP-RC Applications ... 15
    2.5. Repair Techniques for Concrete Structures ... 17
        2.5.1 Near-Surface Mounted Bars (NSMBs) ... 19
        2.5.2 Doweled Bars (DBs) ... 20
    2.6. Strut-and-Tie Model (STM) ... 21
        2.6.1. Beam-Column Joints (BCJs) ... 23
    2.7. FRP bar – concrete Bond ... 25
        2.7.1. Bond Strength ... 26
        2.7.2. Development Length ... 27
        2.7.3. Bond-Slip Relationships ... 30
    2.8. Digital Image Correlation ... 35
    2.9. Gaps in Research ... 36

3. Evaluation of Repair Technique Effectiveness for Bridge Barrier/Deck Systems with Glass-Fibre Reinforced Polymer Bars using Mechanics Based Modelling 38

- 3.1. Introduction 38
- 3.2. Analytical Model 39
  - 3.2.1. Model Idealization 39
  - 3.2.2. Model Development 40
  - 3.2.3. Assumptions 46
  - 3.2.4. Materials 46
  - 3.2.5. Constitutive Models 47
- 3.3. Model Validation 48
  - 3.3.1. Introduction 48
  - 3.3.2. Beam Tests Validation 49
  - 3.3.3. Barrier Tests Validation 51
  - 3.3.4. Experimental Program Validation 55
- 3.4. Parametric Study 56
  - 3.4.1. Results 58
- 3.5. Chapter Conclusions 62

4. Experimental Program 65

- 4.1. Introduction 65
- 4.2. Specimen Description and Fabrication 66
  - 4.2.1. Specimen Description 66
  - 4.2.2. Fabrication Process 69
- 4.3. Material Properties 73
  - 4.3.1. Concrete Properties 73
  - 4.3.2. Steel rebar properties 74

4.3.3. GFRP rebar properties 74

4.3.4. Epoxy Properties 74

4.3.5. Bond-Slip Response 74

4.4. Test Setup and Instrumentation 79

4.4.1. Instrumentation 80

4.5. Test Results and Discussion 82

4.5.1. General Response 83

4.5.2. Load Strain Response 86

4.5.3. Crack Pattern 88

4.5.4. Failure Analysis 93

4.5.5. Repair Effectiveness 99

4.5.6. Effect on Reinforcement Type 100

4.5.7. Comparison to CSA S6:06 Commentaries 101

4.5.8. Comparison with Prior Studies 103

4.6. Additional Considerations 106

4.7. Chapter Conclusions 108

5. Conclusions, Summary and Recommendations 110

5.1. Summary 110

5.2. Conclusions 111

5.3. Recommendations 113

5.4. Limitations 115

References 116

APPENDIX A: Additional Specimen Fabrication Details 128

A.1. First Stage: Deck Slab Fabrication 128

A.2. Second Stage: Barrier Fabrication 132

A.3. Final Appearance 139

APPENDIX B: Modified RILEM Beam Fabrication Details 143

B.1. RILEM Beam Fabrication Process.. 143

B.2. Epoxy Injection Procedure for CE Beam Series 144

B.3. Test Results for Remaining Beam Segments 146

B.4. Notes on Demolition Performed to Tested Specimens. 148

B.4.1. CB Series' Demolition Notes 148

B.4.2. CE Series' Demolition Notes 148

APPENDIX C: Test Details 150

C.1. Additional Test Setup Details 150

C.2. Data Processing Methodology 152

C.3. Load-Rotation Plots 153

APPENDIX D: Ancillary Tests Data 154

D.1. Concrete Cylinder Tests... 154

D.2. Steel Reinforcement Bar Tensile Tests 154

APPENDIX E: Formulation of Proposed Modification to El-Metwally and Chen (2017) Strut-and Tie Model.. 155

APPENDIX F: Solved Example of Barrier-Deck Joint Strength Capacity Using El-Metwally and Chen (2017) Strut-and-Tie Model 158

List of Tables

Table 3.1 Input information for beam tests validation. 49

Table 3.2 Input information for barrier test validations. 51

Table 3.3 Particular bond-slip parameters used for barrier tests validation, according to bond-slip models.. 51

Table 3.4 Test-to-predicted ratios using peak loads from analytical model and tests using various βs.. 55

Table 3.5 Parameter variations investigated... 57

Table 3.6 Reinforcement bar properties used for parametric study (See figure 3.13).......... 57

Table 3.7 Key results obtained by baseline models.. 58

Table 3.8 Axial Bar stiffness determined for each rebar spacing assessed for deck and barrier, considering tension reinforcement.. 61

Table 3.9 Deflections comparison at peak load accounting for slip curves and without them for each assessed model.. 62

Table 4.1 Deck slab and barrier general reinforcement features of as-designed and as-built specimens.. 68

Table 4.2 Activity sequence for bar dowelling repair technique....................................... 72

Table 4.3 Concrete mix properties 73

Table 4.4 GFRP mechanical properties... 74

Table 4.5 Key points from bond-slip curves. 76

Table 4.6 Model parameters calibrated for CB and CE beam series for mBPE bond-slip model. 78

Table 4.7 Expressions for mBPE model according to beam series.................................... 78

Table 4.8 Comparative chart of mBPE model parameters of current and previous studies. 79

Table 4.9 Key test results. 83

Table 4.10 Demand-capacity ratios from failure analysis conducted................................ 96

Table 4.11 values from STM at failure according to CSA S6:19 provisions using strains εs or εf obtained from tests.. 98

Table 4.12 Capacity and peak loads adjusted as per CSA S6:06 C5.7.1.6.3..................... 102

Table 4.13 Comparison chart between present study and Ahmed et al.'s (2010) report.... 106

List of Figures

Figure 2.1 Types of bridge barriers. (a) Steel barriers (Caltrans), (b) Continuous concrete barrier (Sheikh et al. 2011), and (c) Concrete barrier with openings (Caltrans). 6
Figure 2.2 (a) Safety shape and (b) Single-slope barrier profiles (Rosenbaugh et al., 2007). 8
Figure 2.3 Single Slope bridge barrier drawing (Alberta Transportation, 2017). 8
Figure 2.4 Dispersal angles and barrier geometry analyzed for standard capacities suggested (CSA S6, 2006)... 9
Figure 2.5 Typical (a) static (Sennah et al., 2018) and (b) dynamic (El-Gamal et al., 2008) tests setup... 16
Figure 2.6 barriers after (a) static (El-Salakawy et al., 2003) and (b) dynamic (El-Salakawy et al., 2004) tests performed. 17
Figure 2.7 Applications of FRP in structural retrofitting (a) sheets used to enhance confinement in columns (Wu and Pantelides 2017), (b) Shear and flexural strengthening of bridge girders using sheets (ACI 440R 2007), (c) NSMBs used for bridge barrier repair (El-Salakawy and Islam 2009), (d) DBs used for deck slab repair using grout (El-Salakawy et al. 2009), and (e) DBs with epoxy for repair of bridge barriers in current study. 19
Figure 2.8 (a) Typical STM and basic components (ACI 318, 2019), (b) STMs used for post-tensioning anchoring zones (AASHTO, 2017), and (c) definition of D-regions for different element configurations (Schlaich and Schäfer, 1991). 22
Figure 2.9 Types of BCJs (Abdelwahed, 2020). 24
Figure 2.10 Proposed STM to analyze UKJs (El-Metwally and Chen 2017). 25
Figure 2.11 equilibrium condition for a bar embedded into concrete (ACI 440, 2015) Note: μ expresses resisting forces in the image.. 26
Figure 2.12 examples transverse reinforcement interaction with splitting cracks (Jirsa et al. 1979)... 29
Figure 2.13 (a) Pullout failure (Achillides and Pilakoutas, 2004) and (b) Splitting cracks (Vint, 2012). 29
Figure 2.14 (a) BPE model (Ciampi et al., 1982), (b) modified BPE model (Cosenza et al., 1995), (c) CMR model (Cosenza et al., 1997), and (d) Bond-slip analytical model proposed by Rolland et al., (2020). 31
Figure 2.15 Slip model proposed by Sezen and Setzler (2008).. 33

Figure 2.16 Test setups for (a) pullout test (Rolland et al., 2019), (b) modified beam test (Lin and Zhang, 2013), (c) hinged beam test (Pecce et al., 2001), and (d) hinged beam test (Tighiouart et al., 1998)........ 34

Figure 3.1 Deck-Barrier structure (a) test specimen dimensions (units of mm) and (b) idealized model........ 40

Figure 3.2 Cross-sectional analysis performed for a given compressive concrete strain..... 41

Figure 3.3 Iterative procedure for compressive strains to calculate $\boldsymbol{Mr}$ accounting for the effect of axial forces........ 42

Figure 3.4 Bending moment diagram for each load increment along barrier-deck slab structure........ 42

Figure 3.5 $\boldsymbol{M-\psi}$ 3plots adjustment at uncracked-cracked region........ 44

Figure 3.6 Interpolation of curvatures related to acting bending moments........ 44

Figure 3.7 Curvature deflections computed by moment-area theorem........ 45

Figure 3.8 Determining slip related to bond stress and bar elongation and then finding bond-slip deformations........ 45

Figure 3.9 Typical cross-sections for beam tested in (a) Lau and Pam (2010), and (b) Al-Sunna et al., (2012)........ 49

Figure 3.10 Load deflection curves obtained by model (subscript mtb) and those reproduced from original data (subscript exp). Lau and Pam (2010): (a) MD2.1-A90, (b)G2.1-A90, and (c) G0.8-A90 beam tests. Al-Sunna et al. (2012): (d) BG2, (e) BC3, and (f) BS beam tests. 50

Figure 3.11 Specimen geometry and rebar layout details for El-Salakawy et al. (2003) (a and b), Ahmed et al., (2011) (c and d), and Azimi et al. (2014) (e and f). All measurements in mm........ 52

Figure 3.12 (a – b) El-Salakawy (2003) moment deflection curves for PL-3 Steel barrier and PL-3 GFRP barrier tests. (c – d) Ahmed at al. (2011) moment deflection curves for 311-Steel-2, and 311-GFRP-2 barrier tests. (e – f) Azimi et al. (2014) load deflection curves for (e)PL-3 TS, and (f) PL-3 TG1 barrier tests........ 53

Figure 3.13 Load-deflection curves up to peak load from analytical model and sensors from tests at 775 mm above deck slab........ 56

Figure 3.14 Reinforcement layout detail for parametric study........ 57

Figure 3.15 Load-deflection curve for baseline specimens. 59
Figure 3.16 Load-deflection curve for (a) GFRP-xxxx- 100, (b) GFRP-xxxx- 150, and (c) GFRP-xxxx- 200. Overhang length effect assessment. 60
Figure 3.17 Load-deflection curve for (a) GFRP-1000- xxx, (b) GFRP-1500- xxx, and (c) GFRP-2000- xxx. Rebar assembly spacing assessment. 61
Figure 3.18 Representative load deflection curves reported for GFRP-1500-150 serie using. Using mBPE and Sezen and Setzler approaches. 62
Figure 4.1 Typical deck slab overhang – Barrier structure geometry. All dimensions in mm. 67
Figure 4.2 reinforcement layout for (a) SP-01, (b) SP-02, (c) SP-03, and (d) SP-04. Bar covers given in Tables 4.1 and 4.2. Reinforcement details given in Fig. 4.3 67
Figure 4.3 reinforcement dimensions for (a) deck, and (b) barrier. All dimensions in mm. 68
Figure 4.4 Deck fabrication. (a) deck formwork, (b) SP-02 bar assemblies in form, (c) vertical bars for barrier SP-02, (d) lateral bracing for PVC tubes in deck, (e) deck pouring, (f) SP-01's surface roughened where barrier will be fabricated, and (g) SP-01 deck after 7 days curing. 70
Figure 4.5 Barrier fabrication process for control specimens (SP-01 and SP-02). (a) barrier rebar assembly connected, (b) typical barrier formwork installed, (c) concrete pouring for barriers, and (d) formwork stripping after curing process finished. 71
Figure 4.6 Activity sequence for bar dowelling technique. (a) drilling guides positioned, (b) holes drilled on SP-03 (shown) and SP-04 deck slabs, (c) hole preparation, (d) bar dowelling after epoxy adhesive injected into hol€(e) final state of epoxy and bars after being dowelled, and (f) final dowelled rebar vertical assembly. 72
Figure 4.7 (a) typical RILEM beam geometry and reinforcement layout used in this study. All dimensions in mm, unless specified; (b) and (c) Fabrication of RILEM beams; (d) final product after formwork removal; and (e) Test setup for RILEM beam tests. 75
Figure 4.8 Bond-slip curves for (a) CB, and (b) CE series beam-bond tests. mBPE model curve for each series also shown. 76
Figure 4.9 final state of beams from (a) CE series, (b) pullout cracks in CB, (c) typical bar slippage in CE, (d) typical state of bar embedded in CB after demolition, and (e) typical state of bar embedded in CE after demolition. 77

Figure 4.10 Test setup (a) drawing and (b) photo. All dimensions in mm. 80

Figure 4.11 Instrumentation locations (a) lateral, (b) Top view of deck slab. Circles marked positions; (c) typical displacement sensors locations. Measures in mm. 81

Figure 4.12 (a) DIC setup, (b) dotted area under analysis, and (c) DIC area dimensions.... 82

Figure 4.13 Control and repaired specimens' load-deflection curves for (a) horizontal displacement, (b) vertical displacement, and (c) gap opening at barrier front face base. Circles denote specimens' peak loads. Average cracking load for the deck or barrier given for illustration. 84

Figure 4.14 Special cracks generated post-peak of (a) SP-03 and (b) SP-04. 86

Figure 4.15 Load-Strain curves for strain gauges (a) DECK_1, (b) DECK_4, (c) DECK_3, (d) DECK_6, (e) BAR_1, (f) BAR_4, (g) BAR_3, (h) BAR_6. 87

Figure 4.16 Highlights of specimens testing as indicated for each column. 89

Figure 4.17 Plan view of crack patterns in (a) SP-01, (b) SP-02, (c) SP-03, and (d) SP-04.90

Figure 4.18 Elevation views of crack patterns in SP-01 (a, b); SP-02 (c, d); SP-03 (e, f); and SP-04 (g, h). Note: east face images flipped for comparison purposes. 90

Figure 4.19 Typical location and label of markers to track crack development during tests. 91

Figure 4.20 Load-crack width curves of (a) E0, (b) E1, (c) E2, and (d) E3. Solid lines correspond to east face recordings, while dashed lines to west ones. 92

Figure 4.21 Final state of specimens' junctions: SP-01 west (a) and east side (b); SP-02 west (c) and east side (d); SP-03 west (e) and east side (f); and SP-04 west (g) and east side (h). 93

Figure 4.22 DIC principal strains map contour at peak load for qualitative assessment of crack pattern: SP-01 west (a) and east side (b); SP-02 west (c) and east side (d); SP-03 west (e) and east side (f); and SP-04 west (g) and east side (h). Tension positive; strains given in mm/mm. 94

List of Symbols

a	Beam shear span.
A_b	Cross-sectional area of reinforcement bar.
$A_{\tau 1}$	Area under the curve of bond-slip graphs in ascending branch.
A_{tr}	Reinforcement cross-section area resisting splitting forces.
C	Concrete cover parameter, taken as the lesser of the least concrete cover (front or side) and one-half of bar spacing.
c	Neutral-axis depth of a cross-section at a defined strain level.
C_{strut}	Compressive strut force. Used in STM failure analysis.
C_{str-nd}	Capacity of strut at interface with nodal region.
C_{nd}	Capacity of nodal region.
d	Effective depth of tension reinforcement.
d'	Effective depth of compression reinforcement.
d_b	Bar diameter.
d_{cs}	Smallest distance between concrete cover (either front or sides) and two-thirds of centre-to-centre bar spacing.
E_c	Concrete Elastic Modulus.
E_{FRP}	FRP Elastic Modulus.
E_s	Steel Elastic Modulus.
f'_c	Concrete cylinder compressive strength.
$f_{ce,n}$	Stress limit in node region in accordance with ACI 318 (2019).
$f_{ce,s}$	Stress limit in strut-node interface in accordance with ACI 318 (2019).
f_{cn}	Stress limit in node regions in accordance with CSA S6 (2019).
f_{cr}	Concrete tensile (cracking) strength.
f_{cu}	Limiting compressive stress in a strut in accordance with CSA S6 (2019).
f_{fe}	Achievable bar stress with a determined embedment length, l_e.
$f_{u_{FRP}}$	FRP tensile strength.
f_y	Steel bar yield strength.
H_{300}	Height of CB_300 sensors (i.e., 300 mm above deck).
H_{load}	Height of design load with respect of top fibre of deck slab.

I_{cr}	Cracked moment of inertia of a cross-section.
I_e	Effective moment of inertia of a cross-section. Approximation for calculation a smeared moment of inertia between I_g and I_{cr}.
I_g	Gross/uncracked moment of inertia of a cross-section.
j	Cross-section force couple moment arm.
k_1	Bar location factor in accordance with CSA S6 (2019).
k_4	Surface factor in accordance with CSA S6 (2019).
k_b	Reinforcement-bar bond coefficient. Useful for crack width calculations.
k_{tr}	Confinement index in accordance with CSA S6 (2019).
L	Rigid body length.
l_d	Development length. For steel bars, it is the minimum distance a bar must be embedded into concrete to ensure yielding of bars prior to failure. For FRP bars, l_d is the minimum embedment length for bars to avoid bond failure.
L_{dist}	Distribution length for design forces in accordance with CSA S6:06 commentary.
l_e	Embedment length of a bar inside a concrete member, where stress transfer between bar and concrete takes place.
m	Slope of descending branch of bond-slip curve.
M-ψ	Moment-curvature relationship.
n	Number of bars being developed along potential bond-splitting plane.
N_d	Opposite force to T in nodal zones of STM.
P	Ultimate force for calculation of bond strength. Equivalent to P_t.
p	Bond-slip model descending branch constant
P_{act}	Acting force in a system that induces compressive strut force, C_{strut}. Used in STM failure analysis.
T	Tie force in nodal zones of STM.
s	Spacing of transverse reinforcement bars along l_e or l_d; slip related to a particular bond stress, τ.
s_1	Slip related to bond strength, τ_1. Equivalent to s_r and s_{f1}.

s_3	Slip level where stabilization of slip failure occurs (i.e., when τ_3 is reached). Equivalent to s_{f3}.
sp_{width}	Specimen width
V_c	Concrete shear resistance from uncracked compression region, aggregate interlock, and dowel action.
W_{nd}	Nodal zone-strut interface width. Equivalent to w_{cs}.
w_t	Additional width to nodal zone geometry due to tie force, T.
$Y_{a/b}$	Height of tangent line of elastic curve at support A about support B (i.e., front to rear supports of overhang beam). Used in curvature-based deflection calculations.
$Y_{c/b}$	Height of tangent line of elastic curve at tip of overhang (C) about support B (front support). Used in curvature-based deflection calculations.
α	Bar location factor; Bond-slip models constant for ascending branch; Angle from the inclined rebar assembly at the front of the barrier.
β	Bond-slip stabilization region constant.
β_s	Reduction factor of strut capacity at interface with nodal zones in accordance with ACI 318 (2019).
Δ_s	Deflections due to bar slip.
δ	Deflection determined at a particular point of an element due to curvature.
$\delta_{300,avg}$	Average deflection at any load step recorded by CB_300 sensors.
$\delta_{775,avg}$	Average deflection at any load step recorded by CB_775 sensors.
$\delta_{back,avg}$	Average deflection at any load step recorded by LP_BACK sensors.
δ_h	Horizontal deflections recorded along test.
$\delta_{ovg,avg}$	Average deflection at any load step recorded by LP_OVG sensors.
δ_s	Axial bar elongation.
δ_v	Vertical deflection recorded at any load step.
ε_0	Ultimate concrete compressive strain in accordance with Hognestad (1952) stress-strain relationship.
ε_1	Principal tensile strain in accordance with CSA S6 (2019).
ε_{bar}	Strains recorded in tension reinforcement during tests.

ε'_{bar}	Strains recorded in compression reinforcement during tests.
ε_c	Concrete compressive strain.
ε_{cu}	Crushing concrete compressive strain.
ε_f	Tension/compression FRP rebar strain.
ε_s	Tension/compression steel rebar strain.
θ	Angle formed between strut and tie at specified nodal zone; Barrier Rotation recorded at junction at any load step.
θ_s	Rigid body rotation due to bar slip.
ρ_{bf}	Balanced reinforcement ratio of reinforced-concrete member. Ratio assumed to induce an element to a simultaneous failure of concrete and reinforcement.
ρ_f	Reinforcement ratio of reinforced-concrete member. Correlates effective cross-sectional area with reinforcement area in section cut.
τ	Bond stress between reinforcement bar and surrounding concrete.
τ_1	Maximum bond stress concrete sustains before bond failure occurs. Equivalent to τ_m.
τ_3	Stabilization bond stress after bar has slipped.
τ-s	Bond-slip relationship.
ψ	Curvature of a cross-section due to a particular strain level.

1. INTRODUCTION

1.1. Background

Bridges are an important element of road infrastructure in any country. They enable connection of places, reduce travel time, and are vital for goods and services transportation. Bridges are exposed to several environmental conditions and chemicals which induces deterioration over time. Their deterioration becomes a concern as the structure may no longer function as designed and so maintenance is performed to keep bridges operable. The Canadian Infrastructure Report Card (CIRC, 2019) showed that approximately 12% of Canadian bridges were catalogued as “poor” or “very poor”. This is related to the fact that many assessed structures were constructed prior to 2000 (CIRC, 2019), enduring prologued exposure of structural elements to harsh seasonal conditions -principally during winter-. Thus, many Canadian bridges have developed corrosion and cracking-related problems; these result in strength and stiffness loss, particularly in steel-reinforced concrete (steel-RC) members. Even though the federal government invested $244.7 billion to replace bridges and tunnels across the country in 2020 (Statistics Canada, 2023), Canada holds an infrastructure deficit in transportation-related structures that is below average with respect to other countries with populations greater than five million people belonging to OECD (Boston Consulting Group, 2018). This phenomenon is also visible in other countries like the US, where their deficit in surface transportation infrastructure is expected to represent a financial gap of $1,125 billion by 2029 (ASCE Committee on America’s Infrastructure, 2021).

Though maintenance is needed and expected in all structures, the use of chemicals (e.g., de-icing salts) in presence of certain weather conditions (e.g., freeze-thaw cycles) reduce the life span of a bridge, leading to larger maintenance costs (ACI 440, 2015). To diminish these effects, Fibre-Reinforced Polymers (FRPs) were introduced as a cost-effective solution compared to steel reinforcement for bridges exposed to year-round aggressive environments due to their non-corrosive response (ACI 440, 2015). In particular, the most frequent elements to be reinforced with FRPs are deck slabs and bridge barriers, as they are more prone to interact with weather conditions (e.g., rain, snow, hail), and chemicals (e.g., carbon monoxide, de-icing salts) compared to other members of a bridge.

Fibre-Reinforced Polymer-Reinforced Concrete (FRP-RC) technology has shown its structural capability through decades of study and use. In regards of deck slabs, (El-Salakawy et al., 2005) led a live load test on a bridge that had its deck slab reinforced with Glass Fibre-Reinforced Polymers (GFRP) and steel bars in each span. Test outcomes showed a comparable response between spans. Mufti et al., (2007) demonstrated that GFRPs embedded within concrete in field applications did not degrade at same rate nor intensity as those in indoor tests. Findings showed a favourable image of FRPs within manufacturing and construction sectors. In terms of bridge barriers, (El-Salakawy et al., 2003) assessed statically loaded specimens (GFRP-RC and steel-RC), showing similar load capacity. Also, (El-Salakawy et al., 2004) investigated the dynamic response of GFRP-RC members using pendulum impact tests. Though GFRP-RC members absorbed less energy than steel-RC counterparts, their behaviour was comparable. Similar tests completed by El-Gamal et al., (2008) gave comparable conclusions. Evidence collected along the years of FRP-RC applications and research has enabled their inclusion in many design specifications, such as CSA S6 (2019), whereas standards/codes like CSA S806 (2012) or ACI 440.11 (2022) were exclusively created for GFRP-RC design applications. Nevertheless, as survey data published by Kim (2019) suggested more research is required, as well as field applications studied to standardize this technology and increase knowledge among contractors and designers. Moreover, one aspect yet to be fully characterized are repair techniques used for FRP-RC elements.

Studies focused on repair techniques for GFRP-RC decks and barriers are limited. El-Salakawy et al., (2009) studied methods to establish the best demolition technique to remove damaged portions of RC deck slabs to then install doweled bars. El-Salakawy and Islam, (2014) then evaluated these repair protocols on to double-sloped barriers. Results show that bar doweling is an effective method to restore element strength. However, discoveries are limited to a single barrier geometry and Test Levels (TLs) which do not necessarily represent barriers used in highway bridges that Alberta Transportation (AT) manages within the province. TL is a parameter that establishes a minimum strength threshold that barriers must have to sustain large vehicle crashing at a defined speed (NCHRP 350, (1997); MASH, 2009); CSA S6 (2019)). TL-4 embodies most of barriers in current field applications, especially in bridge railings (AASHTO, 2017). AT single-slope walls are fabricated to accomplish these strength requirements and thus evaluating doweling repair technique for this geometry and TL becomes imperative to assess its structural adequacy over other repair protocols.

1.2. Research Objective

The objective of this research is to evaluate the effectiveness of repairing GFRP-RC bridge barriers using reinforcement bars dowelled into deck slabs to connect both elements.

To achieve this objective, the following tasks, and subtasks were completed:

Task 1: Conduct a literature review to understand the mechanical behaviour of FRP-RC elements relevant to GFRP-RC bridge barriers, whether repaired or not.

Task 2: Propose an analytical model that analyzes barrier-deck systems under one-way, monostatic loading; predicts failure mode, and deflection from curvatures and slip.

- *Subtask 2.1*: Validate model with results from other authors to establish its functionality.
- *Subtask 2.2*: Conduct a parametric study to compare how different parameters affect the response of barrier-deck structures.

Task 3: Fabricate four barrier-deck slab overhang specimens for testing.

- *Subtask 3.1:* Fabricate two control specimens to represent an 'as-built' condition.
- *Subtask 3.2:* Fabricate specimens to mimic a 'dowelling' repair technique.

Task 4: Perform mono-static tests on each specimen following CSA S6:19 standards.

Task 5: Analyze and process test data on forces, deformations, and crack propagation.

- *Subtask 5.1:* Establish baseline specimen responses using steel- and GFRP-RC specimens (SP-01 and SP-02, respectively).
- *Subtask 5.2:* Establish repaired specimen responses (GFRP repaired, SP-03, and hybrid repaired, SP-04) and compare with baseline counterparts.
- *Subtask 5.3*: Understand failure modes observed and explain the mechanics that led to failure.
- *Subtask 5.4:* Compare theoretical results from *Task 2* to test results.
- *Subtask 5.5:* Assess bond-slip responses of GFRP bars in concrete both with and without dowel type repairs.

1.3. Research Scope

Four 1500 mm wide specimens composed of a deck slab (2500 mm long and 250 mm thick) and a 915 mm tall edge single-sloped TL-4 bridge barrier was constructed and tested using a mono-static approach. Each structure had a 1500 mm-long overhang by mounting specimens in a setup that enables vertical flexibility of structure. The dimensions of specimens were chosen so a one-way response is induced. This makes the system's strength mainly rely in the deck slab-barrier joint, enabling the assessment of repair dowels. Each specimen used different reinforcement arrangements. Control members (SP-01 and SP-02) were steel and GFRP-reinforced, respectively. SP-03 was also GFRP-reinforced, while SP-04 had a hybrid configuration (i.e., steel-RC deck slab and GFRP-RC barrier). SP-03 and SP-04 used dowelled bars to anchor barrier bars into deck slab using an epoxy adhesive. These serve to assess the feasibility of doweling repair technique to restore the strength a TL-4 barrier according to CSA S6:19 provisions. In all cases geometry and reinforcement configuration were determined following Alberta Transportation drawings (Alberta Transportation, 2017) and commentaries (Alberta Transportation, 2018). Analyses conducted focused on comparing experimental and theoretical results attained from two different approaches. Namely, these are a parametric study previously performed using a FEM analysis (Al-Jaaidi, 2021), and an analytical model based on first principles.

1.4. Thesis Organization

This thesis is composed of the following chapters:

Chapter 1: Introduction to research program, providing a brief background of problem. Definition of objectives and scope of study.

Chapter 2: Literature review of FRP-RC response/behaviour relevant to this thesis, such as barrier testing and mechanical behaviour, repair protocols previously proposed and their outcomes, and topics found useful as experimentation evolved. *Chapter two addresses task 1.*

Chapter 3: Analytical model to predict failure mechanisms and deflections for different types of structures is proposed and functionality explained. Model validation and parametric study is included herein. *Chapter three addresses tasks 2, 2.1, and 2.2.*

Chapter 4: Chapter four is divided in two sections: (1) Experimental program proposed to perform mono-static tests over constructed specimens. Explains the fabrication process each prototype underwent and shows details of material properties, test setup and instrumentation. *This part of the chapter addresses tasks 3, 3.1, 3.2, and part of task 4.* And (2) analysis of experimental results obtained through description of specimens' responses, crack pattern, and failure analysis. Results are compared with FEM and analytical models. Results will be also used to validate some values from parametric study. *This part of chapter four fulfills task 4 and addresses tasks 5, 5.1, 5.2, 5.3, 5.4, and 5.5.*

Chapter 5: Summary, conclusions, and recommendations from this investigation are presented.

2. LITERATURE REVIEW

2.1. Introduction

Roadway safety is a critical aspect that any highway must comply to be traversable. Safety entails several items that provide a sense of security to users while mitigating consequences. Relevant examples include sight distances, curve radii, speed limits, and safety hardware. While the first three are beyond the scope of this thesis, the last one results from research seeking to reduce the consequences of serious accidents on highways. The National Cooperative Highway Research Program (NCHRP) with the American Association of State Highway and Transportation Officials (AASHTO) published their first standard on this subject in 1962. Since then, these entities -among others- have published documentation on highway safety. The latest edition of Manual for Assessing Safety Hardware (MASH) was released in 2016 which establishes requirements for crash testing (MASH, 2009), promoting standardized testing and reporting. This facilitates definitions for safety hardware minimum requirements for operational use. Many safety features are available such as: longitudinal barriers, end-treatments, crash cushions, breakaway devices, and attenuators (MASH, 2009). Longitudinal barriers, specifically those used in bridges, are the main subject of this thesis.

2.2. Bridge Barriers

Bridge barriers are elements located on a bridge superstructure to delineate roadway edges or lanes in opposing directions (i.e., edge or median barriers) (CSA S6 2019). They contain and redirect errant vehicles into a safe stop position without posing hazard to others (MASH, 2009). Barriers are designed to resist vehicle impact forces, prevent vehicle overturning, and dissipate impact energy (Fadaee and Sennah, 2017). Fig 2.1 presents some common barrier types that include steel rails, concrete walls, and concrete posts with beams.

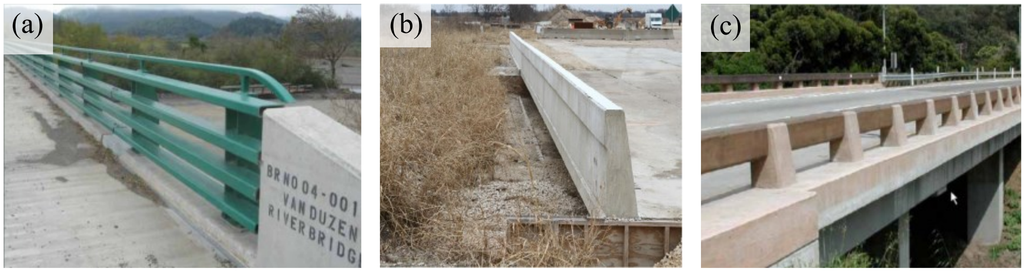

Figure 2.1 Types of bridge barriers. (a) Steel barriers (Caltrans), (b) Continuous concrete barrier (Sheikh et al. 2011), and (c) Concrete barrier with openings (Caltrans).

Two main aspects affect a barrier's crashworthiness: materials and geometry. Steel rebar has been used as traditional reinforcement for reinforced concrete (RC) structures, though fibre-reinforced polymer (FRP) technology has been used in RC barriers as an alternative to steel bars. Their durability and economic appeal enable FRP's use in structural applications in harsh environmental conditions (e.g., freeze-thaw cycles, large temperature fluctuations, and presence of de-icing salts). Past studies presented tests on deck slab-barrier systems reinforced with FRPs ((Ahmed and Benmokrane, (2010); Sennah et al., (2011); Ahmed et al., (2013); Benmokrane et al., (2018)) showing superior mechanical and durability qualities relative to steel-RC counterparts. In regards of geometry, several barrier shapes have shown proficiency during crashes. Fig. 2.2(a) shows some shapes used. First ones tested were the General Motor shape -discontinued due to crash instabilities ((FHWA, 2000)- and the New Jersey (NJ) shape, still used by many transportation ministries. F-shape was later presented, showing superior behaviour over others (NCHRP 350, 1997; FHWA, 2000). Main difference between F-shape and NJ profile are the height where the first slope begins which intends to reduce vehicle probabilities of lifting (FHWA, 2000). Single-slope barriers (Fig. 2.2(b)) were initially conceived as median parapets but tested as edge barriers by (Mak et al., 1994) with positive results. Key features this profile have are: (1) lower probability of vehicle rollover, without increasing damage due to impact (Mak et al., 1994), and (2) accommodate future wearing surface without affecting barrier's location (Alberta Transportation, 2018) relative to surface level of deck slab. Alberta Transportation (2018) considers single-slope barriers (Fig. 2.3) as the preferred standard parapet for bridges on urban roadways due to their aesthetics and acceptable response during collisions with heavy vehicles. The shape is comprised of a trapezoidal section with a longitudinal overhang beam on top. The overhang beam has two functions: shielding lower zones against weather and acting as a stiffener element (Alberta Transportation, 2018). Given their common use within Alberta, this profile was selected as focus of this thesis.

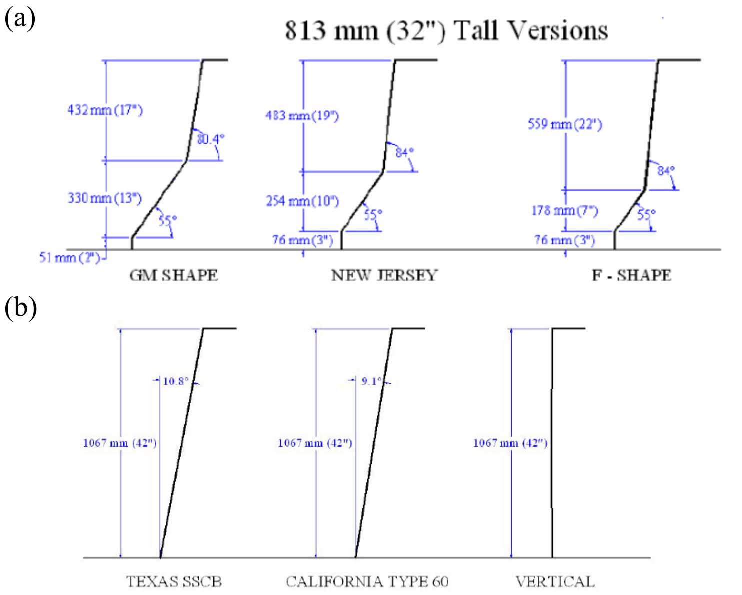

Figure 2.2 (a) Safety shape and (b) Single-slope barrier profiles (Rosenbaugh et al., 2007)

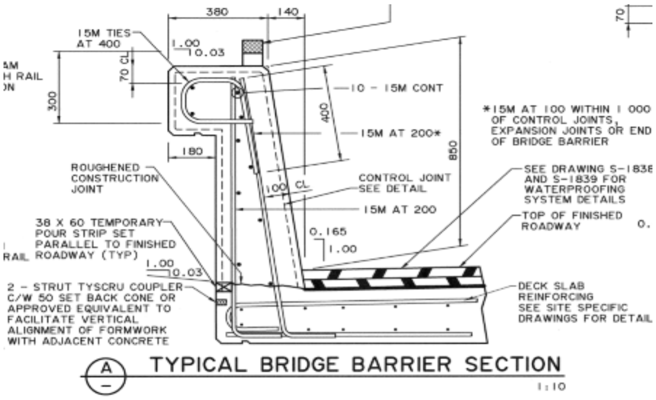

Figure 2.3 Single Slope bridge barrier drawing (Alberta Transportation, 2017).

Barriers are required to undergo tests to verify strength and geometry standards are met to perform at a determined safety level based on anticipated traffic during a highway's lifespan. A performance level, also known as a Test-Level (TL), is defined by CSA S6 (2019) as "the specified level to which a traffic barrier is to perform in reducing the consequences of a vehicle leaving the roadway as required by the applicable crash test requirements". Six TLs were introduced by (NCHRP 350, 1993), where TL-1 was assigned to service roads, and TL-6 to high service highways. Recently this scale has been adjusted by MASH (2009) by merging TL-3 and TL-4 into one performance level, dubbed as TL-4. In Canada, TL selection is based on the Barrier Exposure Index (CSA S6, 2019), that correlates transportation and road engineering parameters to establish the most cost-effective TL that satisfies requirements. As per AASHTO (2017), TLs equal or above TL-4 are often used for bridge railings, where TL-4 embodies most barriers in use.

Barriers undergo design and development stages that consider analytical and experimental tools to analyze the structural response of a barrier and address negative aspects affecting performance (MASH, 2009). Barrier design uses yield line theory as a main approach to predict barrier strength and minimum barrier length. Computed resistance is compared to factored loads which depend on barrier TL. Commentaries from (CSA S6, 2006) provide standard resistances for certain PL-2 and PL-3 (i.e., TL-4 and TL-5) barriers (Fig. 2.4). This commentary shows capacities and explains how forces and moments are spread into deck slab-barrier systems by dispersal angles depending on barrier and deck stiffness and geometry. (Azimi et al., 2014) and (Ahmed et al., 2010) used this methodology to compare capacities of specimens under their test programs and concluded that specimens were well above the capacity barriers should meet by their TLs.

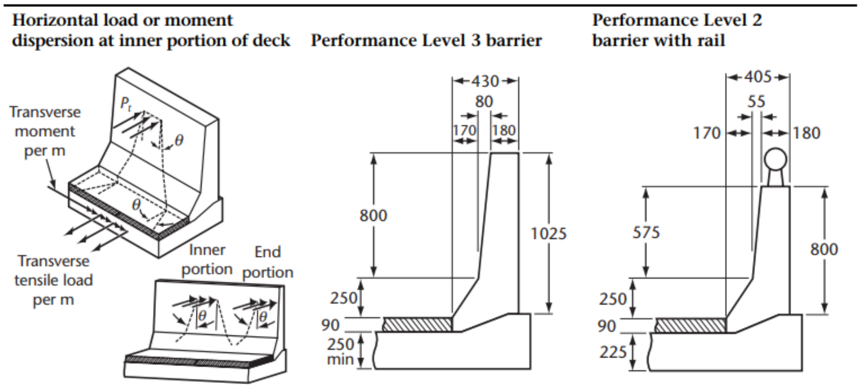

Figure 2.4 Dispersal angles and barrier geometry analyzed for standard capacities suggested (CSA S6, 2006).

Experiments are of great importance with monostatic tests being the most simple and helpful in early phases of development or adjustment assessment (NCHRP 350, 1993). Monostatic tests are used to assess strength and flexibility as well as analyze critical regions such as connections (MASH, 2009). Static tests have limitations as they do not consider dynamic natures of crashes (NCHRP 350, 1993). Dynamic tests obtain data on energy absorption, dynamic connection strength, and subsystems that constitutes the structure (e.g., deck-barrier systems) (MASH, 2009). NCHRP 350 (1993) proposed four dynamic tests with MASH (2009) endorsing their application: gravitational pendulum, drop mass, scale model, and boogie test. Computer simulations are also a handy tool using specialized software such as

LS-DYNA which was conceived for safety device modelling (MASH, 2009). Simulations uses data from static and/or dynamic tests aiming to study interrelations between structure, vehicle, and occupants (MASH, 2009); they are also used to address certain details of full-scale tests to reduce costs.

Crash tests have the same general parameters that vary according to TL. Namely, impact conditions (e.g., speed, collision angle) and test vehicle type (e.g., passenger car, small truck, tractor-trailer) (MASH, 2009) are assessed during crash test. Results are assessed following same evaluation criteria: structural adequacy, occupant risk, and post-impact vehicle trajectory (NCHRP 350, 1993; MASH, 2009). A barrier satisfying evaluation criteria is certified for field applications.

2.3. Fibre-Reinforced Polymers (FRPs)

FRPs are composite materials comprised of fibres, resins (or polymers) and, to a small extent, additional chemical compounds (e.g., adhesives and fillers). Fibres are sensitive to environmental factors that lead to chemical degradation (Cousin et al., 2019) while resins lack sufficient strength to be solely considered for structural purposes. However, when bonded fibres and resins complement each other and produce a product with superior features.

Fibres provide most of the strength and stiffness in FRPs. Two fibres are widely accepted for civil engineering because of their high resistance and economic appeal: carbon and glass. Aramid was used in the past, but their low cost-efficiency ratio is a setback for contemporary use (Barker, 2016). Basalt has started to be used in structures due to its strength, chemical resistance, and stability (Cousin et al., 2019). Fibres are produced in many arrangements ranging from strands to roving and varying from mats to fabrics (ACI 440, 2008).

Polymers surround fibres to protect them from damage. Polymers also allow fibres to transmit forces via shear stresses. Resins are classified as thermoplastic or thermosetting with the main difference being the physicochemical process endured when molded. Thermoplastics (e.g., polyvinyl chloride) only require heat to be formed, while thermosets (e.g., polyester, vinyl-ester, epoxy) require a catalyst and/or heat to cure (ACI 440, 2008). Thermosets are often used in construction, where epoxy resins frequently used for structural strengthening/repairs (Frigione and Lettieri, 2018). Benmokrane et al., (2018) highlighted that vinyl-ester polymers are commonly used for FRP bars. An advantage thermoset FRPs have is their molecular structure that allows them to be formed to an initial shape without the possibility of being reformed if heated afterwards, maintaining its original figure and properties (Masuelli, 2013).

FRPs may be produced in several processes that generate many forms and shapes: pultrusion, filament winding, compression molding, resin transfer molding, vacuum-assisted resin transfer molding, hand lay-up, and centrifugal casting (ACI 440, 2008). Such processes produce pultruded shapes, pultruded bars, or fabrics. Manufacturing processes for polymer matrices depend on its type. For instance, thermoplastics use injection and extrusion, whereas thermosets are shaped by pultrusion (Brózda et al., 2017). FRP bar surfaces are frequently modified to increase bond through deformations (e.g., ribbed, or grooved bars) and/or roughening (e.g., sand-coated) (ACI 440, 2008). (Cosenza et al., 1997) tested FRPs to establish bond behaviour and found that surface coatings are a primary factor for ensuring acceptable bond strength. Sand-coating was found to be the best means to enhance FRP-concrete bond. Bond is discussed in more detail in section 2.7.

FRP's mechanical behaviour depends on many factors. According to (ACI 440, 2008), the most relevant are: (1) Fibre type, (2) Fibre content, (3) Fibre orientation, (4) Resin type, and (5) Service conditions. Other parameters include cost and production volume with further details on these aspects found in the reference mentioned above. FRPs are sensitive to fibre orientation; this gives them an anisotropic response. How composites are manufactured contributes to their uni- or multi-directional behaviour. For bars, most fibres are parallel and kept together by either light cross weave or thermoplastic cross yarn ACI Committee 440. (2008). This leads to uni-directional behaviour (i.e., strongest, and stiffest response in fibre direction) which enables FRP bars to have a linear-elastic behaviour up to failure followed by brittle rupture. Multi-directional composites usually consist of laminates that could have unlimited combinations of responses depending on the arrangement of individual lamina.

Given their anisotropic nature, FRPs react differently depending on the type of loading. Tension is the focus of research and is the most understood and widely accepted use. Standardized procedures to obtain tensile strength and stiffness had been established for FRP (ACI 440, 2015), such as ASTM D7205 (2021). Uni-directional composites are weaker in shear since the direction of shear is transverse to the fibres. To provide minimum shear strength, fabrics or strands are wrapped around longitudinal fibres (ACI 440, 2015). FRP under compression is a matter of extended discussion. Large variations in tests led researchers to conclude that composites in compression fail prematurely. (Wu, 1990) showed that compression leads to early failures, including micro-buckling, diagonal tension, or shear failure. Such findings and lack of standardized test method to determine compressive characteristics of FRP bars -specifically Glass Fibre-Reinforced Polymers (GFRP)- (Khorramian and Sadeghian, 2019) has led design provisions to conservatively neglect or restrict FRPs in compression. (Khorramian and Sadeghian, 2018) showed that studies in the past followed different test methods not conceived to test composite materials resulting in deviated outcomes. (Khorramian and Sadeghian, 2019) then focused efforts on designing a test to obtain compressive properties of FRP (i.e., elastic modulus, strength, and failure strain) so methodology was easy to standardize. They showed that GFRP bars -under proper test conditions- fail by fibre crushing; no early failures were reported. GFRP bar's compressive elastic modulus was like the tension modulus, but the largest compressive strength was ~80% that of tension. This implies that ultimate compressive strain could be larger than what previous authors reported and translates in a larger compression resistance from GFRP bars that enables them to strain even when concrete crushes.

The first known use of FRPs was a boat hull manufactured in the 1930s (ACI Committee 440. 2008). From there, their high strength-to-weight ratio and non-corrosive behaviour enabled their use in industries like maritime, aeronautical (ACI Committee 440. 2008), aerospace (Bakis et al., 2002), and structures (ACI 440, 2015). The latter took place when FRP-RC was first used in facilities with Magnetic Resonance Imaging (MRI) equipment, where non-conductive materials were required. FRP is also often used an alternative to traditional structural strengthening systems (Täljsten, 2004). The mixture between their high strength, light weight, and non-corrosive behaviour gives FRPs an important role for structures subjected to constant contact with highly corrosive chlorides (e.g., de-icing salts). This is the case of elements like bridge barriers or decks, which have been a focus of discussion on FRP-RC (El-Salakawy et al., (2003); El Salakawy et al., (2005); El-Salakawy et al., (2005b); Benmokrane et al., (2007); Ahmed et al. 2013; Benmokrane et al. 2018). The past years has seen the urge to increase lifespans of those members and reduce maintenance costs while maintaining safety standards as it has become a great concern in transportation agencies around the world.

2.4. Fibre-Reinforced Polymer Reinforced Concrete (FRP-RC)

2.4.1. Strength Requirements

FRP-RC refers to a composite element consisting of concrete and FRP bars. FRP-RC elements are characterized by the higher strength and lower modulus FRPs have compared to steel, along with increased resistance to aggressive environments (ACI Committee 440., 2015).

Under tension, FRP bars have primarily linear-elastic response and brittle failure. When used as reinforcement for flexural members, failure modes are dictated by reinforcement ratio (ρ_f) relative to the section's balanced ratio, ρ_{bf}. The latter indicates the bar area in which concrete and FRP simultaneously fail. Two failure modes are considered for FRP-RC flexural elements: concrete crushing and FRP rupture (ACI Committee 440., 2015). The former occurs when $\rho_f > \rho_{bf}$ (i.e., compression controlled), whereas the latter happens if $\rho_f < \rho_{bf}$ (i.e., tension controlled). (Vijay and GangaRao, 2001) suggest that compressive failure, where concrete crushes prior to FRP rupture, is preferred. Tensile failure is permitted by design provisions (e.g., ACI and CSA) provided special measures are taken (Rasheed et al., 2004).

Given the brittle nature of FRP bars, members reinforced with FRP lack ductility seen in steel-RC. Still, FRP-RC may exhibit large deflections before failure which is quantified as a Deformability Factor (DF) relating energy absorbed at failure to that at a defined curvature (Vijay and GangaRao, 2001) which typically relates to service conditions. Kassem et al., (2011) found that elements with a DF larger than 4.0 exhibit a high degree of deformability (i.e., good energy absorption).

As in steel-RC, FRP-RC uses solid mechanics concepts (e.g., strain compatibility, equilibrium), constitutive laws (e.g., strain-stress curves), and assumptions (e.g., plane sections remain plane, perfect bond) for flexural design and analysis. These concepts can be used to create moment-curvature (M-ψ) relationships which are important aids for flexural design. Almusallam (1997) used iterative methods to calculate points along the M-ψ plot for

FRP-RC beams. For design, researchers have proposed idealized bi- and tri-linear $M - \psi$ relationships for FRP-RC (Razaqpur et al., 2000; Rasheed et al., 2004; Yao et al., 2018) with each having good agreement with tests from each study.

2.4.2. Serviceability Requirements

M-ψ also provides handy information for serviceability. Serviceability in RC is based in two aspects: deflections and crack control (ACI 440, 2015). Since FRPs have lower elastic moduli than steel, FRP-RC elements have reduced flexural stiffness relative to steel-RC with the same reinforcement ratio, making FRP-RC susceptible to larger deflections and crack widths. For FRP beams, serviceability often governs design instead of ultimate (El-Salakawy and Benmokrane, 2003).

Deflection calculations has been a topic of discussion for FRP-RC as traditional methods proposed for steel-RC led to inaccurate results (Bischoff, 2005). This is associated with large ratios between gross, I_g, and cracked, I_{cr}, moments of inertia unexpected in steel-RC but common in FRP-RC. Deflection calculations typically use common elastic deflection expressions substituting the moment of inertia for an effective one (I_e). I_e is a smeared value between I_{cr} and I_g, accounting for regions remaining uncracked as stress varies along the member. There are two main approaches to calculate I_e: Branson's expression (Branson, 1965), and Bischoff's equation (Bischoff, 2005). Both have been used for RC deflections regardless of reinforcement type and depend mainly on code provisions used. Steel-RC members could use Bischoff's approach if (ACI 318, 2019) is followed, whereas Branson's equation is the equation that CSA A23.3:19 uses as default. For FRP-RC, ACI 440.11-22 uses Bischoff's expression, while CSA S806-12 uses the procedure by Razaqpur et al. (2000). (El-Nemr and Ahmed, 2013) compared these approaches and concluded that CSA S806's expression gave conservative results relative to tests while modified Branson's expressions had unconservative values. I_e is derived for specific boundary and loading conditions which may not resemble all applications. For other situations, curvature integration using approaches like the moment-area theorem may be used to calculate deflections as shown in Equation (2.1):

$$\delta_{midspan} = \int_0^{L/2} \varphi(x)\, x\, dx \qquad (2.1)$$

Where $\varphi(x)$ is curvature at any point along a member and x is the distance between points of interest (i.e., evaluation and reference). The form of Eq. (2.1) varies depending on boundary conditions, which alters the evaluation limits of the integral or split it into smaller portions, acknowledging special conditions in each region.

Serviceability also comprises crack control. Crack widths are not as limiting for FRP-RC as for steel-RC, given FRP's chloride resistance (Kassem et al., 2011). Nevertheless, restrictions are still imposed due to aesthetics, creep rupture, and shear concerns (ACI 440, 2015). To estimate crack width, codes like ACI 440.11 and CSA S6:19 use a modified version of Gergely and Lutz (1968). This depends on a bond coefficient, k_b, where FRP/concrete bond quality is critical. k_b is heavily dependant on the bar surface finishing (El-Nemr et al., 2013). Studies conducted by these authors and Kassem et al. (2011) found that sand-coating provides better bond compared to helically grooved bars as elements with embedded sand coated bars had more cracks with smaller widths which reflects better stress transfer between bar and concrete. El-Nemr et al. (2013) suggested that crack spacing, and width could be reduced by designing an over-reinforced section or using High-Strength Concrete (HSC) since larger ρ_f leads to reduced bar strain, which translates in smaller tensile stresses generating narrower cracks.

2.4.3. FRP-RC Applications

FRP-RC is more often preferred over steel-RC for applications where structures are subject to chlorides or electromagnetic fields (ACI 440, 2015). Their non-corrosiveness means FRPs do not rust in harsh environmental conditions (e.g., freeze-thaw cycles, marine ecosystems) (ACI 440, 2015). Their non-magnetic feature allows FRP-RC to be used in structures induced to magnetic pulses such as Magnetic Resonance Imaging (MRI) scanners. These advantages grant FRP-RC favourable use in members like bridge decks, traffic barriers, retaining walls, or docks.

Bridge decks reinforced with FRP-RC are becoming a growing option around the world. Kim (2019) showed that 63.2% of FRP-RC applications in North America were bridge decks. This use is owed to FRP-RC's low repair and maintenance costs (ACI 440, 2015). Still, Kim (2019) showed that most FRP-RC structures are considered as 'experimental' (63% in case of decks), and 13% were labeled as 'standard practice'. This is linked to lack of knowledge and expertise when using FRP reinforcement. Efforts have been made to ease contractor and designer concerns. (Khanna et al., 2000) tested decks using steel, CFRP, and GFRP reinforcement. Results showed that elements with similar axial stiffness have comparable strengths, deflections, and crack widths despite the material used. More recent research emphasized the structural performance and durability of elements built in field conditions. El-Salakawy et al., (2005) directed a live load test on a bridge in Cookshire, Québec. The two-span bridge had one span's deck constructed with GFRP bars, while the other one used galvanized steel rebar. Tests showed that strains in both spans were similar; furthermore, visual inspection conducted after 7 months of service showed that bridge did not have large amounts of cracks along the GFRP-RC deck slab. Similar field investigations were performed by others later (Benmokrane et al., (2006); Benmokrane et al., (2007); Mufti et al., (2007)) with similar outcomes.

Traffic barriers are exposed to harsh environmental conditions and FRP bars have been used there as well (El-Gamal et al., 2008). According to Kim (2019), 26.9% of research investment given by transportation entities in bridge barriers is destined to examine their response upon static tests. This highlights the interest from ministries to understand barrier behaviour and transform experimental into standard work. As noted in Section 2.2, a barrier must pass several tests and stages before establishing its crashworthiness and acceptance for construction. Tests are divided into dynamic and static, where the former is used to define energy absorption qualities and dynamic behaviour of components and the latter is mainly used to test the strength of reinforcement and geometry configuration (MASH, 2009). Fig. 2.5 illustrates typical static and dynamic test setups.

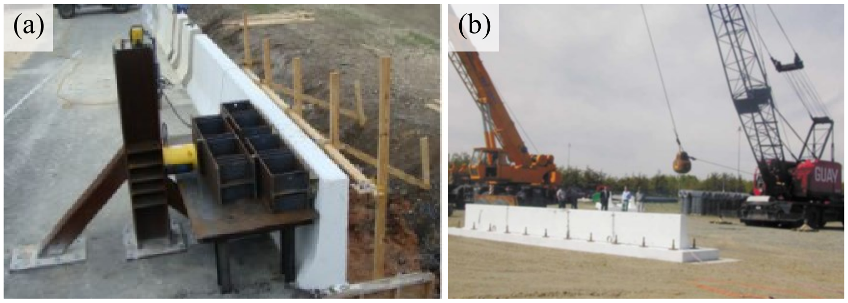

Figure 2.5 Typical (a) static (Sennah et al., 2018) and (b) dynamic (El-Gamal et al., 2008) tests setup.

FRP-RC barriers have been tested to establish their crashworthiness and durability. El-Salakawy et al., (2003) tested PL-2 and PL-3 GFRP-RC specimens under static loading. These were connected to a deck by GFRP bars. Results were compared with steel-RC counterparts, reporting similar ultimate forces between FRP-RC and steel-RC (392 and 414 kN, respectively for PL-2 specimens. 315 and 368 kN for PL-3 barriers). All prototypes failed by shear (Fig. 2.6(a)). El-Salakawy et al., (2004) investigated the same barrier types under dynamic loads. Pendulum impacts were used in eight 10-metre-long specimens. Results exposed a tendency of GFRP-RC to absorb less energy than steel-RC counterparts. This relates to GFRP-RC's smaller flexural stiffness, which indicates both larger crack density and wider cracks (Fig. 2.6(b)). Still, specimens surpassed AASHTO nominal resistance corresponding to their performance levels regardless of reinforcement type.

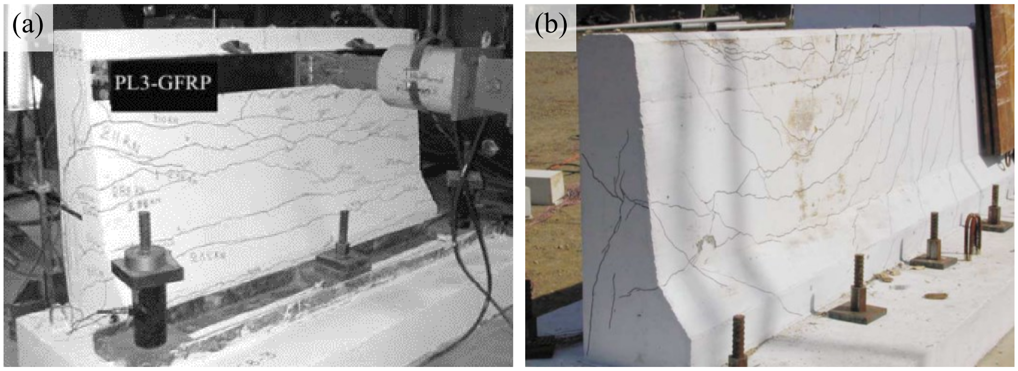

Figure 2.6 barriers after (a) static (El-Salakawy et al., 2003) and (b) dynamic (El-Salakawy et al., 2004) tests performed.

Dynamic tests were completed later by El-Gamal et al., (2008) for similar barriers, reinforced with a new generation of GFRP bars. Similar results to those by El-Salakawy et al., (2004) were seen in terms of strength. However, crack density and width reduced because of the increased elastic modulus in newer bars. More recent studies ((Sennah et al., 2011; Ahmed et al., 2013; Khederzadeh and Sennah, 2014; Sennah et al., 2018; Sennah and Hedjazi, 2019), among others) confirmed the ability of FRP-RC to replace steel-RC barriers. In consequence, more transportation ministries have adopted FRP-RC in new structures. Still, data reported by Kim (2019) showed that more applications are required to standardize this technology. One aspect yet to be properly characterized are repair techniques for FRP-RC elements.

2.5. Repair Techniques for Concrete Structures

RC structures are exposed to chemical agents, shifts in use, larger loads, poor construction detailing, and furtive events that leads to excessive deflections, wider cracks, material overstressing, or element damage to name a few outcomes. Structural strengthening and rehabilitation are done to extend service life. Interest in maintenance has increased in recent years due to the high cost of replacing aging infrastructure. (Raupach and Buttner, 2014) reported maintenance expenses for RC bridges larger than 1€ billion, and more than 20€ billion in other types of structures over Europe. In Canada, the federal government invested $244.7 billion in bridge and tunnel replacement in 2020 (Statistics Canada, 2023). This investment pertains to an infrastructure deficit that places the country in transportation-related structures below average with respect other countries with populations larger than five million people belonging to OECD (Boston Consulting Group, 2018). Thus, the large resources invested in research focused on this topic indicate how relevant structural retrofitting is in the industry.

In the past, strengthening for RC structures commonly used steel elements externally bonded to members in need of repair. However, due to corrosion, their applications were limited, and alternatives were explored. (ACI 440, 2008) mentioned studies around FRP's use in structural retrofitting dating as early as 1990. FRP's noncorrosive behaviour, low weight, simplicity of handling, and economic appeal posed these composite materials as a competitive solution to traditional methods (Täljsten, (2004); ACI 440, (2008)).

Typical FRP repair techniques used in RC are classified in two groups: externally bonded reinforcement (EBR) and internally bonded reinforcement (IBR). EBR systems use FRP fabrics to strengthen elements under flexure, shear, or axial load or to enhance ductility (ACI 440, 2008) and applicable when either partial or complete repair of damaged element is needed. IBR techniques are usually used for full replacement of an element. Here, FRP bars are used to fabricate the to-be-replaced element reinforcement assembly and connected to adjacent existing members to maintain continuity. Connections are made using adhesive agents (e.g., epoxy resins, grouting cement) that transfer stresses between new and existing concrete. Fig. 2.7 illustrates EBR and IBR systems. Due to the scope of this thesis and the large knowledge base on structural retrofitting, discussion will focus on retrofit systems used in bridge barriers, decks, and structures combining these elements. Few sources focused on retrofitting deck-barrier structures were found; to the writer's best knowledge, two repair techniques have been used: Near-Surface Mounted Bars (NSMBs) and Doweled Bars (DBs).

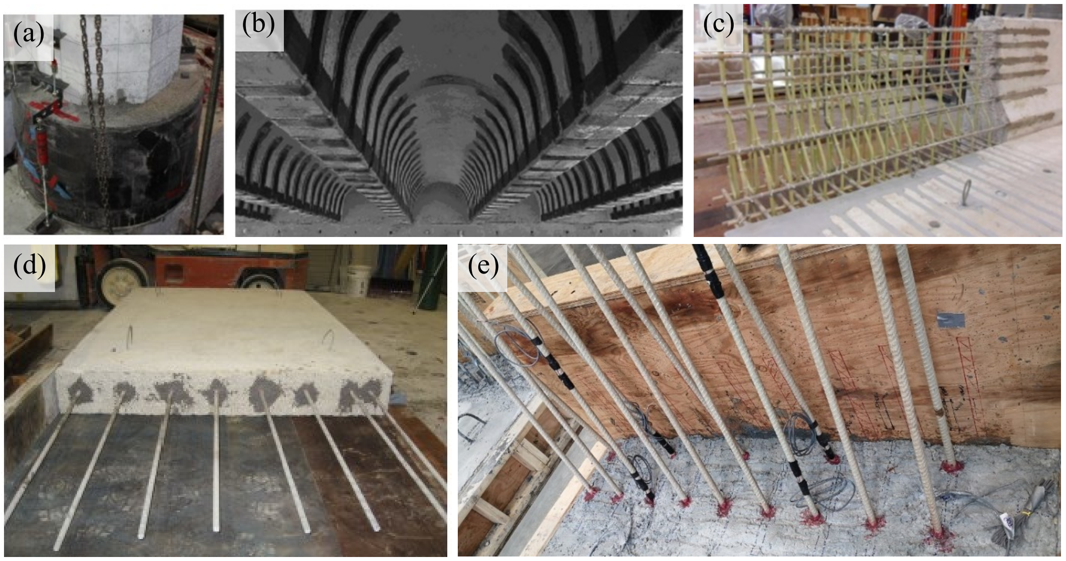

Figure 2.7 Applications of FRP in structural retrofitting (a) sheets used to enhance confinement in columns (Wu and Pantelides 2017), (b) Shear and flexural strengthening of bridge girders using sheets (ACI 440R 2007), (c) NSMBs used for bridge barrier repair (El-Salakawy and Islam 2009), (d) DBs used for deck slab repair using grout (El-Salakawy et al. 2009), and (e) DBs with epoxy for repair of bridge barriers in current study.

2.5.1 Near-Surface Mounted Bars (NSMBs)

NSMBs are a type of retrofit that consists of reinforcement bars located in the periphery of an RC element. Bars are embedded into saw-cut grooves filled with adhesive agent. NSMBs are an efficient solution for structures with weak, rough surface, or those in need of significant preparation (ACI 440, 2008); moreover, it does not present durability issues seen in EBR systems (e.g., early debonding of laminates) (Lee and Cheng, 2011). This technique is commonly used for flexural and shear strengthening (ACI 440, 2008). Still, NSMBs face challenges in terms of bonding with existing concrete substrate. Studies found that multiple factors affect NSMBs performance. Amongst these, groove dimensions (depth and width), their surface condition (roughened or smooth), filling material, bar diameter, and bar coating are most relevant with details provided elsewhere (ACI 440, 2008).

Past studies used NSMBs for deck and barrier repair. El-Salakawy et al. (2009) constructed 16 GFRP-RC decks and compared responses of specimens retrofitted with two techniques (NSMBs and DBs) to control (undamaged) elements. Decks with NSMBs had a portion at midspan demolished where this technique was applied. Results showed that specimens using epoxy resin had 13% larger capacity than those using grout. It was also noted that while performing a full demolition of the element deflections increased by 50% at failure relative to partially demolished counterparts, with their capacity remaining almost the same. Authors mentioned that the anchorage length used for this case ($30d_b = 480$ mm) was not sufficient as it led to an early failure due to bar debonding. Lee and Cheng (2011) tested 11 decks with a 1500 mm-long overhangs and varying thicknesses. Vertical load was applied at the tip of the overhang to assess retrofit effectiveness. Tests showed the efficacy of NSMBs at restoring and exceeding the capacity of control specimens by up to 38%. Finally, El-Salakawy and Islam (2014) compared NSMBs and DBs to repair deck-barrier structures. Three full-scale specimens with 6000 mm width were fabricated. Each one had a PL-2 RC barrier connected to a 200 mm-thick slab placed at a 700 mm overhang tip. Specimens were first tested under lateral monotonic loading until failure in two locations: middle and edge portions. Segments were then retrofitted using NSMBs and re-tested to compare to control specimens and other portions repaired with DBs. Specimens behaved in two-way fashion due to their width (6000 mm). Initially undamaged specimens failed by two-way shear and a combination of this with joint failure for middle and edge segments, respectively. Repaired specimens exceeded the undamaged specimen loads; tests with NSMBs had larger capacities than DBs counterparts. Authors attributed this increase to the larger NSMB effective depth which enhances both flexural and shear capacity. finally, NSMB-repaired elements exceeded current CSA S6 strength threshold for PL-2 bridge barriers.

2.5.2 Doweled Bars (DBs)

DBs are another IBR retrofit system used when damaged elements require full substitution given their state of damage or deterioration. Element demolition is followed by fabrication of reinforcement cages that are anchored/connected to existing elements by dowelling bars in holes partially filled with a bonding agent. This anchoring allows stress transfer between connected elements. Four parameters are relevant to assure proper performance of DBs: (1) demolition, (2) surface roughening, (3) drilled holes' depth (i.e., anchorage length), and (4) bonding agent. El-Salakawy et al. (2009) assessed demolition methods (jackhammer, expansive agents) and concluded that jackhammers were more efficient even though minor damage to reinforcement bars in existing concrete may be expected. (Ahmed et al., 2012) had similar findings. Surface roughening is done by using a light-weight jackhammer over the existing concrete matrix to increase bond between new and existing structures (El-

Salakawy et al. 2009) through interface shear friction. DB development is critical when thin members are used as anchoring elements due to short drilling depths, which directly affects pullout resistance. Development length depends on various factors with the main ones being reinforcement material and its surface finishing (Tighiouart et al., (1998); (Achillides and Pilakoutas, (2004); Newman et al., (2010); ACI Committee 440., (2015)). A detailed discussion on FRP-concrete bond is given in Subsection 2.7.

Bonding agents link the new with old structure and enables stress transfer between elements. Multiple products are available as adhesives (e.g., grout, epoxy resins, latex resins). These products must have high-strength, fast curing time, high chemical resistance, and strong adhesion. These properties allow these products to perform under several conditions. Their use is guided by manufacturer's instructions to guarantee proper performance. El-Salakawy et al. (2009) used grout and epoxy adhesives for their test program, finding that epoxy adhesives performed better than grout-based agents, regardless of retrofit technique. Lee and Cheng (2011) and El-Salakawy and Islam (2014) used epoxy without noting negative effects related to said adhesive.

El-Salakawy and Islam (2014) used DBs with epoxy bonding agents in their deck-barrier testing (Subsection 2.5.1). They found that middle portions achieved 94% of control counterparts while end segments achieved 92% of the control when using DBs. In all cases, the PL-2 strength threshold required by CSA S6 was exceeded. Moreover, this repair type helped restore the element's stiffness in mid-sections as smaller deflections were recorded in both barriers and slabs after retrofitting with DBs. This may be related to continuity in the new segment and differences in material stiffnesses between GFRP bars and epoxy resin.

2.6. Strut-and-Tie Model (STM)

Typical design methodologies follow Bernoulli theory to analyze sections of elements to obtain internal forces and enable proper design. Those regions are dubbed as B-regions. In contrast, regions where this theory does not apply are known as distortion or discontinuity regions (i.e., D-regions). These areas are characterized by non-linear strain profiles caused by factors like large load concentrations and/or sudden geometry discontinuities (Schlaich and Schiifer, 1991); (El-Metwally and Chen, 2017). Given these features, other methods like

STM are required to determine internal forces within D-regions for analysis and design. These regions are usually contained in a length approximated equal to the thickness of the member under analysis with D-regions being located close to load concentrations or geometric discontinuities. B-regions will be those areas of a member outside or in between D-regions.

Figure 2.8(a) shows the basic form and components of a STM while 2.8(b) show STMs used to model multiple structures; Fig. 2.8(c) show some examples of D-regions for different element geometries. STM is a form of a truss analogy where internal stress flow in RC is approximated using concrete struts as compression and reinforcement ties for tension. To maintain equilibrium, struts and ties meet at nodal zones.

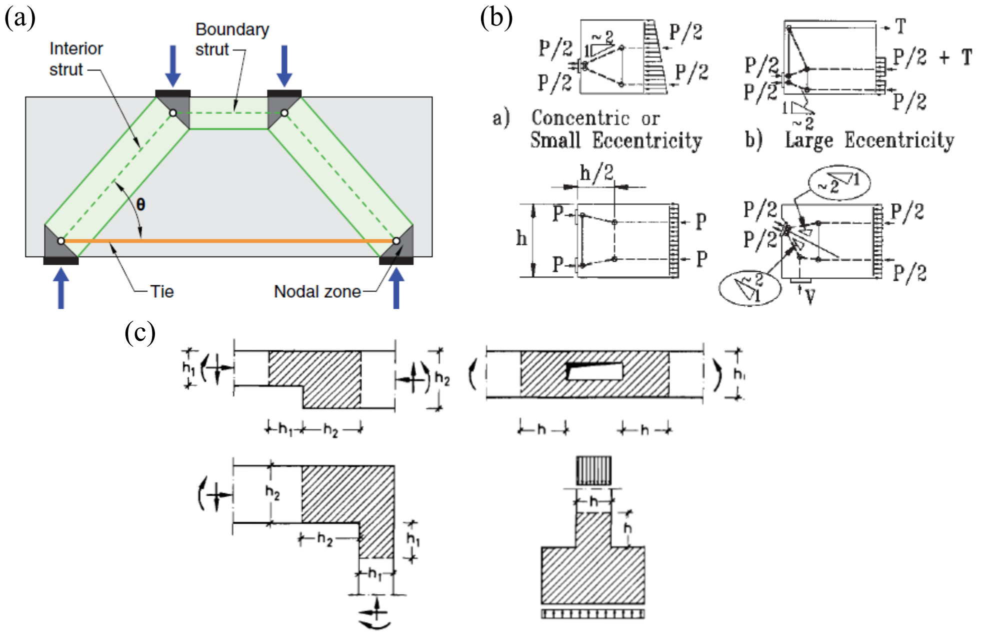

Figure 2.8 (a) Typical STM and basic components (ACI 318, 2019), (b) STMs used for post-tensioning anchoring zones (AASHTO, 2017), and (c) definition of D-regions for different element configurations (Schlaich and Schäfer, 1991).

Typically, concrete's compressive strength controls capacity of struts and nodal zones, while ties are reinforced and controlled by reinforcement strength. Given the brittle nature of concrete and the fact that STM is a lower-bound theorem of plasticity (Schlaich and Schäfer, 1991), strut and nodal zone capacities are usually underestimated to provide conservative results by providing stringent safety factors that vary according to several aspects and code provisions. For instance, ACI 318-19 (2019) proposes reduction factors to strut capacity that account for tensile stresses in concrete and differences between stress fields complexity that occurs in the concrete member versus the one approximated for STM analysis (Matamoros and Wong, 2003). Schlaich and Schäfer (1991) proposed limiting stresses according to some typical strut stress fields. El-Metwally and Chen (2017) used reduction factors for STM components per ACI 318-14 provisions. However, CSA S6 (2019) estimates reductions in strut capacity by calculating a concrete efficiency factor, ν, that accounts for cracked concrete due to transverse tensile strains (Matamoros and Wong, (2003); Andermatt and Lubell, (2013) obtained from Modified Compression Field Theory (MCFT; Vecchio and Collins, 1985). Nodal zone capacity is usually dictated by the type of stresses acting on each face of the node and whether nodes are hydrostatic or non-hydrostatic. A node is hydrostatic when all faces of node are subjected to same stress level (i.e., no shear stress is induced); non-hydrostatic node does not comply with this condition and is exposed to normal and shear stresses (Birrcher et al., 2008).

The wide applications of STMs highlight the versatility of this tool to design complex systems including beam-column joints. STM is commonly used and found to be a reliable at properly analyzing these connections. By analogy, a knee beam-column joint STM has applicability for barrier-deck interfaces in this thesis since one-way action due to limited specimen width induce barrier-deck junctions to large, non-planar stresses.

Acceptance and applicability of STMs in FRP-RC structures had increased in recent years as more studies including these tools and technologies are done around the world (e.g., Andermatt and Lubell, 2013). This methodology, however, remains under revision for codes like ACI 440.11 (2022) as concerns around the brittle response of GFRPs and how this code dimensions STM components pose an unsafe condition of design. Other codes like CSA S6 (2019) show similar provisions for either GFRP-RC or steel-RC structures. This is due to how this code reduces compressive strength of nodal zones and struts in function to the tensile principal strain acting in those regions.

2.6.1. Beam-Column Joints (BCJs)

A beam-column joint (BCJ) refers to the space where two RC elements with orthogonal longitudinal axes connect and form a joint. Combined actions between element geometries and large stresses produce a distorted area within BCJs. In earthquake-resistant structures, BCJs are of great importance since they are commonly used for moment redistribution after elements exceed their elastic capacity, creating plastic hinges at the BCJ. Fig. 2.9 presents common BCJs; classification varies according to geometry (e.g., interior, exterior or knee joint) and confinement level (i.e., if joint has transverse reinforcement or not).

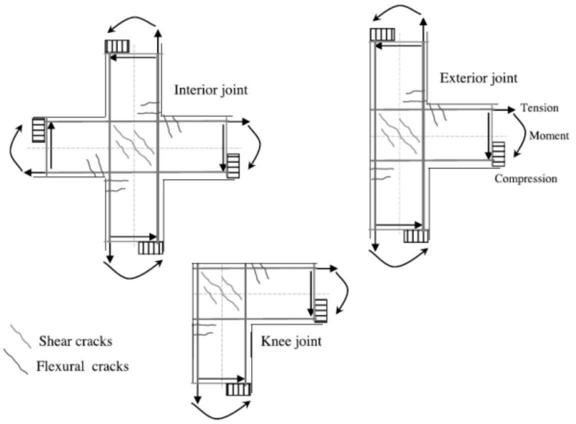

Figure 2.9 Types of BCJs (Abdelwahed, 2020).

A knee joint (KJ) is the closest connection type to the barrier-deck joint presented later in this thesis. KJs can include transverse reinforcement to confine the compressive strut in this space caused by opening or closing moments. This reinforcement dictates the form of the STM at the joint. Transverse reinforcement may be placed in various forms with stirrups arranged in orthogonal directions frequently used. (Mogili and Kuang, 2019) found that reinforced KJs have a relatively better capacity under closing moments rather than opening moments and attributed this to weakened strut capacity related to tensile forces within the joint. An Unreinforced Knee Joint (UKJ) does not have transverse reinforcement, affecting its ability to strain and rotate without early failure. UKJs' under opening action are prone to fail by diagonal tension (El-Metwally and Chen, 2017) when the diagonal compressive strut's strength is exceeded by acting forces travelling in the rear corner. Other effects such as reinforcement type and tensile internal forces in the joint also weaken the STM. (El-Metwally and Chen, 2017) proposed STMs to assess their applicability to analyze these joints and (Fig. 2.10). This model comprises a strut connecting both compression zones of connecting elements in the outside joint corner with triangular nodal zones.

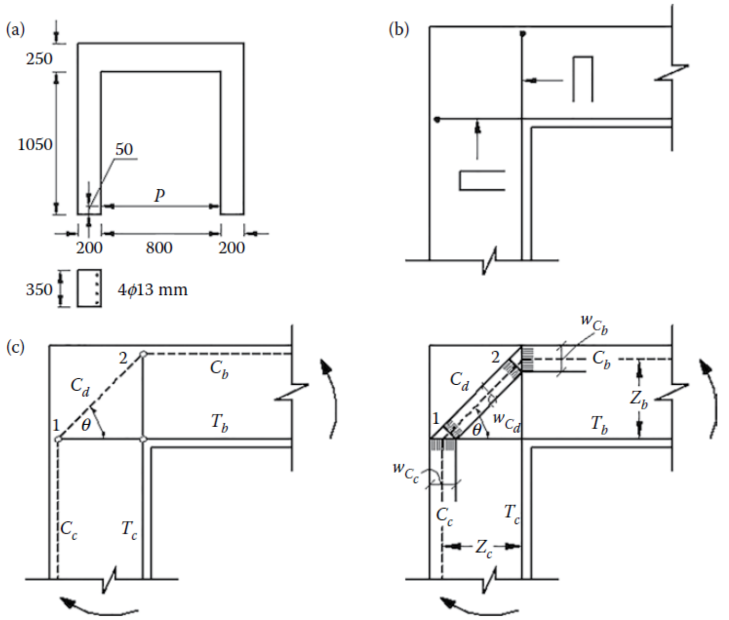

Figure 2.10 Proposed STM to analyze UKJs (El-Metwally and Chen 2017).

This model has been implemented to some extent in other experimental programs. (Mashhadi et al., 2023) adjusted parts of this STM to determine an expression for shear strength for exterior knee joints, finding positive outcomes when comparing with test results. Finally, a study carried out by (Park and Mosalam, 2012) proposed a more complex STM, composed of two struts: one (ST1) developed by presence of 90° hooks from the connecting beam, and another (ST2) created by bond strength of concrete around the embedded bar. Tests showed that even though the analysis was closer to test results used as reference, the main diagonal compressive element is the one connecting the nodal zones at the joint and dictated the peak load of exterior knee joints.

2.7. FRP bar – concrete Bond

Bond between reinforcement and concrete allows an element to achieve a defined strength that satisfies design conditions and project specifications. Design assumptions are often based on a ‘perfect’ bond that assures a predictable response (Ahmed et al., 2008). A lot of research has been done on bond between concrete and ribbed mild steel reinforcement (Orangun et al., 1977; Jirsa et al., 1979; Ciampi et al., 1982; Eligehausen et al., 1983, among others). This work led to an understanding of reinforcement-concrete bond reflected in design codes. However, this knowledge does not necessarily apply to other reinforcement types

(Achillides and Pilakoutas, 2004). The introduction of FRP-RC has encouraged researchers to characterize FRP-concrete bond for design. Challenges include the large variance of FRP products (related to lack of well-established standards (Cosenza et al., 1997), to limited understanding of FRP-concrete bond behaviour (Newman et al., 2010). Nevertheless, the introduction of FRP design provisions and quality testing procedures (e.g., CSA S806, ACI 440.11, ASTM) has helped diminish these challenges.

Bond is critical for elements with limited available embedment length, like barrier-deck joints. This section addresses three topics relevant to this study: bond strength, development length, and bond-slip relationships.

2.7.1. Bond Strength

Bond strength, τ, is the maximum average perimeter stress carried by reinforcement in concrete immediately before bond-related failure occurs. This average bond strength may be visualized and related to pullout forces using Fig. 2.11 and equation 2.2.

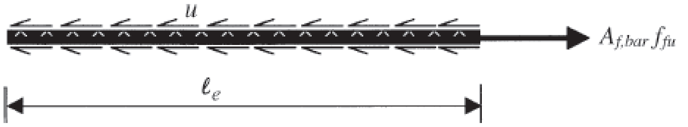

Figure 2.11 equilibrium condition for a bar embedded into concrete (ACI 440, 2015) Note: μ expresses resisting forces in the image.

$$\tau = \frac{P}{\pi d_b l_e} \tag{2.2}$$

Where P is the ultimate force, d_b bar diameter, and l_e is the embedded length of bar into concrete. This expression estimates an average bond stress since force is assumed to linearly vary from zero to P along l_e. From a mechanics standpoint, τ is the stress at which force equilibrium is broken between bar tensile forces (i.e., pullout action) and resisting forces along l_e. Empirically derived expressions using test data may be used for same purpose using numerical methods. (Wambeke and Shield, 2006) performed a two-variable linear regression based on the results of 71 beam tests with splitting failures. The final equation, (Eq. 2.3) relates development length and reinforcement achievable stress.

$$\tau = \left(4 + 0.3\frac{C}{d_b} + 100\frac{d_b}{l_e}\right)\sqrt{f'_c} \tag{2.3}$$

Here, C is the smallest between concrete cover (front or side) and one-half of bar spacing (centre-to-centre) and f'_c is concrete's compressive strength. d_b and l_e were defined for equation 2.2.

Regardless of reinforcement type, three resistive forces come into play: chemical adhesion, friction, and mechanical interlock (Newman et al., 2010). The first two create shear load transfer paths, and depend on materials' physicochemical properties (e.g., concrete's viscosity, presence of rust, bar surface roughness). The last one adds a radial stress diffusion system attributed to bar surface deformations. Tighiouart et al., (1998) found that bond strength from tested GFRP-RC specimens were governed by adhesion and friction. They concluded that surface deformations for tested bars were not strong enough as these failed before concrete crushed. A more recent study by Achillides and Pilakoutas (2004) showed that surface deformations improve bond response of FRP bars.

Although FRP-RC and steel-RC members have same resistive systems, bond responses seem to be controlled by different factors. Achillides and Pilakoutas (2004) noted that FRP-concrete bond depends considerably on bar diameter rather than concrete's shear strength, as seen in steel-RC members. This may be attributed to shear lag through the FRP bar cross-section. Their work also exposed the impact of six variables on bond: bar surface type, embedment length, concrete compressive strength, bar diameter, cross-section shape, and surface finishing. Similar results to Achillides and Pilakoutas (2004) were obtained by (Ahmed et al., 2008) where the impact of d_b over bond strength magnitude was highlighted. In addition, they noted that imperfections in concrete mixtures (e.g., voids, shrinkage effects) contribute to τ reduction and have larger impacts as d_b increases. Finally, (Baena et al., 2009) explained how bar elastic modulus influenced element response with specimens reinforced with deformed steel bars had larger bond stresses at smaller bar elongations, whereas FRP-RC members attained larger elongations at same stress levels.

2.7.2. Development Length

Force transmission is crucial for structural continuity and stiffness. For steel bars the development length, l_d, is the minimum distance a bar must be embedded into concrete, so reinforcement yields (Jirsa et al., 1979) prior to a bond/development failure. This ensures that structural systems requiring ductile responses (e.g., earthquake-resistant systems) can perform within the plastic range without collapsing. In contrast, FRPs rarely need to develop the full bar strength since many FRP-RC members are compression-controlled (ACI 440, 2015). In this case, l_d is based on the bar embedment length required to cause failure by concrete crushing without causing bond failure.

Orangun et al., (1977) proposed an empirically derived expression for l_d of deformed steel bars that served as foundation for ACI 318's l_d expression (ACI 440, 2015). Adjustments were proposed later by Jirsa et al. (1979) to limit unconservative estimates. Said adjustments were associated with concrete cover, rebar spacing, and presence of transverse reinforcement that were excluded initially. These expressions are still used in current steel-RC provisions and adjusted to produce l_d expressions for FRP-RC. CSA S6:19 uses a similar expression for l_d as the one developed by Jirsa et al. (1979) in Section 16 on fibre-reinforced structures. This equation includes a modular ratio between steel and FRP to account for material stiffness differences. Wambeke and Shield's (2006) expression included in ACI 440.11 (2022) was derived following an empirical approach like Orangun et al., (1977). Equations 2.4 and 2.5 depict CSA S6 (2019) and ACI 440.11 (2022) l_d expressions for FRP-RC elements, respectively.

$$l_d = 0.45 \frac{k_1\, k_4}{\left[d_{cs} + k_{tr} \frac{E_{FRP}}{E_s}\right]} \left[\frac{f_{u_{FRP}}}{f_{cr}}\right] A_b \tag{2.4}$$

$$l_d = \frac{d_b}{13.6 + \frac{C}{d_b}} \left[\frac{\alpha\, f_{fe}}{0.083\sqrt{f'c}} - 340\right] \tag{2.5}$$

For expression 2.4, k_1 and k_4 account for bar location and surface factors, respectively. d_{cs} is the smallest distance between concrete cover (either front or sides) and two-thirds of centre-to-centre bar spacing. k_{tr} is a confinement index, while E_{FRP} and E_s are FRP and steel elastic moduli. $f_{u_{FRP}}$ is the ultimate strength for FRP bars being developed, f_{cr} is concrete's tensile strength, and A_b is the bar cross-sectional area. As noted by (Ehsani et al., 1996), reinforcement location affects bond strength and bottom reinforcement layers resist larger stresses than top layers. Wambeke and Shield (2006) relate this effect to voids, liquids, and fine particles prone to move up an element's cross-section during pouring and curing. CSA S6:19 has a k_1 of 1.3 for horizontal bars with more than 300 mm of concrete cast below. d_{cs}

establishes the direction at which splitting failure occurs (i.e., the cracking path that requires less energy to initiate) (Jirsa et al., 1979). k_{tr} directly interacts with failure plane direction (i.e., d_{cs}). k_{tr} expression is shown in Eq 2.6, based on (CSA S6, 2019).

$$k_{tr} = \frac{A_{tr} f_y}{10.5sn} \tag{2.6}$$

Here, A_{tr} is the reinforcement cross-section area that resists splitting forces (Jirsa et al., 1979). Fig. 2.12 shows some examples of A_{tr} – splitting cracks interaction for illustration; remaining parameters' definition are available in CSA S6 (2019).

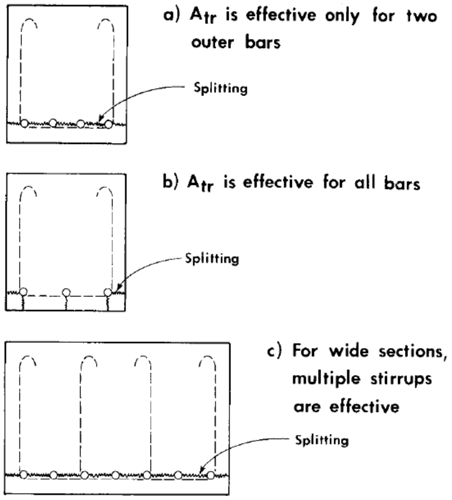

Figure 2.12 examples transverse reinforcement interaction with splitting cracks (Jirsa et al. 1979).

A $2.5d_b$ limit was imposed to the denominator in equation 2.4 when failure shifts between pullout and splitting (Jirsa et al., 1979). Bar pullout occurs when bars have short embedment length and is pulled from concrete matrix (Fig. 2.13(a)); concrete splitting occurs when acting stresses along the bar exceeds concrete's shear capacity (Fig. 2.13(b)).

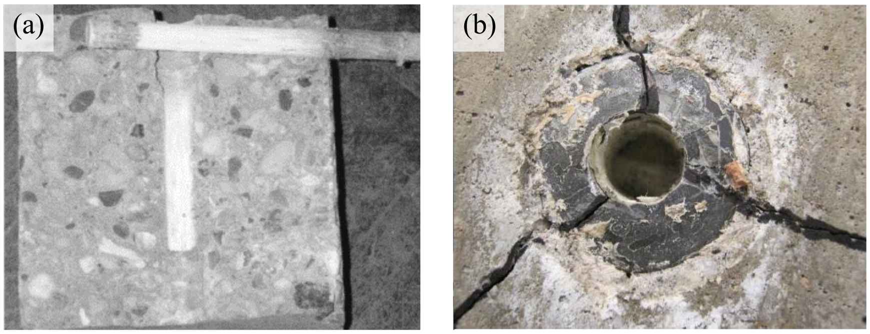

Figure 2.13 (a) Pullout failure (Achillides and Pilakoutas, 2004) and (b) Splitting cracks (Vint, 2012).

In equation 2.5, C is the smallest dimension between concrete cover (front or side) and one-half of centre-to-centre bar spacing, α is the bar location factor, f_{fe} is the required stress to be developed by reinforcement. Both 2.4 and 2.5 expressions contain almost same parameters though only 2.4 accounts for confinement effects. Wambeke and Shield (2006) observed that confinement had little effect on GFRP bond strength due to low rib area of GFRP bars. This was deduced as tests showed that confined concrete enhanced τ in steel bars with large rib areas relative to those with smaller ones (Darwin et al., 1996). ACI 440 (2015) states that their equation only applies for embedment equal to at least $20d_b$, where a linear stress distribution from 0 to f_{fe} is assumed. Bond stress response with less embedment remains not well characterized.

2.7.3. Bond-Slip Relationships

2.7.3.1. Constitutive Law and Models

Bond-slip (τ-s) relationship is a constitutive law that relates bond stresses with bar elongation under external axial force. This relationship allows extraction of bar stiffness, bond strength, and resisting force data. T-s is based on three mechanics concepts: force equilibrium, material constitutive laws (e.g., stress-strain plots), and strain compatibility. Ciampi et al., (1982) based their work on equation 2.7 to relate these concepts and obtain bond-slip relationship.

$$\frac{dN(x)}{dx} - \mathrm{q(x)} = 0 \tag{2.7}$$

Where $N(x) = A\ \sigma(x)$ (A is the cross-sectional area of the bar and $\sigma(x)$ the bar axial stress at location x) and $q(x) = \pi d_b \tau(x)$. This expression represents force equilibrium of an infinitesimal bar element under axial stress illustrated in Fig. 2.11. Further treatment to this equation including material mechanical properties and compatibility leads to equation 2.8.

$$\frac{d^2 s}{dx^2}\mathrm{A\sigma} - \tau\big(\mathrm{s(x)}\big)\pi d_b = 0 \tag{2.8}$$

Equation 2.8 shows equilibrium between external and bond forces as the bar elongates. Equation solutions depend on boundary conditions. Ciampi et al., (1982) mentioned three solution techniques: finite differences, finite elements, and a ‘shooting technique’. These were used to solve this expression and modelled τ-s relationships alongside other approaches (Pecce et al., 2001). Graphical expression of this expression has been done by different models: BPE model (Ciampi et al., 1982; Eligehausen et al., 1983), which is the default approach for RC design in CEB-FIP, (1990), modified-BPE (mBPE) model (Cosenza et al., 1995). More recent studies resulted in approaches for FRP-RC by others (Malvar, 1995; Cosenza et al., 1997; Rolland et al., 2020). All models rely on parameters that required test data for calibration. Fig. 2.14 shows typical curves of some bond-slip models.

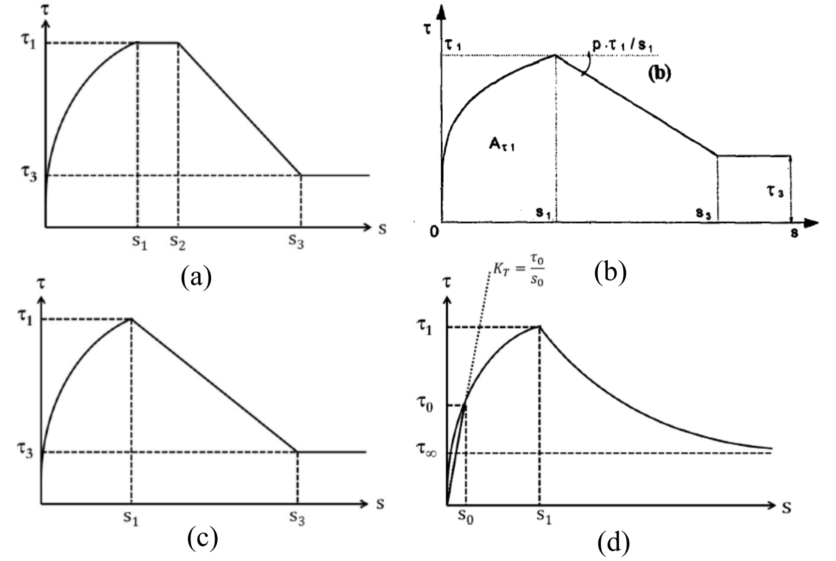

Figure 2.14 (a) BPE model (Ciampi et al., 1982), (b) modified BPE model (Cosenza et al., 1995), (c) CMR model (Cosenza et al., 1997), and (d) Bond-slip analytical model proposed by Rolland et al., (2020).

Curve applicability varies depending on material and bar surface finishing. Steel rebar τ-s models are three-phased with an ascending, plateau, and descending regions. First branch grows from zero to (s_1, τ_1) with τ_1 being the ultimate bond strength and s_1 is the slip when τ_1 is achieved. This region is controlled by joint action of adhesion and mechanical interlock (Yan et al., 2016). Next zone corresponds to a constant bond stress between (s_1, τ_1) and (s_2, τ_1) (Fig. 2.14(a)), where concrete cracks spread along bars and lugs start to crush concrete. Post-peak response is two-phased: the first part sees bond stress loss until (s_3, τ_3) followed by a residual, constant, bond stress of τ_3. This response is attributed to the loss of bearing capacity due to concrete smoothening via lug interaction with concrete (Yan et al., 2016). In contrast, FRP-RC models consist of a two-phased response with rising and descending branches. Depending on bar surface type, each region is governed by different bond mechanisms. Cosenza et al., (1997) explained these regions for smooth (i.e., bar with surface treatments and without surface deformations) and deformed (i.e., bar with lugs/ribs and possible surface treatments) bars from a mechanical perspective. For smooth bars, ascending branch is controlled by chemical adhesion. Once adhesion breaks down, bar slip greatly increases and τ decreases. Deformed bar response is dictated by mechanical interlock. Their rising branch stiffness is governed by joint action of lugs, adhesion, and friction; this increases bond strength while reducing slip (Vint, 2012). Once lugs are damaged, bond degradation begins. For either type of bars, friction is the main resistant force in the descending branch.

Past studies showed effectiveness and drawbacks of these models. Cosenza et al. (1997) determined parameters for modified-BPE (mBPE) and CMR τ-s relationships for multiple FRP bar types. This study provided a graphical approach to calibrate mBPE model parameters. Vint (2012) used this approach to obtain bond-slip curves from pullout tests and found reasonable parameters for different FRP bars with various surface finishings and anchoring conditions (straight, headed and, hooked bars). (Focacci et al., 2000) proposed methods to calibrate CMR or mBPE models using MSE criterion through iteration. (Pecce et al., 2001) proposed a similar procedure for mBPE models. Both studies remarked on the impact of embedment length (l_e) has relative to l_d: when $l_e \geq l_d$ slip is negligible at the free end, simplifying model calibration relative to when this condition was not met ($l_e < l_d$). The inclusion of end slip increases computational effort to obtain bond-slip parameters (Focacci et al., 2000), resulting in a cumbersome process.

Finally, other approaches do not require test data and are derived from mechanics. (Sezen and Setzler, 2008) proposed a model for steel-RC where bar stresses from external forces are related to corresponding strains. This approach assumes a linear strain profile along the embedded bar that varies from 0 (free end) to ε_s (loaded end). Strain is integrated along the embedment length to get slip elongation. This model accounts for yielding and strain hardening where additional anchorage length, l_d', is needed to develop larger stresses (Fig. 2.15) than f_y. This model was compared with other τ-s models; results showed good agreement. A drawback is that the model is based on $l_e \geq l_d$ to ensure linear strain variation from 0 to ε_s is feasible and free end slip is negligible. $l_e < l_d$ produces instability in this model as bar free end slips, failing to satisfy equilibrium conditions and making this approach inadequate.

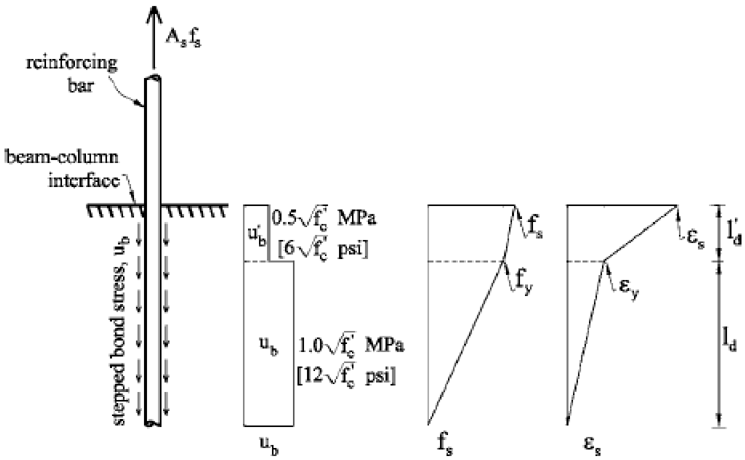

Figure 2.15 Slip model proposed by Sezen and Setzler (2008).

Bar elongation causes rigid body rotation of the anchored member. With rotation and element length, slip-based deflections can be estimated and added to other deflection types such as curvature by superposition. Equations 2.9 and 2.10 show slip rotation and deformation expressions, respectively (Sezen and Setzler, 2008).

$$\theta_s = \frac{\delta_s}{d - c} \tag{2.9}$$

$$\Delta_s = \theta_s L \tag{2.10}$$

δ_s is bar elongation (slip), d is the effective depth of tension reinforcement, c is cross-section neutral axis depth at a determined load level, and L is the rigid body length.

2.7.3.2. Testing Methods to Characterize Bar-Concrete Bond

Models depend on parameters that require calibration based on test data. Bond tests are used to characterize bond response. These tests are divided into pullout tests and beam-bond tests. Pullout tests are most common due to their simple setup and economical accessibility to collect test data (Achillides and Pilakoutas, 2004). The test setup consists of a concrete cylinder or prism with bars embedded to a defined length (Fig. 2.16(a)). The bar is then pulled out of the concrete. Load-slip data is collected to determine bond strength and build a τ-s curve. Given the loading condition, support conditions, and concrete cover used in this approach, results attained provide an upper-bound bond-slip response (Lin and Zhang, 2014). More realistic values may be found from bond-beam tests, where specimens are not subjected to lateral compression that increases confinement while also having smaller concrete covers representative of beams in practice. The combination of these aspects creates flexural cracks, which significantly reduce bond strength (Tighiouart et al., 1998). Bond-beams are tested under four-point bending with differences in setups varying depending on method followed. There are three well-established guidelines to characterize bond response through bond-beam tests: ACI 208, (1958), (BSI 12269-1 (2000), and RILEM TC-RC5 (1994), illustrated in Figs. 2.16(b-d). Since these were conceived for steel-RC, researchers modified setups for FRP-concrete bond behaviour. Tighiouart et al., (1998) tested 64 RILEM beams using different bar materials (GFRP and steel), diameters, and embedment lengths. They proposed an alternate expression applicable for the ascending branch of the CMR bond-slip model by (Cosenza et al., 1997). This study also suggested l_d modification factors used in North American design provisions (Subsection 2.7.2). Pecce et al.'s (2001) tests were used to demonstrate the effectiveness of a procedure to calibrate parameters for mBPE models (Cosenza et al., 1995). (Makhmalbaf and Razaqpur, 2022) fabricated beams following ACI 208 and RILEM TC-RC5. Their investigation compared these different methods and analyzed the validity of assuming a uniform stress distribution along bar embedded length. They concluded that both specifications give similar results and recommended ACI's notched beams over RILEM's hinged beam as the former were easier to fabricate. Results also showed that the stress distribution within the embedded bar was far from uniform.

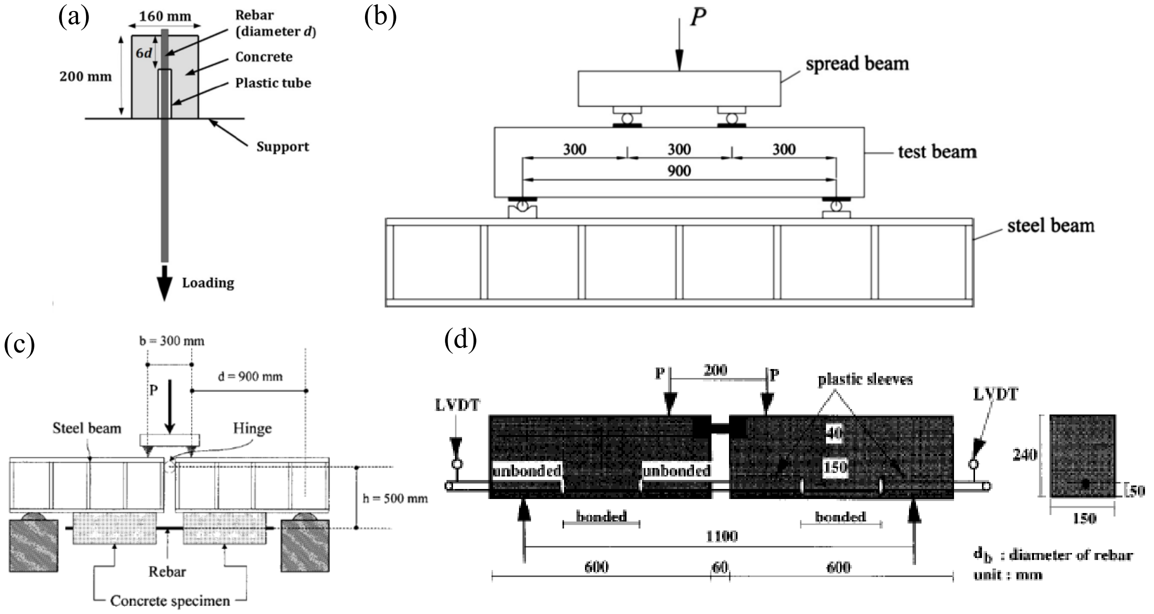

Figure 2.16 Test setups for (a) pullout test (Rolland et al., 2019), (b) modified beam test (Lin and Zhang, 2013), (c) hinged beam test (Pecce et al., 2001), and (d) hinged beam test (Tighiouart et al., 1998).

2.8. Digital Image Correlation

Digital Image Correlation (DIC) is a non-contact optical technique used to capture surface deformations in an area of interest from strains and displacements (Mccormick and Lord, 2010). Basic DIC hardware is composed of a high-resolution camera (or two for 3-dimensional measurements), lights, textures, and image processing software. Lighting is optional but typically used to prevent light changes like shadows from affecting measurements. DIC works by tracking movements of defined unique texture patches of pixels (or voxels in 3-D systems). The uniqueness of patches is created by imposing textures (or speckles) randomly on a surface so that the image processing software can track movements of patches relative to a reference image. Textures (or speckles) vary in dot size/spacing and are determined according to the size of the area of interest; a good dot pattern will capture very small shifts, within subpixel (or subvoxel) precision, in images. Finally, image processing software extracts images and processes them through a predefined algorithm to establish differences between a reference image subset with a target subset (Pan, 2011). These differences are reported as strains or displacements that can be used for determining curvatures and other measures.

According to (Sutton et al., 2009), DIC roots are date to the 1950s when first efforts in image correlation were registered when analog photographs were compared to highlight features from different views by Gilbert Hobrough. In the following decades the growing of artificial intelligence marked the developing of vision-based algorithms which contributed to photogrammetry field. Advances on this field after the 1980s focused on improving the quality of images taken and reducing difficulties to process images through algorithms, optimization methodologies, and reduction of errors. A milestone was attained when Sutton et al., (1983) proposed an algorithm which will be known as 2D-DIC. This algorithm matched optical images in a test setting. This analysis mainly focuses on processing images without in-plane changes (i.e., 2-D); if in-plane changes are a concern, 3D-DIC tools should be used. Regardless of what type of DIC is used, it is an alternative to other sensors like strain gauges that may be more complex to install and depend on several external factors (e.g., noise, vibrations, light) to draw precise data. DIC's primary advantage is that it provides data over an entire collection region rather than at a single point like many conventional sensors.

DIC has been used in structural engineering in experimental and practical applications. For field applications, McCormick and Lord (2010) proposed its use for structural health monitoring as a cost-effective alternative to visual inspections by field engineers which could be biased and subjective due to inspector fatigue. (Oats et al., 2022) reviewed recent studies following this premise and found positive feedback from DIC. Tests using DIC are common and widely used in many setups and structures. Their main applications are to track material strength, crack patterns, and failure mechanisms. For instance, (Fayyad and Lees, 2014) tested beams in under three-point bending to establish DIC's accuracy in quantifying fracture properties in reinforced concrete, obtaining good agreement with results obtained with other sensors.

2.9. Gaps in Research

Though there is a wealth of work on bond-slip, FRP-RC, and other facets presented in this chapter, gaps in research related to the thesis objective were identified. It was noticed that limited tests on AT single-slope barriers have been performed with only one technical report presenting work on this shape (Ahmed et al., 2010). Moreover, most sources presenting barrier tests did not include realistic overhang lengths which is a key factor for flexibility and strength (Ahmed et al., 2011). All sources reviewed provided test results or theoretical ones derived from finite element analysis. However, a source where analytical models were proposed to analyze this type of systems was not found. Even though finite element modelling is a far-reaching tool, it may become cumbersome to use or interpret while analytical models are simpler to build and understand.

Few studies have considered the dowelling repair technique on bridge decks or barrier-deck joints. To the author's beset knowledge, the most recent was performed in 2014 by El-Salakawy and Islam (2014). There are no available standards or codes to regulate this repair technique, particularly with FRP bars. This raises questions on how these structures are being repaired and how industry is attempting to build expertise to increase FRP's viability for designers and project managers.

Finally, given the total width of structures tested, these are expected to be subjected to one-way action leading to squat behaviour which could be analyzed by STMs. To the writer's best knowledge, limited to no literature was found where STMs were used to analyze bridge barrier/deck joints.

3. EVALUATION OF REPAIR TECHNIQUE EFFECTIVENESS FOR BRIDGE BARRIER/DECK SYSTEMS WITH GLASS-FIBRE REINFORCED POLYMER BARS USING MECHANICS BASED MODELLING

3.1. Introduction

Fibre-Reinforced Polymer Reinforced Concrete (FRP-RC) has emerged as an appealing option for bridge element construction. FRP’s chloride resistance and high strength provides a cost-effective substitute to steel-RC under harsh environmental conditions. Still, many FRP-RC applications are considered experimental (Kim, 2019). This is attributed to lack of knowledge and expertise using FRP reinforcement, which raised questions regarding long-term performance in the past (Uomoto, 2000). Despite these, many authors have shown FRP-RC’s potential in construction (Benmokrane et al., 2006; Benmokrane et al., 2007; Mufti et al., 2007) which had favoured FRP-RC elements use in bridges with deck slabs and barriers the most common applications.

FRP-RC barriers have been tested to establish their crashworthiness and durability. Studies show that FRP-RC barriers achieve similar strength and energy absorption relative to steel-RC counterparts (El-Salakawy et al., 2003; El-Salakawy et al., 2004; El-Gamal et al., 2008). To attest this, static and dynamic tests are used (e.g., monostatic, pendulum impact, and crash tests) to assess performance prior to consideration for real applications. However, most studies are done with a sound, continuous concrete matrix. Moreover, most of support conditions specimens were subjected to do not reflect real life boundary conditions (e.g., overhang deck slabs with limited anchoring space for reinforcement bars), not to mention that repair techniques were not included in their experimental program.

Limited work has been done in bridge barriers mimicking real life support conditions. (Matta et al., 2009) built specimens with a 914 mm long deck slab overhang. Test results highlight the importance of deck capacity on the overall structural performance. (Ahmed et al., 2011) found similar conclusions. Other tests (Rostami and Dehnadi, 2016); (Rostami et al., 2018); and (Rostami et al., 2019) evaluated the anchorage capacity of GFRP-RC barriers with different bar types (e.g., bent bars, headed-ends). Findings suggest that these bars could sustain loads without exhibiting significant damage. Still, tests were performed on overhangs smaller than 1000 mm. Other studies ran dynamic tests in overhang-barrier systems (Sennah et al., 2018) using crash tests to establish the crashworthiness GFRP bars with headed ends in a 30 m-long specimen. Even though there are many studies conducted on barrier performance, to the writer's best knowledge, no studies were found upon deck slab overhangs larger than 1000 mm, which is common in real bridges. Moreover, most research found was experimental with some computational modelling in recent studies. No analytical models using any programming software was found.

This chapter proposes an analytical approach to analyze the behaviour of a barrier – deck overhang structure subjected to an incremental static loading. This model was written in MATLAB using cross-sectional analysis based on M-ψ relationships. Curvature and bond-slip deformations were determined. Failure analysis was performed to define peak load and failure modes. The model was be compared to results from tests in literature to establish limitations and accuracy. Finally, a parametric study was be conducted to analyze the impact of some variables in the response of the structures under study.

3.2. Analytical Model

3.2.1. Model Idealization

3.2.1.1. Original Structure Description

The program was developed to analyze a deck overhang–barrier system that simulates the tests described in Chapter 4 (Fig. 3.1(a)). The model assumes the structure is supported on one end (simulating girders) with a barrier wall attached on the other end. The structure is subject to monostatic loading 775 mm from the top of the deck. The overhang permits vertical movement of the deck.

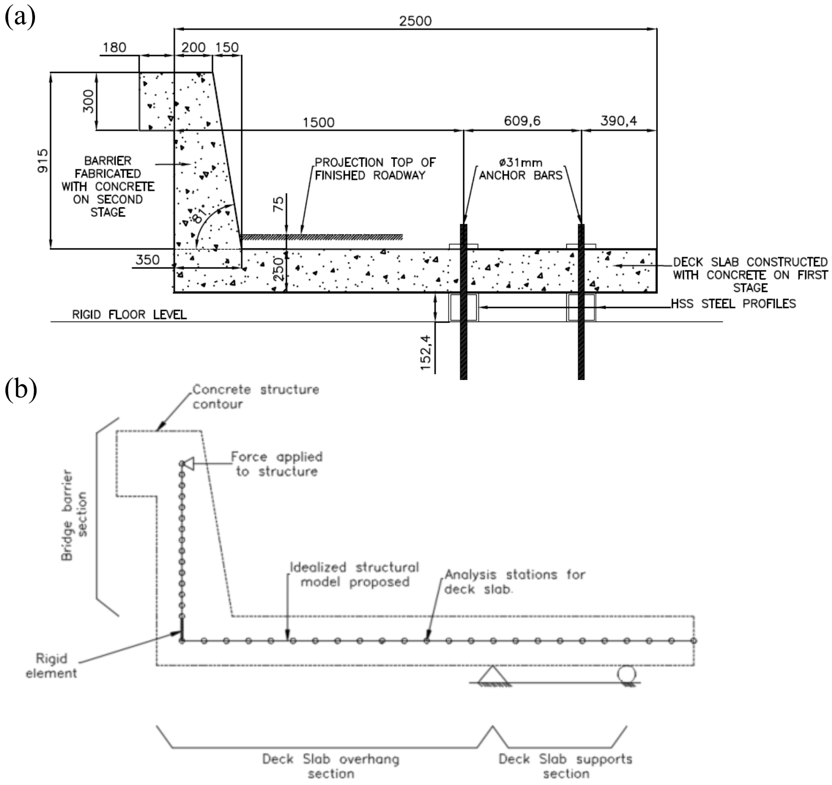

Figure 3.1 Deck-Barrier structure (a) test specimen dimensions (units of mm) and (b) idealized model.

3.2.1.2. *Structure Modelled by Program*

Idealization was done to reduce analysis complexity (Fig. 3.1(b)). The structure was modelled as a beam with an overhang section. Though it increases complexity, rotation of the deck slab between front and rear deck slab supports had an important contribution to deflections. A rigid element at the barrier/deck interface was used as this region is not expected to experience curvature-based deformations.

The program discretizes the barrier along its height until the load point. Sections above the load point are neglected since they are not expected to contribute to strength. The structure is divided into analysis stations where cross-sectional and material specifications is stored.

3.2.2. Model Development

The analytical model is composed of four steps: cross-sectional analysis, failure analysis, curvature deflections, and slip deflections.

3.2.2.1. *Cross-sectional Analysis*

1. An arbitrary top fibre compressive strain and neutral-axis depth are used to begin iterative analysis. Forces are calculated for each bar and concrete layer where stresses are recorded. Material stresses are computed following Subsection 3.2.4.

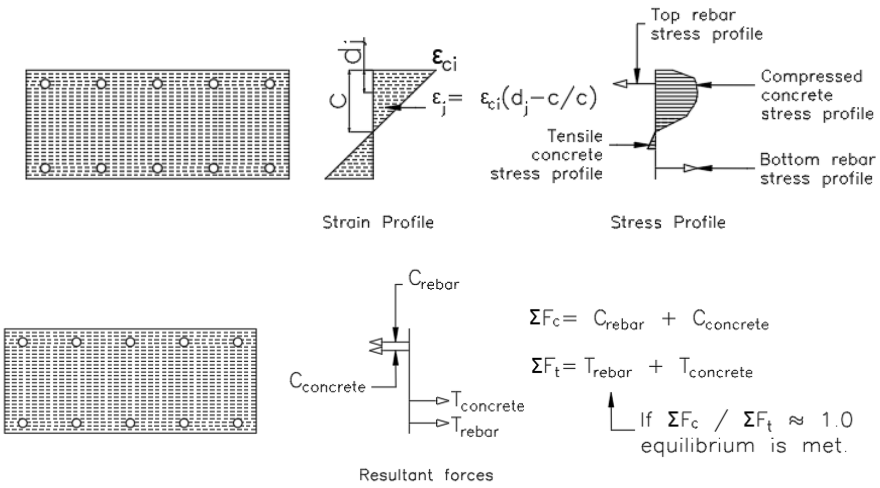

Figure 3.2 Cross-sectional analysis performed for a given compressive concrete strain.

2. Force equilibrium is achieved by changing the neutral-axis depth. Neutral axis depth is changed until tension and compression forces are approximately equal (iteration stopped once difference was less than 0.2%).
3. Moment is calculated about the top fibre using forces and moment arms derived from Steps 1 and 2.
4. Concrete compressive strain shifts to the next increment. Increments depend on the condition of the cross-section (e.g., cracking, first yielding). For all types of structures, the initial strain increment is 1×10^{-5}. GFRP-RC elements use an increment from cracking until failure of 2×10^{-5}. Steel-RC will use increments of 1×10^{-5} from cracking to first yielding and 1×10^{-4} from yielding to concrete crushing. Steps 1 through 3 are repeated until concrete compressive strain reaches crushing (i.e., $\varepsilon_{cu} = -0.0035$).
5. The process from Steps 1-4 is repeated for other cross-sections where properties (depth, reinforcement ratio) change. The model also performs cross-sectional analysis for elements under combined flexural-tension (such as the deck) or flexural-compression. Combined flexure/axial load is accounted for in Step 2 by

adding an axial force acting at the cross-section centroid. The process is repeated for a family of axial forces declared by the user. Fig. 3.3 describes this procedure.

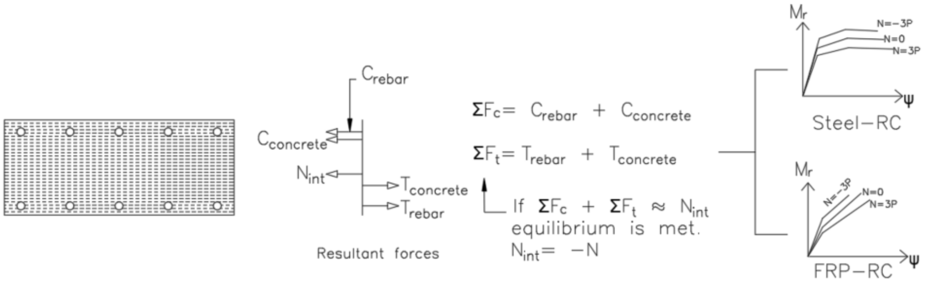

Figure 3.3 Iterative procedure for compressive strains to calculate M_r accounting for the effect of axial forces.

3.2.2.2. *Loading and Failure Analysis*

1. Load-control test features are inputted by user, such as maximum load and number of load stages. This gives loading rate increments.
2. Program calculates moments at each station at each loading stage up to maximum force defined in Step 1.

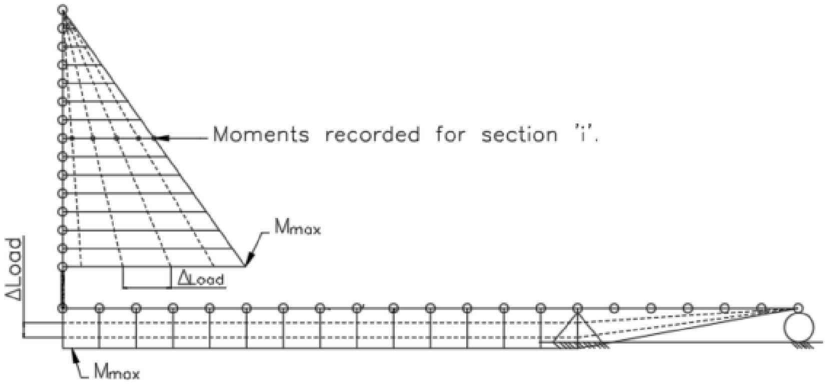

Figure 3.4 Bending moment diagram for each load increment along barrier-deck slab structure.

3. **Flexural failure:** Program determines which station would fail first according to their flexural strength from M-ψ and the applied load that is needed to create this moment. The program indicates which is the critical element (i.e., deck or barrier).
4. **Bond failure:** Bond-critical capacity based on bar stresses found from cross-sectional analyses accounting for monolithic (i.e., sound concrete) and repaired (i.e., doweled bars of bridge barrier) conditions. For FRP-RC members, an achievable bar stress is determined using Eq. 3.1 and 3.2. Steel-RC members

undergo similar analysis for bond-critical strength based on expressions from CSA S6:19 for straight and hooked bars.

$$f_{fe} = \frac{0.083\sqrt{f'_c}}{\alpha}\left(13.6\frac{l_e}{d_b} + \frac{C}{d_b}\frac{l_e}{d_b} + 340\right) \tag{3.1}$$

$$f_{fe} = \frac{l_e f_{cr}}{0.45k_1k_4}\left(d_{cs} + k_{tr}\frac{E_{FRP}}{E_s}\right) \tag{3.2}$$

Terms for Eq. 3.11 and 3.12 are the same as those in Subsection 2.7.2 for Eq. 2.5 and 2.4.

5. **One-way Shear failure:** CSA S6:19's general method is used to compute concrete's shear resistance (V_c) at each load step until the step when failure by shear is expected to occur in the barrier (i.e., when acting shear force surpasses capacity). These structures have negligible shear in the deck, so deck shear was not checked.
6. **Barrier-Deck Interface Failure:** El-Metwally and Chen's (2017) STM approach for knee joints under opening is used. This method relates acting force P_{act} to compressive force in the strut C_{strut} and determines the load when the acting force exceeds strut capacity at its interface with nodal zones (i.e., when the interface fails). Capacity of nodal zones and struts follow ACI 318-19 reduction factors for nodes and strut strength (see ACI 318-19 Chapter 23 and Section 2.6 for details). Given the load and support conditions structures are idealized, concrete components of STM are prone to more severe action with respect to ties and thus it is assumed that these are not excessively stressed.

3.2.2.3. Curvature-based Deflections

1. Program adjusts M-ψ diagram where uncracked-cracked transition occurs. Due to stiffness loss from cracking, curvatures in that zone have more than one possible moment which causes problems with linear interpolation. Thus, this region is approximated as a positive slope line which connects points immediately before and after cracking (Fig. 3.5).

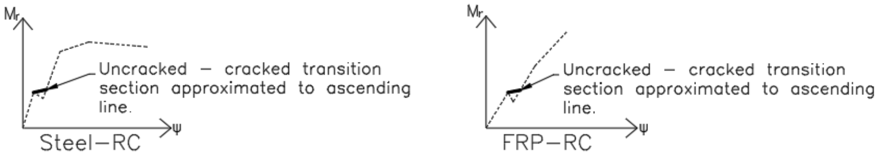

Figure 3.5 $M - \psi$ 3plots adjustment at uncracked-cracked region.

2. Linear interpolation on adjusted M-ψ plots from the previous step is done to obtain curvatures related to acting moments in each station and at each load stage. Program accounts an initial bending stresses due to overhang self-weight from deck slab and barrier to acting moments from each load step so interpolated curvatures account for these at each analysis station. Fig. 3.6 depicts this analysis.

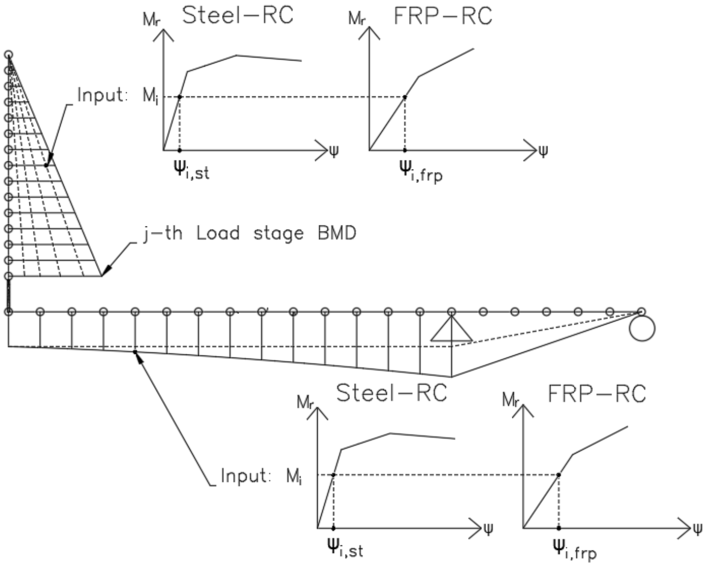

Figure 3.6 Interpolation of curvatures related to acting bending moments.

3. Curvatures are used to calculate deflections using moment-area theorem. For an overhang beam, the contribution of the portion of the element between supports adds up to the total overhang deflection (Fig. 3.7). Deflection $Y_{a/b}$ is determined and then by similar triangles $Y_{c/b}$ is computed as the slope at both sides of Support B are the same. Y_{curv} is added to $Y_{c/b}$ to have find deflections at the overhang tip.

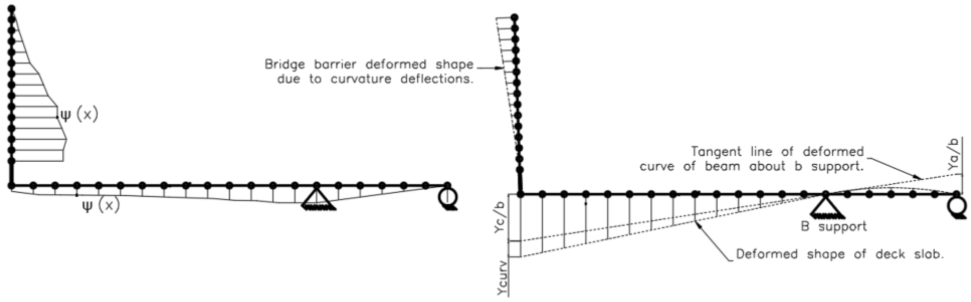

Figure 3.7 Curvature deflections computed by moment-area theorem.

3.2.2.4. *Slip-based Deflections*

1. Reinforcement stress, known from M-ψ, is recorded at the base of the barrier where bond-slip deformations are expected.
2. Bond-slip models are plotted for steel-RC and FRP-RC. Multiple models were generated for each material (Subsection 3.3.2.1).
3. Program calculates bond stresses based on reinforcement tensile force and bar geometry (diameter and embedment depth) at each load stage using Eq. 2.1.
4. Bond stress is used to interpolate slip elongation using BPE, mBPE, and CMR models. In the case of Sezen and Seztler's (2008) approach, elongation is obtained by calculating the strain of a particular bar stress level using mechanics. Fig. 3.8 shows the procedure to determine slip deflections.

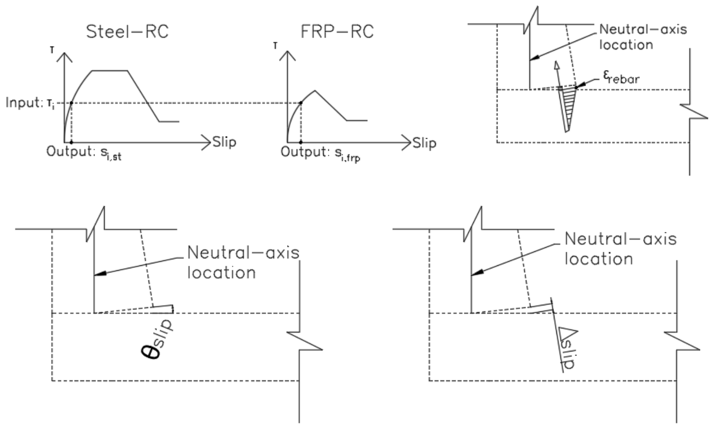

Figure 3.8 Determining slip related to bond stress and bar elongation and then finding bond-slip deformations.

5. Slip elongations are used to calculate rotations and bond slip deformations along the barrier wall (Fig. 3.8).

6. With slip and curvature-based deflections calculated, program uses superposition to report total deformation.

3.2.3. Assumptions

The following assumptions were considered:

1. Plane sections remain plane.
2. Shear deformations are negligible.
3. Systems dominated by one-way action (two-way action ignored).
4. Free-end slip of bars was negligible to reduce the complexity of analysis and allowed the use of selected bond-slip models.
5. For bond-critical sections, Clause 25.4.2.4 from ACI 440.11 (2022) and CSA S6 (2019) clause 16.8.4.1 were used to predict the maximum developable bar stress as a function of embedment length (Eq. 3.1 and 3.2). The smallest stress computed with these terms was chosen to determine bond-critical capacity. The proposed systems have minimum embedment around $12\ d_b$ which are less than ACI and CSA minimums. Applicability of these expressions will be compared to tests in Chapter 4.

3.2.4. Materials

3.2.4.1. Concrete

Concrete's compression stress-strain relationship was modelled using (Hognestad, 1952) parabolic model (Equations 3.3-3.5). This model was selected as it generally depicts concrete compressive response well for most analyses, although the model is intended for normal strength concretes. This implies that its use for higher strength concrete would lead to small strength differences which are not expected to affect the overall response of the analyzed structure.

$$f_c(\varepsilon_c) = f'_c\left(\frac{2\,\varepsilon_c}{\varepsilon_0} - \left(\frac{\varepsilon_c}{\varepsilon_0}\right)^2\right) \tag{3.3}$$

$$\varepsilon_0 = \left(\frac{2\,f'_c}{E_c}\right) \tag{3.4}$$

$$E_c = 12680 + 460\,f'_c \tag{3.5}$$

Expression 3.3 determines concrete stress (f_c) at a defined strain, ε_c. Equations 3.4 and 3.5 for ε_0 and E_c are the compressive peak strain and the tangential initial Elastic Modulus, respectively. In all equations, f'_c is the concrete cylinder compressive strength.

The cracking strength of concrete, f_{cr}, follows CSA S6:19 unless papers used for comparison reported f_{cr} from material tests. Tensile stress-strain development was considered linear with a slope of E_c until f_{cr} was exceeded (see Equation 3.6). After this point, no tension stiffening was accounted by the program.

$$f_{cr} = 0.4\sqrt{f'_c} \tag{3.6}$$

3.2.4.2. *Steel Reinforcement*

A bilinear elastic-plastic constitutive model was used for steel stress-strain curve (Eq. 3.7 and 3.8). Response for tension and compression was assumed to be the same.

$$f_s(\varepsilon_s) = \varepsilon_s\, E_s \qquad \varepsilon_s \leq \varepsilon_y \tag{3.7}$$

$$f_s(\varepsilon_s) = f_y \qquad \varepsilon_s > \varepsilon_y \tag{3.8}$$

Where E_s is the Elastic Modulus of steel (assumed to be 200 GPa), and f_y is the steel yield stress, assumed as 400 MPa unless reported otherwise.

3.2.4.3. *GFRP Reinforcement*

GFRP is assumed to be linear elastic to failure (Eq. 3.9). GFRP's contribution in compression was considered but effects of GFRP in compression were negligible for the members considered.

$$f_f(\varepsilon_f) = \varepsilon_f\, E_{FRP} \qquad \varepsilon_f \leq \varepsilon_u \tag{3.9}$$

Here E_{FRP} is the GFRP elastic modulus and ε_u the ultimate GFRP strain. Specific values considered are discussed in Subsection 3.3.

3.2.5. Constitutive Models

3.2.5.1. *Bond-Slip (τ-s) models*

Two bond-slip models were considered for steel-RC elements (BPE (Ciampi et al., 1982) and Sezen and Setzler (2008)) and three for GFRP-RC members (m-BPE (Cosenza et al. 1995), CMR (Cosenza et al., 1997), and Sezen and Setzler (2008)). More details are found in Subsection 2.7.3.1.

FRP-RC τ-s models are highly dependant on bar surface finishing (Cosenza et al., 1997). Steel-RC is more sensitive to confinement effects (CEB-FIP 1990). There is a wide variety of surface finishing for FRPs, and each requires parameters calibrated with test data. In absence of this information, parameters from different sources (CEB-FIP, 1990; Cosenza et al., 1997; Focacci et al., 2000; Pecce et al., 2001; Vint, 2012) were considered. Parameters are presented in Subsection 3.4.3 for each study selected for comparison.

To generate τ-s curves, Equations 3.10 through 3.12 were used for BPE, mBPE, and CMR model, respectively.

$$\tau(\mathrm{s}) = \tau_1 \left(\frac{\mathrm{s}}{s_1}\right)^{\alpha} \qquad \mathrm{s} \leq s_1 \qquad (3.10)$$

$$\tau(\mathrm{s}) = \tau_1 \left(\frac{\mathrm{s}}{s_1}\right)^{\alpha} \qquad \mathrm{s} \leq s_1 \qquad (3.11)$$

$$\tau(\mathrm{s}) = \tau_m \left(1 - \mathrm{e}^{-\frac{s}{s_r}}\right)^{\beta} \qquad \mathrm{s} \leq s_r \qquad (3.12)$$

The analytical program only plots the ascending branch of each model as the response up to peak load was the primary focus.

3.3. Model Validation

3.3.1. Introduction

The program was validated at first against tests performed by other authors that studied similar materials and structures to those within the scope of this thesis. Model validation is a three-stage process: (1) beam, (2) barrier validation, and (3) current experimental program. Beam tests establish the program's accuracy to predict simply supported element deflections. Selected papers tested specimens under three-point and four-point bending (Lau and Pam, (2010), Al-Sunna et al., (2012)). Beams were reinforced with different FRPs and steel bars so both responses were analyzed.

Barrier validation is based on three papers: El-Salakawy et al., 2003; Ahmed et al., 2011; and Azimi et al., 2014. These tests were performed monostatically on barriers with different geometries, support conditions, and widths.

Finally, analytical model was exposed to tested structures from proposed experimental program from this study to establish its agreement with their actual response. Details on the tests are given in Chapter 4.

3.3.2. Beam Tests Validation

Table 3.1 reports validation input information. Tests were organized using the nomenclature reported in each paper. Fig. 3.9 shows element cross-sections; details on test setups are available in corresponding studies.

Table 3.1 Input information for beam tests validation.

Study	**Specimen ID**	**Reinforcement type**	**Beam dimensions (width × height × length), mm**	**f'_c / f'_{cu}, MPa**	**f_r, MPa**	***F_y / f_{fu}, MPa***	***Es / Ef, GPa***	***ρ, %***
Lau and Pam (2010)	MD2.1-A90	Mild steel	280×380×4600	45.9	$4.07^{\dagger}$	400	200	2.1
	G2.1-A90	GFRP		41.3	$3.86^{\dagger}$	582	38	2.1
	G0.8-A90	GFRP		36.6	$3.63^{\dagger}$	593	40	0.8
Al-Sunna et al. (2012)	BG-2	GFRP	150×250×2550	47.7^{*}	$3.8^{\ddagger}$	620	41.6	0.77
	BC-3	CFRP		51.8^{*}	$3.8^{\ddagger}$	1475	119	1.16
	BS	High strength steel		52^{*}	$4.1^{\ddagger}$	590	200	0.69

*: Values reported for cube compressive strength.

†: Authors did not specify modulus of rupture. Reported values calculated using expressions from CSA S6.

‡: Values reported for split cylinder tests.

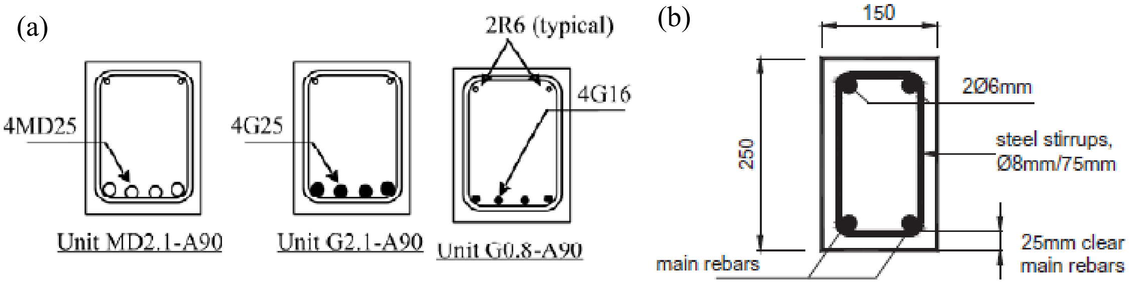

Figure 3.9 Typical cross-sections for beam tested in (a) Lau and Pam (2010), and (b) Al-Sunna et al., (2012).

Al-Sunna et al.'s (2012) properties were found using different tests to those used in Canada (cube compressive or split cylinder tests). Values used as input for the model were calculated using Eq. 3.13 and 3.14. Elwel and Fu (1985) established that the cylinder/cube compressive strength ratios range between 0.65 and 0.90. An 0.80 factor was selected as it was close to the average value between low and upper boundaries.

$$f'_c = 0.80f'_{cu} \tag{3.13}$$

$$f_r = 0.6\sqrt{f'_c} \tag{3.14}$$

Figure 3.10(a - c) shows load-deflection curves for tests by Lau and Pam (2010) and those obtained by the model. Graphs from Lau and Pam (2010) (Fig. 3.10(d - f)) started at 20 kN; data below 20 kN was unavailable.

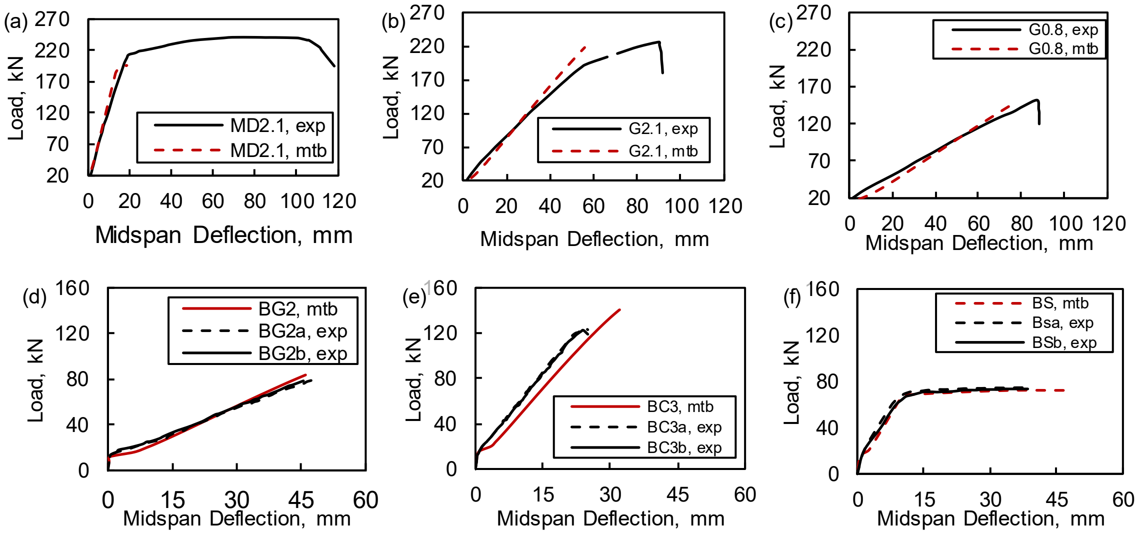

Figure 3.10 Load deflection curves obtained by model (subscript mtb) and those reproduced from original data (subscript exp). Lau and Pam (2010): (a) MD2.1-A90, (b)G2.1-A90, and (c) G0.8-A90 beam tests. Al-Sunna et al. (2012): (d) BG2, (e) BC3, and (f) BS beam tests.

For Lau and Pam (2010), analytical curves have similar stiffnesses to test counterparts. MD2.1 test curves (Fig. 3.10(a)) did not report similar yielding and could be attributed to different material strengths than used for the validation given the lack of information available in said paper. Moreover, the model curve was unable to track the yielding plateau which is related to the load-control nature of the program which terminates program before yielding occurs, deriving in plotting irregularities. For G2.1 (Fig. 3.10(b)), program reached peak load at a higher load of what test reported (217 versus 192 kN), but almost same deflection than experimental counterpart (55.9 mm and 56 mm, accordingly). G0.8 (Fig. 3.10(c)) show that peak load had a good agreement between test and analytical results with a 1.05 ratio (experimental/analytical); deflections reported a 1.16 ratio. In any of the plots, post-peak responses observed in experimental curves were not modelled by the program as the model used a load-control philosophy.

Al-Sunna et al. (2012) tests are compared to the model in Fig 3.10(d - f). In general terms, analytical results show good resemblance to test data. Uncracked regions had almost the same slope and cracking load. Cracked regions have slight variations for BG2 (Fig. 3.10(d)) and BS (Fig. 3.10(f)), but more notable in BC3 curves (Fig. 3.10(e)), where the model had larger deformations, but similar stiffness (slope) compared to tests. Model peak loads were like tests: BG2's ultimate response was reached by program at a 0.97 ratio (experimental/analytical), while BC3 and BS at 0.87 and 1.03 ratios, respectively. Peak loads were in all cases in agreement between experimental and analytical results with slight percentage differences in BC3 curves. Peak deflections on the other hand were close in specimens assessed with some differences recorded in BG2 and BC3 analytical plots. For the case of BS beams, the curves from either test or program were in good agreement depicting almost the same response along the tests.

3.3.3. Barrier Tests Validation

Table 3.2 shows validation input information. Test IDs are the same as listed by the original authors of each paper. Fig. 3.11 illustrate cross-section geometries, reinforcement layouts, and test setups for each paper. Slip deflections were accounted as well through multiple parameters and models. Results were compared to assess which showed better resemblance with test curves since that information on these relationships is absent from considered papers. Models used were mentioned in Subsection 3.2.5 with further details given in Subsection 2.7.3; Table 3.3 shows some of the parameters used to generate bond-slip curves for each study used for validation.

Table 3.2 Input information for barrier test validations.

Study	Specimen ID	Reinforcement type	Specimen width (mm)	f'_c (MPa)	f_r (MPa)	F_y / f_{fu} (MPa)	E_s / E_f, (GPa)
El-Salakawy et al. (2003)	PL-3 Steel	Mild steel	2000	45	4.03†	400	200
	PL-3 GFRP	GFRP				640	41
Ahmed et al. (2011)	311-Steel-2	Mild steel	2600	39.4	2.51†	400	200
	311-GFRP-2	GFRP				656	47.6
Azimi et al. (2014)	PL-3 TS	Mild steel	1200	32	2.26†	400	200
	PL-3 TG1	GFRP		30	2.19†	1188	64

†: Authors did not specify modulus of rupture. Reported values calculated using CSA S6:19.

Table 3.3 Particular bond-slip parameters used for barrier tests validation, according to bond-slip models.

Barrier test Source	Bond-slip Model Source	mBPe Model		CMR Model	
		S_1 (mm)	τ_1 (MPa)	S_r (mm)	τ_m (MPa)
El-Salakawy et al. (2003)	Cosenza et al. (1997)	2.83*	7.07†	2.83*	7.07†
	Focacci et al. (2000)	-	4.70‡	-	-
Ahmed et al. (2011)	Cosenza et al. (1997)	2.66*	8.08†	2.66*	8.08†
	Focacci et al. (2000)	-	5.07‡	-	-
Azimi et al. (2014)	Cosenza et al. (1997)	7.63*	6.58†	7.63*	6.58†
	Focacci et al. (2000)	-	11.80‡	-	-

†: Values obtained by using Wambeke and Shield (2006) expression using recorded stresses in materials.
*: Slip elongation determined by using mechanics-derived expression relating bar stress, stiffness, and bond-stress (see †).
‡: Focacci et al. (2000) provided a fixed value for slip elongation used to calculate bond-stress using mechanic-based expressions.

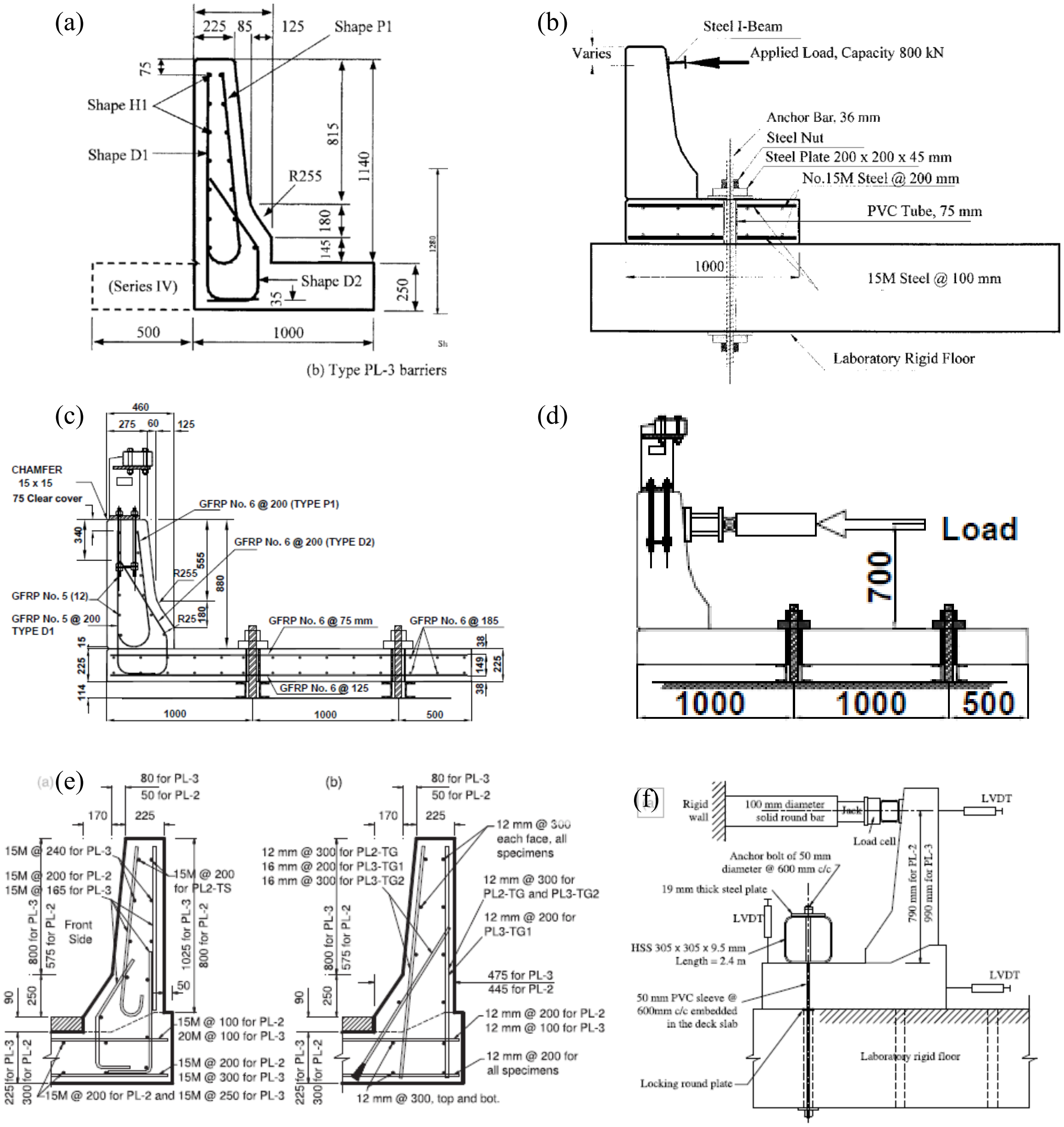

Figure 3.11 Specimen geometry and rebar layout details for El-Salakawy et al. (2003) (a and b), Ahmed et al., (2011) (c and d), and Azimi et al. (2014) (e and f). All measurements in mm.

Figure 3.12(a – b) show load deflection curves from El-Salakawy et al. (2003); Fig. 3.12(c – d) from Ahmed et al. (2011); and Fig. 3.12(e – f) from Azimi et al. (2014). Each curve plotted used different bond-slip relationships that best suited experimental graphs, though bar slippage did not have a significant impact with test outcomes. Moreover, applied loads or moment at base were used as y-axis from graphs. This is consistent with how authors reported their curves in corresponding papers.

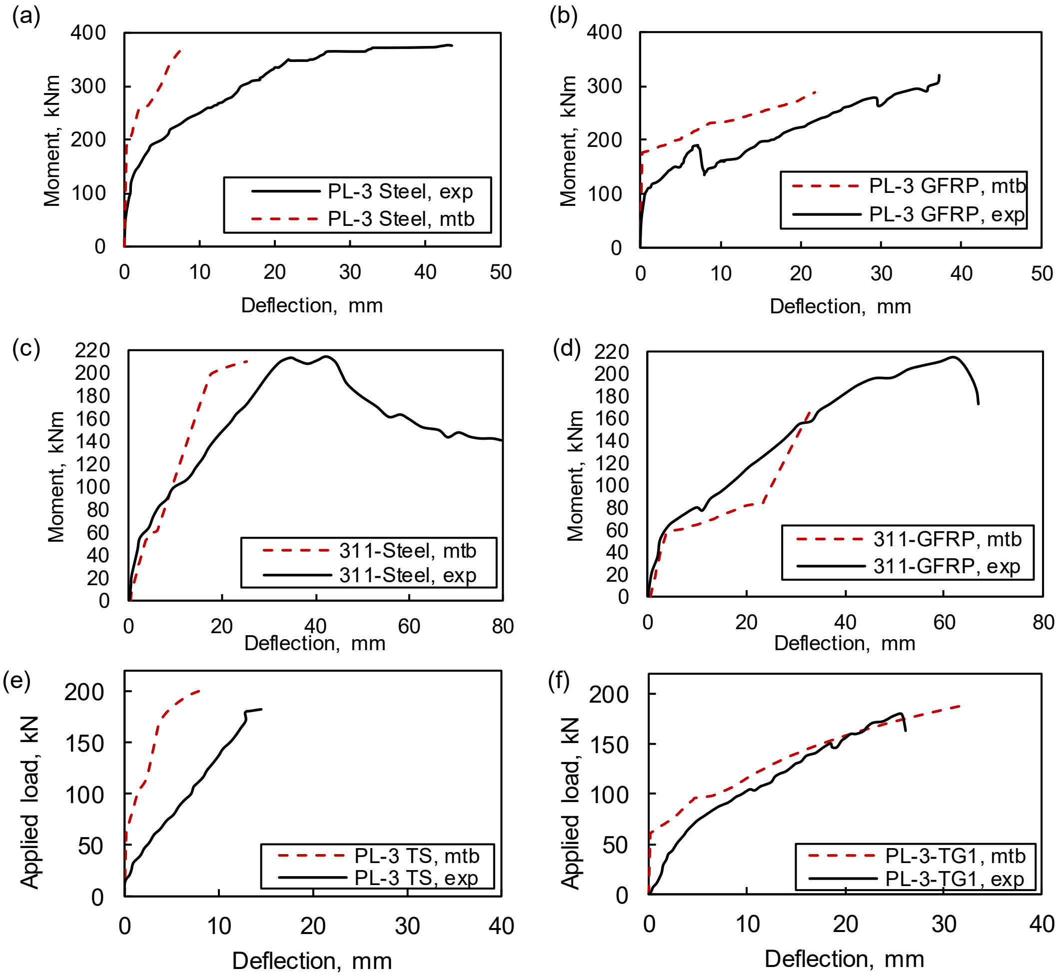

Figure 3.12 (a – b) El-Salakawy (2003) moment deflection curves for PL-3 Steel barrier and PL-3 GFRP barrier tests. (c – d) Ahmed at al. (2011) moment deflection curves for 311-Steel-2, and 311-GFRP-2 barrier tests. (e – f) Azimi et al. (2014) load deflection curves for (e)PL-3 TS, and (f) PL-3 TG1 barrier tests.

In all cases, peak loads and failure modes were generally predicted well (with 10% of tests), except for 311-GFRP curve which was 26% off. Stiffnesses had a great variation with El-Salakawy et al. (2003) and Azimi et al. (2014) reporting an overestimation of deflections by model curves; plots from Ahmed et al. (2011) showed that GFRP curve underestimated deflections, whereas steel one did the opposite. Plot discrepancies could be related to different aspects, like test setups selected papers used with respect to the model's assumptions and idealization. For example, El-Salakawy et al. (2003) and Azimi et al. (2014) had similar test arrangements where the deck was anchored to the strong floor (i.e., no overhang). This subjected the barrier to larger stresses that result in non-negligible shear deformations and a squat section in the case of El-Salakawy et al. (2003). Ahmed et al. (2011)

accounted deck slab contribution to the structure by mounting specimens on rigid elements in such a way that an overhang condition was formed. This induced deck to tensile forces that could have increased curvatures in its cross-section. This is the same load and support condition model was idealized. However, structures' widths control response inducing two-way action. Moreover, program presented some limitations related to its conception (e.g., no tension stiffening accounted, adjustments at cracking in $M - \psi$ curves), as well as the scope under it was created (i.e., analysis of structures under one-way response) affected plotted curves presented with respect to experimental analogues.

El-Salakawy et al. (2003) models were stiffer than tests (Fig. 3.12(a – b)) and attributed to aspects previously discussed. Despite these differences, PL-3 Steel curves had same peak load, while PL-3 GFRP curves recorded 1.11 peak load ratio. Cracking moments, however, were different. Moreover, program predicted same failure mechanism as tests (shear failure). Finally, models did not detect the drop in load around 7-8 mm displacement seen in the tests which was attributed to shear crack formation.

Ahmed et al. (2011) structures are compared to the program in Fig. 3.12(c – d). Both test and model curves saw the impact of axial tensile forces in the deck by softening structural response. Cracking moments (~60 kNm) were similar for both modelled and tested barriers; post-cracking sees significant stiffness variations as previously noted. For 311-Steel, yielding is observed prior to yielding at a moment around 200 kNm between a deflection of 30-40 mm; the model found same failure path with a 2.6% error at peak load but at smaller deflection. For 311-GFRP, the model had a dissimilar peak load from the test and at around half of deflection at failure. It is feasible that unaccounted displacements (e.g., relative slippage between specimen and strong floor, additional rotations due to support conditions) contributed to test deflections leading to these differences. Despite this, program was able to record failure by concrete splitting due to failure of compressive strut generated at barrier-deck joint.

Regarding Azimi et al. (2014) (Fig. 3.12(e – f)), similar response to El-Salakawy et al.'s (2003) steel-RC barrier test validation is observed here. For this case, peak load recorded agreed with the experimental results with an 8.9% error. PL-3 TG1 *mtb* curve showed stiffer response up to cracking reaching this state at a similar load than experimental analogue (62 and 55 kN-m for *mtb* and *exp* datasets, correspondingly) but at smaller deflection (0.30 mm versus 3.21 mm). Post-cracking region for both curves tend to have similar response up to failure. In terms of peak load, values were similar (0.94 ratio was attained), whereas corresponding deflection attained by model was larger than test observations, representing a 22.8% increment in deformability. This curve has a better agreement to other curves shown in this section and might be related to the width that specimens handled (1200 mm), restraining specimens' response to one-way action.

3.3.4. Experimental Program Validation

Table 3.4 reports test/predicted ratios obtained with analytical models when compared to test results from the experimental program presented in Chapter 4. See Chapter 4 for more background on the test setup and results. Figure 3.13 shows load deflection curves from tests (see Fig. 4.13) and program. A solved example of how the model analyze joint strength by STM is shown in Appendix F. Regarding strength, program was able to predict the same failure mode as tests and at similar peak loads when using $\beta_s = 0.4$, with SP-01, SP-02, and SP-03 having best agreement between measured and predicted peak loads. Using $\beta_s = 0.6$ prevented analytical model from drawing ratios close to unity for any specimens. A $\beta_s = 0.4$ is reasonable in this case as joints were subject to tension given the specimen loading and support conditions. Discrepancies found in SP-04 related to the early failure this specimen reported during tests compared with the response recorded by the program.

Table 3.4 Test-to-predicted ratios using peak loads from analytical model and tests using various β_s.

Specimen ID	Demand ratio, $\beta_s = 0.6$	Demand ratio, $\beta_s = 0.4$
SP-01 (peak load: 145 kN)	0.71	1.02
SP-02 (peak load: 93.5 kN)	0.73	0.97
SP-03 (peak load: 105 kN)	0.76	1.09
SP-04 (peak load: 103 kN)	0.77	0.84

In terms of load-deflection curves, analytical model curves were able to record first cracking of tested specimens. Post-cracking stiffness regions were underestimated for GFRP-RC in the model. However, a change of slope in curves after cracking shows how program-derived plots cross experimental ones, leading to a stiffer response up to peak load in all cases. Main reason for this slope change is related to moment-curvature adjustments at cracking and how curvatures in said area where obtained (i.e., linear interpolation), which could have drawn the imperfections observed in the graphs. More refined numerical methods, for instance including tension stiffening, may increase the accuracy of post-cracking curvatures. Despite this, analytical curves were able to provide accurate predictions in terms of loading stages, such as first cracking and peak loads.

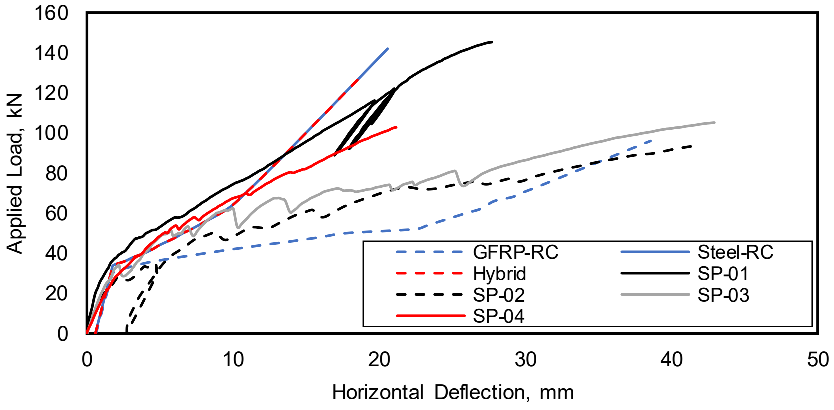

Figure 3.13 Load-deflection curves up to peak load from analytical model and sensors from tests at 775 mm above deck slab.

3.4. Parametric Study

A parametric study is presented with three parameters: overhang length, top/front bar spacing, and bond-slip models. Results are compared between each other as well as related to two control specimens. In total, 19 models were run. Table 3.5 presents values considered for each parameter; Table 3.6 defines reinforcement properties. Concrete cover details are given in Fig. 3.14; lateral concrete cover was 65 mm in all cases. Concrete used a compressive strength of 45 MPa, and a crack strength of 2.68 MPa (based on CSA S6:19 expression for normal density concrete). The same properties were used for both decks and barriers. An aggregate size of 20 mm was assumed. These specifications followed Alberta Transportation (2018) for cast-in-place decks and barriers in highway bridges. Concrete elastic modulus was computed using CSA S6:19 Clause 8.4.1.5.3, which gave 23.5 GPa. Finally, specimen width used for all models was 1500 mm, consistent to the width of specimens fabricated in Chapter 4.

Variables selected were shown in previous studies to have an important contribution to response during test: Ahmed et al. (2011) reported in their findings how the overhang of the deck contributed to the strength of tested barrier-deck structures. Other work conducted by El-Nemr et al. (2013) showed the importance of reinforcement axial stiffness, EA, to elements strength; this parameter is better visualized by increasing/reducing main rebar layout spacing. Fig. 3.14 illustrates these layouts, labelled with rebar IDs 1 and 3 for top and front assemblies, respectively. Referring to compression reinforcement, rebar ID-2 has the same spacing as ID-1, while ID-4 has double the spacing of ID-1 or 3. That means if front and top bars are placed at 150 mm, ID-2 will have a 150 mm spacing, and ID-4 will have 300 mm spacing. This applies to all rebar assemblies used in this parametric study. Two approaches to determine slip deflections were used: mBPE model (Cosenza et al., 1995) and Sezen and Setzler's (2008) approach. These were previously defined in Subsection 2.7.3 with their implementation to model explained in Subsection 3.2.2. Constants provided by Vint (2012) were used for mBPE model. Their selection was done to compare results from a constitutive model and a mechanical-based approach. Finally, different failure modes were assessed to determine which one recorded first failure. Namely, mechanisms entertained were failure by flexure, one-way shear, pullout, or diagonal tension. Curves plotted were captured until peak load (i.e., first failure) was attained.

Table 3.5 Parameter variations investigated.

Parameter	Variation 1	Variation 2	Variation 3
Overhang length (mm)	1000	1500	2000
Top/front rebar spacing (mm)	100	150	200
Bond-slip models	mBPE	Sezen and Setzler (2008) (S&S)	-

Table 3.6 Reinforcement bar properties used for parametric study (See figure 3.13).

Rebar ID	Area (mm²)	Elastic Modulus (GPa)	Ultimate / Yielding Stress (MPa)
G-1	285	62.7	1150
G-2, G-3, G-4	200		
S-1	300	200	400
S-2, S-3, S-4	200		

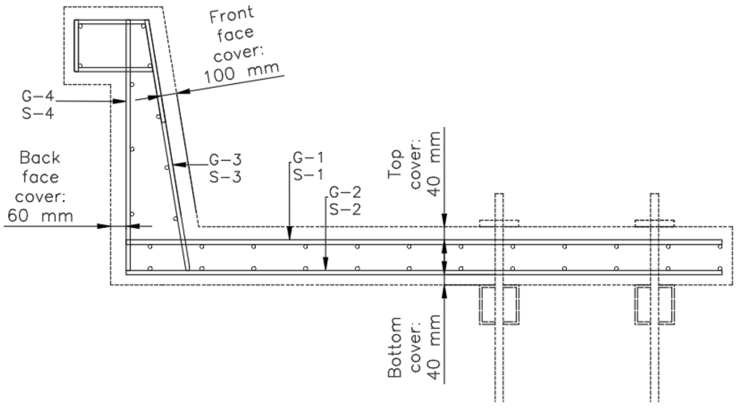

Figure 3.14 Reinforcement layout detail for parametric study.

3.4.1. Results

Table 3.7 presents results from all analyzed models with corresponding loads to reach each failure mode assessed in elements mentioned therein. Nomenclature used follows the following example: reinforcement material- overhang length- rebar spacing- bond slip model. So, GFRP-2000-150-mBPE is a GFRP-RC specimen with a 2000 mm overhang, 150 mm spacing for front/top rebar assemblies, and accounting for slip deformations using the mBPE model. Peak loads were compared with factored design load specified by CSA S6:19, which is 170 kN. Deflections reported were measured horizontally at the same height where load is applied (i.e., 775 mm from top of deck). As seen, no model reached S6 force threshold as governing failure mode (i.e., diagonal tension) happened first. This type of failure is related to large stress concentrations at a geometric discontinuity induced by a squat section given a restrained element width that derives in one-way action which was exacerbated by the presence of tensile forces in the joint, which greatly reduces the capacity of STM components (ACI 318R-19; CSA S6:19).

Moreover, it was noted that no other failure type assessed was close to diagonal tension's low peak load. Failure by flexure-tension action is not expected in any structure as it recorded the largest peak load, transition between shear to bond failure was recorded as bar spacing increases from 100 mm to 150 and 200 mm, though this did not collaborate to first failure recorded in any case.

Table 3.7 Key results obtained by baseline models.

Load needed to reach each considered failure mode, kN							
Model ID	**Flexure-Tension (Deck)**	**Pullout (Barrier)**	**One-way Shear (Barrier)**	**Diagonal tension (Deck, joint)**	**Governing (kN)**	**Deflection at peak (mm)**	**Critical element**
STEEL-1500-150-S&S				140	140	11.8	Deck slab, Joint.
GFRP-1000-100-mBPE	431	239	212	108	108	23.3	
GFRP-1500-100-mBPE	431	239	212	108	108	38.2	
GFRP-2000-100-mBPE	431	239	212	108	108	13.5	
GFRP-1000-150-mBPE	376	182	169	96	96	27.4	
GFRP-1500-150-mBPE	376	182	169	96	96	45.1	
GFRP-2000-150-mBPE	376	182	169	96	96	16.5	
GFRP-1000-200-mBPE	320	114	162	82	82	33.2	
GFRP-1500-200-mBPE	320	114	162	82	82	53.8	
GFRP-2000-200-mBPE	320	114	162	82	82	12.8	
GFRP-1000-100-S&S	431	239	212	108	108	24.3	
GFRP-1500-100-S&S	431	239	212	108	108	39.2	
GFRP-2000-100-S&S	431	239	212	108	108	13.5	
GFRP-1000-150-S&S	376	182	169	96	96	27.5	
GFRP-1500-150-S&S	376	182	169	96	96	45.2	
GFRP-2000-150-S&S	376	182	169	96	96	16.5	
GFRP-1000-200-S&S	320	114	162	82	82	33.2	
GFRP-1500-200-S&S	320	114	162	82	82	53.8	
GFRP-2000-200-S&S	320	114	162	82	82	11.8	

3.4.1.1. Baseline Response

Figure 3.15 shows the load-deflection curve of control specimens GFRP-1500-150-S&S and STEEL-1500-150-S&S. These were chosen as baseline since they possess the same overhang length and rebar spacing as specimens in Chapter 4. Curves agree with expected behaviours of GFRP-RC and steel-RC members. Cracking occurred around 14 kN for both. Reason behind this low cracking load is the low concrete tensile strength used for this study (2.68 MPa) and initial stress state of the structure due to barrier and deck slab's self-weight; this was comprehended as explained in Subsection 3.2.2.3. The combined effect with acting tensile loads in the deck derives to the response exhibited in the curve and shows the relevance of this to structural stiffness. Steel-RC has a stiffer response relative to its GFRP-RC counterpart after cracking. Both models reported failure by diagonal tension at barrier-deck joint which prevented them to exceed S6 load threshold for TL-4 barriers (GFRP-RC model was 43.5% weaker than S6 force threshold, whereas steel-RC 16.5%).

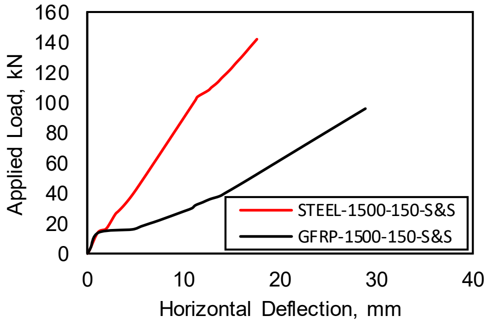

Figure 3.15 Load-deflection curve for baseline specimens.

3.4.1.2. Overhang Length Effect

Figure 3.16 presents load-deflection curves obtained using different overhang lengths. Each graph bundles same bar spacings for comparison purposes. Sezen and Setzler (2008) was used to determine bond-slip deflections. As reported in Table 3.6, barrier-deck joint governed peak load attained. Overhang length mainly affected stiffness: the larger it gets; the smaller stiffness will get. This is linked to the deck slab's ability to rotate (i.e., smaller rigidities allowed larger deflections and vice-versa). Moreover, the self-weight load increment with overhang length also contributed to loss of stiffness, which is why the initial stiffness of curves varied among overhangs lengths assessed. Same rebar spacing specimens attained the same peak loads, but corresponding deflection increased with overhang length.

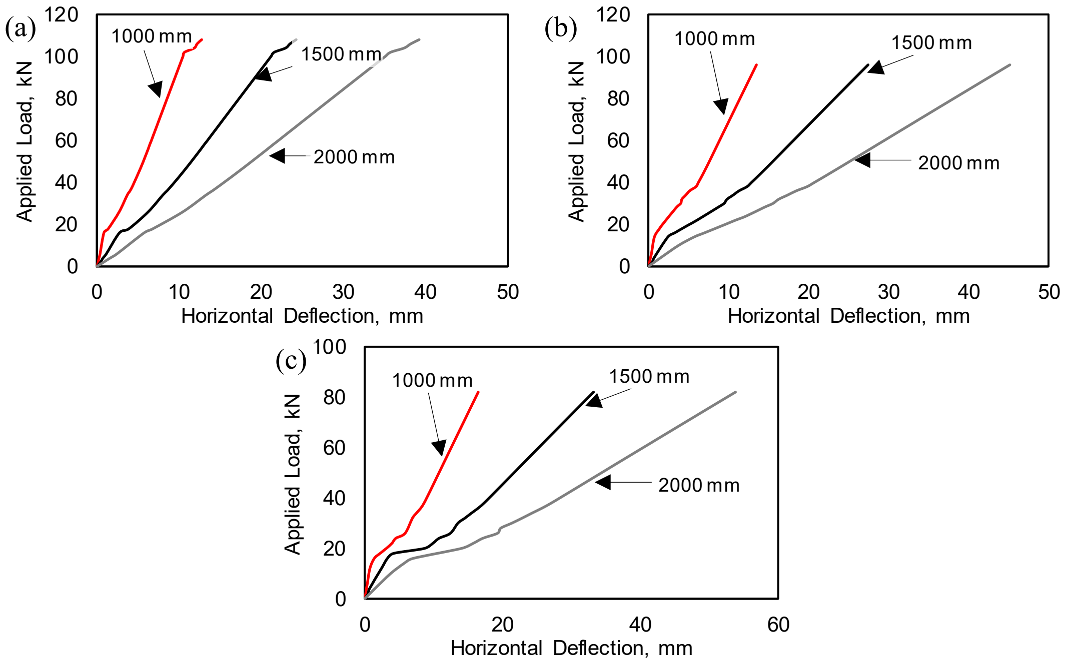

Figure 3.16 Load-deflection curve for (a) GFRP-xxxx- 100, (b) GFRP-xxxx- 150, and (c) GFRP-xxxx- 200. Overhang length effect assessment.

3.4.1.3. Rebar assembly Spacing

Figure 3.17 shows the load-deflection plots from structures with same overhang lengths but different bar spacings; table 3.8 reports the axial bar stiffness considering tension reinforcement for barrier and deck slab per each bar spacing assessed. Sezen and Setzler (2008) were considered to compare effects of bar spacings. The figure shows that as bar spacing decreased, the structure developed larger strength at lower deflections. Contrary to what was observed with overhang lengths variations, larger deflections were observed at lower capacities (i.e., when bar spacings were larger). Larger bar spacing resulted in a more flexible but less resistant structure (i.e., stiffness rises and ultimate load decreases). Under the same logic the system becomes stiffer and stronger as spacing decreases.

By considering the tensioned bar axial stiffness, EA, the largest values obtained of this parameter corresponded to structures modelled with the smallest bar spacing. Their response showed largest peak load with smallest respective deflection of all. This establishes a direct relationship between EA with strength and stiffness of a system, as mentioned by El-Nemr et al. (2013).

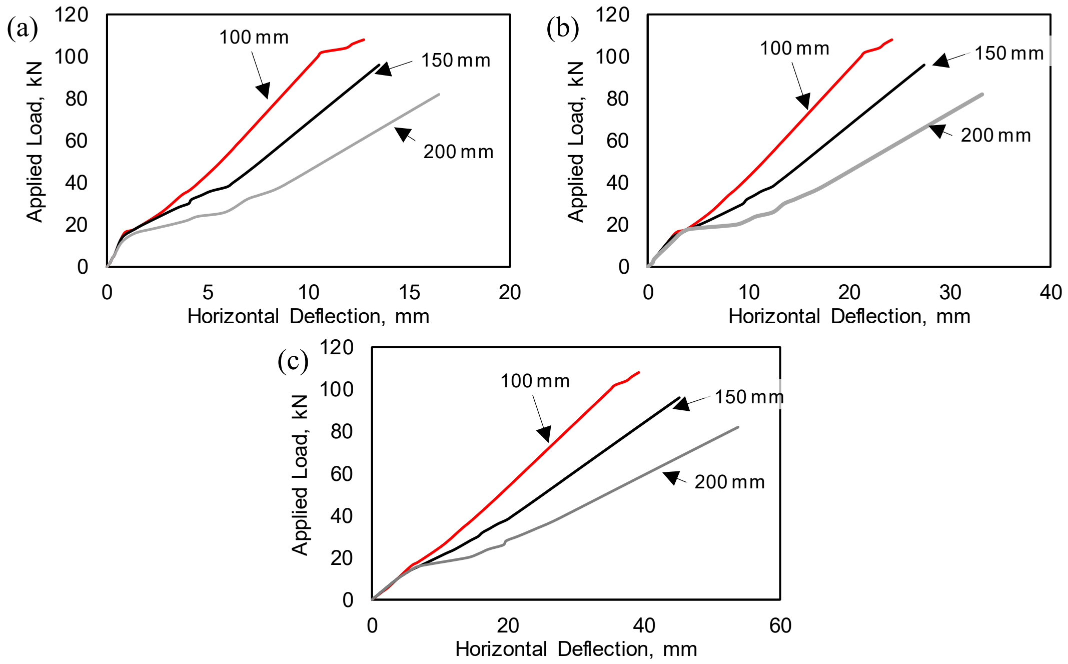

Figure 3.17 Load-deflection curve for (a) GFRP-1000- xxx, (b) GFRP-1500- xxx, and (c) GFRP-2000- xxx. Rebar assembly spacing assessment.

Table 3.8 Axial Bar stiffness determined for each rebar spacing assessed for deck and barrier, considering tension reinforcement.

Model	As total, deck (G-1) (mm^2)	As total, barrier (G-1) (mm^2)	EA, deck (MN)	EA, barrier (MN)
GFRP-xxxx-100-xxxx	3705	2600	232	163
GFRP-xxxx-150-xxxx	2565	1800	161	113
GFRP-xxxx-200-xxxx	1710	1200	107	75

3.4.1.4. Bond-slip Models

Figure 3.18 is a representative graph for GFRP-1500-150 series using both bond-slip methods previously mentioned and a curve without bond-slip deflections (NS) for comparison purposes. Table 3.9 shows deflection differences at peak load recorded by Sezen and Setzler (S&S), and mBPE model with NS. Given the low peak load all elements attained, bar slippage was not a big contributor to deflection curves. This talks about the low stresses at which barrier at base was subjected when failure occurred and that deflections were governed by deck slab overhang action. Thus, percent differences were small (1 to 5% difference) in all cases.

Table 3.9 Deflections comparison at peak load accounting for slip curves and without them for each assessed model.

Model	mBPE model Δ_{ult} (mm)	S&S approach $\Delta_{ult,}$ (mm)	No slip (NS) Δ_{ult}, (mm)	Diff, % (mBPE / NS)	Diff, % (S&S / NS)
GFRP-1000-100-mBPe	11.8	-	11.7	1.01	-
GFRP-1000-100-Sez	-	12.8		-	1.09
GFRP-1000-150-mBPe	13.5	-	13.4	1.00	-
GFRP-1000-150-Sez	-	13.5		-	1.01
GFRP-1000-200-mBPe	16.5	-	16.4	1.00	-
GFRP-1000-200-Sez	-	16.5		-	1.00
GFRP-1500-100-mBPe	23.3	-	23.2	1.01	-
GFRP-1500-100-Sez	-	24.3		-	1.05
GFRP-1500-150-mBPe	27.4	-	27.4	1.00	-
GFRP-1500-150-Sez	-	27.5		-	1.00
GFRP-1500-200-mBPe	33.2	-	33.1	1.00	-
GFRP-1500-200-Sez	-	33.2		-	1.00
GFRP-2000-100-mBPe	38.2	-	38.1	1.00	-
GFRP-2000-100-Sez	-	39.2		-	1.03
GFRP-2000-150-mBPe	45.1	-	44.2	1.02	-
GFRP-2000-150-Sez	-	45.2		-	1.02
GFRP-2000-200-mBPe	53.8	-	53.7	1.00	-
GFRP-2000-200-Sez	-	53.8		-	1.00

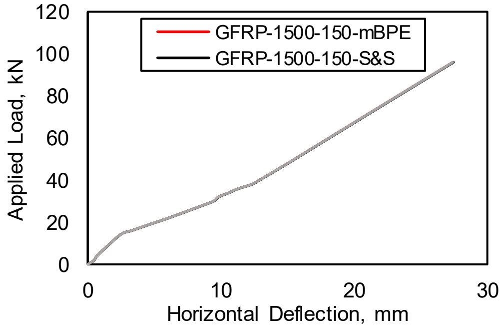

Figure 3.18 Representative load deflection curves reported for GFRP-1500-150 serie using. Using mBPE and Sezen and Setzler approaches.

3.5. Chapter Conclusions

This chapter presented the development and validation of an analytical model that predicts deflections, failure mechanism, and peak load of reinforced-concrete elements with various reinforcement materials. Assumptions, constitutive models, and validation results are presented. A parametric study was performed to analyze the impact of parameters assessed within the response of barrier-deck overhangs. Based on the results obtained, the following was determined:

1. The developed model was able to assess possible failure mechanisms due to load and support conditions. Deflections were computed by using first principles with effects added via superposition when applicable. Some assumptions during model development to reduce programming complexity were done that may contribute to performance limitations. For instance, neglecting concrete tension stiffening may

impact post-cracking stiffness The use of more refined constitutive model for concrete may increase model accuracy. Finally, it is also acknowledged that some additional effects were not studied given their complexity and not being aligned with this thesis's research objectives nor scope. For instance, the impact of D-regions in deflections, the softening of concrete in deck due to acting tensile forces, accounting for two-way response along the specimens' width or neglecting shear deflections are amongst these additional effects not considered for this model.

2. The model was able to predict response of GFRP-RC and Steel-RC members subject to simple load tests and similar support conditions and measures to those that the program was initially conceived to analyze. For beams used in validation, the program predicted loading stages (e.g., cracking, yielding, and peak load) with corresponding loads and deflections at peak with good agreement to test data. However, post-peak response was not predicted due to the model being load-controlled. Barrier tests validation showed that program was able to capture same failure mechanisms as previous research reported with good agreement of peak loads in most cases. Moreover, program predicted within decent agreement common loading stages of tested structures from selected papers. Deflections, however, showed how model assumptions or unaccounted aspects limited its performance. This and lack of test specifications found in references exacerbated discrepancies found between test and model results.
3. From parametric study, it was visible that parameters affected the system response. In terms of overhang length, rigidity of the structure was mainly affected. Structures with same bar layout but different overhang lengths deflect more as overhang length increases. Regarding bar spacing, element strength increased as spacing was decreased. This parameter also impacts the rigidity of the system as said larger loads will be attained at lower deflections. This is related to the larger axial stiffness reported with small bar spacings. Slip-related deflections contribution to total deformations increased as bar spacing reduced, where larger ratios were recorded in relation to no slip models. Meaning that stiffer structures are prone to larger stresses which derives into larger bar elongations at joints between barrier and deck. Due to the low load levels that all structures failed this phenomenon was not completely

captured and differences between selected approaches to capture bar slippage reported very close results. Finally, in any analyzed case structures exceeded CSA S6:19 force threshold as all models reported failure by diagonal tension. This type of failure is consistent to a squat response induced by one-way action due to limited specimens' widths which resulted in large stress concentrations at the barrier-deck joint.

4. EXPERIMENTAL PROGRAM

4.1. Introduction

Given the exposure to hazardous agents (e.g., de-icing salts, corrosive chemicals, freeze-thaw cycles) in some regions, GFRP-RC is an option for bridge deck-barrier structures when these agents may compromise steel-RC counterparts. Past studies have shown comparable behaviour between GFRP-RC and steel-RC barriers in terms of strength and energy absorption (El-Salakawy et al., 2003; El-Salakawy et al., 2004; and El-Gamal et al., 2008). GFRP's anchorage capacity has been analyzed using different bar types (Rostami and Dehnadi, 2016; Rostami et al., 2018; Rostami et al., 2019), with adequate results under static and dynamic loads. Previous studies focused on specimens built in ideal conditions without degradation or with non-realistic overhang deck lengths, which affects capacity (Ahmed et al., 2011) and rigidity (Torres Acosta and Tomlinson, 2023).

Despite FRP being used in construction since the 1980's, El-Salakawy et al. (2009) argued that FRP bars need more research to be considered as a conventional structural material as limited retrofitting guidelines and knowledge on post-repair response was available. More recent work by Kim (2019) found that many FRP-RC applications are still deemed experimental given the lack of expertise and knowledge that contractors and transportation ministries have with this technology. Investigation of FRP repair conditions in tests using realistic dimensions are needed to reduce uncertainty for owners and designers.

Little consideration with repair has been done with FRP-RC. El-Salakawy et al. (2009) studied repair and demolition procedures in 16 GFRP-RC slabs. Repairs used Near-Surface Mounted (NSM) and dowelling bar (DB) techniques. Both techniques restored capacity, with NSM elements having a stiffer response over DB. They reported that DB specimens using epoxy adhesive had an 80% larger capacity than those using grout. Demolition by jackhammer was recommended over other methods assessed; Ahmed et al. (2012) supported this premise. El-Salakawy and Islam (2014) tested three 6-metre-long PL-2 barriers. Barriers were loaded until damage was observed then repaired using NSM and DB methods in both barrier and decks in affected regions (i.e., edge and middle zones). In all cases, ultimate capacities of retrofitted structures exceeded strengths of unrepaired specimens. NSM members had larger strengths, attributed to NSM's larger effective depths. To the author's best knowledge, El-Salakawy and Islam (2014) is the most recent on repair of FRP-RC deck-barrier systems. Although this study showed the feasibility of these techniques, the retrofit included partial demolition of the overhang to install new bars in the deck. Though good results were reported, this solution may not be the most time and cost efficient if damage is limited to the barrier wall. Features of these specimens raised questions and need further analysis, such as the contribution of overhangs with lengths closer to those used in common practice, or the evaluation the barrier/deck joint's ability to transfer internal forces. These aspects were not considered by this study due to short overhang (700 mm) and two-way action induced by the 6 m-long width that enabled different stress distribution, restraining the structures from the most severe forces at the barrier-deck interface, especially in retrofitted specimens.

This chapter presents a test program conducted on four barrier-deck specimens. Two specimens served as controls, mimicking monolithic structures, while the remaining two evaluated barrier repair using DB methods. Ancillary tests are discussed with special attention to a modified RILEM beam-bond test for developing bond-slip parameters for GFRP bars which will be useful to predict slip deformations using the analytical model described in Chapter 3. Test results will be discussed and then compared to analytical results.

4.2. Specimen Description and Fabrication

4.2.1. Specimen Description

Four specimens were built. Specimens comprised a single-sloped barrier constructed over a deck with geometries shown in Fig. 4.1. Regardless of bar material, all specimens had the same reinforcement nominal area and layouts (Fig. 4.2). This 1:1 substitution of steel with GFRP was suggested by bar suppliers based on previous experience in other regions of Canada. Table 4.1 show reinforcement information, with Fig. 4.3 showing bar dimensions. Two specimens acted as controls: SP-01 (Steel-RC) and SP-02 (GFRP-RC). Both structures mimic monolithic structures. The remaining two specimens (SP-03 and SP-04) simulate barrier repairs using doweled bars. SP-03 is fully reinforced with GFRP bars; SP-04 comprises a steel-RC deck and a GFRP-RC barrier. This latter case constitutes a scenario when a new GFRP-RC barrier is fabricated over an old deck. Control specimens establish a baseline for determining whether repairs could restore/exceed control specimen strengths and CSA S6:19 threshold demands for TL-4 barriers.

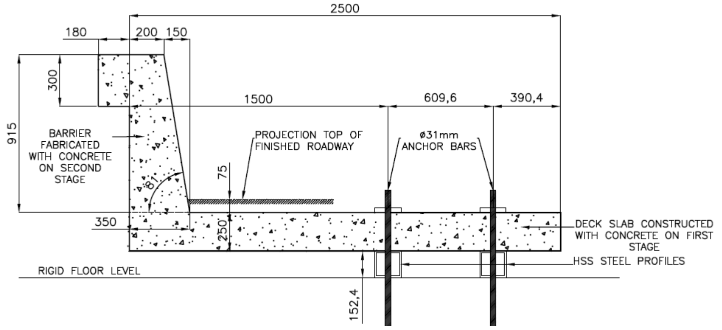

Figure 4.1 Typical deck slab overhang – Barrier structure geometry. All dimensions in mm.

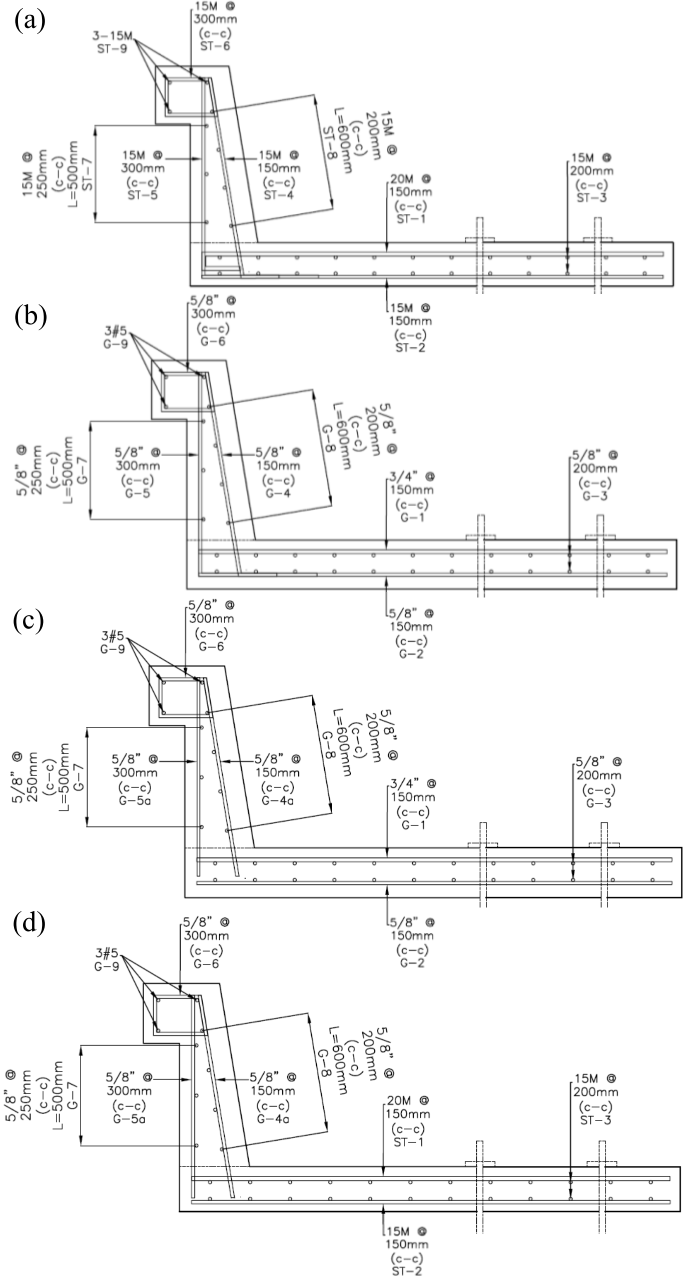

Figure 4.2 reinforcement layout for (a) SP-01, (b) SP-02, (c) SP-03, and (d) SP-04. Bar covers given in Tables 4.1 and 4.2. Reinforcement details given in Fig. 4.3

Table 4.1 Deck slab and barrier general reinforcement features of as-designed and as-built specimens.

Specimen ID[†]	SP-01	SP-02	SP-03	SP-04
Top bars, longitudinal	20M @ 150 mm (c-c)	#6 @ 150 mm (c-c)	#6 @ 150 mm (c-c)	20M @ 150 mm (c-c)
Bottom bars, longitudinal	15M @ 150 mm (c-c)	#5 @ 150 mm (c-c)	#5 @ 150 mm (c-c)	15M @ 150 mm (c-c)
Top cover[*], mm	52	52	52	52
Bottom cover[*], mm	40	40	40	40
Front face bars	15M @ 150 mm (c-c)	#5 @ 150 mm (c-c)	#5 @ 150 mm (c-c)	#5 @ 150 mm (c-c)
Back face bars	15M @ 300 mm (c-c)	#5 @ 300 mm (c-c)	#5 @ 300 mm (c-c)	#5 @ 300 mm (c-c)
Front face cover[*], mm	100	100	100	100
Back face cover[*], mm	60	60	60	60
Barrier front cover[‡], mm	90	90	100	100
Barrier back cover[‡], mm	60	60	60	60
Deck top cover[‡], mm	52	52	52	52
Deck bottom cover[‡], mm	40	40	40	40

[†]: All elements had transverse reinforcement in the top/bottom mats with same diameter as bottom reinforcement assembly and spaced every 200 mm (c-c); horizontal bars from barrier had same reinforcement configuration.

[*]: Measured to the face of longitudinal/vertical reinforcement.

[‡]: As-built concrete covers measured to the face of longitudinal/vertical reinforcement.

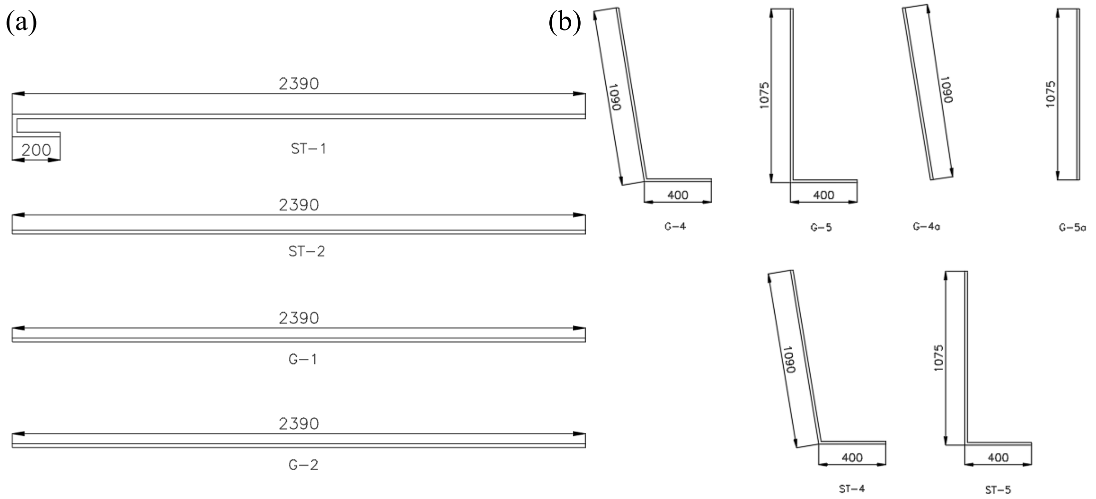

Figure 4.3 reinforcement dimensions for (a) deck, and (b) barrier. All dimensions in mm.

All specimens were 1500 mm wide and 2500 mm long. The width is expected to lead to a one-way response which places barrier-deck joints under large stresses that allow for conservative analysis of joint response and bar anchorage. Barriers have a 1500 mm long overhang, followed two rows of support anchors at 610 mm spacing (on centre) between each row, and 390 mm from the last anchor row to the back face of the deck. Deck overhang length and thickness (250 mm) were selected to represent real applications. The 1500 mm overhang is justified by Ahmed et al. (2011), where they showed that the deck with overhang action may govern capacity as it failed before the barriers. Additionally, overhang length contributes to flexibility and energy absorption ability (Torres and Tomlinson, 2023).

TL-4 barriers require a ≥800 mm height from top of roadway to top of barrier (CSA 2019); tested barriers used Alberta Transportation (2017) geometries for single-sloped barriers (Fig. 2.3) which exceed this limit by 40 mm. Barriers had a height (deck top to barrier top) of 915 mm which accounts for 75 mm of road surface, and 840 mm above this line. The barrier base is 350 mm wide and tapers at a 0.165:1.00 (horizontal:vertical) slope along the height. The barrier top includes a spandrel beam with cross-sectional dimensions of 180×300 mm. This spandrel stiffens the barrier under two-way action, though this action is not expected for these tests given the limited specimen width. For constructability, measurements were rounded to the nearest 5 mm increment and a 10 mm tolerance was considered during fabrication.

Given the specimens' size, it was decided to build one specimen for each of the four test conditions to reduce fabrication and testing time. Practical considerations with lab space and budget limitations also dictated the number of specimens that could be feasibly tested in this program. This affected repetition which prevented us from capturing a statistical mean structural response, including variability in strength and stiffness, for each specimen type. To balance this effect, repetition of ancillary tests to determine material properties used in the fabrication of the barrier-deck structures was done. Results are given in Subsection 4.3 and Appendices B and D. This practice has been used in other studies with similar structures whose dimensions make testing multiple specimens of the same type cumbersome to perform (Ahmed et al., 2010; Ahmed and Benmokrane, 2011; El-Salakawy and Islam, 2014; Azimi et al., 2014).

4.2.2. Fabrication Process

Specimens were fabricated in the Morrison Structures Lab at the University of Alberta. Fabrication comprised two stages: (1) deck fabrication and (2) barrier fabrication. Additional information on fabrication of each specimen can be found in Appendix A.

4.2.2.1. Deck Slab Fabrication

Formwork was built using 19 mm plywood and 38×89 mm sawn lumber (Fig. 4.4(a)). Reinforcement mats were placed on chairs to maintain cover (Fig. 4.4(b)). After placing reinforcement, vertical bars for SP-01 and SP-02 barriers was placed and connected. Vertical bars were placed using wooden guides to maintain desired inclination and cover (Fig. 4.4(c)). PVC tubes were installed to facilitate anchoring specimens to the floor and braced with plywood to avoid shifting during casting (Fig. 4.4(d)). Some bars were shifted 25 to 37 mm from the design position to prevent conflict with PVC tubes (Appendix A).

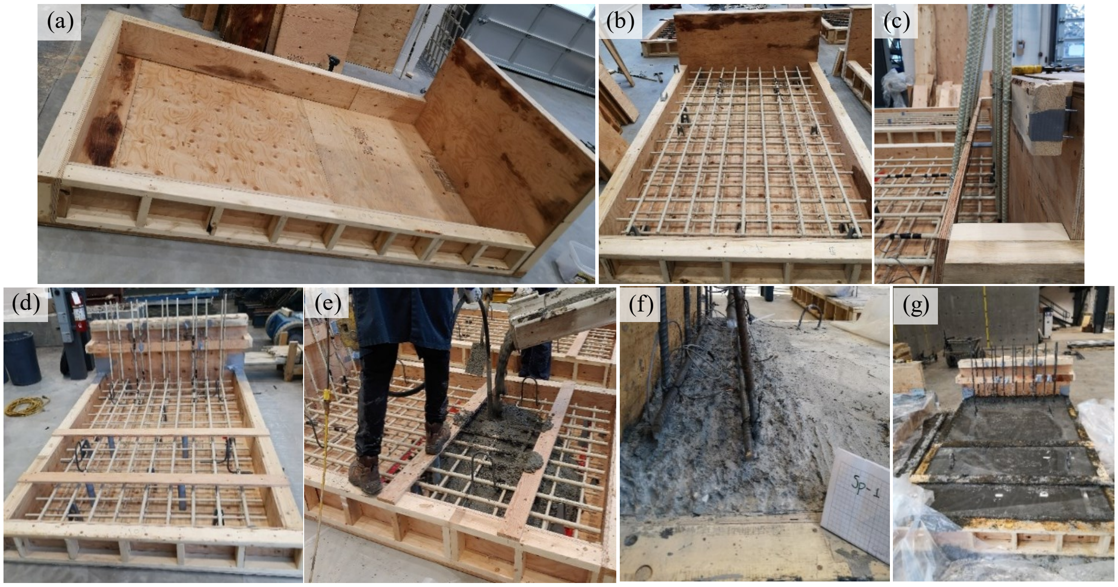

Figure 4.4 Deck fabrication. (a) deck formwork, (b) SP-02 bar assemblies in form, (c) vertical bars for barrier SP-02, (d) lateral bracing for PVC tubes in deck, (e) deck pouring, (f) SP-01's surface roughened where barrier will be fabricated, and (g) SP-01 deck after 7 days curing.

The next step was to cast deck concrete (Fig. 4.4(e)) which took place on January 25th, 2023. A total of 0.94 m^3 of concrete were poured into each form. Concrete was vibrated during pouring, screeded, and finished with a trowel.

In accordance with Alberta Transportation (2017), deck concrete under the future barrier location was roughened ±6 mm with a 1:0.03 (horizontal/vertical) slope towards the back of the barrier. This detail intends to increase shear friction resistance of the barrier/deck interface. Roughening was achieved using sharp edge of trowels (Fig. 4.4(f)). For SP-01 and SP-02, vertical reinforcement made it difficult to achieve this detail, but it was approximated as much as possible. For SP-03 and SP-04 the process was easier due to the lack of vertical bars. Roughening of SP-03 and SP-04 simulates the concrete surface after saw cutting and locally roughening concrete with a jackhammer or similar tool.

After pouring, specimens were covered with plastic sheets and cured for seven days. Specimens were watered daily to assist with curing. After seven days, plastic sheets were removed (Fig. 4.4(g)), and the second fabrication stage began.

4.2.2.2. Barrier Fabrication (SP-01 and SP-02)

For specimens SP-01 and SP-02, barrier reinforcement assemblies followed layouts shown in Figs. 4.2(a) and (b), and 4.3. Barrier fabrication was relatively easy since vertical bars were already anchored into the deck. Horizontal bars were placed, leveled, and tied at the designed spacing (Fig. 4.5(a)). For the front bar assembly, the horizontal bar at the base was tied as close to the deck's top fibre. Barrier wall formwork was constructed (Fig. 4.5(b)), concrete cast on April 20th, 2023 (Fig. 4.5(c)), and formwork stripped after 7 days of curing under plastic with daily watering (Fig. 4.5(d)).

Figure 4.5 Barrier fabrication process for control specimens (SP-01 and SP-02). (a) barrier rebar assembly connected, (b) typical barrier formwork installed, (c) concrete pouring for barriers, and (d) formwork stripping after curing process finished.

4.2.2.3. Second Stage: Barrier Fabrication (SP-03 and SP-04)

Bar configuration for SP-03 and SP-04 was the same as SP-01 and SP-02 but without bars embedded into the deck. Instead, the dowelling technique described in Subsection 2.5.2 was used. Dowelling is summarized in Fig. 4.6 and Table 4.2. Details, including estimates for how long it takes to complete each task, are given in Appendix A. Steps 1 and 2 were not done since specimens were fabricated to achieve a similar result as those activities.

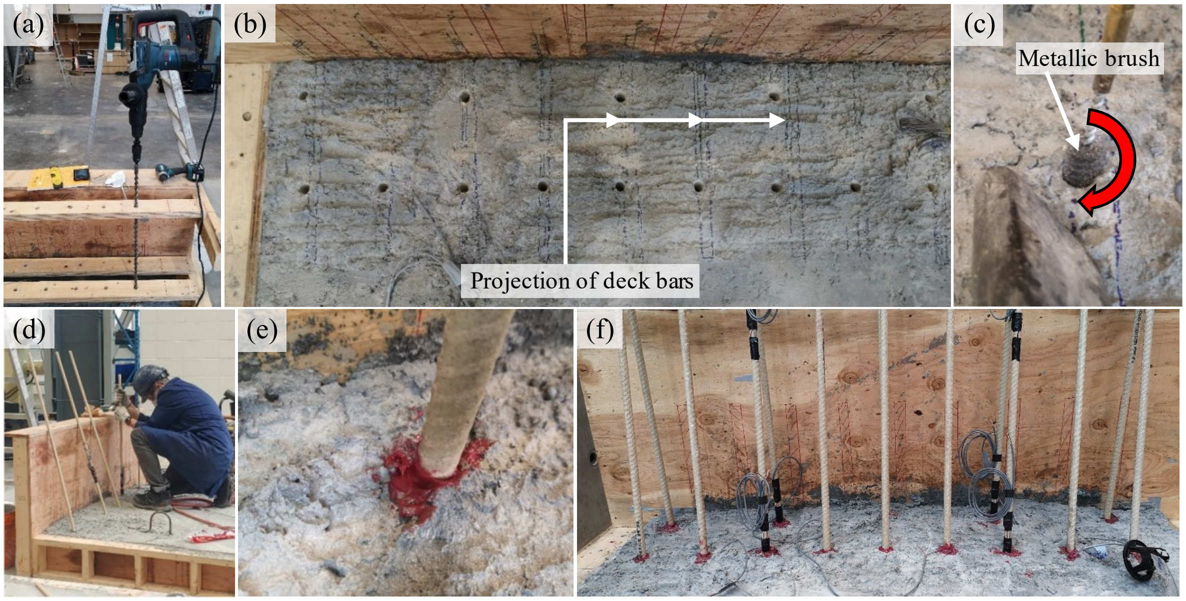

Figure 4.6 Activity sequence for bar dowelling technique. (a) drilling guides positioned, (b) holes drilled on SP-03 (shown) and SP-04 deck slabs, (c) hole preparation, (d) bar dowelling after epoxy adhesive injected into hol€(e) final state of epoxy and bars after being dowelled, and (f) final dowelled rebar vertical assembly.

Table 4.2 Activity sequence for bar dowelling repair technique.

Activity ID	Activity Name	Activity Details
1	Damaged concrete demolition.	Concrete demolition by jackhammer or other proven techniques.
2	Debris removal.	Remove demolished concrete so new concrete is poured over a clean area.
3	Surface roughening	Surface roughening by partially demolishing concrete smooth area to increase friction (Fig. 4.4(f)).
4	Hole allocation.	Locate holes according to bar layout, considering interferences with existing bars (Fig. 4.6(a)).
5	Hole drilling.	Use a rotary hammer drill to desired depth (Fig. 4.6(b)).
6	Hole preparation.	Use a metallic brush and compressed air valve to remove dust particles that remain inside holes (Fig 4.6(c)).
7	Epoxy / Grout application in holes.	Adhesive applied inside of holes according to manufacturer's instructions.
8	Bar dowelling into holes.	Bars inserted into holes with adhesive (Fig. 4.6(d)).
9	Rebar cage assembly	Once adhesive has hardened (Fig 4.6(e)), assemble bar cages.

4.2.2.4. Final Appearance

During formwork removal each specimen was inspected (Appendix A contains relevant inspection images). Specimen conditions were acceptable. SP-01 and SP-02 did not have any notable irregularities. SP-03 had minor concrete spalling (~ 10-15 mm depth) in the bottom surface of the deck. The effect of this spalling on SP-03's response during tests was found to be negligible. For SP-04, a deck corner chipped during demolding but was in a superficial location; not observed to affect response of SP-04.

As-built measurements for comparing with designed specimens (See Figs. in Appendix A). Table 4.1 shows the final measured covers. Measurements reported are the average from five locations along specimens. Specimens were constructed within the 10 mm tolerance desired in Subsection 4.2.1; no large variations were recorded, except for SP-01 and SP-02's barrier front assembly cover which was 10 mm below specified; this may affect response as the bars' effective depth was larger than SP-03 and SP-04. Effects on this are discussed in Subsections 4.5.4 and 4.5.5.

4.3. Material Properties

4.3.1. Concrete Properties

A High-Performance Concrete (HPC) mix with a minimum design compressive strength of 45 MPa was used. This follows Alberta Transportation (2018) for cast-in-place decks and barriers in highway bridges. Per Alberta Transportation (2018), HPC mix must have a water-to-cement ratio of 0.38 with minimum cement content of 335 kg/m^3; silica fume and fly ash mass content ranged between 6-8% and 11-15% of cementitious materials used. The concrete mix temperature at discharge should be between 10 to 20°C. This was accomplished by the supplier adding ice chips to the mixer truck. Concrete was mixed and batched by LaFarge and cast in the Morrison Structural Lab. Table 4.3 reports mixture properties.

Table 4.3 Concrete mix properties

Pour ID	**Pour date**	**Mix properties**			**28-day properties**		**Test day properties**
		Slump, mm	**Air content , %**	**Temperature, °C**	**E_c, GPa (±SD)**	**f'_c, MPa (±SD)**	**f_r, MPa (±SD)**
1st	25/01/23	140	7.5	10	23.2±0.1	45.9±3.5	5.32±0.3
2nd	20/04/23	120	7.2	16	20.8±2.7	41.8±0.6	4.91±0.2

For each pour, 15 cylinders (100×200 mm) and three beams were sampled to determine mechanical properties including elastic modulus (E_c) (ASTM C469, 2014), compressive strength (f'_c) (ASTM C39, 2018), and modulus of rupture (f_r) (ASTM C78, 2018). Elastic modulus and compressive strength were determined 28 days after pouring by testing three cylinders; remaining cylinders were tested for test day strengths. More details are found in Appendix D.

4.3.2. Steel rebar properties

Steel rebar coupons were tested to establish their yield strength (f_y) and elastic modulus, E_s, per ASTM E8 (2022). Five coupons were tested for each diameter. The yield strain, yield strength, and elastic modulus of 15M bars (nominal area 200 mm^2) were 0.00198 ± 0.00029, 446 ± 2.1 MPa, and 211 ± 8.2 GPa respectively. For 20M bars (nominal area 300 mm^2), the yield strain, yield strength, and elastic modulus were 0.00211 ± 0.00024, 450 ± 2.1 MPa, and 213 ± 12.6 GPa respectively. More details are found in Appendix D.

4.3.3. GFRP rebar properties

GFRP mechanical properties provided from bar manufacturer TUFBAR and tests conducted by (Al-Jaaidi, 2021) on same bar set and specified in Table 4.5. Tests were performed per ASTM D7205. All bars were assembled with vinyl ester resin and E-CR glass fibres.

Table 4.4 GFRP mechanical properties.

Bar type	A_f real, mm^2	d_b real, mm	E_f, GPa	f_{fu}, MPa
#5, straight	240[†]	17.4[†]	53.6[*]	1339[*]
#5, bent	240[†]	17.4[†]	50[‡]	1000[‡]
#6 , straight	325[†]	20.3[†]	62.7[‡]	1150[‡]

[*] *Average values from Al-Jaaidi (2021). Bar diameter used to find $\boldsymbol{E_f}$ and $\boldsymbol{f_{fu}}$ was 17.1 mm.*

[†] Values determined for present study.

[‡] Values extracted from manufacturer's catalogues.

4.3.4. Epoxy Properties

Properties were found from producer (HILTI, 2022a). Bond strength after 14 days curing should be 11.7 MPa (ASTM C882, 2013); Compressive (ASTM D695, 2010), and tensile (ASTM D638, 2014) strength are 82.7 and 49.3 MPa, respectively. Tensile strength reported is after 7 days curing.

4.3.5. Bond-Slip Response

4.3.5.1. Beam-bond Specimen Description

General descriptions of beam-bond tests and bond-slip curves are given in this section. Further details on construction, detailing, and discussion are given in Appendix B. Beam-bond tests were done following general specifications from (RILEM TC-RC5, 1994).

Fig. 4.7(a) shows a general scheme of tested RILEM beams. Specimens comprise two RC segments with dimensions selected and stirrups provided to ensure failure by pullout. Each segment had a 200×300 mm cross-section and length of 475 mm; segments were connected by a GFRP bar at the bottom. A 110 mm gap separates segments, where two 51×51×6.3 steel angles were anchored into concrete near tops of each segment. Angles support a steel rod placed which carries compression between segments during testing. Gap width was dictated by available angle sizes; gaps were filled with Styrofoam to maintain distance during pouring. Bars were embedded into 225 mm of concrete and consistent with deck embedment depth (Subsection 4.2.2). Acrylic tubes (125 mm-long) controlled embedment depth.

Concrete and GFRP were the same as those used in the barrier. A different rebar supplier was used for 10M stirrups and hanger bars with those bars having f_y of 466 MPa and E_s of 200 GPa reported by the supplier. Fig. 4.7 shows construction, details in Appendix B.

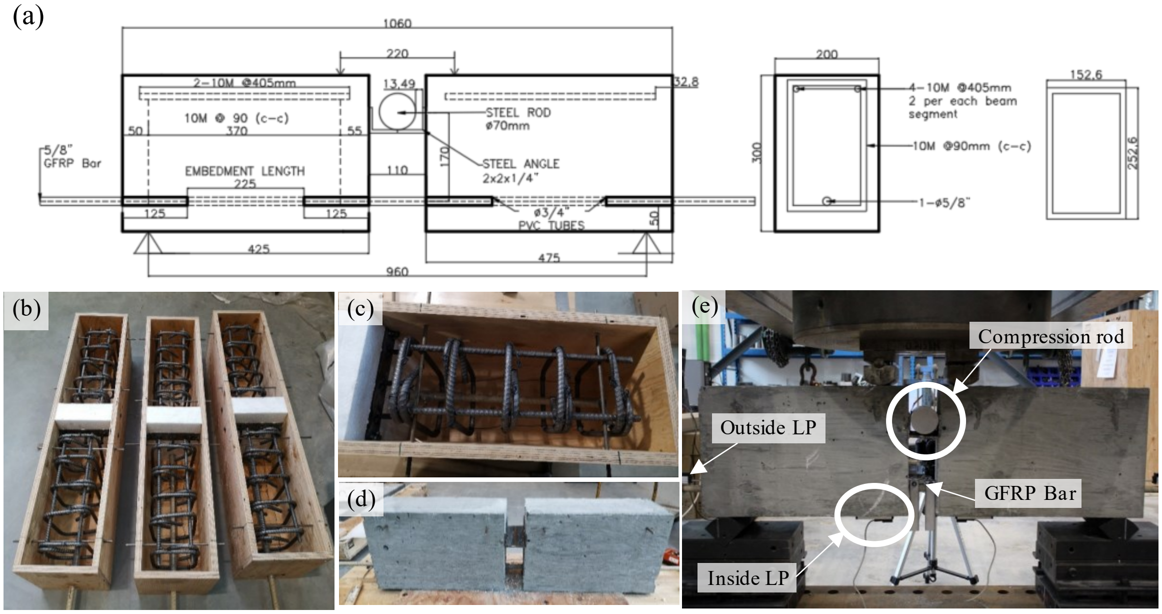

Figure 4.7 (a) typical RILEM beam geometry and reinforcement layout used in this study. All dimensions in mm, unless specified; (b) and (c) Fabrication of RILEM beams; (d) final product after formwork removal; and (e) Test setup for RILEM beam tests.

Two beam series were built: CB and CE. CB assessed bond-slip between concrete and GFRP. CE assessed bond-slip between GFRP surrounded by epoxy resin. Previous studies of how to construct CE specimens were not found so a novel procedure was developed to insert epoxy after concrete was hardened with details given in Appendix B.

4.3.5.2. Bond Beam Test Setup and Instrumentation.

Per RILEM TC-RC5 (1994), beam-bond tests are subject to four-point-bending. Fig. 4.7(a) shows setup dimensions with a photo provided in Fig. 4.7(e). Load was transmitted through a spreader beam from an MTS universal machine with 6000 kN capacity and displacement-controlled at 1 mm/min. Linear potentiometers (LP)s measured bar slip. For CB, LPs were located at external/unloaded side of segments; for CE, LPs were placed in loaded and unloaded ends of bar. This enabled the capturing of data on both extremes of each segment to determine if significant differences were present.

4.3.5.3. Results

Results from beam-bond tests are shown in Fig. 4.8. Subscripts N and S correspond to North and South LPs. Plots correspond to LPs that captured pullout, which are most representative; remaining plots are given in Appendix B. Table 4.6 depicts relevant points from tests used for model calibration in Subsection 4.3.5.3. Bond stress, τ, was found using Eq. 4.1:

$$\tau = \frac{P_t a}{2\pi d_b l_e j} \tag{4.1}$$

Where P_t is the total load applied, a is the shear span, d_b is the GFRP measured bar diameter, l_e is embedment length in each beam segment, and j is the moment arm (~170 mm) between tension and compression forces.

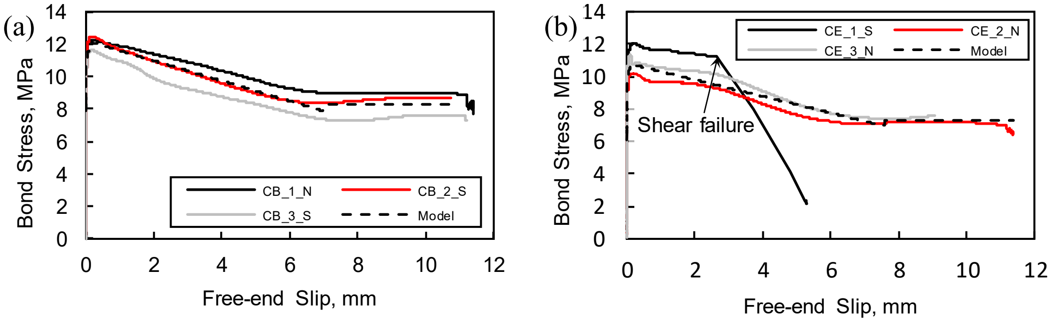

Figure 4.8 Bond-slip curves for (a) CB, and (b) CE series beam-bond tests. mBPE model curve for each series also shown.

Table 4.5 Key points from bond-slip curves.

Point	CB Beam series					CE Beam series				
	CB_1	CB_2	CB_3	Avg	SD	CE_1	CE_2	CE_3	Avg	SD
τ_1, MPa	12.23	12.47	11.62	12.1	0.438	12.04	10.19	11.32	11.2	0.929
s_{f1}, mm	0.21	0.16	0.15	0.17	0.031	0.36	0.18	0.11	0.2	0.127
τ_3, Mpa	8.99	8.47	7.31	8.3	0.86	10.98	7.17	7.44	8.5	2.131
s_{f3}, mm	6.96	6.11	7.92	7.0	0.90	2.75	7.83	7.33	6.0	2.796

CB_1 had an imperfection related to movement (~50 mm) of Styrofoam during concrete pouring. This resulted in one segment being larger than the other one though CB_1 behaved similarly to counterparts. CE_1 failed in shear shortly after pullout occurred, characterized by diagonal cracking in a segment followed by GFRP bar rupture (Fig. 4.8(b)). CE_1 was not used for model calibration as it was inconsistent with other specimens for post-peak response. CE_3 experienced bar pullout from both segments at around the same time. The north slips were used for model calibration as they reported the largest slips after reaching τ_1. Other tests did not have any construction issues or unexpected events during test.

Partial demolition was completed after testing to confirm failure modes (Fig. 4.9). Overall, CB beam's surface coating peeled off the GFRP bar coating leading to slip, whereas CE beams failed due to slip between concrete and epoxy. All specimens failed by pullout, even CE_1, with large rotation about the hinge (Fig. 4.9(a)). Some beams, particularly CB beams, exhibited pullout cracks in the middle gap (Fig. 4.9(b)); CE beams however did not show cracks; only large bar slippage was observed (Fig. 4.9(c)).

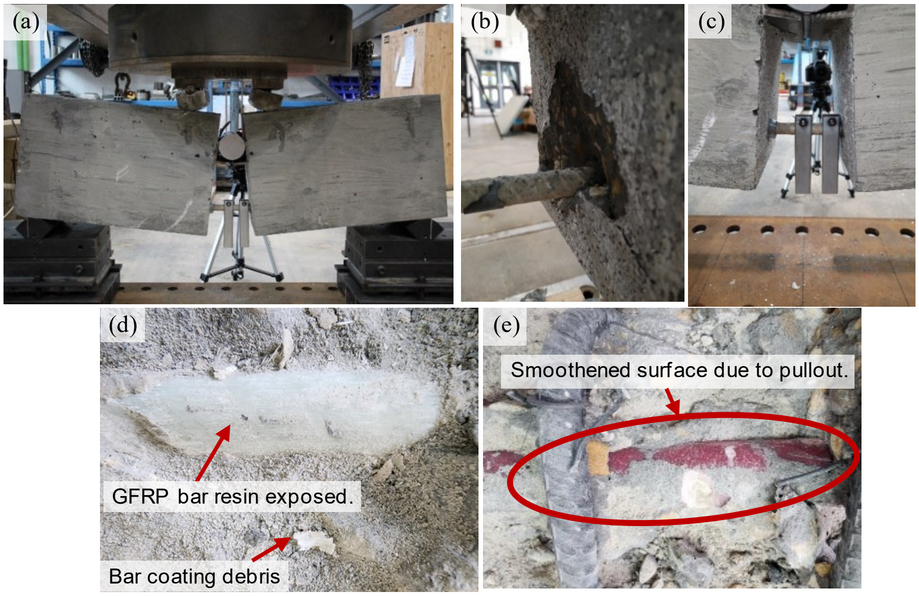

Figure 4.9 final state of beams from (a) CE series, (b) pullout cracks in CB, (c) typical bar slippage in CE, (d) typical state of bar embedded in CB after demolition, and (e) typical state of bar embedded in CE after demolition.

4.3.5.4. Bond-Slip Model Calibration

Subsection 2.7.3.1 introduced three bond-slip models for concrete and GFRP bars: mBPE (Cosenza et al., 1995), CMR (Cosenza et al., 1997), and Sezen and Setzler (2008). Cosenza et al.'s (1995) mBPE model was selected, and parameters calibrated following a graphical approach from Cosenza et al. (1997). mBPE was successfully used by Vint (2012) for bars with similar features to those used in this study.

The graphical method is composed of three steps to calibrate coefficients α,p, and β. For α, the area under curve, $A_{\tau 1}$, between (0,0) and (s_{f1},τ_1) is calculated using trapezoidal integration and computed with Eq. 4.2:

$$\alpha = \frac{\tau_1 s_{f1}}{A_{\tau 1}} - 1 \tag{4.2}$$

Where τ_1 is the maximum bond stress and s_{f1} is the slip corresponding to τ_1. Linear regression of the descending branch was done then Eq. 4.3 used to get p.

$$p = m\frac{s_{f1}}{\tau_1} \tag{4.3}$$

Where $\boldsymbol{m}$ is the slope of the line. $\boldsymbol{\beta}$ is the ratio between $\boldsymbol{\tau_3}$ and $\boldsymbol{\tau_1}$ (Eq. 4.4), where $\boldsymbol{\tau_3}$ is the weighted average of bond stresses recorded in the bond-slip stabilization zone.

$$\beta = \frac{\tau_3}{\tau_1} \tag{4.4}$$

Calibrated parameters are shown in Table 4.7. Different parameters were obtained for CB and CE, expected given that CE used epoxy resin. Table 4.8 contains expressions for each region of the plot per CB series tested. Model curves for each series were shown in Fig. 4.8.

Table 4.6 Model parameters calibrated for CB and CE beam series for mBPE bond-slip model.

Item	**CB Beam series**					**CE Beam series**				
Specimen ID	**CB_1_N**	**CB_2_S**	**CB_3_S**	**Avg**	**SD**	**CE_1_S**	**CE_2_N**	**CE_3_N**	**Avg**	**SD**
α	0.044	0.056	0.041	$\underline{0.048}$	0.008	0.057	0.059	0.049	$\underline{0.055}$	0.005
p	0.00885	0.00886	0.00826	$\underline{0.009}$	0.0003	0.0073	0.0085	0.0052	$\underline{0.007}$	0.002
β	0.734	0.687	0.648	$\underline{0.69}$	0.043	N/A	0.707	0.66	$\underline{0.68}$	0.033
τ_1, MPa	12.23	12.47	11.62	$\underline{12.11}$	0.438	12.04	10.19	11.32	$\underline{11.18}$	0.929
s_{f1}, mm	0.21	0.16	0.15	$\underline{0.17}$	0.031	0.36	0.18	0.11	$\underline{0.22}$	0.127
τ_3, MPa	8.99	8.47	7.31	$\underline{8.26}$	0.86	10.98	7.17	7.44	$\underline{8.53}$	2.131
s_{f3}, mm	6.96	6.11	7.92	$\underline{6.99}$	0.90	2.75	7.83	7.33	$\underline{5.97}$	2.796

Table 4.7 Expressions for mBPE model according to beam series.

$\boldsymbol{\tau(s)}$, **CB Beam series**	$\boldsymbol{\tau(s)}$, **CE Beam series**	**Plot region (value ranges)**
$12.11\left(\frac{s}{0.17}\right)^{0.048}$	$11.18\left(\frac{s}{0.22}\right)^{0.055}$	Ascending branch ($s \le s_{f1}$)
$12.11\left[1 - 0.009\left(\frac{s}{0.17} - 1\right)\right]$	$\tau_1\left[1 - 0.007\left(\frac{s}{0.22} - 1\right)\right]$	Descending branch ($s_{f1} < s \le s_{f3}$)
$0.69\,\tau_1$	$0.68\,\tau_1$	Stabilization ($s_{f3} > s$)

Results are compared with other studied in Table 4.9. Majority of comparisons were performed with similar surface coatings as those used in this study, except ribbed bars. Overall, ascending branch parameters (e.g., α, τ_1, s_{f1}) from this study were like others. Values for grain covered bars (Cosenza et al., 1997) were like this study though τ_1 for CE beams was slightly smaller. Braided, sanded-coated bars were similar though τ_1 was much larger than that in this study. From Vint (2012), ascending branch from sand coated-helical wrapped bars were like this study, but s_{f1} was much larger. Cosenza et al. (1997) had very large descending slopes, p, and smaller τ_3 and β than this study. p from Vint (2012) was closer to those in this study but still differed more than 30%. Vint (2012) only reported τ_3 or β values for ribbed bars, where both values were smaller than CB and CE's. Further investigation on these parameters, and the applicability of the proposed method for bond-slip curves for doweled GFRP bars, should be completed in future.

Table 4.8 Comparative chart of mBPE model parameters of current and previous studies.

	Present study		Vint (2012)			Cosenza et al. (1997)	
Specimen ID / Coating type	**CB**	**CE**	**Sand coated, helical wrap**	**Sand coated**	**Ribbed**	**Grain covered**	**Braided + sand coated**
α	0.048	0.055	0.0622	0.21	0.11	0.067	0.069
τ_1, MPa	12.11	11.18	11.26	14.36	11.50	12.05	17.78
s_{f1}, mm	0.17	0.22	0.556	0.504	0.423	0.13	0.15
p	0.009	0.007	0.0131	-	0.0296	3.11	0.95
τ_3, MPa	8.26	8.53	-	-	5.07	3.17	7.13
β	0.69	0.68	-	-	0.434	0.263	0.401

4.4. Test Setup and Instrumentation

Figure 4.10 shows the test setup. More background information on setup and instrumentation is given in Appendix C. Specimens were anchored to the lab strong floor through two steel 152×152×12.7mm HSS members. The centre of the first HSS was 1500 mm from barrier back face; the centre of the second HSS was 610 mm from the first one. Specimens thus had a 1500 mm-long overhang. Holes were drilled in the HSS members and polyvinylchloride (PVC) tubes cast into the deck to allow anchoring of the specimen to the lab strong floor using four 1800 mm-long and 38.1 mm diameter threaded anchor rods. This clamping prevents horizontal displacement or rotations and mimics connections between decks and girders in practice. The specimens were placed beside a reaction wall with an actuator installed to apply load horizontally 775 mm from the top of the deck. The actuator and load cell were connected by a hinged plate bolted to a 1050 mm-wide spreader beam connected to the tapered face of the barrier by 12.7 mm diameter concrete anchors to prevent sliding during testing with grout used to fill the gap created from the barrier's slope. Grout ensures an even force distribution along the spreader beam during testing.

Specimens were tested monostatically until failure. Precise servo-controlled loading systems were unavailable at the time of testing, but the mechanical release system used allowed for relatively stable displacement-controlled loading at ~1 mm/min. Specimens were loaded such that peak load would occur around after 35-40 minutes. Tests were stopped once load dropped more than 50% from the peak load to assess if any interesting redistributions of stresses took place after failure.

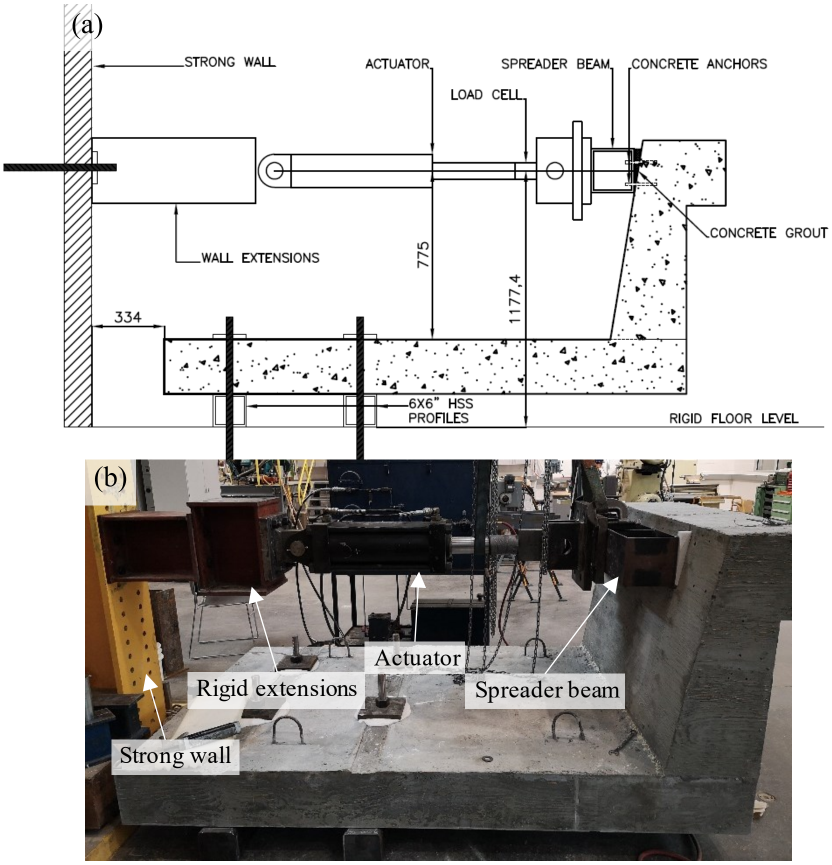

Figure 4.10 Test setup (a) drawing and (b) photo. All dimensions in mm.

4.4.1. Instrumentation

Specimens were instrumented with twelve 5 mm 120 Ω electrical resistance strain gauges placed on reinforcement. Gauges were installed where large stresses were expected during test. Location selection and installation was completed by Al-Jaaidi (2021). Figs. 4.11(a) and (b) show strain gauges' locations; the same layout was used on each specimen.

Figure 4.11(c) shows the position of sensors recording deflections. Both cable transducers and Linear Potentiometers (LPs) were used. Barriers had two sets of cable transducers installed: one at the elevation where load was applied, and the other 300 mm above the deck top surface. Sets were located near specimen edges (centred approximately 25 mm from side faces) to track possible twisting and referenced to the lab strong floor. Vertical deflection was measured by two LPs located at the tip of the overhang. Relative horizontal slip between specimens and the strong floor was measured by two LPs placed behind each specimen.

Finally, an LP was placed halfway along the specimen width to measure gap (i.e., crack) formation at the barrier-deck interface.

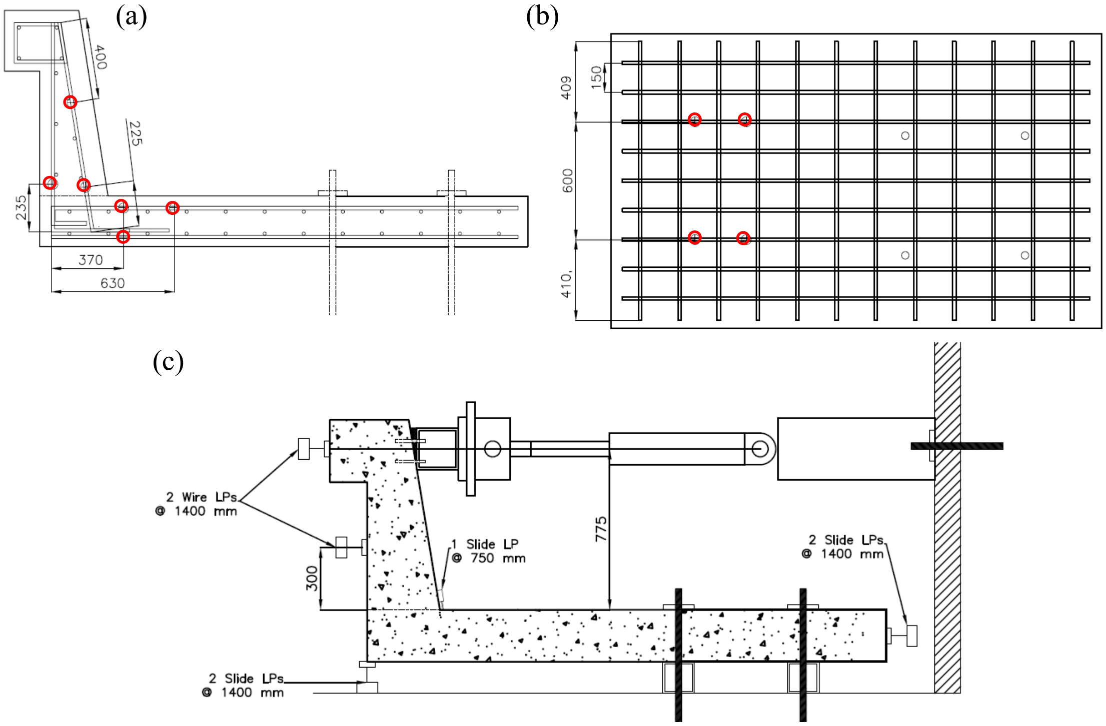

Figure 4.11 Instrumentation locations (a) lateral, (b) Top view of deck slab. Circles marked positions; (c) typical displacement sensors locations. Measures in mm.

Figure 4.12 shows the zone captured by a 3D Digital Image Correlation (DIC) camera system. DIC data was captured on either side of each specimen with focus on barrier-deck junctions where large stress concentrations were expected (Fig. 4.12(a)). DIC cameras had a 5 MP resolution (2448-pixel width) which takes photos at a desired frequency (1 Hz here) to produce time-lapse images that are then processed to measure distributed strains and displacements. Tracking was enabled through a dotted texture drawn using a special roller and paint (Fig. 4.12(b)). Dot size was 1.27 mm and selected considering the camera resolution and field of view (i.e., size of region being captured) size to ensure good resolution of results (i.e., 5+ pixels per dot (Correlated Solutions, 2021a)). The area included the joint itself and one element depth away from the joint in both the deck and barrier (Fig. 4.12(c)). This area was chosen as a D-region was probable to form given the geometry discontinuity and large stress of the knee joint connecting both elements until failure. DIC images were processed with VIC DIC 3D-9 software using default options of the program to obtain concrete surface strains, displacements, and crack widths as discussed later. Program was calibrated using speckle images with a calibration board provided by manufacturer which allowed DIC camera system to map the area of interest prior further analyses were performed. Calibration scores for each specimen was: 0.031 (SP-01), 0.029 (SP-02), 0.034 (SP-03), and 0.028 (SP-04). These values represent the mean distance between extracted and predicted location of calibration points from calibration board expressed in hundredths of pixels (Correlated Solutions, 2021b). Score values below 0.1 are acceptable calibration scores with those closer to zero more precise.

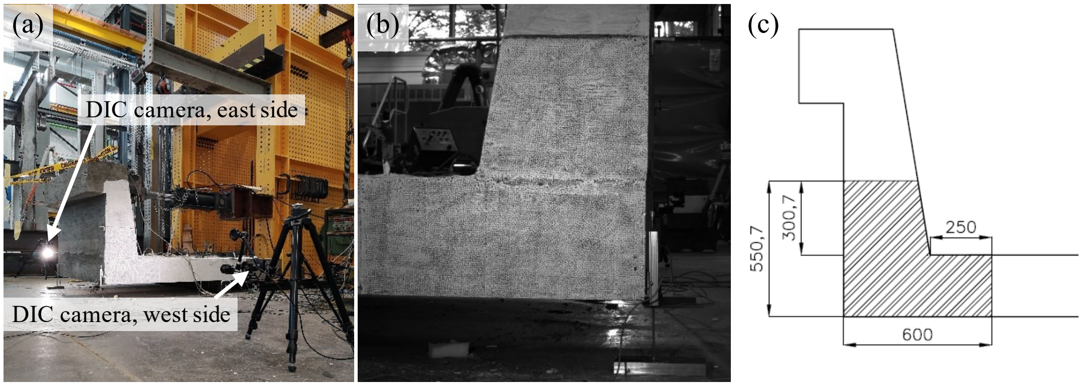

Figure 4.12 (a) DIC setup, (b) dotted area under analysis, and (c) DIC area dimensions.

4.5. Test Results and Discussion

Key results from each test are shown in Table 4.9. Load-displacement curves (horizontal and vertical) are shown in Fig. 4.13. Deflections showed correspond to average values that sensors at load point (CB_775) and tip of overhang reported (LP_OVG) during the tests (see Appendix C.1 for sensor locations). Horizontal deflections reported were calculated by subtracting averaged deflections at loading point with horizontal slip measured between specimen and strong floor. Barrier rotations were calculated relative to a vertical axis referenced from the rear vertical face of the barrier and horizontal deflections reported by CB_300 sensor. These two points were selected since curvature-based deformations in this region very negligible based on strain and limited barrier damage observed during testing. Energy absorption was computed by calculating the area under the horizontal load-deflection curves (Fig. 4.13(a)). In all cases, specimen twisting about a vertical axis was negligible since transducers gave similar readings on the east and west sides of all specimens. Appendix C.2

shows relevant expressions used to process deflection and rotations, as well as rotation curves.

Table 4.9 Key test results.

Item	Key stages[a], location	SP-01	SP-02	SP-03	SP-04
Load, kN	Cracking, deck	27.3	28.9	28.4	28.4
	Cracking, barrier	57.6	53.8	59.6	57.6
	Peak	145	93.5	105	103
Horizontal deflection, mm	Sensors used	CB_775	CB_775	CB_775	CB_775
	Cracking, deck	0.91	1.95	2.48	2.03
	Cracking, barrier	5.46	10.9	9.96	8.12
	Peak	27.7	41.7	43	21.2
Vertical Deflection, mm	Sensors used	LP_OVG	LP_OVG	LP_OVG	LP_OVG
	Cracking, deck	1.42	2.20	1.39	1.94
	Cracking, barrier	7.02	13.4	11.8	8.75
	Peak	27.4	38.5	39.0	19.4
Rotation, rad	Sensor used	CB_300	CB_300	CB_300	CB_300
	Cracking, deck	0.0016	0.011	0.0054	0.0022
	Cracking, barrier	0.0098	0.031	0.021	0.010
	Peak	0.050	0.092	0.094	0.033
Strains, με	Sensors used	DECK_1 / BAR _1	DECK_1 / BAR _1	DECK_4 / BAR _1	DECK_1 / BAR _1
	Cracking, deck	78.3	29.3	33.5	34.6
	Cracking, barrier	104.6	130.5	73.4	144.7
	Peak (deck, barrier)	2769 / 1119	2069 / 3197	2795 / 2268	521 / 1397
Energy absorbed, J		2500	2717	3122	1393
Failure mode		Diagonal Tension	Diagonal Tension	Diagonal Tension	Diagonal Tension
Failure location		Deck-Barrier Junction	Deck-Barrier Junction	Deck-Barrier Junction	Deck-Barrier Junction

[*] Yielding not observed in any test.

4.5.1. General Response

Figure 4.13 presents load-deflection curves for various types of displacements. The response of all specimens was similar until first cracking occurred in the deck near the support. This was expected as response prior to cracking is dominated by concrete and not reinforcement. After this point, structures with steel-reinforced decks (SP-01 and SP-04) had larger stiffness than those with GFRP-reinforced decks (SP-02 and SP-03). Similar responses were seen with rotations (see appendix C.3). The post-cracking region was generally linear with load drops corresponding to crack formation and propagation across the deck. Load drops were more noticed in SP-02 and SP-03 and attributed to the stiffness of reinforcement used in each deck. At a load around 60 kN, the LP measuring gap at barrier-deck interface (Fig. 4.13(c)) began reading non-negligible deformations, corresponding with cracking at the barrier-deck interface. Following barrier cracking, specimens showed largely linear responses until failure. Rotations were similarly consistent with reinforcement stiffness differences with stiffer reinforcement having less rotation.

During testing of SP-01, sudden slip between specimen and strong floor occurred at around 120 kN. There were three sudden load drops until the anchor bars reached the edges of holes in the strong floor. Data indicates that this slip did not affect the overall response of SP-01. In SP-02, there was a mechanical problem with the hydraulic system soon after deck cracking (~30 kN). This created an unintended load-unload cycle but is not expected to affect peak load. No unexpected events were observed during SP-03 and SP-04 tests.

All specimens failed due to diagonal tension inside the barrier-deck joint. For control specimens, SP-02 had 36% less strength than its steel-RC counterpart (SP-01). However, SP-02 had 50% larger horizontal deflection than SP-01 at failure with similar observations for vertical deflection. For repaired specimens, SP-03 was 12% stronger than SP-02, but 27% weaker than SP-01. SP-04 was 9.9% stronger than SP-02 but 29% weaker than SP-01. More insight on the effect of reinforcement type on response and repair effectiveness are given in Subsections 4.5.5 and 4.5.6, respectively.

SP-04 recorded considerably smaller deflections than other specimens at failure, while SP-03 reported similar deflections to SP-02 at failure. Similar observations were noted with rotations at failure. SP-04's smaller rotations and deflections at failure is attributed to the use of steel bars to reinforce its deck.

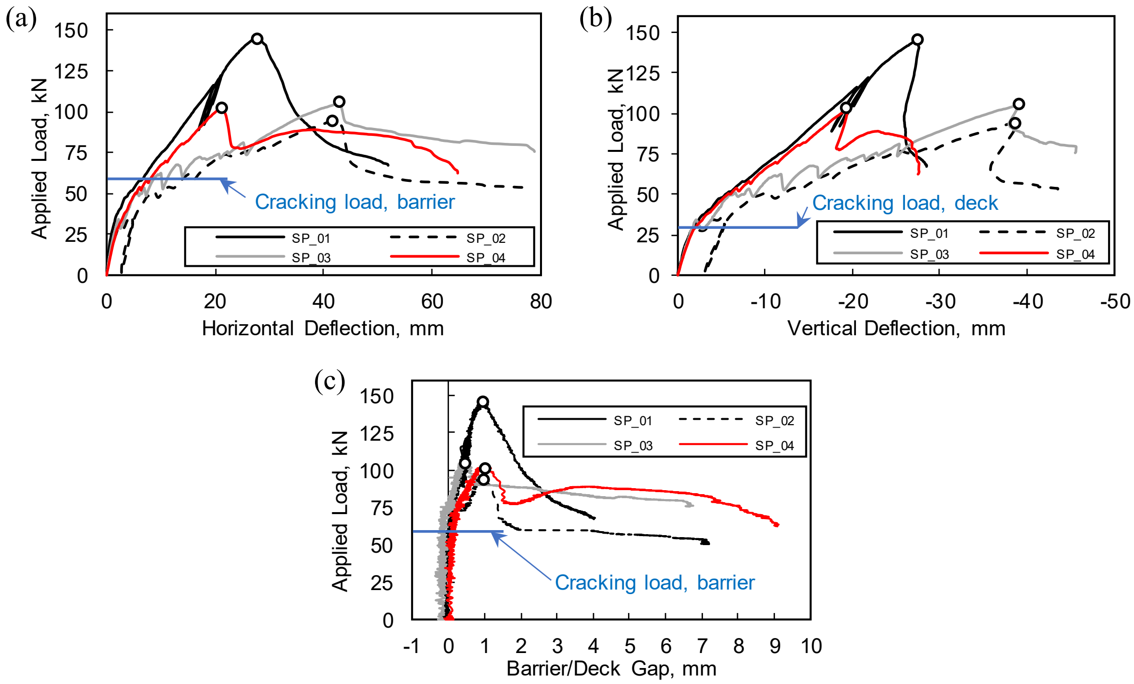

Figure 4.13 Control and repaired specimens' load-deflection curves for (a) horizontal displacement, (b) vertical displacement, and (c) gap opening at barrier front face base. Circles denote specimens' peak loads. Average cracking load for the deck or barrier given for illustration.

After reaching peak load, SP-01 and SP-01 saw a gradual loss of load with increasing displacement until tests were stopped when load decreased to 50% of peak. SP-03 and SP-04 were terminated at 65 and 60% of peak load, respectively, for safety reasons as excessive cracking noises and damage was noted right before tests were stopped. Shortly after specimens reached their peak loads, deck horizontal deformation decreased as energy released and further deformations in the barrier/deck interface reduced strain in the deck and corresponding curvature-based deformation. Specimens had different features at and after failure. For instance, SP-01 and SP-04 had similar responses up to failure of SP-04, which happened at lower load than failure of SP-01. Even though both decks were reinforced with steel, two factors are believed to cause this difference: (1) the use of hooks in both vertical and horizontal bars crossing the junction in SP-01, and (2) the reinforcement material used for vertical bars. Hooks create added confinement in the concrete at the junction, which contributes to joint strength in knee joints (see Subsection 2.6.1) (Mogili and Kuang, 2018; El-Metwally and Chen, 2017). Hooks encases the diagonal compressive strut that flows in the rear corner and improves the specimen's ability to strain more, subsequently impacting failure load. The lower stiffness of GFRP bars used in SP-04 with respect to steel bars in SP-01 may induce larger tensile strains into the concrete, reducing the capacity of the compressive strut and nodal zones. The combined effect of these aspects is observed in peak loads recorded by SP-01 and SP-04 (145 and 103 kN, respectively). This is consistent to the response that SP-02 and SP-03 reported at failure, where neither of the structures had 180-degree hooks within the joint and were fully GFRP-reinforced. More details on this in Subsection 4.5.4.

In SP-03, a vertical crack on the barrier's west side face of the barrier formed after peak load (Fig. 4.14(a)). This crack was related to combined action of excessive tensile stresses in concrete and reinforcement being closer to that face than planned during fabrication (Appendix A), leading to a concrete splitting crack. Another relevant post-peak crack was observed in SP-04, which reported a concave down crack at the deck top (Fig. 4.14(b)). This crack was observed after the specimen's second peak load (i.e., around 83 kN) and may be related to an anchorage failure related to combined action of excessive rotation (around 0.047 rad) and weakened joint that had already begun to fail. After SP-04 initially failed, it sustained load between 78 and 89 kN for considerably more deformation. Strain gauges in the top longitudinal rebar in the deck reported strains below yield, leaving room to deck slab to strain more after first peak load was attained. SP-04 found a new resistive force system within the structure, evident by the plateau-like region seen in the load-deflection curves. This plateau ended when a second diagonal crack formed followed by the concave down crack mentioned earlier.

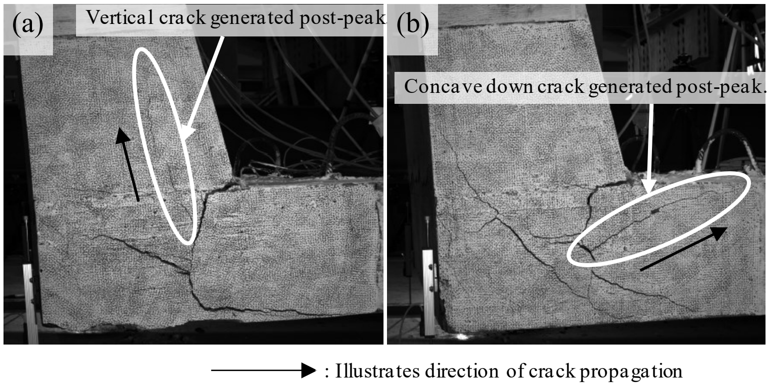

Figure 4.14 Special cracks generated post-peak of (a) SP-03 and (b) SP-04.

4.5.2. Load Strain Response

Load strain curves are presented in Fig. 4.15. Strains displayed similar trends to load-deflection curves. Strains were very small prior to cracking but increased rapidly, particularly for bars on the flexural tension side of the element, after cracking (Table 4.9). Strain gauges located on the flexural compression sides of barriers and decks (i.e., BAR_3 and BAR_6; DECK_3 and DECK_6, respectively) had a sign convention shift as tests approached peak load. This is attributed to cracks propagating close to these sensors as the neutral axis changed with loading, putting these bars under tension. However, in the deck this shift is particularly linked to the presence of axial tension in the deck which led to neutral axes were smaller than the reinforcement depth. Note that SP-02's barrier sensors in compressive reinforcement (i.e., BAR_3 and BAR_6) seemed to have been damaged as BAR_3 did not record strains, and BAR_6 reported large positive strains readings during the entire test. This impacted failure analysis proposed in Subsection 4.5.4.

By comparing strains in SP-01's deck (Fig. 4.15(a)) from DECK_1 strain gauge with those from tensile tests (Subsection 4.3.2), it may be inferred that deck slab's top reinforcement bars yielded prior to the element attained its peak load. However, responses in the other gauge, DECK_4, at the same location (Fig. 4.15(b)) show no evidence of material yielding.

The lack of yielding was consistent with damage observed in the top deck and load-displacement responses. Gauge DECK_1 is suspected to have been damaged when the specimen slid on the floor which may explain why that gauge gave inconsistent results after that sliding compared to other sensors. Moreover, theoretical calculations reported that the yielding would corresponding to a force of 229.46 kN. Peak load is 37% smaller than yield load, discarding the possibility of observing yielding of this specimen.

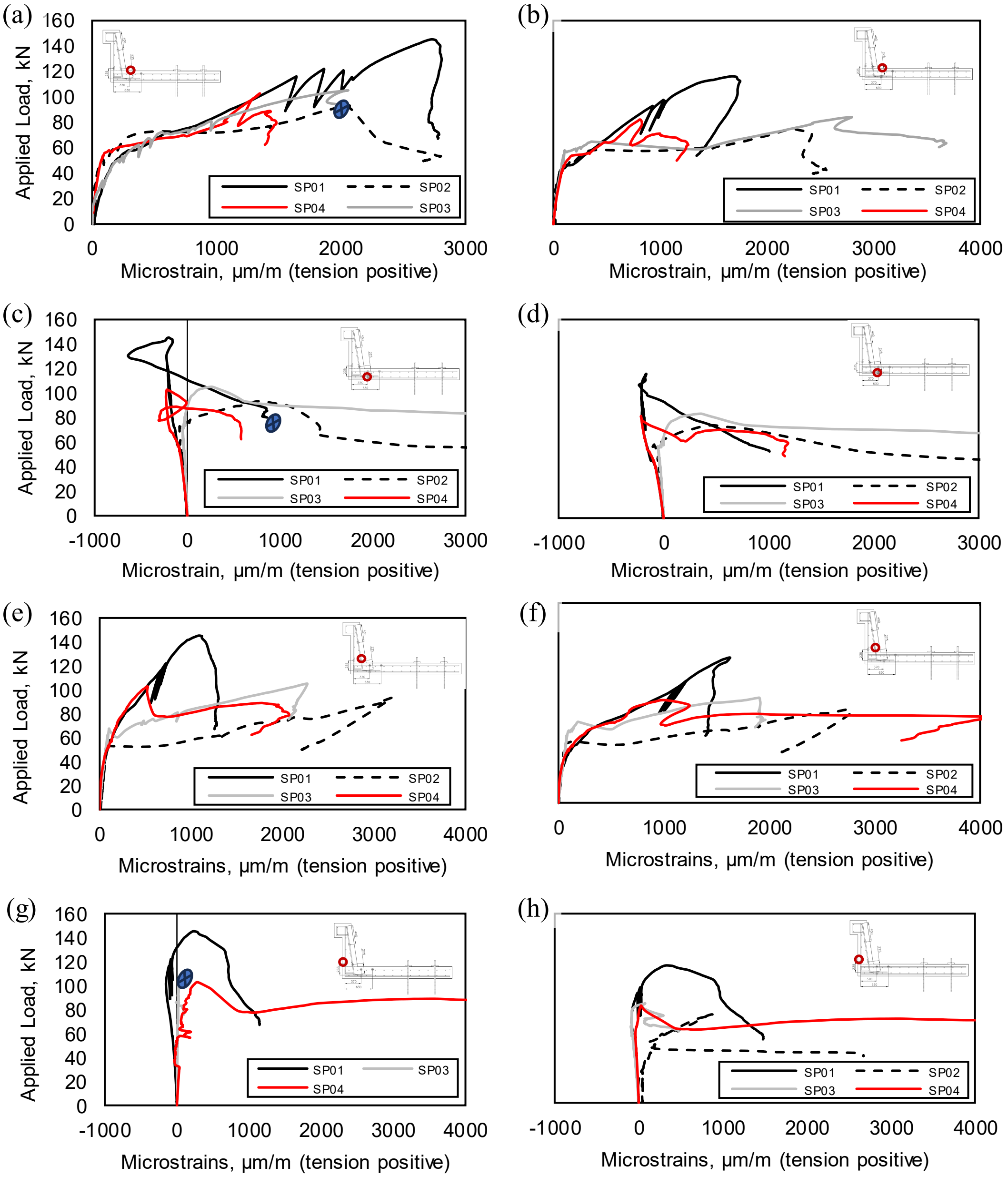

Note: ⊕denotes strain gauge failure. BAR_3 strain gauge from SP-02 was damaged.

Figure 4.15 Load-Strain curves for strain gauges (a) DECK_1, (b) DECK_4, (c) DECK_3, (d) DECK_6, (e) BAR_1, (f) BAR_4, (g) BAR_3, (h) BAR_6.

4.5.3. Crack Pattern

Crack patterns after testing are presented in Figs. 4.17 (plan) and 4.18 (elevation). Crack formation was observed in load-deflection (Fig. 4.13) and load-strain (Fig. 4.15) curves as load drops and strain increases. DIC was used to track joint crack propagation and reported later in this section. Decks experienced almost all cracks formed as they were subject to combined flexure and axial tension. Top surfaces had the largest crack concentrations with the majority being perpendicular to the loading direction; consistent with flexure-tension cracks formed under negative moments.

No flexural cracks were observed in barriers, except for a horizontal crack that formed at the deck connection around 60 kN (Table 4.9, Fig. 4.16). A few vertical cracks formed post-peak in SP-02, SP-03, and SP-04 above the barrier-deck joint though with little contribution to specimen response. Their origin is related to excessive strain in the joint after failure.

The critical crack formation was observed in the joints. For each barrier, a vertical crack in the deck near the barrier's front face connected to a horizontal crack formed at the base of the barrier. This phenomenon was recorded at large strains, observed in timelapse images, in the front layout's vertical reinforcement (Fig. 4.16). As more deformation was induced in the joint diagonal, cracks begin to appear and are related to the governing failure mode. Nuances of this are given in Subsection 4.5.4.

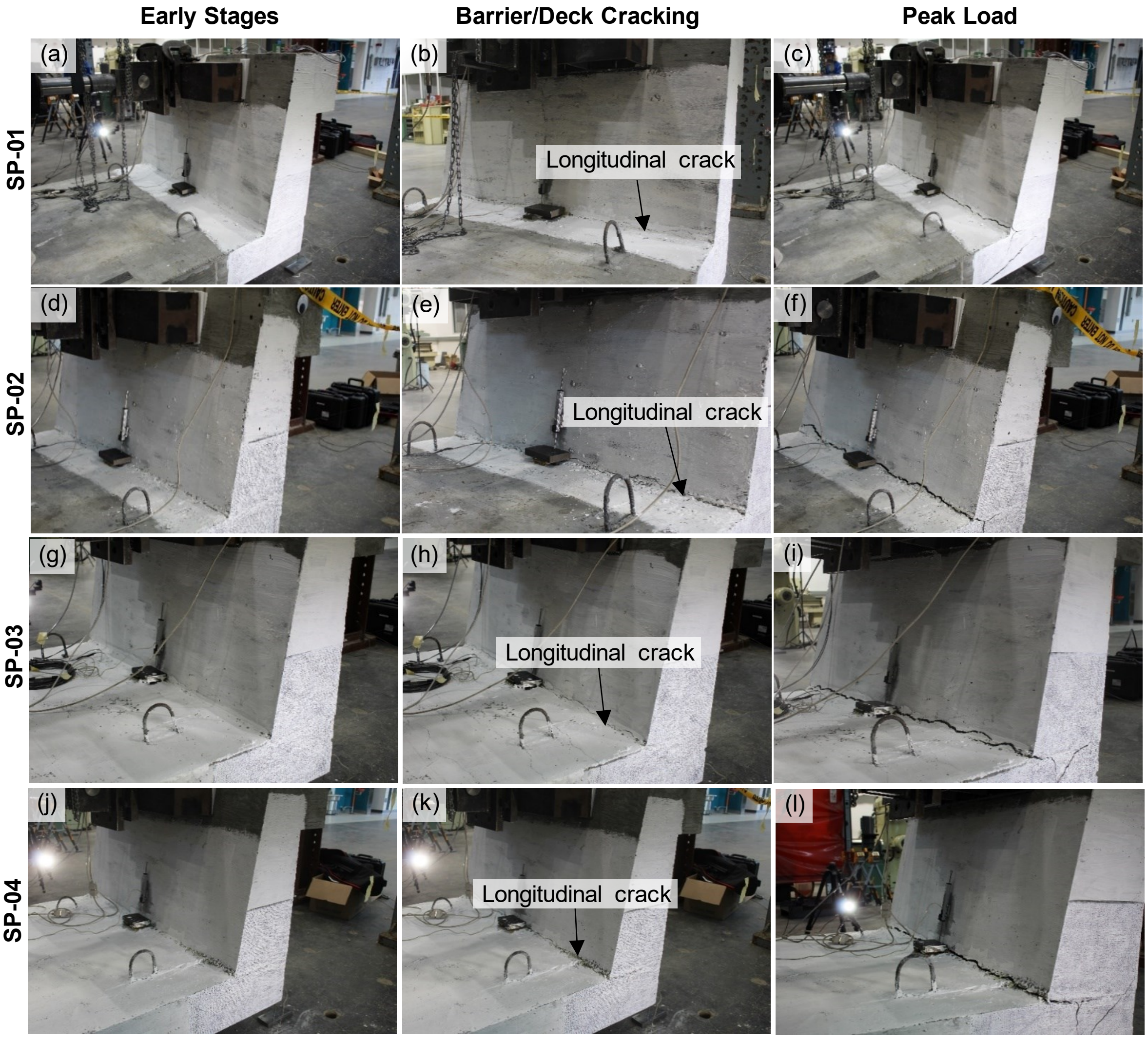

Figure 4.16 Highlights of specimens testing as indicated for each column.

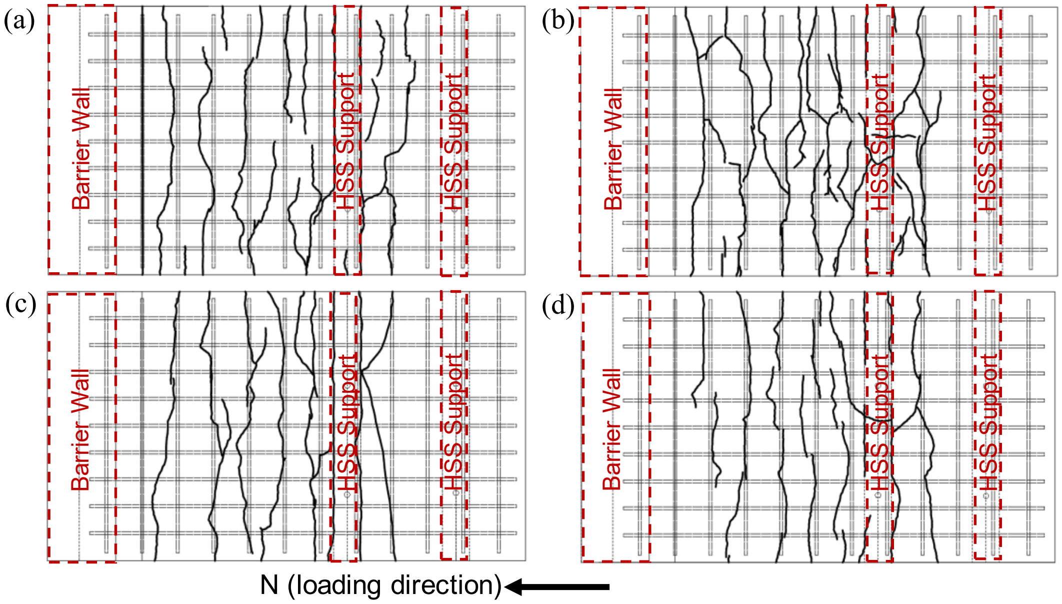

Figure 4.17 Plan view of crack patterns in (a) SP-01, (b) SP-02, (c) SP-03, and (d) SP-04.

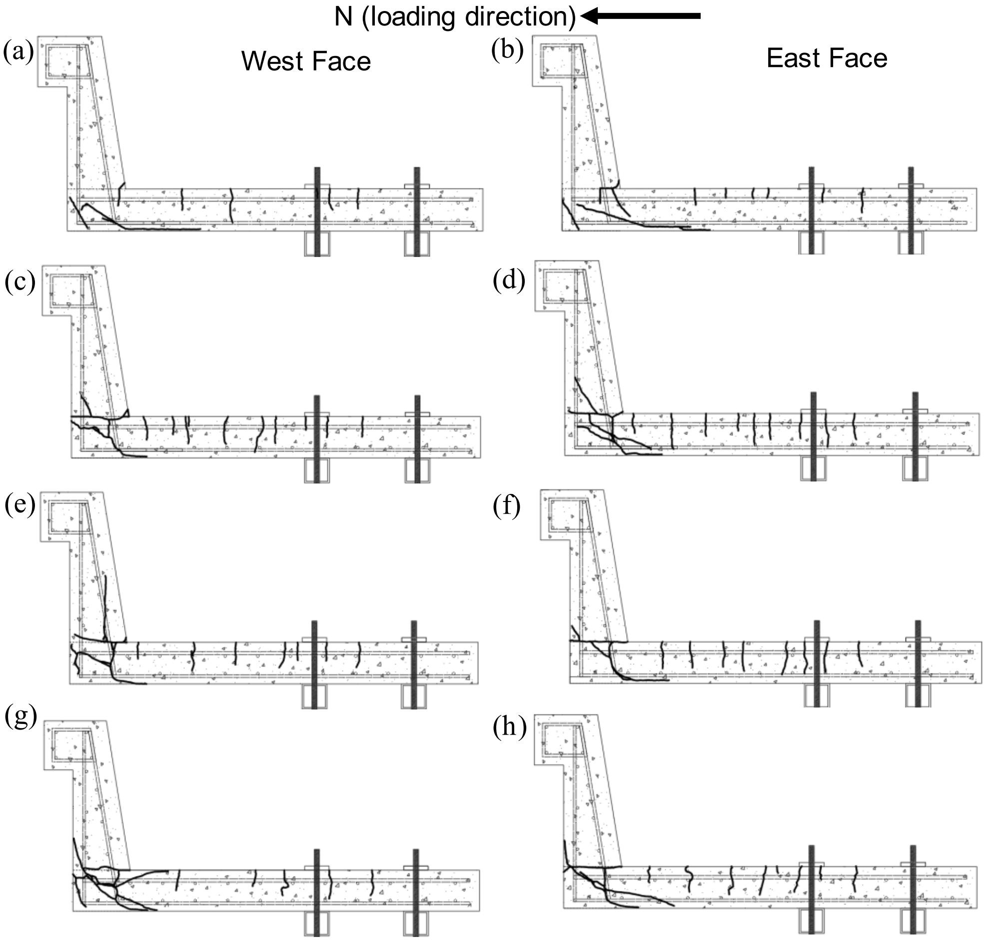

Figure 4.18 Elevation views of crack patterns in SP-01 (a, b); SP-02 (c, d); SP-03 (e, f); and SP-04 (g, h). Note: east face images flipped for comparison purposes.

Crack widths were measured using images taken from DIC systems in tests and processed with VIC-3D 9 software (Correlated Solutions, 2021). Tracked cracks are shown in Fig. 4.19 with load-crack width curves in Fig. 4.20. Crack widths were found with virtual extensometers which connects two reference points at an initial distance and monitors these points to record change of length in subsequent images. Virtual extensometers were placed perpendicular to each analyzed crack. Cracks chosen for measurement were found in all specimens at around the same locations. E0 tracks cracking near the barrier-deck interface ~20 mm from the barrier front face. E1 captured a vertical crack that formed after E0. E1 was placed ~10 mm below the barrier-deck interface. E2 and E3 tracked the main diagonal crack. E2 tracks cracking at the edge of the barrier-deck interface, while E3 tracks cracking near the centre of the joint. E2 was placed by drawing a vertical line from the intersection of the barrier/deck inside corner to its intersection with the diagonal crack. E3 was placed ~20 mm right from E1. In all cases, length of digital extensometers was set to 20 mm which assured sensors were placed in regions where no possible debris or imperfections could affect crack width recording. Larger extensometer lengths (e.g., 25 and 30 mm) were considered but found similar results to those with 20 mm extensometers.

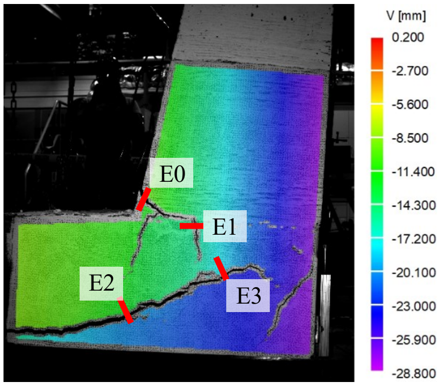

Figure 4.19 Typical location and label of markers to track crack development during tests.

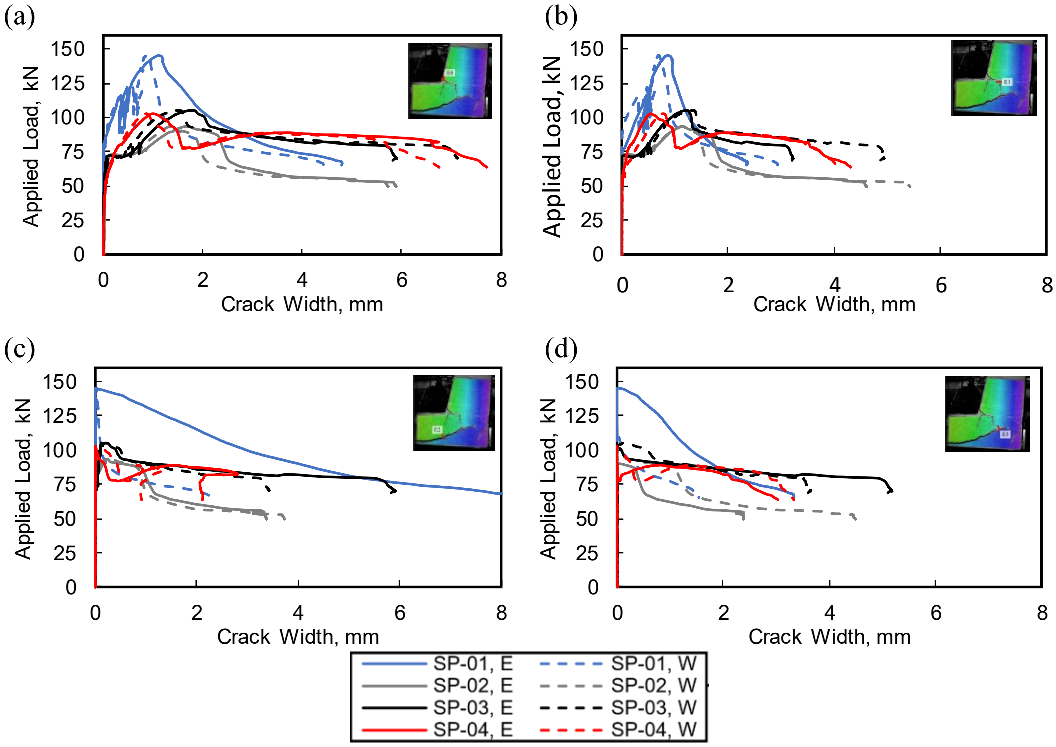

Figure 4.20 Load-crack width curves of (a) E0, (b) E1, (c) E2, and (d) E3. Solid lines correspond to east face recordings, while dashed lines to west ones.

As per CSA S6:19 limits crack widths for GFRP-RC under service loads to 0.5 and 0.7 mm for members subjected to aggressive environments and other members, correspondingly. For steel-RC structures, however, CSA S6:19 limits are based on limiting tensile stresses according to exposure category. These limits are given for comparison purposes as crack widths are not a concern in extreme event structures (i.e., their design is mainly governed by strength), as barriers are. In the case of deck slabs, crack width limits are a common serviceability check as these are linked to safety and aesthetic aspects, although for the scope of this study did not have significant impact.

All cracks showed expected responses for RC members with steel and GFRP bars. E0 (Fig. 4.20(a)) and E1 (Fig. 4.20(b)) have measurable crack widths when load reaches 80 kN for SP-01 and 70 kN for the other tests. Shortly after this, widths grew consistently larger until failure. At failure, crack widths in SP-01 and SP-04 are similar, while SP-02 and SP-03 have generally the same behaviour. Post peak responses show progressive, and dramatic, crack widening until test end. As seen in Fig. 4.20, crack widths were similar on the east and west side of each specimen.

Crack E2 (Fig. 4.20(c)) started to report non-negligible crack widths in GFRP-RC decks after 70 kN. Steel-RC decks, however, only began reporting non-zero crack widths at the point where peak load was reached. This crack then propagated diagonally towards the joint top rear, as measured by E3 (Fig.4.20(d)). This means that the diagonal crack propagated from the lower region of the joint (i.e., near the bottom of deck) and spread upwards. Following failure, crack widths grew larger until tests were terminated. Cracks E0 and E2 at the interface between the deck and the barrier-deck joints had the largest cracks in all specimens, exceeding 6 mm in some cases. Prior to failure, the largest crack widths (regardless of extensometer) were reported in SP-02 and SP-03 as these specimens had lower stiffness. SP-01 had, in almost all cases, the smallest crack widths except for E2 at the east face joint. SP-04 was consistently between these extremes, attributed to the hybrid reinforcement used in that specimen. These responses are attributed to reinforcement stiffness and the presence of hooks in the joint. A different response was exhibited by E2 in SP-04, where its crack-width curve exhibited a short recession in crack width, when test reached an 88 kN load post-peak. This is related to formation of additional cracks in the joint that shifted deformation elsewhere.

4.5.4. Failure Analysis

Figure 4.21 presents the final state of the joint in each test and Fig. 4.22 the principal tensile strain contours using VIC-3D (Correlated Solutions, 2021b). Principal strain contours are an effective way of qualitatively visualizing cracks in DIC. Damage mainly occurred within the barrier-deck joints with all specimens failing under diagonal tension (Table 4.10).

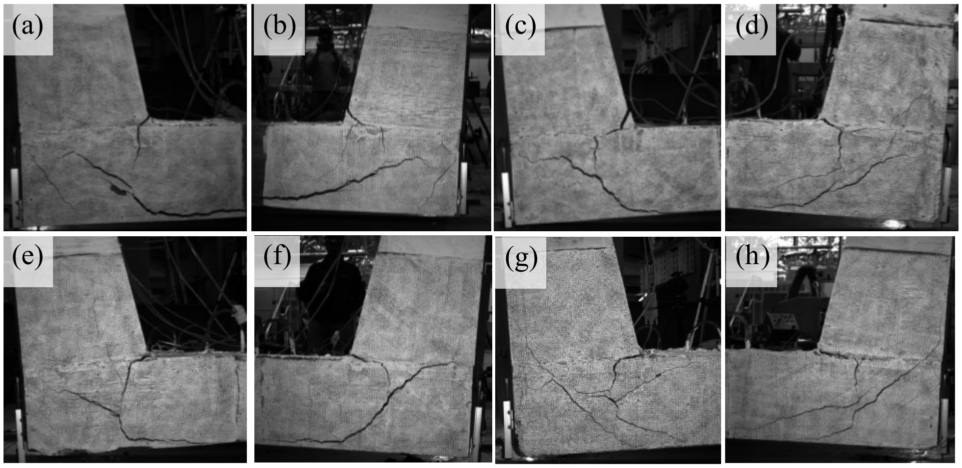

Figure 4.21 Final state of specimens' junctions: SP-01 west (a) and east side (b); SP-02 west (c) and east side (d); SP-03 west (e) and east side (f); and SP-04 west (g) and east side (h).

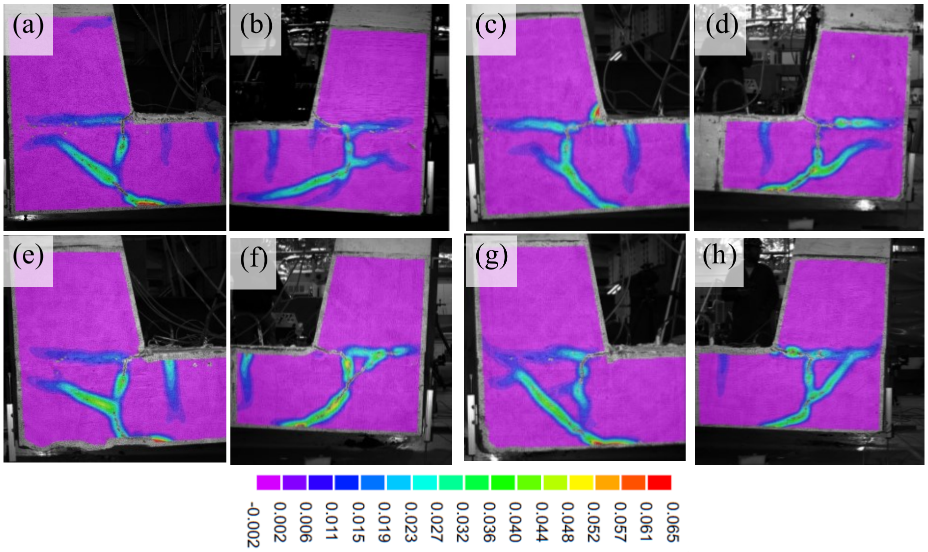

Figure 4.22 DIC principal strains map contour at peak load for qualitative assessment of crack pattern: SP-01 west (a) and east side (b); SP-02 west (c) and east side (d); SP-03 west (e) and east side (f); and SP-04 west (g) and east side (h). Tension positive; strains given in mm/mm.

In all cases, joint capacity dictated peak load. Diagonal tension failure happens when compressive stresses travelling through a diagonal strut connecting compression regions from adjoining members exceed strut capacity. Failure results in the formation of a diagonal crack along the strut as observed in each test. These regions are not suitable to analyze with plane section analysis; instead, Strut-and-Tie Model (STM) was considered as described in Subsection 2.6.1.

Though specimens failed by diagonal tension (DT), analysis was conducted on several failure modes to determine if they may be a concern. Four failure modes were assessed: flexure (F) (including deck flexural-tension, dubbed as F+T), pullout (PO), shear (V), and DT. These were selected as potential failure modes based on test setup and literature (Azimi et al., 2014; Rostami et al., 2018), though these papers did not consider STM.

Table 4.10 presents demand-capacity ratios for each failure mode; ratios were computed as test-to-predicted load ratios. Capacities were determined using the analytical model described in Chapter 3 with materials and geometry based on Section 4.3. For pullout, capacity was computed using the approach presented in Subsection 3.3.5.1 and using Eq. 2.4 and 2.5 to define bond-critical moment resistance which was transformed to a force and used to calculate the ratio reported in Table 4.11.

For DT, capacity ratios reported were obtained using three approaches: (1) an STM proposed by El-Metwally and Chen (2017) (Subsection 2.6.1), (2) a modification of (1) where contribution of tensile forces to nodal zone size is accounted by force equilibrium at each node (Appendix E), and (3) using code expressions relevant to this type of analysis from CSA S6:19. Acting forces and bar stresses were defined using load cell data and strains (Fig. 4.15) recorded during tests, respectively. Strains were converted into stresses and bar forces using reinforcement's geometric and mechanical properties (Section 4.3). Strains in all cases were the averages from strain gauges at the same locations on both sides (i.e., east, and west). Strains recorded in barriers and deck reinforcement close to joint (see Appendix C for locations) were used to calculate neutral axis depth, c, by strain compatibility assuming sections remain plane outside the joint. This was done to calculate nodal zone widths for the compressive strut at either end of the joint. Eq. 4.8 was used in an iterative procedure to determine c.

$$\frac{d' - c}{d - c} - \frac{\varepsilon'_{bar}}{\varepsilon_{bar}} = 0 \tag{4.8}$$

d' and d are the locations of compressive and tensile reinforcement inside the cross-section, respectively; ε'_{bar} and ε_{bar} are strains recorded for compressive and tension reinforcement near the joint, respectively. Recorded barrier strains were used to create a linear equation to extrapolate strains, at the top of the joint given that strain gauges were 50 mm above this point. This seemed appropriate as this region was subjected to large variation in moment along its length. Given the near constant bending moment in the deck, no extrapolation was performed for those strains since large strain variation were not expected. Note that some limitations were found when using Eq 4.8 to obtain compression regions for SP-02's barrier due to faulty sensors in compressive reinforcement, as explained in Subsection 4.5.2. This prevented the use of Eq. 4.8 to estimate c as previously described. Thus, compression regions from same load levels were taken from analytical model and used for analyses described herein.

Table 4.10 Demand-capacity ratios from failure analysis conducted.

Specimen	Failure Mode	Method used	Predicted force to cause failure mechanism, kN	Test/Predicted ratio
SP-01 (peak load: 145 kN)	F (barrier)	See 3.3.5.1	250	0.58
	F+T (deck)	See 3.3.5.1	220	0.66
	Pullout, PO	See 3.3.5.1	265	0.55
	Shear†, V	See 3.3.5.2	302	0.48
	Diagonal Tension, DT	See 3.3.5.2	126	1.15
		See Appendix E	126	1.15
SP-02 (peak load: 93.5 kN)	F (barrier)	See 3.3.5.1	520	0.18
	F+T (deck)	See 3.3.5.1	302	0.31
	Pullout, PO	See 3.3.5.1	191	0.49
	Shear†, V	See 3.3.5.2	346	0.27
	Diagonal Tension, DT	See 3.3.5.2	88	1.06
		See Appendix E	86	1.08
SP-03 (peak load: 105 kN)	F (barrier)	See 3.3.5.1	527	0.20
	F+T (deck)	See 3.3.5.1	300	0.35
	Pullout, PO	See 3.3.5.1	191	0.55
	Shear†, V	See 3.3.5.2	292	0.36
	Diagonal Tension, DT	See 3.3.5.2	103	1.02
		See Appendix E	104	1.01
SP-04 (peak load: 103 kN)	F (barrier)	See 3.3.5.1	527	0.20
	F+T (deck)	See 3.3.5.1	220	0.48
	Pullout, PO	See 3.3.5.1	191	0.54
	Shear†, V	See 3.3.5.2	292	0.35
	Diagonal Tension	See 3.3.5.2	104	0.99
		See Appendix E	N/A	N/A

†: Shear ratios reported correspond to barriers.

Demand-capacity ratios are consistent with test observations. Barriers did not show signs of flexural cracking during the tests, beyond the crack at the base, hence flexural-related ratios were in all cases well below unity. SP-01 showed a larger ratio than other tests given the lower strength of mild steel relative to GFRP. Deck capacity ratios for F+T showed steel-RC members having larger ratios than GFRP-RC ones; also related to material strength differences. The presence of axial tension in the deck contributed to a reduction in F+T capacity which also was exacerbated with different reinforcement layouts than barriers that led to larger ratios than those reported for barriers under flexure.

Failure by PO was determined by estimating a pullout force that exceeded barrier's rebar tensile stress determined with relevant development length equations shown in Subsection 2.7.2. For this case, specimens reported ratios were smaller than unity, meaning that failure by PO was not a concern.

Failure by one-way shear was checked in barriers with results indicating that no barriers at risk of one-way shear failure prior to DT failure. Deck shear failure was not expected as the deck carried negligible shear during testing and this shear was not even checked.

Finally, DT ratios computed are the closest to unity. This is expected as STMs are lower-bound solutions to theorems of plasticity (i.e., STMs underpredict capacities from tests, leading to slightly conservative results provided the STM is reasonably and deformation of STM components is minimized) (El-Metwally and Chen, 2017). Most STM analyses predicted strut failure at the bottom node (i.e., Nodal Zone 1) which is consistent with DIC-tracked crack formation (Fig 4.20). Node 1 is located at the bottom of the joint and Node 2 is at the top of the joint at the barrier-deck interface. Appendix E presents these locations in more detail. Finally, no STMs provided a lower-bound solution for SP-04. This could be attributed to small strains recorded at failure that provided larger compression zones (i.e., more strut capacity) than expected. The critical capacity of the STM was in all cases the one representative of the strut-nodal zone interface. The contribution of severe strut coefficients, β_s, to reduce node strength was assessed with two scenarios were considered: (1) strut assumed as bottle-shaped as joint is unreinforced (i.e., no stirrups provided), leading to use $\beta_s = 0.6$. This assumption was used by El-Metwally and Chen's (2017). (2) As the strut is formed within a member under tensile forces, a more stringent β_s was used by the modification proposed in Appendix E, using $\beta_s = 0.4$. This is consistent with ACI 318R-19 requirements for struts inside tension members, like the decks in the tested specimens. This could have contributed to joint weakening, reducing its capacity. Finally, barrier's effective depth variation related to different concrete covers used during fabrication showed to have an adverse impact to nodal zone widths. This is related to geometry and trigonometry relations used to find this measurement that depends on a strut angle. As neutral axis depth reduced for post-cracking load stages, moment arm increases between compression and tension couple forces. This length increases also by small concrete covers, resulting in a wide angle that will decrease nodal zone widths at a faster pace in elements with smaller concrete covers with respect to elements with larger ones.

The use of ACI 318-19's STM provisions over CSA S6:19's was mainly based on the implementation of El-Metwally and Chen's (2017) STM which used ACI 318-19's expressions to estimate limiting capacities of nodal zones and strut. Moreover, as shown in Table 4.11, it was found that CSA S6:19's STM expressions predicted failure for some structures (e.g., SP-01, SP-02, and SP-03) before or at same peak load attained, while overestimated capacity of the STM used in the remaining structure, where failure was recorded with post-peak strains.

Table 4.11 values from STM at failure according to CSA S6:19 provisions using strains ε_s or ε_f obtained from tests.

Clause used	SP ID	Experimental ε_s or ε_f, με	θ, deg	ε_1, με	$f_{cu}{}'^{\dagger}$ MPa	$f_{cn}{}'^{\dagger}$, MPa	W_{nd}, mm	C_{str-nd}, kN	C_{nd}, kN	C_{strut}, kN
Nodal zone 1 (bottom of joint)										
§8.10	SP-01	1300	44.5	4600	28.9	23.7	54.8	2376	1947	1425
	SP-04	1500	43.6	5400	26.8	23.7	42.8	1717	1518	877
§16.8.11	SP-02	3000	42.4	9100	19.6	25.8	17.3	508	671	542
	SP-03	2400	40.7	8300	20.8	25.8	23.0	717	891	683
Nodal zone 2 (top of joint)										
§8.10	SP-01	1800	36.6	8800	20	23.7	47.5	1420	1685	1425
	SP-04	1100	37.4	6400	24.3	23.7	24.5	891	868	877
§16.8.11	SP-02	1900	38.5	8100	21.1	25.8	39.9	1261	1545	542
	SP-03	2400	40.3	8600	20.3	25.8	50.2	1530	1944	683

†: Concrete compressive strength used: 45.9 MPa.

Table 4.11 reports steel-RC and GFRP-RC strut and nodal regions capacities corresponding to same load when CSA S6:19 expressions for STM reported failure. Here, ε_s and ε_f are experimental strains of tie reinforcement at node of interest; θ is the angle formed between strut and tie at the specified nodal zone. Strain values were extracted from sensors attached to relevant bars to this analysis. ε_1 is the principal strain as defined in S6:19 to estimate the limiting compressive strength of strut, f_{cu}. Meanwhile, f_{cn} is the limiting stress for node regions with a tension tie in one direction (§16.8.11.5.1(b)). W_{nd} is the nodal zone width at its interface with diagonal strut. Like ACI 318R-19, CSA S6:19 shows in figures relevant to STM analysis an h_a width linked to tie reinforcement; however, no guidelines are given to compute it. Thus, its contribution was calculated from expressions shown in Appendix E. Finally, C_{str-nd}, and C_{nd} correspond to the strut capacity at strut-node region interface and the nodal region capacity, respectively. C_{strut} is the acting compressive force at defined load stage for reference.

CSA S6:19 provisions predicted failure by diagonal tension for control specimens at smaller loads than test peak loads. SP-01 and SP-02 reported failure at a test-to-predicted ratio of 1.09. SP-03 had the same test and CSA S6:19 predicted failure load (ratio of 1.00). SP-04, however, reported failure with strain levels corresponding to post-peak load stages, equivalent to a 1.20 ratio. Failure location, however, was sometimes not consistent with test observations: while SP-02 and SP-03 reported failure at node 1, SP-01 and SP-04 reported failure in node 2.

It was noted that the strut limiting stress governed the capacity of the STM using S6:19 expressions. Limiting strut stress depends on tensile strain at the node of interest which subsequently dictates principal strain, ε_1, magnitude. This strain is magnified by the cotangent of θ and ultimately reduces strut capacity. By looking at the data gathered, principal tensile strains at failure were at least 8300με, leading to limiting stresses around 20 MPa. These stringent stresses combined with low strut widths at failure node contributed to strut failure. For SP-04, failure attained by code expression was more related to small compression regions than ε_1 magnitude. This is related to small strains recorded by sensors during the test and attributed to an early failure of the joint.

4.5.5. Repair Effectiveness

To analyze the effectiveness of a structural retrofit, it is necessary to assess three aspects: strength, stiffness, and energy absorption. In all cases, repaired members should report equal or better response. Both repaired structures exceeded SP-02's strength by 13% and 9.9% (SP-03 and SP-04, respectively), while neither structure using dowelled bars reached the same strength as SP-01 (i.e., SP-03 was 27% weaker than SP-01, while SP-04 was 29% weaker). Strength was also affected by different effective depths that each element had. If all specimens would have same concrete covers, it is feasible that this percentual gaps slightly increase from those shown here. SP-04's peak load was unexpected as it was believed it would attain a larger load at failure given its hybrid reinforcement (i.e., an intermediate response between GFRP-RC and steel-RC was expected). However, its peak load was closer GFRP-RC's, indicating that additional aspects inherent from repairs influenced performance. Lack of joint confinement since reinforcement from this structure did not have hooks could have prevented this specimen from reaching larger peak loads. This aspect could have also impacted the performance of other specimens (aside from SP-01) which lacked joint confinement partially or completely. Repaired structures had the same failure mode as controls. This indicates that the dowelling process, including choice of bonding agent and drilling depth, was effective for the tested specimens.

For energy absorption, Table 4.9 reports energy absorbed until failure. Though this aspect is better assessed under dynamic testing, it helps comparing responses independent of specimen reinforcement type. SP-02 and SP-01 had similar energy absorption (SP-02 was 8.7% larger). SP-03 absorbed the largest energy, while SP-04 had the lowest (3122 and 1393 J, respectively). Based on this factor, SP-03 was the most flexible, while SP-04 was the most brittle. The fact that an earlier failure occurred in SP-04 subsequently impacted the energy absorbed. Two reasons for this outcome are believed: (1) additional aspects different from repairs performed and previously mentioned in this section related to lack of joint confinement, which showed to be more severe in SP-04 than SP-03. (2) by examining the load-rotation curves (Appendix C.3) it is observed that SP-04's barrier was rotating at a similar rate as SP-01 up to failure. Large rotations are related to low GFRP stiffness relative to steel's that generated large crack widths and strains (Fig. 4.15 for BAR_1 and BAR_4 sensors curves). This generated tensile strains in the joint that could have weakened strut capacity as mentioned in Subsection 4.5.4. This phenomenon in presence of (1) exacerbated SP-04's limited energy absorption. This leads to the impression that repair effectiveness was not a concern in this case, but other factors came into play governing final state of structures. More into SP-04's response, post-peak force redistribution was observed before final loss of strength. This redistribution is linked to low strain levels in deck slab reinforcement at peak load that allowed structure to strain more as new force transmitting systems were activated. Redistribution was also allowed as barrier-deck connection did not show large strain levels to pullout barrier reinforcement from deck slab.

An interesting fact was that deflections between controls and repairs were consistent to reinforcement stiffness magnitudes: SP-03 was closer to SP-02 as both used GFRP bars. SP-04, however, showed agreement with horizontal deflections from SP-02 at after cracking as barrier was reinforced with same material. Vertical displacements after cracking had similar behaviour but in relation to SP-01's as both shared same reinforcement material in deck slabs. By comparing deflections recorded from decks and barriers, it is observed that barrier deflections were not a large contribution to deformation as most of the deflection was due to rotations that carried over from the deck. Barrier's main contribution to this deflection was mainly to rigid body rotation with small bond-slip deflections. This concludes that, in this case, barrier reinforcement effective depth differences did not contribute to the deflections recorded.

4.5.6. Effect on Reinforcement Type

Three main responses were found during testing dictated by the stiffness of reinforcement used to fabricate each specimen. SP-01 (steel-RC) showed the stiffest response while SP-02 and SP-03 (GFRP-RC) were softest. SP-04 (hybrid structure) showed an intermediate behaviour with traits closer to GFRP-RC in horizontal deflections and to steel-RC for vertical ones. Rotations showed similar response with smaller rotations at failure in SP-01 and SP-04 and the largest in SP-02 and SP-03.

Reinforcement strength showed little if any contribution to peak load. Differences between peak loads were most controlled by reinforcement stiffness. As discussed before, presence of tensile forces acting in the joint weakens the concrete and induces failure of the diagonal compressive strut. Failure occurred earlier with lower stiffness reinforcement which saw larger cracks and weaker response. Interestingly, though fabricated as a hybrid, SP-04 did not reach a capacity midway between SP-01 and the other tests. Instead, SP-04 was like SP-02 in peak load, though this was achieved at smaller deflections. This is related to the lower stiffness of GFRP used as barrier reinforcement and the lack of 180-degree hooks in deck longitudinal bars. This may have also impacted the peak load of SP-02 and SP-03 as these did not have hooks or reinforcement detailing at the joint. Although gathered data could verify these observations, past studies endorse use of reinforcement detailing for beam column knee joints, such as the use of transverse reinforcement in orthogonal directions (Mogili and Kuang, 2018), or using various reinforcement layouts to control additional tensile force related to diagonal tension stresses (El-Metwally and Chen, 2017; Park and Mosalam, 2012) and could be beneficial for these kinds of connections, provided squat behaviour is expected. These details, however, could be challenging to install in barrier-deck joints, due to reinforcement congestion and reduced dimensions these areas could have that prevents transverse reinforcement from being installed.

4.5.7. Comparison to CSA S6:06 Commentaries

Table 4.13 reports required strengths following CSA S6:06 commentaries. These requirements establish minimum strengths per unit length derived using a distribution length, L_{dist}, that depends on barrier location (inner or edge segment), geometry, and stiffness to provide dispersal angles. However, commentaries do not provide methods to determine these values for geometries different to the one shown in that section. CSA S6:19 demands a refined analysis through different methods to design the overhanging portion of decks by merging all forces acting upon it to find design forces. In absence of more data, dispersal angles and strengths indicated in S6-06's commentary for an inner portion of a TL-4 barrier were used to estimate acceptability of the tested specimens. Table 4.12 shows the strength used as reference for calculation of moment and force resistance per CSA S6:06 commentary

C5.4. Capacities are obtained by using a design force of 170 kN with corresponding dispersal angles to estimate a larger L_{dist} that should be added to the 1050 mm-long force distribution length. With load applied at height $H_{load} = 700$ mm, L_{dist} obtained are 3348 and 1722 mm for moment and force conditions; these lengths are needed to reach indicated load levels used as reference. Since the setup used in this test program had a larger H_{load} (i.e., 775 mm), L_{dist} for moment and force will be larger. These lengths could not be accommodated within the 1500 mm specimen width (L_{dist}, real) and thus L_{dist} was set as 1500 mm to perform calculations to compute adjusted capacities for moment and force. Adjusted peak load is the product of calculations using H_{load} and L_{dist}, real, respectively.

Table 4.12 Capacity and peak loads adjusted as per CSA S6:06 C5.7.1.6.3.

Test ID	L_{dist}, Theoretical; mm		H_{load}, mm	L_{dist}, real; mm	Capacities, CSA S6 (2006) C5.4		Capacity adjusted to H_{load} and L_{dist}, real		Peak load adjusted H_{load} and L_{dist}, real	
	Moment	Force			Moment, kN-m/m	Force, kN/m	Moment, kN-m/m	Force, kN/m	Moment, kN-m/m	Force, kN/m
SP-01	3348	1773	775	1506	38	100	87.5	113	74.7	96.5
SP-02				1505			87.5	113	48.1	62.1
SP-03				1503			87.6	113	54.2	70
SP-04				1503			87.6	113	53	68.4

Results from Table 4.13 show the shift between the original baseline force and moment threshold and the ones determined for this study. This is due to the reduced available width in test specimens and the larger load height used. The restrained width causes two effects that need to be considered when comparing test results to these limits: (1) increased capacity threshold to exceed, and (2) specimen is subject to one-way action rather than two-way. As seen in tests, specimens failed due to excessive stresses at the barrier-deck joint induced by one-way action that prevented them from attaining larger peak loads. This led to specimens having unsatisfactory performance when comparing capacities to thresholds in the CSA S6:06 commentaries. However, by analyzing these thresholds it is noticeable that these thresholds are intended for analyzing wider specimens undergoing two-way action. Thus, two outcomes are expected to affect force thresholds: (1) reduction of force per length unit as more distribution is allowed in wider structures, and (2) structures under two-way action will have a stronger response as they will transfer forces in both vertical and horizontal directions. This is particularly important for the single slope barriers considered in this program as the spandrel beam on top of the barrier is intended to carry loads along the width of the barrier and have a significant contribution to resistance that was not assessed in this test program.

4.5.8. Comparison with Prior Studies

4.5.8.1. Al-Jaaidi (2021)

As a first approach to this study, Al-Jaaidi (2021) ran Finite Element Analysis (FEA) modelling on similar barrier-deck overhangs. Modelling was done in VecTor2 where structures were conceived as 2D elements, like that shown in Fig. 4.1. Five specimen types were modelled but only four are relevant here: two as control and two repaired which correspond to the specimens tested in this program. Models were run with different reinforcement materials (e.g., steel and GFRP).

FEA analysis performed by Al-Jaaidi (2021) showed agreement with test results. Al-jaaidi (2021) predicted the same failure modes observed in tests. Regarding deflections at failure, FEA and tests show some consistency, except for SP-04 and the FEA counterpart, where the former reported a stiffer response than the latter by 59%. Peak loads, however, were quite different: in all cases, FEA overestimated capacities of tested specimens, where the largest difference corresponded to SP-04 and counterpart's capacities (46%), whereas the closest capacity recorded was between SP-03 and its counterpart (56%).

Multiple aspects should be considered when analyzing these strength variations including both material properties and geometry. Regarding materials, considerable differences are observed between concrete's compressive strength, elastic modulus, and modulus of rupture. Geometric differences were found in test setups and specimen dimensions: (1) height of applied load (700 and 775 mm for FEA models and tests, respectively), and (2) deck thicknesses (225 and 250 mm for FEA and tests, respectively). These combined effects resulted in strength differences reported by Al-Jaaidi (2021) and the present study, not to mention other factors (e.g., model assumptions, concrete covers) that also contribute to dissimilarities previously mentioned. By comparing these capacities to those in Table 4.14, it is concluded that Al-Jaaidi (2021) exceeded this limit, whereas this current study did not.

4.5.8.2. El-Salakawy and Islam (2014)

As described in Section 2.5, tests by El-Salakawy and Islam (2014) consisted of a barrier-deck system with considerably different dimensions from those tested in the present study. Main difference is found in specimen width (6000 mm versus 1500 mm, for that study and current one, respectively). Other aspects like overhang length (700 mm used in El-Salakawy and Islam's (2014) study and 1500 mm in current study) also contribute to response differences. El-Salakawy and Islam's (2014) found that retrofitted specimens were able to almost restore the original strength with repaired middle and end portions attaining 94% and 92% of control counterparts' strength, respectively. The tests loaded in mid segments failed by two-way shear, while edge portions failed by combined action of punching shear with barrier-deck joint failure. In terms of crack patterns, critical lengths (i.e., length measured at top of the wall from start to end of trapezoidal-shaped cracks) observed in repaired and control specimens were consistent among control and repair structures and varied according to segment tested (3000 mm and 1800 mm for middle and end segments, respectively).

El-Salakawy and Islam's (2014) results are closer to what a barrier-deck system behaviour would have in real-life due to its width causing two-way action compared to this study's one-way action. Main reason of this discrepancy being that this study focused on analyzing joint strength, which is more stressed under one-way action, while the other study compared responses between different repair techniques assessed in a two-way system. Shifts between one-way to two-way action also impact failure modes, all tests in this study failed by diagonal tension, while those tested by El-Salakawy and Islam (2014) failed by punching shear. El-Salakawy and Islam (2014)'s specimens exceeded CSA S6:19's force threshold for TL-4 barriers. Two-way action contributed and allowed those tests to surpass this limit; in addition, reduced overhang length may have led to a stiffer response that could otherwise have subjected the barrier to larger stresses, shifting failure mode.

4.5.8.3. Azimi et al. (2014)

Azimi et al. (2014) tested four full-scale specimens comprised of a barrier anchored to a deck. Different barrier geometries and Test Levels were considered. All specimens had a 1200 mm width and connected to a strong floor without considering overhang effects. Results showed that given the support condition, barriers exhibited more damage - contrary to what was observed in this study. However, Azimi et al. (2014) prevented failure of the barrier-deck junction which may not be representative of a system with an overhang. Crack patterns observed by Azimi et al. (2014) were consistent with flexural tension combined with anchorage failure, and diagonal tension. This latter failure mechanism showed cracking consistent with knee joints under closing action (Mogili and Kuang 2018). This effect was related to a compression reaction force at rear corner of the deck which created a diagonal strut in an opposite direction to what was reported in this study (see Subsection 4.5.3). The only comparable results from Azimi et al. (2014) to the current program are in terms of reinforcement materials (i.e., PL3-TS was fully reinforced with steel bars, whereas PL3-TG1 and PL3-TG2 were GFRP-RC). Azimi et al. (2014) did not consider retrofitted structures. Even though study had a closer barrier geometry to that used in CSA S6:06 commentaries to define acceptable load levels, authors did not perform additional calculations to determine a load strength despite having shorter widths than those determined using corresponding dispersal angles.

4.5.8.4. Ahmed et al. (2010) Barrier Report

Table 4.13 presents a comparison between results from this study to those reported by (Ahmed et al., 2010) who conducted tests on AT single-sloped barriers at Sherbrooke University. Their objective was to capture the response of barrier with reinforcement varied between GFRP and steel, while decks were in all cases reinforced using epoxy-coated steel bars. Four barrier-deck specimens were fabricated with all decks having measurements of 3000 (long) × 2500 (wide) × 225 mm (thickness) with a 1000 mm-long overhang in all cases. Barriers with same geometry as Alberta Transportation (2017) drawings were used in two specimens (S-1650), while the other two (S-1642) were built with a curb-railing system. None of their structures mimicked a repair condition; all barriers used bent bars at the deck connection. Given that these structures were tested with a wider spreader beam (1500 mm) than usual distribution length (1050 mm), this study referred to CSA S6:06 commentary section to establish a design capacity equal to 163 kN, following a moment resistance of 38 kNm/m and corresponding dispersal angles.

Table 4.13 Comparison chart between present study and Ahmed et al.'s (2010) report.

Item	Present Study				Ahmed et al. (2010)	
Specimen ID	**SP_01**	**SP_02**	**SP_03**	**SP_04**	**S-1650, Steel**	**S-1650, GFRP**
Peak Load, kN/m† (kN)	96.5	62.1	70	68.4	(169)	(197)
Deflection at Failure, mm	27.7	41.7	43	21.2	19	26
Failure mode	Yielding + Diagonal Tension	Diagonal Tension	Diagonal Tension	Diagonal Tension	Yielding + Concrete Splitting	Concrete Splitting.

†: Results taken from table 4.13.

Tests from Ahmed et al. (2010) from S-1650 specimens reported a concrete splitting failure recorded at the deck, near the joint between two members with S-1650 Steel structure yielding prior to concrete splitting. This failure mode is consistent with specimens from this study, with differences in splitting cracks in terms of their slope. Authors mentioned that low bond strength from epoxy-coated steel bars in the deck may have contributed to this failure. Regardless, the crack pattern was like those observed in this study, including deck cracks consistent with flexural-tension. Deflections at peak load from this study were larger than those from Ahmed et al. (2010) with exception of SP-04. Larger deflections at failure are related to larger overhang lengths that specimens in this study had relative to Ahmed et al. (2010). Barriers from that test program did not exhibit any visible damage, despite having enough width to accommodate two-way behaviour. Despite this, specimens were able to exceed the estimated threshold per CSA S6:06 commentary.

4.6. Additional Considerations

After examining the response of tested specimens and how all underperformed per CSA S6:19 for TL-4 barriers, some limitations from the current test program need to be discussed. Geometric limitations governed specimen response with one-way action being the most relevant limitation that reduced capacity by placing additional stresses on the barrier-deck interface. A fixed overhang length may be another limitation as it restrained rotations in specimens, subjecting them to large stresses that might be excessive for real-life scenarios. A test program accounting various overhang lengths and two-way action would be a step forward in this research to define the impact of these variables in their capacity and to analyze structures closer to what an actual barrier-deck overhang response would be in real life. Other aspects could also be included in future studies using similar test setup. For instance, the use of dowelled bars to repair the farthest section of the deck from a support to fabricate a new deck and barrier. Assessing other repair techniques beyond dowelled bars with epoxy should be considered to establish differences and similarities between results obtained. Moreover, repair techniques should not be limited to flexural retrofitting (e.g., NSM, DB), but joint retrofit must be considered as well, based on results found in this study. This could be done by installing reinforcement at the joint to control tensile stresses and enhance capacity of the diagonal compressive strut, following reinforcing details proposed by other authors (El-Metwally and Chen, 2017; Mogili and Kuang, 2018), or even using novel reinforcement layouts. Transverse reinforcement at the barrier-deck interface could also be considered though may cause even more congestion at the joint. It is noticeable that one-way action induced structures to a squat behaviour and this kind of detailing will only be necessary if testing similar structures exposed to two-way action that have similar joint strength issues.

Furthermore, it is acknowledged that an indoor laboratory environment brings amenities that are not available in field applications. Among these is the knowledge of GFRP bar locations inside of elements which is helpful when repairs are conducted so bars are not drilled through during the repair, especially since GFRP bars are non-magnetic and cannot be detected using rebar covermeters usually used for steel-RC. Alternative detection systems have been recently assessed to track GFRPs embedded into concrete. Malla et al., (2023) conducted tests comparing different sensors: Ground Penetrating Radar (GPR) and Phased Array Ultrasonic (PAU) methods. These methods have been used in the past to track damages in concrete structures, but limited information in their use for other applications was found in the literature. Tests showed that GPR with an increased frequency can detect the location of GFRP bars embedded into concrete; PAU tests, however, showed poor performance for non-metallic bars embedded into concrete. Authors mentioned that post processing algorithms may also help tracking GFRP bars down using different methodologies. Further studies in this field seem to be required to enhance current detecting tools, whether real time or post processing tools.

Finally, regarding beam-bond tests, other reinforcement layouts should be investigated as it was found to be cumbersome to assemble bar cages. The way epoxy resin was injected into CE beam series to create bond between bar and concrete may have not been the most effective way and other approaches must be assessed to define guidelines to conduct these kinds of tests as it is important to understand bond behaviour in GFRP embedded into concrete using epoxy resin as a bonding agent.

4.7. Chapter Conclusions

Information related to fabrication process, instrumentation, and test setup of four barrier-deck slab overhang structures is given in this chapter. Structures were tested until failure and results from each test were used to analyze its response from different standpoints. Namely, deflections, strains, crack patterns, and failure analysis were included in the discussion of results. Moreover, Subsections in repair effectiveness and effect of reinforcement type were included. Finally, results were compared to prior studies as well as with relevant code provisions. The following was concluded from this chapter:

1. One-way action induced all barrier-deck joint to large stresses, a product of squat behaviour that led to the response observed and failure by diagonal tension. This response enabled STM joint analysis considering a knee joint under opening action, which predicted failure with a load below or close to peak loads attained by tests. Moreover, the modification to the STM proposed in this study reported similar failure load to what other STMs registered. However, CSA S6 (2019) STM provisions predicted failure at smaller loads than tests for control specimens. SP-03's predictions were the same as the test peak load. In SP-04 failure was recorded using strain levels from a post-peak load stage, when compression region was small enough to reduce strut capacity.
2. Regarding strength, SP-01 was strongest (145 kN) and SP-02 was weakest (93.5 kN). SP-03 and SP-04 failed almost at same load (105 and 103 kN, respectively). Differences in capacities were attributed to four factors: (1) elastic modulus differences between GFRP and steel bars which induced concrete to larger cracks for GFRP-RC structures. (2) tension in the deck weakened concrete capacity, which also affected joint strength by placing larger tension than otherwise expected. (3) absence of hooked reinforcement limited confinement and thus strength at the joint (aside from SP-01, which had hooks). (4) one-way action exacerbated previous factors by generating large stresses at the joint through squat behaviour. The combination of

these aspects prevented specimens from exceeding TL-4 force thresholds from CSA S6 Commentaries, though it is also noted that these limits are better suited for structures under two-way rather than one-way action.

3. Repairs on SP-03 and SP-04 showed that dowels can restore SP-02's strength. However, as previously mentioned, additional factors unrelated to dowels prevented specimens to achieve larger and closer peak loads. Repairs had the same failure mode of control specimens without showing any bond-critical issues. Crack patterns at the joint showed that specimens were exposed to similar stresses to controls. This leads to the conclusion that the protocol followed is adequate to restore barriers with the considered parameters (e.g., bonding agent, drilling depth). No major setbacks were found during its execution; the procedure was clear and easy to perform.
4. Analytical model proposed in Chapter 3 predicted failure at similar loads as tests' using El-Metwally and Chen's (2017) STM and a $\beta_s = 0.4$. Load-deflection curves had some agreement with tests and were able to predict first cracking and failure loads well. Post-cracking deflection inaccuracies were found in all program-based curves and attributed to $M - \psi$ curve adjustments around cracking region. This effect was less pronounced in GFRP-RC compared to SP-02 and SP-03. Despite this, model curves exhibited the same trend as tests.
5. The 1:1 bar replacement by nominal area used to generate GFRP-RC reinforcement layouts in this study may not be the most appropriate for this situation. The impact of GFRP's lower elastic modulus led to lower capacity compared to steel-RC. An alternative replacement could be considered using reinforcement layouts with comparable axial stiffness, EA, which effectively means tripling the GFRP reinforcement ratio. which could lead to more comparable strength between steel and GFRP-RC structures. The effect of EA in strength and stiffness was observed and commented in Subsection 3.4.1. An aspect to ponder in this approach is reinforcement congestion as spacings for GFRP specimens would likely be tighter to achieve a similar EA to steel-RC.

5. CONCLUSIONS, SUMMARY AND RECOMMENDATIONS

5.1. Summary

The aim of this study was to evaluate the effectiveness of repairing GFRP-RC bridge barriers using reinforcement bars dowelled into deck slabs to connect both elements. To do so, four barrier-deck overhang specimens were fabricated and tested to failure under static loading. Two specimens served as controls: SP-01 and SP-02 (steel-RC and GFRP-RC, respectively); and the other two were repaired: SP-03 and SP-04 were GFRP-RC and hybrid structures. Peak loads, deflections, and strains were recorded in critical locations to understand the differences on responses. Data gathered was used to determine failure mechanism, crack pattern, deflections, and strength. In general terms, specimens were governed by one-way action that induced failure by diagonal tension at the barrier-deck joint. Crack patterns in that area showed a diagonal crack propagated from bottom to top of deck where compressive strut failed. The early failure captured by specimens was linked to a weakened joint due to tensile forces which softened the deck slab concrete. This prevented specimens from reaching CSA S6:19 force thresholds for TL-4 barriers. An analytical model proposed predicted similar peak loads under same failure as tests, providing an acceptable estimation. Deflection calculations after cracking, however, underestimated flexibility of real structures. Based in all these discoveries, the author of this thesis concludes that the proposed objective for this study was succeeded.

To justify this, Chapter 2 presented concepts and past research needed to understand rationale and processes used in models and testing. Namely, concepts like bridge barrier testing and rating, FRP-RC versus steel-RC response differences, and repair techniques used in FRP-RC members are explained. Chapter 3 presented an analytical model written in MATLAB software. This model can predict failure loads and plot load-deflection curvatures of barrier-deck structures under one-way action. Model validation and a parametric study are also presented therein. Chapter 4 presented the experimental program including fabrication, test methods, results, and respective discussion. Appendices provide ancillary details of several aspects that were left out of the main body of the thesis.

5.2. Conclusions

The following conclusions are drawn from the thesis:

1. Chapter 2 proposed a literature review where relevant components to GFRP-RC bridge barriers were studied and understood. Gaps were observed in the literature on repairing with GFRP as well as tests on barriers with realistic overhang lengths. *This accomplished Task 1 of the research objective.*
2. Chapter 3 proposed an analytical model to analyze barrier-deck slab overhang structures under one-way action. This program enables estimation of peak load under different failure modes and computes deflections from curvatures and slip. Overall, validation showed the ability of model to predict similar peak loads under same failure modes as validation tests. Limitations in the model related to geometry and load constraints (e.g., non-negligible shear deformations or two-way action), or aspects that aimed to reduce programming complexity (e.g., concrete tension stiffening). Moreover, program exhibited imperfections when calculating deflections, linked to how model adjusted $M - \psi$ curves at cracking and interpolation to obtain curvatures. Parametric study showed effects of different overhang lengths, bar spacing, and bond-slip models in load-deflection curves, failure mechanism, and peak load for assessed models. Overhang length has a direct relation with structural rigidity; bar spacing contributes to element strength and rigidity where both outcomes increase as bar spacing is reduced. Bond slip models showed little contribution to deflections and was related to low stress levels barrier rebar was exposed up to peak load. Failure was governed by diagonal tension which prevented models to reach CSA S6:19 force threshold for TL-4. Barriers. *This accomplished Task 2 from research objective.*
3. Chapter 4 described the fabrication of four barrier-deck overhang specimens with two used as control specimens as these had barriers' reinforcement monolithically connected to the deck; the two remaining specimens were used to mimic a repair condition using dowels. Each specimen was tested in a mono-static setting until failure. Structures were instrumented in such a way that data could be used to analyzed results later. Nuances are given in Chapter four. *This accomplished Tasks 3 and 4 from research objective.*

4. From work shown in Chapter 4, it was noted that the response of all specimens was governed by reinforcement material. All specimens exhibited typical loading stages corresponding to GFRP-RC and Steel-RC structures. Stiffness variations, load and support conditions interacted with deflections and failure mode reported by structures. SP-01, with the largest reinforcement stiffness, had the largest peak load, while SP-02 with the lowest reinforcement stiffness failed at the lowest load. SP-04 reported post-peak strain redistribution attributed to low strains in the steel-reinforced deck reinforcement at peak load that allowed element to deform more after initial strut failure. All structures failed at lower loads than CSA S6:19 force thresholds for TL-4 bridge barriers. Furthermore, the use of dowels as repair of bridge barrier showed to restore strength from SP-02; though for SP-01 it is not feasible to conclude on this as no steel dowels were used. *This fulfilled Subtasks 5.1, and 5.2 from research objective.*
5. Specimen failure modes and peak load were controlled by two large factors: one-way action, and axial tension in the deck. One-way action induced joints to large stresses as a squat section while axial tension contributed to concrete softening, affecting their capacity to sustain larger loads. An additional factor seemed to have contributed to low peak loads and related to lack of joint confinement which restrained the formation of a sturdier compressive strut as the joint strained more. All specimens failed by diagonal tension at the barrier-deck joint. Predicting failure using STM used in previous studies for beam-column joints was suitable to analyze barrier-deck joint capacity. Results from this method showed good agreement to test peak loads, where the closest estimate was 1% of peak load, and the farthest 15%. Using ACI 318-19 or CSA S6:19 methodologies to reduce stress capacity at nodes or strut with β-coefficients or principal strain, respectively, showed conservative outcomes. In the case of SP-04, CSA methodology recorded failure when exposed to post-peak load stage strains. Nodal zone proportioning using the code expressions, however, derived in large, unrealistic geometry of STM components. Among the reasons of this can be mentioned a gap found in these code provisions to properly define h_a length used for nodal zones' width at the interface with strut. It is not clear on how to estimate it. *This accomplished Subtask 5.3 from research objective.*

6. The model described in Chapter 3 predicted with good agreement peak loads and failure type that real structures failed in. For SP-01, program predicted failure at 98% of peak load attained in actual tests; for GFRP-RC structures (SP-02 and SP-03) model reached a peak load at a load 12% and 1% larger of real peak loads. In the case of SP-04, the analytical model predicted failure at a load 19% larger than what was observed in test. In terms of deflections, analytical model underestimated real deflections, especially in post-cracking regions. Deflection errors at failure reported were: 35% larger (SP-01), 1% smaller (SP-02), 2% larger (SP-03), and 13% larger for SP-04. *This accomplished Subtask 5.4 from research objective.*
7. RILEM beam-bond tests showed that using epoxy presented similar bond-slip curves as a bar embedded into concrete alone with epoxy reduced bond strength by 7.4% on average. Beams from both series failed by bar pullout with CB series' bar coating peeled off resin and CE series bar with surrounding epoxy resin pulled out from concrete. A novel method was used to inject bonding agent into hole of RILEM beam-bond tests, CE beams showed good performance and resemblance to CB counterparts. This may mean that the proposed protocol was properly planned and executed and did not affect specimens' performance. However, fabrication of RILEM beams, particularly with epoxy connections was cumbersome. More work was needed to align and level segments so secondary effects were not significant during tests and posterior calculations upon them. *This accomplished Subtask 5.5 from research objective.*

5.3. Recommendations

1. For the analytical model, future work should consider exploring alternatives to adjust more effectively the cracking region of $M-\psi$ curves which seemed to have impacted how curvature-based deflections were estimated in that region. The effect of concrete tension stiffening may contribute to better deflection predictions after cracking. Also, the load-control nature of the analysis may be changed to deflection-control analysis to better capture post-peak response. Finally, as barrier-deck structures in real life are prone to two-way action, it would be a step forward to account for two-way effects to be able to capture differences between two and one-way action.

2. For barrier-deck overhangs, given the significant contribution of one-way action to the overall response and the somewhat unrealistic response this showed to be with respect to real-life bridge barrier-deck systems will be subjected to (i.e., two-way action), future research should consider investigate the response of dowels to repair barriers in wider structures to assess their two-way response. In case joint capacity still governs strength of element, reinforcement detailing of the joint should be investigated to establish its effectiveness to control stresses at joint. This detailing could be done by adding additional bars to control and develop tensile forces in the rear corner due to compressive strut action; moreover, the use of stirrups in the joint might be useful to confine the strut and prevent it from an early failure. An additional item to ponder to establish its impact in a test program would be using hooked bars in reinforcement at the joint so the joint its confined and study whether this enhance or not performance of specimens.
3. As information was gathered and read for Chapter 2, it was noticed that limited testing of bridge barriers using realistic overhang measurements and/or incorporating repair techniques are limited and requires further analysis and study to provide results closer to real life applications. Although studies in the past performed similar testing towards barrier-deck slab systems, there are still limited repair regulations for this application. Future studies should focus on accounting realistic measures to obtain closer responses to what structures are subjected to in real life.
4. Exploring a 1:1 bar replacement by axial stiffness in future work could lead to more comparable strength between steel and GFRP-RC structures by tripling GFRP reinforcement ratio. This tendency was observed while performing the parametric study proposed in Chapter 3, where models with larger EA showed to have stiffer and stronger response as bar spacing decreased. Having similar or comparable EA will incur in reduced bar spacings in elements reinforced with GFRPs to attain similar EAs as steel-RC counterparts. Their constructability will be impacted as rebar congestion complexity increases.
5. For RILEM beam-bond tests, it is recommended for future experiments to investigate different ways to seal off the tubing to prevent epoxy from getting in and potentially adding resistance to the specimen than initially calculated. Efforts towards

standardizing beam-bond tests for FRP using bonding agents should be done as no protocols were found to perform this kind of test.

5.4. Limitations

Given the monostatic testing specimens were subjected to, they were induced to slowly increasing deformations. The specimens were incrementally subjected to forces that enables structural components to find load paths to transfer stresses as tests are performed until failure. In this case, acceleration and dynamic effects are negligible. By applying a dynamic load, elements are exposed to additional aspects that alter response (e.g., damping, mass) that are not observed in monostatic testing. These and how accelerated loads are applied to the system (e.g., pendulum tests, crash vehicle tests) change how loads are transferred internally as well as deformations within the structure as materials respond differently with respect to static loading. This may lead to different failure modes than what was observed in tests conducted for this study and vary their peak loads to probably lower magnitudes. Moreover, dynamic loading could also shift crack patterns observed in original tests by inducing more damage to barriers, as observed in other studies where dynamic testing was conducted on bridge barriers (El-Salakawy et al., 2004).

As stated before, the width of specimens narrowed their response to one-way action that led to probably unrealistic level stresses in the joint to what these regions will be exposed to in real-life barrier-deck junctions. Though this allowed for a proper joint strength assessment, the combination of these stresses with loading and support boundary conditions induced structures to additional aspects that prevented structures to exceed CSA S6 (2019) force threshold for TL-4 bridge barriers.

The experimental program was limited to assess a scenario where barrier substitution was required. This, however, is not always the case in bridge superstructure repairs, where partial substitution of the deck slab overhang could be also required. This adds complexity to the analysis and fabrication of specimens mimicking this repair, although results would contribute to current contractors doing such tasks in real-life projects.

REFERENCES

AASHTO. (2017). *AASHTO LRFD bridge design specifications, Part I : Sections 1-6.*

Abdelwahed, B. (2020). A review on reinforced concrete beam column joint: Codes, experimental studies, and modeling. In *Journal of Engineering Research (Kuwait)* (Vol. 8, Issue 4, pp. 63–79). University of Kuwait. https://doi.org/10.36909/JER.V8I4.8043

Achillides, Z., Pilakoutas, K. (2004). Bond Behavior of Fiber Reinforced Polymer Bars under Direct Pullout Conditions. *Journal of Composites for Construction* , *8*(2), 173–181. https://doi.org/10.1061/ASCE1090-026820048:2173

ACI 208. (1958). *Test procedure to determine relative bond value of reinforcing bars*.

ACI 318. (2019). 318-19 Building Code Requirements for Structural Concrete and Commentary. In *318-19 Building Code Requirements for Structural Concrete and Commentary*. American Concrete Institute. https://doi.org/10.14359/51716937

ACI 355.2. (2000). *evaluating the performance of post-installed mechanical anchors in concrete*.

ACI 440. (2008). *Guide for the design and construction of externally bonded FRP systems for strengthening concrete structures*. American Concrete Institute.

ACI 440. (2015). *Guide for the design and construction of structural concrete reinforced with fiber-reinforced polymer FRP bars*. American Concrete Institute.

ACI 440.11. (2022). *Building code requirements for structural concrete reinforced with glass fiber reinforced polymer (GFRP) bars - Code and Commentary*.

Ahmed, E. A., Benmokrane, B. (2011). *Static Testing of Full-Scale Concrete Bridge Barriers Reinforced with GFRP Bars*.

Ahmed, E. A., Dulude, C. (2012). *Repair of Concrete Structures Reinforced with Fibre-Reinforced Polymer (FRP) Bars*. https://www.researchgate.net/publication/258839961

Ahmed, E. A., Dulude, C., Benmokrane, B. (2013). Concrete bridge barriers reinforced with glass fibre-reinforced polymer: Static tests and pendulum impacts. *Canadian Journal of Civil Engineering*, *40*(11), 1050–1059. https://doi.org/10.1139/cjce-2013-0019

Ahmed, E. A., El-Salakawy, E. F., Benmokrane, B. (2008). Bond Stress-Slip Relationship and Development Length of FRP Bars Embedded in Concrete. *HBRC Journal*, *4*(3), 1–17. https://www.researchgate.net/publication/258835428

Ahmed, E., Dulude, C., Benmokrane, B. (2010). *Static Testing of Alberta Transportation Concrete Bridge Barrier Walls of Type PL-2 Reinforced with GFRP and Steel Bars*.

Alberta Transportation. (2017). *Single Slope Bridge Barrier Detail*.

Alberta Transportation. (2018). *Bridge Structures Design Criteria*.

Al-Jaaidi, A. (2021). *Modelling Repair Techniques for Reinforced Concrete Bridge Barriers using Glass Fibre Reinforced Polymer Bars*. University of Alberta.

Almusallam, T. (1997). Analytical Prediction of Flexural Behavior of Concrete Beams Reinforced by FRP Bars. *Journal of Composite Materials*, *31*(7), 640–657.

Al-Sunna, R., Pilakoutas, K., Hajirasouliha, I., Guadagnini, M. (2012). Deflection behaviour of FRP reinforced concrete beams and slabs: An experimental investigation. *Composites Part B: Engineering*, *43*(5), 2125–2134. https://doi.org/10.1016/j.compositesb.2012.03.007

Andermatt, M. F., Lubell, A. S. (2013). Strength Modeling of Concrete Deep Beams Reinforced with Internal Fiber-Reinforced Polymer. *ACI Structural Journal*, *110*(4), 595–605.

ASCE Committee on America's Infrastructure. (2021). 2021 Infrastructure Report Card. *American Society of Civil Engineers*.

ASTM C39. (2018). *Standard test method for compressive strength of cylindrical specimens*.

ASTM C78. (2018). *Standard test method for flexural strength of concrete using simple beam with third-point loading*.

ASTM C469. (2014). *Standard test method for static modulus of elasticity and Poisson's ratio of concrete in compression*.

ASTM C882. (2013). *Standard test method for bond strength of epoxy-resin systems used with concrete by slant shear*.

ASTM D638. (2014). *Standard test method for tensile properties of plastics*.

ASTM D695. (2010). *Standard test method for compressive properties of rigid plastics*.

ASTM D7205. (2021). *Standard test method for tensile properties of fiber reinforced polymer matrix composite bars*.

ASTM E8. (2022). *Standard Test Methods for Tension Testing of Metallic Materials*.

Azimi, H., Sennah, K., Tropynina, E., Goremykin, S., Lucic, S., Lam, M. (2014). Anchorage Capacity of Concrete Bridge Barriers Reinforced with GFRP Bars with Headed Ends.

Journal of Bridge Engineering, *19*(9). https://doi.org/10.1061/(asce)be.1943-5592.0000606

Baena, M., Torres, L., Turon, A., Barris, C. (2009). Experimental study of bond behaviour between concrete and FRP bars using a pull-out test. *Composites Part B: Engineering*, *40*(8), 784–797. https://doi.org/10.1016/j.compositesb.2009.07.003

Bakis, C. E., Bank, L. C., Brown, V. L., Cosenza, E., Davalos, J. F., Lesko, J. J., Machida, A., Rizkalla, S. H., Triantafillou, T. C. (2002). Fiber-Reinforced Polymer Composites for Construction-State-of-the-Art Review. *Journal of Composites for Construction*, *6*(2), 73–87. https://doi.org/10.1061/ASCE1090-026820026:273

Barker, C. (2016). *The Feasibility of Fibre Reinforced Polymers as an Alternative to Steel in Reinforced Concrete*.

Benmokrane, B., Ehab El-Salakawy, Amr El-Ragaby, Lackey, T. (2006). Designing and Testing of Concrete Bridge Decks Reinforced with Glass FRP Bars. *Journal of Bridge Engineering*, *11*(2), 217–229. https://doi.org/10.1061/ASCE1084-0702200611:2217

Benmokrane, B., El-Salakawy, E., El-Ragaby, A., El-Gamal, S. (2007). Performance evaluation of innovative concrete bridge deck slabs reinforced with fibre-reinforced-polymer bars. *Canadian Journal of Civil Engineering*, *34*(3), 298–310. https://doi.org/10.1139/L06-173

Benmokrane, B., Nazair, C., Loranger, M.-A., Manalo, A. (2018). Field Durability Study of Vinyl-Ester–Based GFRP Rebars in Concrete Bridge Barriers. *Journal of Bridge Engineering*, *23*(12). https://doi.org/10.1061/(asce)be.1943-5592.0001315

Birrcher, D., Tuchscherer, R., Huizinga, M., Bayrak, O., Wood, S., Jirsa, J. (2008). *Strength and Serviceability Design of Reinforced Concrete Deep Beams (FHWA/TX-09/0-5253-1)*. www.ntis.gov.

Bischoff, P. H. (2005). Reevaluation of Deflection Prediction for Concrete Beams Reinforced with Steel and Fiber Reinforced Polymer Bars. *Journal of Structural Engineering*, *131*(5), 752–767. https://doi.org/10.1061/ASCE0733-94452005131:5752

Boston Consulting Group. (2018). *CanInfra Challenge*.

Branson, D. E. (1965). *Instantaneous and time-dependent deflections of simple and continuous reinforced concrete beams*.

Brózda, K., Selejdak, J., Koteš, P. (2017). Analysis of Properties of the FRP Rebar to Concrete Structures. *Applied Engineering Letters*, *2*(1), 6–10.

BSI 12269-1. (2000). *Determination of the bond behaviour between reinforcing steel and autoclaved aerated concrete by the "beam test" - Short term test*.

Carvalho, E. P., Ferreira, E. G., da Cunha, J. C., Rodrigues, C. de S., Maia, N. da S. (2017). Experimental investigation of steel-concrete bond for thin reinforcing bars. *Latin American Journal of Solids and Structures*, *14*(11), 1932–1951. https://doi.org/10.1590/1679-78254116

CEB-FIP. (1990). CEB-FIP Model Code for Concrete Structures. In *Comite Euro-International du beton*.

Ciampi, V., Eligehausen, R., Bertero, V. V, Popov, E. P. (1982). *Analytical model for concrete anchorages of reinforcing bars under generalized excitations*.

CIRC. (2019). Monitoring the State of Canada's Core Public Infrastructure: The Canadian Infrastructure Report Card 2019. In *Canadian Infrustructure*.

Correlated Solutions. (2021a). *Speckle Kit User Manual* (Vol. 1, Issue 5).

Correlated Solutions. (2021b). *VIC-3D* (9).

Cosenza, E., Manfredi, G., Realfonzo, R. (1995). Analytical modelling of bond between FRP reinforcing bars and concrete. In L. Taerwe (Ed.), *Proceedings 2nd Int. RILEM Symp*.

Cosenza, E., Manfredi, G., Realfonzo, R. (1997). Behavior and Modeling of Bond FRP Rebars to Concrete. *Journal or Composites for Construction*, *1*(2), 40–51.

Cousin, P., Hassan, M., Vijay, P. V., Robert, M., Benmokrane, B. (2019). Chemical resistance of carbon, basalt, and glass fibers used in FRP reinforcing bars. *Journal of Composite Materials*, *53*(26–27), 3651–3670. https://doi.org/10.1177/0021998319844306

CSA S6. (2006). *Commentary on CAN/CSA-S6-06, Canadian Highway Bridge Design Code*. www.ShopCSA.ca

CSA S6. (2019). *Canadian highway bridge design code*.

CSA S806. (2012). *Design and construction of building structures with fibre-reinforced polymers*.

Darwin, D., Zuo, J., Tholen, M. (1996). Development Length Criteria for Conventional and High Relative Rib Area Reinforcing Bars. *ACI Structural Journal*, *93*(3), 347–359.

Ehsani, M., Saadatmanesh, H., Tao, S. (1996). Design Recommendations for Bond of GFRP Rebars to Concrete. *Journal of Structural Engineering*, *122*(3), 247–254.

El-Gamal, S., Benmokrane, B., Goulet, S. (2008, June). *Testing of Concrete Bridge Barriers Reinforced with New Glass FRP Bars*. https://www.researchgate.net/publication/268391267

El-Gamal, S. E., El-Gamal, S., Benmokrane, B., Goulet, S. (2008). *Testing of Concrete Bridge Barriers Reinforced with New Glass FRP Bars Structures with GFRP bars View project FRP Reinforcements for Concrete Structures: Design, Testing, and Field Applications View project TESTING OF CONCRETE BRIDGE BARRIERS REINFORCED WITH NEW GLASS FRP BARS*. https://www.researchgate.net/publication/268391267

Elighausen, R., Popov, E. P., Bertero, V. V. (1983). *Local Bond Stress-Slip Relationships of Deformed Bars Under Generalized Excitations*.

El-Metwally, S. E.-D., Chen, W.-F. (2017). *Structural Concrete Strut-and-Tie Models for Unified Design*. https://lccn.loc.gov/2017015368

El-Nemr, A., Ahmed, E. A., Benmokrane, B. (2013). Flexural Behavior and Serviceability of Normal-and High-Strength Concrete Beams Reinforced with Glass Fiber-Reinforced Polymer Bars. *ACI Structural Journal*, *110*(6), 1077–1088. www.concrete.org

El-Salakawy, E., Benmokrane, B. (2003). *Serviceability of Concrete Bridge Deck Slabs Reinforced with FRP Composite Bars*.

El-Salakawy, E., Benmokrane, B., Briere, F. (2005). Glass FRP Composite Bars for Concrete Bridge Barriers. *Science and Engineering of Composite Materials*, *12*(3).

El-Salakawy, E., Benmokrane, B., El-Ragaby, A., Nadeau, D. (2005). Field Investigation on the First Bridge Deck Slab Reinforced with Glass FRP Bars Constructed in Canada. *Journal of Composites for Construction*, *9*(6), 470–479. https://doi.org/10.1061/ASCE1090-026820059:6470

El-Salakawy, E., Benmokrane, B., Masmoudi, R., Brière, F. (2003). Concrete Bridge Barriers Reinforced with Glass Fibre-Reinforced Polymer Composite Bars. *ACI Structural Journal*, *100*(6), 815–824.

El-Salakawy, E., Islam, M. R. (2014). Repair of GFRP-Reinforced Concrete Bridge Barriers. *Journal of Bridge Engineering*, *19*(6). https://doi.org/10.1061/(asce)be.1943-5592.0000584

El-Salakawy, E., Masmoudi, R., Benmokrane, B., Brière, F., Desgagné, G. (2004). Pendulum impacts into concrete bridge barriers reinforced with glass fibre reinforced polymer composite bars. *Canadian Journal of Civil Engineering*, *31*(4), 539–552. https://doi.org/10.1139/L04-006

El-Salakawy, E., Mufti, A., Elragaby, A. (2009). *Laboratory Investigations on the Repair of GFRP-Reinforced Concrete Bridge deck Slabs*.

Elwell, D. J., Fu, G. (1995). Compression Testing of Concrete: Cylinders vs. Cubes. *Report FHWA*, *SR-95/119*.

Fadaee, M., Sennah, K. (2017, May). *Investigation on Impact Loads for Test Level 4 of Concrete Bridge Barriers*. https://www.researchgate.net/publication/317851054

Fayyad, T. M., Lees, J. M. (2014). Application of Digital Image Correlation to Reinforced Concrete Fracture. *Procedia Materials Science*, *3*, 1585–1590. https://doi.org/10.1016/j.mspro.2014.06.256

FHWA. (2000). *Basics of Concrete Barriers*. Public Roads. https://highways.dot.gov/public-roads/marchapril-2000/basics-concrete-barriers

Focacci, F., Nanni, A., Bakis, C. E. (2000). Local Bond-Slip Relationship for FRP Reinforcement in Concrete. *Journal of Composites for Construction*, *4*(1), 24–31. https://doi.org/10.1061/(asce)1090-0268(2000)4:1(24)

Frigione, M., Lettieri, M. (2018). Durability issues and challenges for material advancements in FRP employed in the construction industry. In *Polymers* (Vol. 10, Issue 3). MDPI AG. https://doi.org/10.3390/polym10030247

Gergely, P., Lutz, L. A. (1968). *Maximum Crack Width in Reinforced Concrete Flexural Members*.

HILTI. (2022a). *Anchor Fastening Technical Guide*. www.hilti.ca

HILTI. (2022b). *Instruction for use HILTI HIT-RE 500 V3*.

Hognestad, E. (1952). Fundamental Concepts in Ultimate Load Design of Reinforced Concrete Members*. *Journal of the American Concrete Institute*, 809–830.

Jirsa, J., Lutz, L. A., Gergely, P. (1979). Rationale for Suggested Development, Splice and Standard Hook Provisions for Deformed Bars in Tension. *Concrete International*, 47–61.

Kassem, C., Farghaly, A. S., Benmokrane, B. (2011). Evaluation of Flexural Behavior and Serviceability Performance of Concrete Beams Reinforced with FRP Bars. *Journal of Composites for Construction*, *15*(5), 682–695. https://doi.org/10.1061/(asce)cc.1943-5614.0000216

Khederzadeh, H., Sennah, K. (2014). Development of cost-effective PL-3 concrete bridge barrier reinforced with sand-coated glass fibre reinforced polymer (GFRP) bars: Static load tests. *Canadian Journal of Civil Engineering*, *41*(4), 368–379. https://doi.org/10.1139/cjce-2013-0394

Khorramian, K., Sadeghian, P. (2018). *New Testing Method of GFRP Bars in Compression*.

Khorramian, K., Sadeghian, P. (2019). Material characterization of GFRP bars in compression using a new test method. *Journal of Testing and Evaluation*, *49*(2). https://doi.org/10.1520/JTE20180873

Kim, Y. J. (2019). State of the practice of FRP composites in highway bridges. *Engineering Structures*, *179*, 1–8. https://doi.org/10.1016/j.engstruct.2018.10.067

Lau, D., Pam, H. J. (2010). Experimental study of hybrid FRP reinforced concrete beams. *Engineering Structures*, *32*(12), 3857–3865. https://doi.org/10.1016/j.engstruct.2010.08.028

Lee, D., Cheng, L. (2011). Assessing the Strengthening Effect of Various Near-Surface-Mounted FRP Reinforcements on Concrete Bridge Slab Overhangs. *Journal of Composites for Construction*, *15*(4), 615–624. https://doi.org/10.1061/(asce)cc.1943-5614.0000182

Lin, X., Zhang, Y. X. (2014). Evaluation of bond stress-slip models for FRP reinforcing bars in concrete. *Composite Structures*, *107*(1), 131–141. https://doi.org/10.1016/j.compstruct.2013.07.037

Mak, K. K., Gripne, D. J., Mcdevitt, C. F. (1994). *Single-Slope Concrete Bridge Rail*.

Makhmalbaf, E., Razaqpur, A. G. (2022). Development length of glass fibre reinforced polymer (GFRP) rebar based on non-uniform bond stress. *Canadian Journal of Civil Engineering*, *49*(3), 420–431. https://doi.org/10.1139/cjce-2020-0400

Malla, P., Khedmatgozar Dolati, S. S., Ortiz, J. D., Mehrabi, A. B., Nanni, A., Dinh, K. (2023). Feasibility of Conventional Non-Destructive Testing Methods in Detecting Embedded FRP Reinforcements. *Applied Sciences (Switzerland)*, *13*(7). https://doi.org/10.3390/app13074399

Malvar, J. (1995). Tensile and Bond Properties of GFRP Reinforcing Bars. *ACI Materials Journal*, *92*(3). https://doi.org/10.14359/1120

MASH. (2009). *Manual for Assessing Safety Hardware*.

Mashhadi, R., Dastan Diznab, M. A., Tehrani, F. M. (2023). A Strut-and-Tie Model for Predicting the Shear Strength of Exterior Beam–Column Joints Strengthened with Fiber-Reinforced Polymers. *Journal of Composites for Construction*, *27*(1). https://doi.org/10.1061/jccof2.cceng-3692

Masuelli, M. A. (2013). Introduction of Fibre-Reinforced Polymers − Polymers and Composites: Concepts, Properties and Processes. *Fiber Reinforced Polymers - The Technology Applied for Concrete Repair*. https://doi.org/10.5772/54629

Matamoros, A. B., Wong, H. (2003). Design of Simply Supported Deep Beams Using Strut-and-Tie Models. *ACI Structural Journal*, *100*(6), 704–712.

Matta, F., Nanni, A. (2009). Connection of Concrete Railing Post and Bridge Deck with Internal FRP Reinforcement. *Journal of Bridge Engineering*, *14*(1), 66–76. https://doi.org/10.1061/ASCE1084-0702200914:166

Mccormick, N., Lord, J. (2010). Digital Image Correlation. *Materials Today*, *13*, 52–54.

Mogili, S., Kuang, J. S. (2019). Reversed cyclic performance of reinforced concrete knee joints under variable closing and opening stresses. *Engineering Structures*, *178*, 116–127. https://doi.org/10.1016/j.engstruct.2018.10.025

Mufti, A. A., Onofrei, M., Benmokrane, B., Banthia, N., Boulfiza, M., Newhook, J. P., Bakht, B., Tadros, G. S., Brett, P. (2007). Field study of glass-fibre-reinforced polymer durability in concrete. *Canadian Journal of Civil Engineering*, *34*(3), 355–366. https://doi.org/10.1139/L06-138

NCHRP 350. (1993). *National Cooperative Highway Research Program NCHRP Report 35 Safety Performance Evaluation*.

NCHRP 350. (1997). *National Cooperative Highway Research Program NCHRP Report 350 Safety Performance Evaluation*.

Newman, N., Ayoub, A., Belarbi, A. (2010). Development length of straight FRP composite bars embedded in concrete. *Journal of Reinforced Plastics and Composites*, *29*(4), 571–589. https://doi.org/10.1177/0731684408100262

Oats, R. C., Dai, Q., Head, M. (2022). Digital Image Correlation Advances in Structural Evaluation Applications: A Review. *Practice Periodical on Structural Design and Construction*, *27*(4). https://doi.org/10.1061/(asce)sc.1943-5576.0000725

Orangun, C., Jirsa, J. O., Breen, J. E. (1977). A Reevaluation of Test Data on Development Length and Splices. *ACI Journal Proceedings*, *74*(3), 114–122.

Pan, B. (2011). Recent Progress in Digital Image Correlation. *Experimental Mechanics*, *51*(7), 1223–1235. https://doi.org/10.1007/s11340-010-9418-3

Park, S., Mosalam, K. M. (2012). Analytical Model for Predicting Shear Strength of Unreinforced Exterior Beam-Column Joints. *ACI Structural Journal*, *109*(2). https://doi.org/MS No. S-2009-317.R4

Pecce, M., Manfredi, G., Realfonzo, R., Cosenza, E. (2001). Experimental and Analytical Evaluation of Bond Properties of GFRP Bars. *Journal of Materials in Civil Engineering*, *13*(4), 282–290.

Rasheed, H. A., Nayal, R., Melhem, H. (2004). Response prediction of concrete beams reinforced with FRP bars. *Composite Structures*, *65*(2), 193–204. https://doi.org/10.1016/j.compstruct.2003.10.016

Raupach, M., Buttner, T. (2014). *Concrete Repair to EN 1504*. Taylor & Francis.

Razaqpur, A. G., Svecova, D., Cheung, M. S. (2000). Rational Method for Calculating Deflection of Fiber-Reinforced Polymer Reinforced Beams. *ACI Structural Journal*, *97*(1), 175–183.

RILEM TC-RC5. (1994). *Bond test for reinforcement steel. 1. Beam test, 1982*.

Rolland, A., Argoul, P., Benzarti, K., Quiertant, M., Chataigner, S., Khadour, A. (2020). Analytical and numerical modeling of the bond behavior between FRP reinforcing bars and concrete. *Construction and Building Materials*, *231*. https://doi.org/10.1016/j.conbuildmat.2019.117160

Rosenbaugh, S., Sicking, D. L., Faller, R. K. (2007). *Development of a TL-5 Vertical Faced Concrete Median Barrier Incorporating Head Ejection Criteria* (Vol. 38). http://digitalcommons.unl.edu/ndor/38

Rostami, M., Sennah, K., Afefy, H. M. (2018). Ultimate capacity of barrier-deck anchorage in MTQ TL-5 barrier reinforced with headed-end, high-modulus, sand-coated GFRP bars. *Canadian Journal of Civil Engineering*, *45*(4), 263–278. https://doi.org/10.1139/cjce-2017-0002

Rostami, M., Sennah, K., Dehnadi, S. M. (2016, June). *Experimental Study on the Capacity of Barrier Deck Anchorage in MTQ PL-3 Barrier Reinforced with HM-GFRP Bars With Headed Ends*.

Rostami, M., Sennah, K., Hedjazi, S. (2019). GFRP bars anchorage resistance in a GFRP-reinforced concrete bridge barrier. *Materials*, *12*(15). https://doi.org/10.3390/ma12152485

Schlaich, J., Schiifer, K. (1991). Design and detailing of structural concrete using strut-and-tie models. *The Structural Engineer*, *69*(6), 114–125.

Sennah, K., Hedjazi, S. (2019). Structural qualification of a developed GFRP-reinforced TL-5 concrete bridge barrier using vehicle crash testing. *International Journal of Crashworthiness*, *24*(3), 296–313. https://doi.org/10.1080/13588265.2018.1480582

Sennah, K., Juette, B., Weber, A., Witt, C. (2011). *Vehicle Crash Testing on a GFRP-Reinforced PL-3 Concrete Bridge*.

Sennah, K., Tropynina, E., Ibrahim, Z., Hedjazi, S. (2018). Structural Qualification of a Developed GFRP-Reinforced Concrete Bridge Barrier using Ultimate Load Testing. *International Journal of Concrete Structures and Materials*, *12*(1). https://doi.org/10.1186/s40069-018-0284-1

Sezen, H., Setzler, E. J. (2008). Reinforcement Slip in Reinforced Concrete Columns. *ACI Structural Journal*, *105*(3), 280–289.

Shervan, O. (2000). Experimental investigation of the role of reinforcement in the strength of concrete deck slabs. In *Canadian Journal of Civil Engineering* (Vol. 27).

Statistics Canada. (2023). *The Daily — Canada's Core Public Infrastructure Survey: Replacement values, 2020*. https://www150.statcan.gc.ca/n1/daily-quotidien/230320/dq230320a-eng.htm

Sutton, M. A., Orteu, J. J., Schreier, H. (2009). *Image Correlation for Shape, Motion and Deformation Measurements: Basic Concepts,Theory and Applications*. Springer Science & Business Media.

Sutton, M., Wolters, W., Peters, W., Ranson, W., McNeill, S. (1983). Determination of displacements using an improved digital correlation method. *Image and Vision Computing*, *1*(3), 133–139. https://doi.org/10.1016/0262-8856(83)90064-1

Täljsten, B. (2004). FRP strengthening of concrete structures: new inventions and applications. *Progress in Structural Engineering and Materials*, *6*(3), 162–172. https://doi.org/10.1002/pse.174

Tighiouart, B., Benmokrane, B., Gao, D. (1998). Investigation of bond in concrete member with fibre reinforced Ž. polymer FRP bars. In *Construction and Building Materials* (Vol. 12).

Torres Acosta, J., Tomlinson, D. G. (2023). Evaluation of repair technique effectiveness of bridge barrier/deck systems with glass-fibre reinforced polymer bars using mechanics based modelling. *Canadian Society of Civil Engineering Conference Proceedings*.

Uomoto, T. (2000). Durability of FRP as Reinforcement for Concrete Structures. In J. L. Humar & A. G. Razaqpur (Eds.), *Proceedings of the 3rd International Conference on Avance Composite Materials in Bridges and Structures* (pp. 3–17). Canadian Society for Civil Engineering.

Vecchio, F., Collins, M. (1985). The Modified Compression-Field Theory for Reinforced Concrete Elements Subjected to Shear. *ACI Journal*, *83*(22), 219–231.

Vijay, P. V., GangaRao, H. (2001). Bending Behavior and Deformability of Glass Fiber-Reinforced Polymer Reinforced Concrete Members. *ACI Structural Journal* , *98*(6), 834–842.

Vint, L. M. (2012). *Investigation of Bond Properties of Glass Fibre Reinforced Polymer Bars in Concrete Under Direct Tension*. University of Toronto.

Wambeke, B. W., Shield, C. K. (2006). Development Legth of Glass Fiber-Reinforced Polymer Bars in Concrete. *ACI Structural Journal*, *103*(1), 11–17.

Wu, W. P. (1990). *Thermomechanical Properties of Fiber Reinforced Plastic (FRP) Bars*. West Virginia University.

Yan, F., Lin, Z., Yang, M. (2016). Bond mechanism and bond strength of GFRP bars to concrete: A review. *Composites Part B: Engineering*, *98*, 56–69. https://doi.org/10.1016/j.compositesb.2016.04.068

Yao, Y., Aswani, K., Wang, X., Mobasher, B. (2018). Analytical displacement solutions for statically determinate beams based on a trilinear moment–curvature model. *Structural Concrete*, *19*(6), 1619–1632. https://doi.org/10.1002/suco.201700150

APPENDIX A: ADDITIONAL SPECIMEN FABRICATION DETAILS

A.1. First Stage: Deck Slab Fabrication

Table A.1 shows deck reinforcement and concrete cover details. The reinforcement layout was initially proposed, and bars obtained by Al-Jaaidi (2021), who also placed strain gauges at specified locations (see Section 4.4).

Table A 1 Deck general reinforcement features.

Specimen ID†	Top rebar assembly, longitudinal	Bottom rebar assembly, longitudinal	Top concrete cover*, mm	Bottom concrete cover*, mm
SP-1	20M @ 150 mm (c-c)	15M @ 150 mm (c-c)	51.9	40
SP-2	¾” @ 150 mm (c-c)	5/8” @ 150 mm (c-c)	51.9	40
SP-3	¾” @ 150 mm (c-c)	5/8” @ 150 mm (c-c)	51.9	40
SP-4	20M @ 150 mm (c-c)	15M @ 150 mm (c-c)	51.9	40

†: All elements had a transverse reinforcement in the top/bottom mats with same diameter as bottom reinforcement assembly and spaced every 200 mm (c-c).

*: Measured to the face of longitudinal reinforcement.

All reinforcement was tied with steel rebar ties or zip-ties, depending on the type of reinforcement used (i.e., steel rebar used metallic ties, whereas GFRP used zip-ties). After mat installation, vertical reinforcement for barriers in SP-01 and SP-02 was placed and connected using the same ties. Vertical reinforcement was placed using wooden guides to maintain designed bar inclination and concrete cover (Fig. A.1).

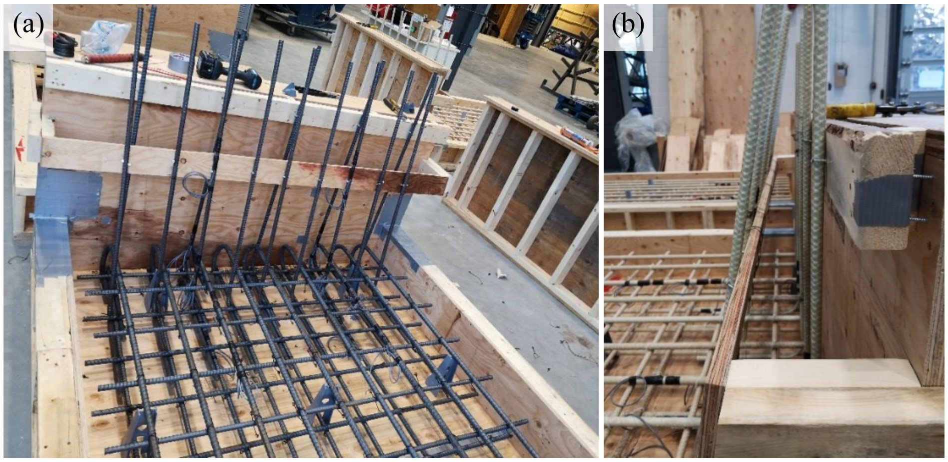

Figure A 1 Vertical reinforcement installation process for control specimens (a) front view of bars showing 2x4 in. sticks as guides, and (b) lateral view of wood guides used in SP-02.

PVC tubes were installed to allow 1800 mm-long, 31 mm diameter anchor bolts to pass through and connect specimens to the strong floor of Morrison Structures Lab (Fig A.2(a)). Due to placement conflict between some anchor bolts from deck mats, bars were moved 25 mm to 37 mm from planned (Fig. A.32(b)). After final adjustments, formwork was completed (Fig. A.3).

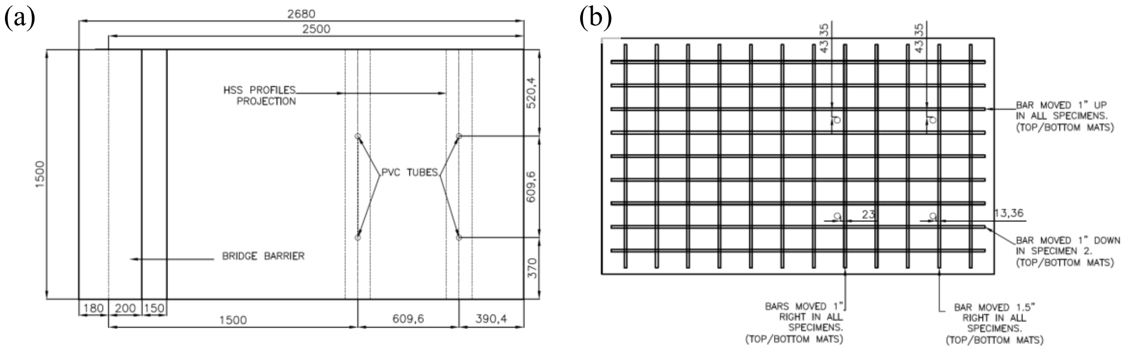

Figure A 2 (a) Typical plan view of specimens with final location of PVC tubes for connection to rigid floor, and (b) plan view of rebar adjusted due to interferences with PVC tubes. Measures in mm or as indicated.

Figure A 3 Final formworks for (a) SP-01, (b) SP-02, (c) SP-03, and (d) SP-04 deck slab.

Concrete pour took place on January 25th, 2023 (Fig. A.4). Volume and concrete mixture details are given in Chapter 4. Concrete was vibrated during casting with care not to rest the vibrator on reinforcement. Finishing of the decks was done first using a wood board to screed the surface then using a trowel.

Figure A 4 Concrete pour process for first fabrication stage (a) Concrete casted into SP-02 while being vibrated, (b) Concrete spread with shovel, (c) Concrete vibrated and distributed, and (d) Final surface detailing with trowel.

During the pour of SP-03's deck, formwork was moved so the concrete truck's chute could pour directly into the formwork. In this process, the reinforcement cages for SP-03 shifted and this movement was recorded and shown in Fig. A.5, representing an offset in the front of rebar assemblies of about 0.5 inches (12.7 mm). The shift was accounted for in second stage of the fabrication process when considering dowel bar locations.

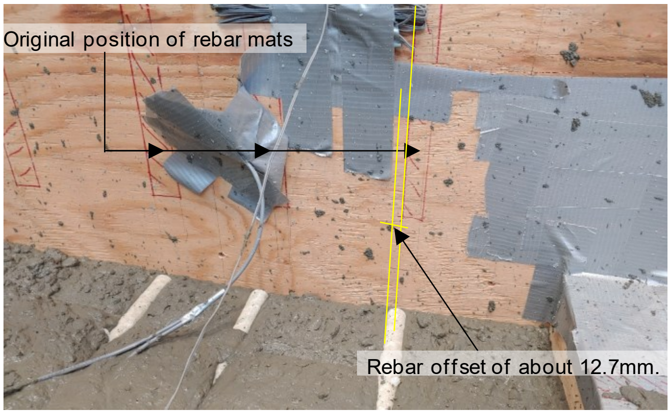

Figure A 5 Shift of SP-03 reinforcement mats during deck concrete pour.

In accordance with Alberta Transportation (2017) drawings, a roughened surface was done at the barrier-deck interface (see Subsection 4.2.1 for details). Fig. A.6 show this surface finish.

Specimens were covered with poly sheets and cured for seven days after pouring. During that time, specimens were watered daily to assist with curing. Fig. A.7 shows SP-01 and SP-04 ((a) and (b), respectively) immediately after concrete was poured; Fig. A.7(c) illustrates all structures during curing process. After seven days, the second stage of fabrication began.

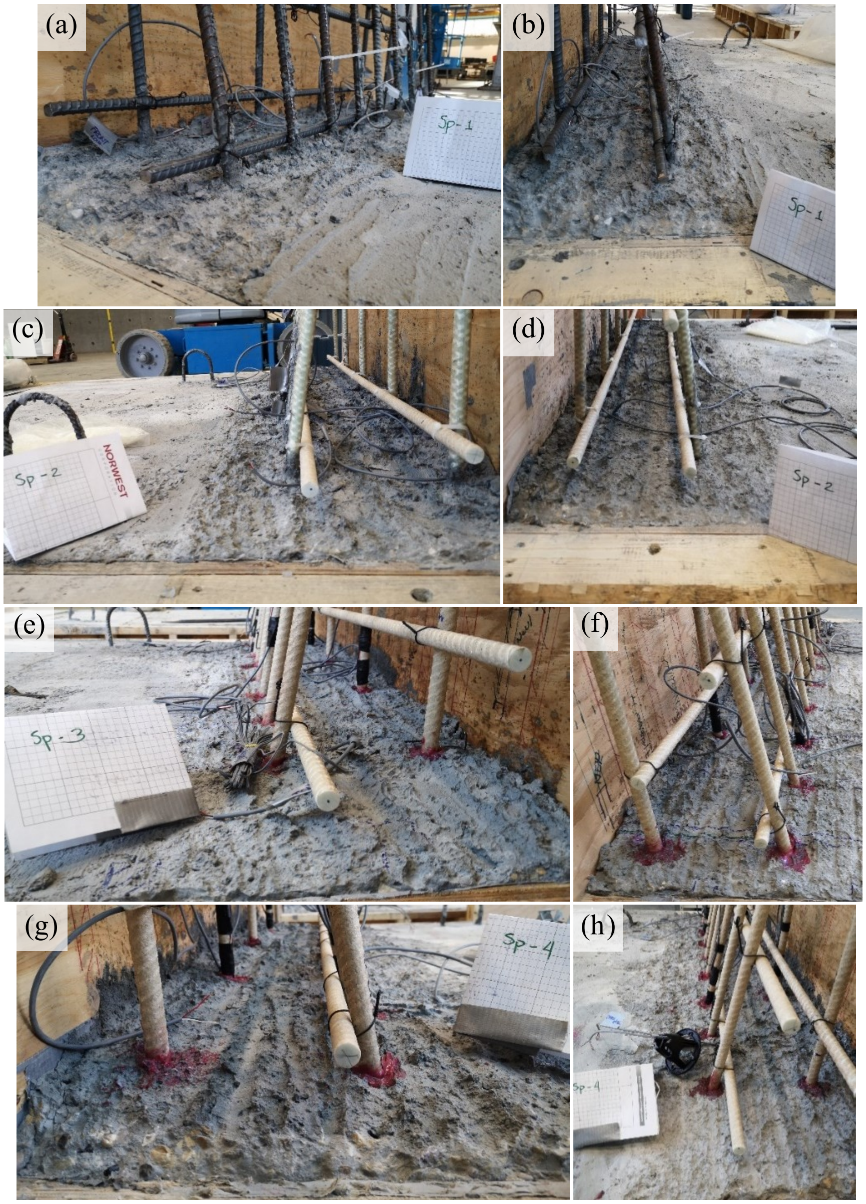

Figure A 6 Deck slab surface finish where barrier will be constructed for SP-01 (a and b), SP-02 (c and d), SP-03 (e and f), and SP-04 (g and h).

Figure A 7 (a and b) final product for SP-01 and SP-04 respectively, and (c) general photo of all specimens during curing.

A.2. Second Stage: Barrier Fabrication

Barrier reinforcement cages were built in accordance with drawings shown in Figs. 4.2 and 4.3. For SP-01 and SP-02, cages were easy to assemble since vertical bars were already anchored into the deck. Horizontal bars from back and front faces of the barrier were tied at corresponding spacing. Bars were checked with a level to confirm that they were installed horizontally. Once bars were tied, formwork up to the bottom of the spandrel beam was added to existing forms using 19 mm plywood and 38×89 mm lumbar. With this assembled, spandrel bar cages were connected to the vertical bars. Fig. A.8 show final shape of SP-01 and SP-02 barrier and spandrel beam rebar cages.

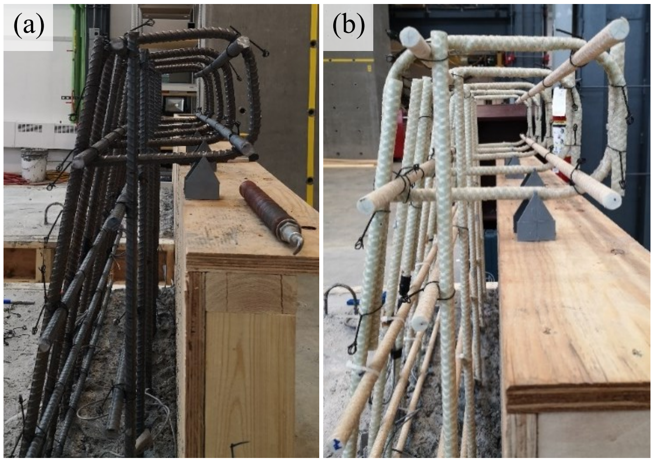

Figure A 8 Final reinforcement layout fabricated for barrier of (a) SP-01, and (b) SP-02.

The reinforcement configuration for SP-03 and SP-04 was the same as SP-01 and SP-02. However, SP-03 and SP-04 lacked bars embedded into the deck and required a different anchoring system which was achieved by dowelling bars into the deck. This process mimics the dowel repair technique frequently used in steel-RC with small usage known with GFRP-RC bridge barriers (El-Salakawy and Islam, 2014). Table A.2 explains the activity sequence needed to conduct the repair.

Table A 2 Activity sequence for bar dowelling repair technique.

Activity ID	Activity Name	Activity Details
1	Damaged concrete demolition.	Concrete demolition by jackhammer or other proven techniques are feasible to do.
2	Debris removal.	Demolished concrete should be completely removed so new one is poured over a clean area.
3	Surface roughening	Surface roughening by partially demolishing concrete smooth area so friction is increased.
4	Hole allocation.	Location of holes according to rebar layout, considering interferences with existing reinforcement.
5	Hole drilling.	Uses a rotary hammer drill to desired depth
6	Hole preparation.	Uses a metallic brush and compressed air valve to remove dust particles that remain inside holes.
7	Epoxy / Grout application in holes.	Adhesive of choice applied inside of holes according to manufacturer's instructions.
8	Bar dowelling into holes.	Bars inserted into holes partially with adhesive.
9	Rebar cage assembly	Once adhesive has hardened, it is possible to assemble rebar cages.

Surface roughening is typically done to enhance shear friction between different pours. When preparing a concrete surface, a jackhammer can roughen surfaces. Here the roughened surface was achieved as described in Subsection 4.2.2.1 and illustrated in Fig. A.6.

Hole allocation is the first step to perform their drilling. Their location should avoid interfering with existing reinforcement. Drilling guides (Fig. A.9) were fabricated and positioned where dowelled bars were needed to construct the barriers over SP-03 and SP-04's decks. These pieces were composed of two 38×89 mm lumber glued together. Holes had the same spacing as vertical bars in SP-01 and SP-02. Two sets of guides were manufactured: one for the front rebar assembly with inclined leads that had the same slope as the tapered face of the barrier (i.e., 9.37°), and another one for the vertical bars. Each set comprised two pieces installed in two locations: one around the top of the barrier and another one near its base. This was done to fix the drill bit position while being used. Existing reinforcement bar location was drawn on the plywood in the front part of the formwork so interference between drilled holes and deck reinforcement was avoided.

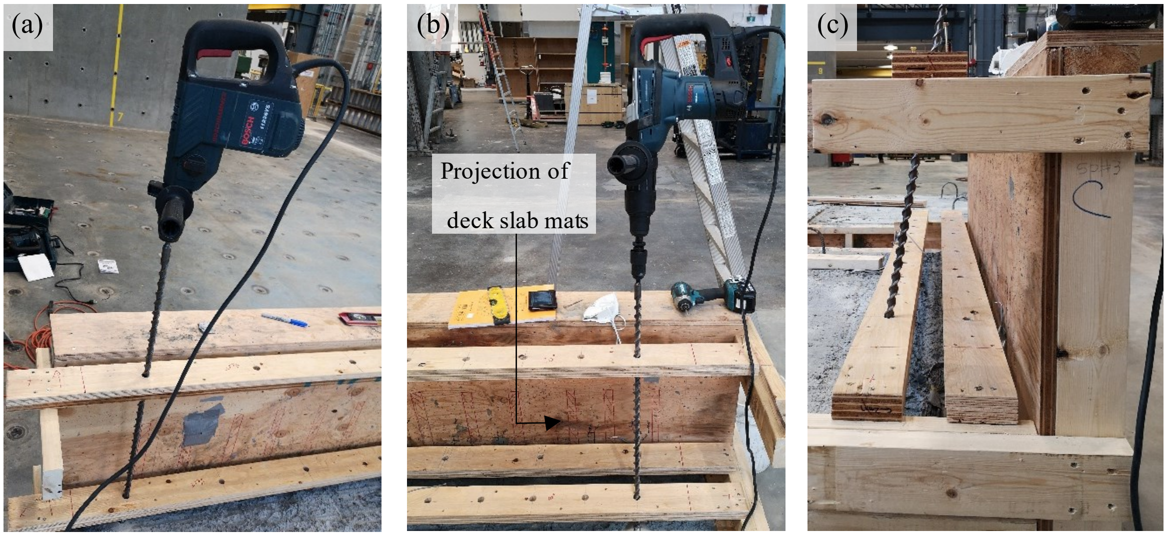

Figure A 9 Drilling guides for (a) for back rebar assembly, (b) front rebar assembly. (c) Shows lateral view of front drilling guide where inclination is observed.

With guides positioned, next step was to drill holes. A carbide drill bit was used with a diameter of 19 mm, 3 mm larger than dowelled bars. The drill itself was a BOSCH rotary hammer drill. The drilling depth objective was 220±15 mm and this length was marked on the bit for reference. Table A.3 breaks procedure into tasks; this protocol was applied for all holes. In total, 26 holes were drilled (13 on each deck). Fig. A.10 show the final position of drilled holes for SP-03 and SP-04.

Table A 3 Activity discretization for hole drilling using rotary hammer drill.

Activity ID	Activity Name	Activity details	Approximate time to complete
1	Install drill inside guide	Leveling of bit; prepare the drill in a comfortable position for user.	1 min
2	Initial drilling	First drilling of hole.	1 min
3	Dust Vacuum	Remotion of dust around hole region.	30 sec.
4	Second drilling	Final drilling to required depth.	1 min
5	Final vacuum	Remotion of dust around hole region.	30 sec.
6	Check drill depth	Using line marked in bit check if depth is adequate or not.	30 sec.
7	Removing of drill	Once depth has been cleared, drill is removed and ready for next hole to be drilled.	30 sec.
		Total	**5 minutes**

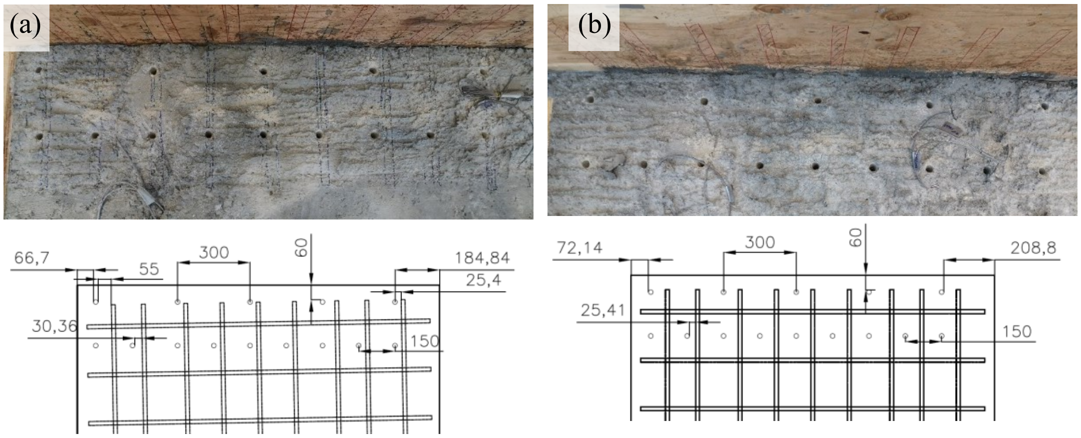

Figure A 10 Holes drilled for Specimen 3, including approximate measures and distances between existing and dowelled bars for SP-03 (a) and SP-04 (b). All measures in mm.

Hole final positions attempted to leave a distance of $1.6d_b$ (i.e., 25.4 mm) between the hole edge and deck reinforcement. Given that there were some alterations in rebar spacings from top and bottom mats from deck slab this distance was set as a minimum. In addition, SP_03 had to account for displacements during the 1st concrete pour; its spacing ranged between 25 and 55 mm, whereas SP-4 from 25 mm to 76 mm. El-Salakawy et al. (2009) and El-Salakawy and Islam (2014) used a spacing of $3.0d_b$ between bars, in accordance with ACI 355.2, (2000). Both reinforcement mats were closer to west side edge of specimens due to space restrictions mentioned above. This resulted in SP-03 barrier reinforcement having a lateral cover of 66 mm and 72 mm for SP-04.

Following hole drilling, bar doweling preparation began. This process followed the adhesive's manufacturer instructions. Holes were cleaned with a metallic brush to roughen the surface while a vacuum removed dust particles. The brush was inserted until the bottom of hole and extracted by pulling up in a circular motion at least two times. Compressed air is pumped into the hole to remove dust particles after wall brushing is finished. A vacuum hose was placed next to the hole being cleaned during the entire process to capture dust. Fig. A.11 show the tools used for hole preparation and the process itself.

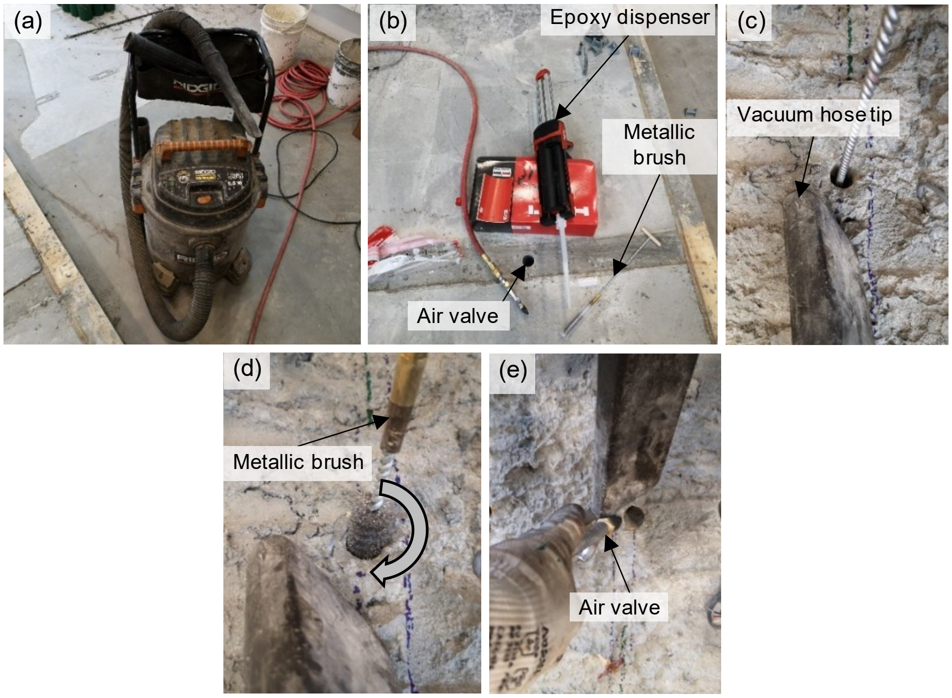

Figure A 11 Tools used for hole preparation (a) Industrial vacuum, (b) Additional tools to clean holes from dust contained within, (c) metallic brush insertion, (d) metallic brush pullout in circular motion, and (e) compressed air pumped into hole. All steps had the vacuum hose tip nearby.

Adhesive injection was then performed using an epoxy adhesive to anchor bars to existing concrete. Epoxy was used due to its frequent use in industry and since past studies reported good performance (El-Salakawy and Islam, 2014; El-Salakawy et al., 2009). The epoxy selected was HILTI HIT-RE 500 V3; its use followed instructions of manufacturer.

HILTI HIT-RE 500 V3 epoxy comes with a two-container cartridge and a mixer nozzle. Each container holds chemicals to produce the epoxy adhesive when mixed. Mixing is done in the nozzle as liquids are pushed out the cartridge by the dispenser's piston rods. By manufacturer's recommendations, the first three injections from each cartridge are not suitable and discarded (HILTI, 2022b).

To begin epoxy adhesive injection, the nozzle was inserted into the holes. When the nozzle tip reached the bottom of the hole, the first epoxy injection was applied. Subsequent injections were added as the nozzle was slowly retracted from the hole. Between three to four injections of mortar were needed in each hole, equivalent to 2/3 of the hole depth (HILTI, 2022b). Bars were dowelled into holes immediately after adhesive was injected. Bars were inserted with a circular motion to break voids that may have formed within the epoxy. This movement was done until bars reached the end of the hole. Some epoxy flushed from the hole as bars were dowelled. Excess epoxy was cleaned while trying to keep a thin layer on the surface around dowelled bars. Fig. A.12 shows dowelled for each specimen.

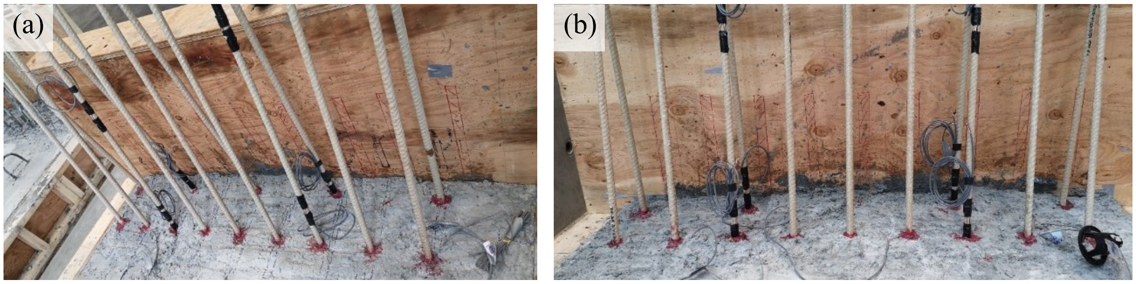

Figure A 12 dowelled bars for barrier reinforcement of (a) SP-03, and (b) SP-04.

Considering hole preparation, mortar injection, and bar dowelling, ~8 minutes per hole was required to perform the doweled repair protocol following manufacturer's instructions. This time was below the handling time recommended by HILTI for a room temperature of 22°C (25 min). Full curing under this temperature is expected after 6.5 hours. After this time, it was possible for further activities on dowelled bars (e.g., tying reinforcement). For this program, bars were left at least 24 hours after dowelling prior to moving onto the next phase. Table A.4 describe the approximate times each activity required.

Table A 4 Activity discretization for bar doweling.

Activity ID	Activity Name	Activity details	Approximate time to complete
1	Wall brushing	Metallic brush used to remove dust using a circular motion while pulling tool out. Minimum two passes; 45 seconds per passing.	1.5 min.
2	Compressed air pumped	Air pumped inside holes.	30 sec.
3	Dust vacuuming	Dust vacuum while and after dust is being removed from holes.	30 sec.
4	Mortar dispenser preparation	Epoxy adhesive foil pack installation inside dispenser and mortar mixing following manufacturer's instructions.	2 min.
5	Mortar injection	Minimum three shots applied into drilled holes, while retrieving nozzle.	2 min.
6	Bar dowelling	Bar insertion in hole with epoxy. Apply a circular motion to eliminate possible voids formed in mortar.	1 min.
7	Epoxy excess cleaning	Surface cleaning of epoxy excess around bar dowelled.	30 sec.
		Total minutes	**8 minutes**

Finally, reinforcement bar assemblies are configured for barriers of SP-03 and SP-04 in the same way as described for SP-01 and SP-02. Following the completion of cage assembly in all specimens, strain gauges were organized and extended so cables reached the top of each barrier. Then, the barrier formwork was finished. Sealing foam was used at the bottom of the barrier formwork to close gaps between the form and deck surface. Fig. A.13 shows the barrier reinforcement and formwork prior to form closure.

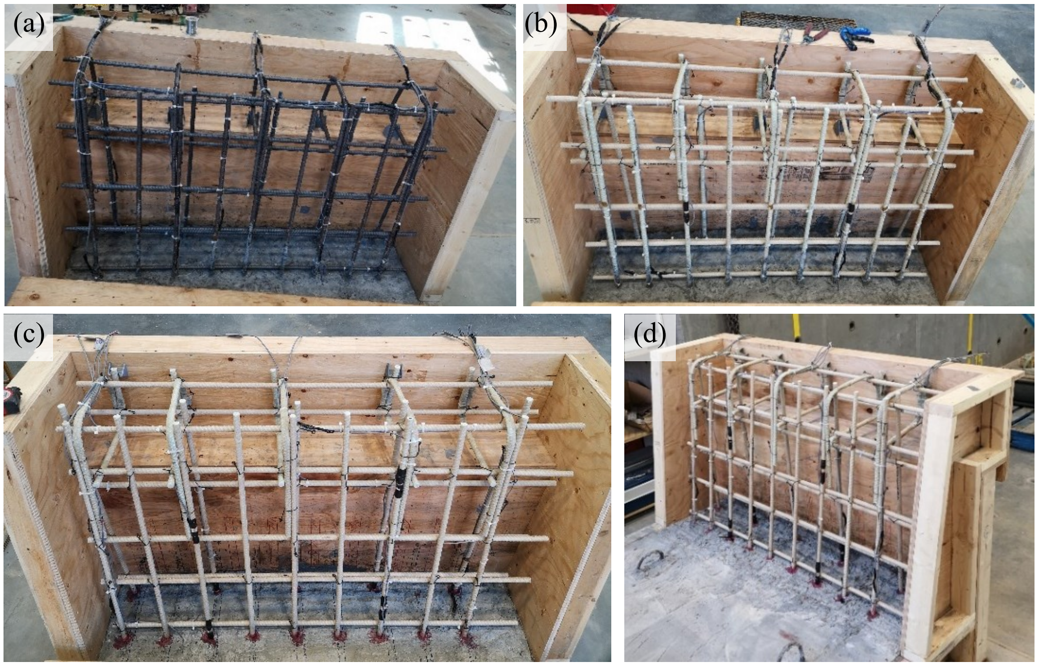

Figure A 13 Formwork and reinforcement cages completed for (a) SP-01, (b) SP-02, (c) SP-03, and (d) SP-04.

The second concrete pour took place on April 20th, 2023. Fig. A.14 shows the casting, curing, and stripping process. A concrete volume of 0.46 m^3 was cast into each barrier. The same concrete mix was ordered as specified in Subsection 4.3.1. Same processes of concrete vibration, troweling and levelling were used as the deck fabrication. When all surfaces were smoothed, poly sheets were installed on each specimen to begin the 7-day curing process. Like in the 1st concrete pour, specimens were watered during that time to limit microcracking and following typical construction processes. After seven days, the poly was removed, and specimens were ready to be removed from formwork. Barrier formwork was removed by hand and the deck forms were removed by lifting the specimen with a 10-ton overhead crane and hammering the deck formwork until it separated from the concrete. Structures were lifted using four steel hooks placed to minimize tilting when specimens were lifted.

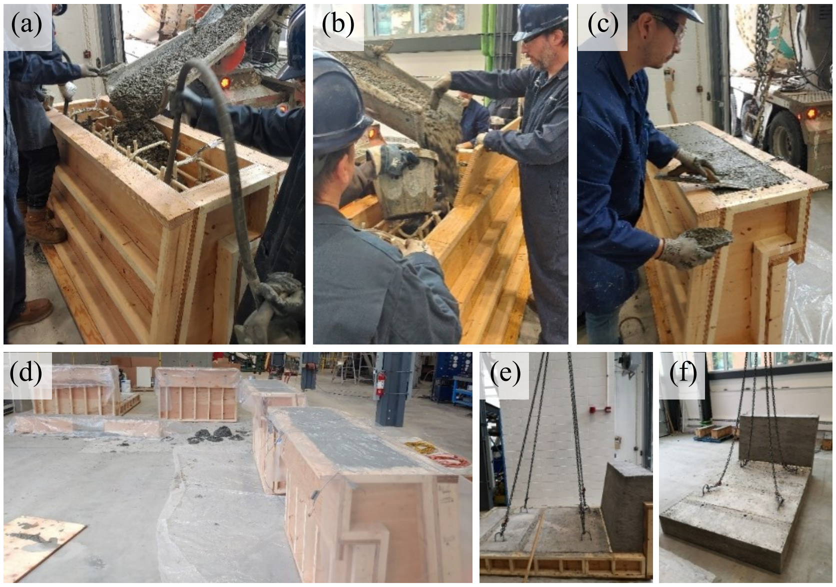

Figure A 14 2nd concrete pour. (a) Concrete mix pour while vibrated, (b) Concrete pour into formwork of specimen 1, (c) Surface finishing using wet trowel, (d) specimens under curing process after casting was finished, (e) removal using crane system from facility, and (f) Structure without formwork.

A.3. Final Appearance

Following visual inspection (see Subsection 4.2.2.4), as-built measurements were taken. This will enable future theoretical or other comparisons to have complete information. Figs. A.15 through A.18 report as built measurements and Table A.5 describes the final concrete covers provided for main reinforcements. It is worth mentioning that measures reported are the average taken from five different locations in both the barrier and deck.

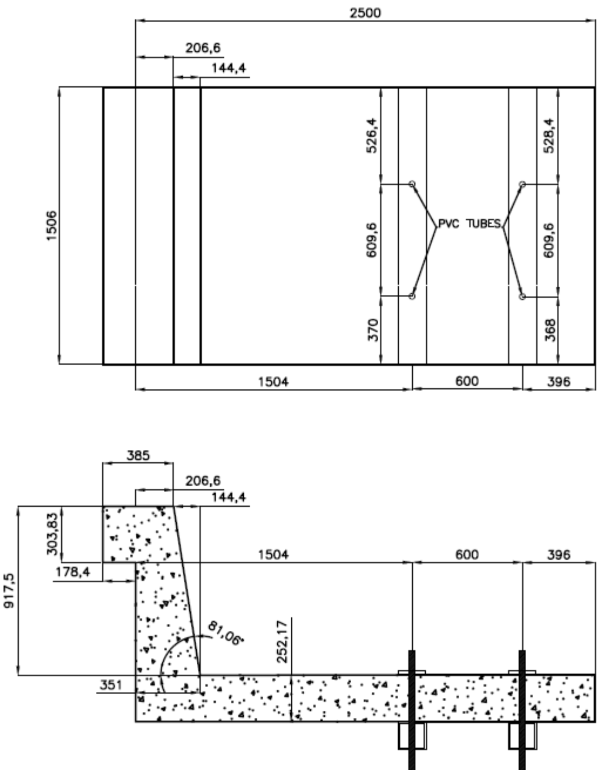

Figure A 15 As-built dimensions for SP-01. All dimensions in mm.

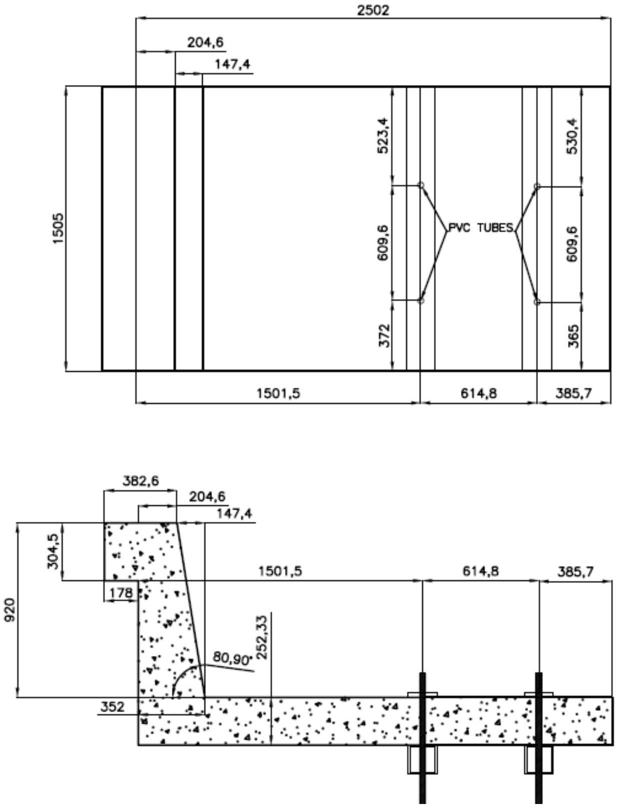

Figure A 16 As-built dimensions for SP-02. All dimensions in mm.

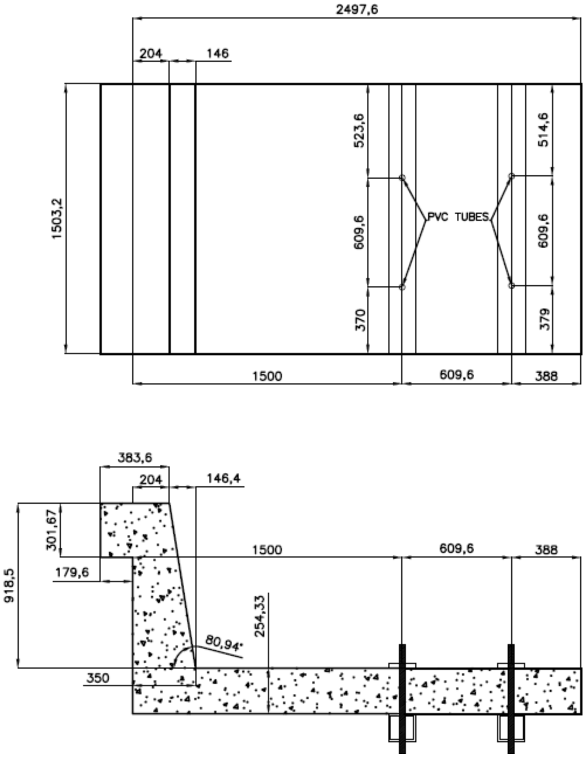

Figure A 17 As-built dimensions for SP-03. All dimensions in mm.

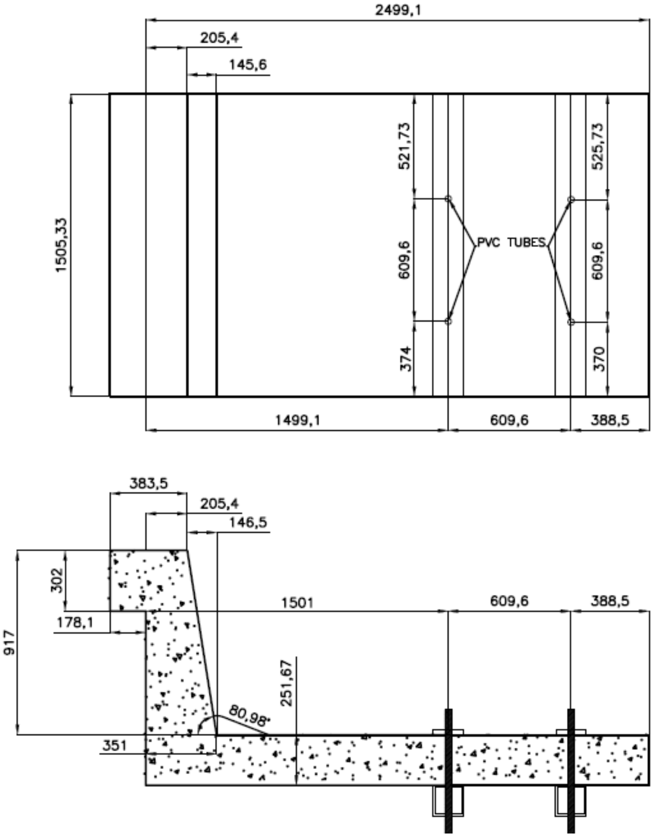

Figure A 18 As-built dimensions for SP-04. All dimensions in mm.

Table A 5 Final concrete covers in as-built specimens.

Specimen ID	Barrier front rebar assembly cover*, mm	Barrier back rebar assembly cover*, mm	Deck slab top concrete cover*, mm	Deck slab bottom concrete cover*, mm
SP-01	90	60	51.9	40
SP-02	90	60	51.9	40
SP-03	100	60	51.9	40
SP-04	100	60	51.9	40

*: Measured to the face of longitudinal reinforcement.

As mentioned in Subsection 4.2.2.4, from inspection imperfections on specimens SP-03 (Figs. A.19(a) through (c)) and SP-04 (Figs. A.19(d) and (e)) were observed.

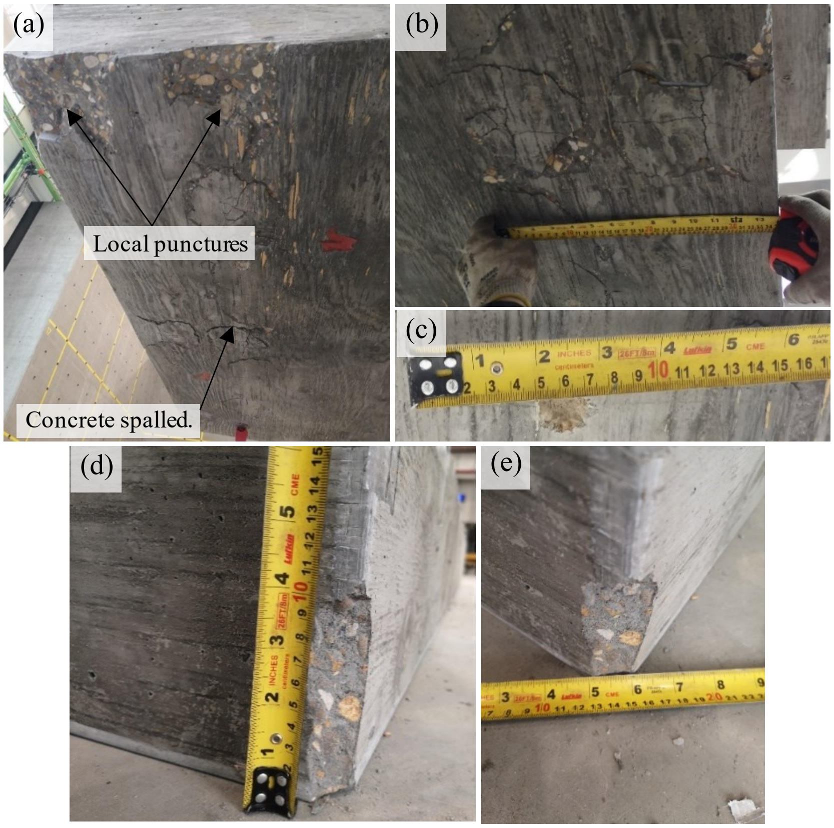

Figure A 19 (a) affected region in bottom of SP-03's deck, Concrete spalled radius (around 120 mm), (c) puncture diameter (around 20 mm), (d) and (e) reports damaged corner of SP-04's deck.

APPENDIX B: MODIFIED RILEM BEAM FABRICATION DETAILS

B.1. RILEM Beam Fabrication Process

RILEM beams were constructed by following different test setups and details from previous studies (Tighiouart et al., 1998; Carvalho et al., 2017; Makhmalbaf and Razaqpur, 2022). Specimens were designed so failure would be due to bar pullout. Different failures were considered (flexural, shear, and pullout) to ensure that pullout would likely occur first. Concrete cracking was also considered as a failing state as it may alter slip readings due to additional rotations in the system. Table B.1 shows the predicted failure moments at each analyzed state with corresponding analysis/code provisions used. Predictions were made based on materials and specimen dimensions reported in Chapter 4.

Table B 1 Failure mode comparison for RILEM beam design.

Failure mechanism	Moment at failure, kNm	Type of analysis/Code provisions used
Flexure	49.7	Cross-sectional Analysis
Shear	65.9	CSA S6 (2019)
Cracking	15.3	CSA S6 (2019)
Bar pullout	11.3	ACI 440.1R (2015)

Beam fabrication consisted of four stages: formwork assembly, rebar cage positioning, GFRP installation, and concrete pouring. Formwork was assembled using 19 mm plywood cut at desired dimensions and connected by screws. Holes were drilled in the plywood to allow the GFRP bar to be inserted as well as where anchors for the steel angles supporting the hinge would be inserted. As a first step to assemble the formwork, steel angles with anchors welded to them (to prevent the angles from separating from concrete) were positioned and bolted to the plywood (Fig. B.1(a)). Then, Styrofoam previously cut to desired dimensions and with a hole drilled in it to facilitate insertion of the GFRP was placed where the gap between the concrete segments would be located (Fig. B.1(b)). Following this the bottom and front formwork boards were screwed to these boards to complete the formwork. The rebar cage comprised steel longitudinal bars at the top and 1.5 mm-diameter steel wire in the lower end to maintain spacing and vertical alignment. These elements were tied to 10M stirrups placed every 90 mm. This spacing complied with CSA S6:19 code requirements to prevent shear failure. Once cages were ready, they were placed inside formwork and mounted on two 6.25 mm diameter steel bars crossing the formwork transversely at a fixed height from top of formwork for constructability (Fig. B.1(c)). Once these phases were done, the GFRP bar was installed. This was done by placing acrylic tubes at fixed positions along the bar, leaving a 225 mm-long embedment region, and then it was pushed through front faces' holes in formwork (Fig. B.1(d)). Concrete pouring was done at the same date when barriers were cast (Fig. B.1(e)). CE beam series' GFRP bar had an acrylic tube covering the entire bar during pouring as these beams were investigating bond between bar and concrete that included epoxy resin that must be added after concrete hardened. Fig. B.1(f) shows these beams.

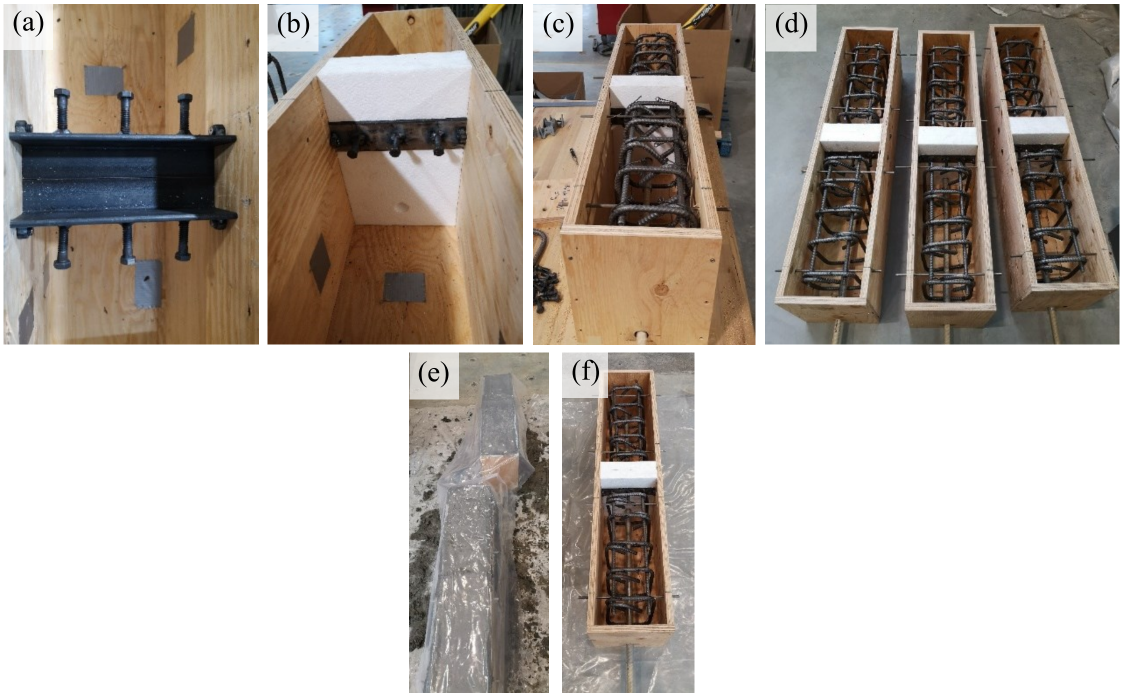

Figure B 1 (a) connection of lateral plywood boards through steel plates, (b) Styrofoam positioning inside formwork, (c) typical location and mounting system for rebar cages assembled, (d) longitudinal bars placed along formwork, I RILEM beams during curing process, and (f) CE beam series with longitudinal acrylic tube.

B.2. Epoxy Injection Procedure for CE Beam Series

As mentioned in Subsection 4.3.5.1, CE beams were built to analyze bond between bar-epoxy-concrete. Since this type of analysis or test processes is lacking in the literature, there was not much information to fabricate elements with this kind of bond. A protocol to assemble RILEM beams was developed that includes bonding agents in their fabrication. Up to this stage, RILEM beams from CE series were fabricated as described in Section B.1.

Step 1: Once concrete hardened (end of Section B.1), remove the GFRP bar and acrylic tube from the beam segments. This was done by pulling on the bar while hammering from the opposite side (Figs. B.2(a) and (b)).

Step 2: Position of longitudinal hole, stirrups, and de-bonded areas drawn on the side faces of beam sections. This will be used as references in later steps of this process.

Step 3: To ensure better bond with epoxy, hole walls were roughened with a rotary jack hammer, so these holes had similar texture to those drilled in repaired decks. A drill bit of the same or slightly larger diameter than the hole was used for this purpose and each segment was clamped to keep them fixed (i.e., prevent rotation during drilling). At least two drill bit passes were completed per longitudinal hole (Fig. B.I(c)).

Step 4: Lateral holes are drilled with rotary jack hammer (Fig. B.2(d)). A 5/16 in. (7.94 mm) drill bit was used, sized so the epoxy nozzle could still enter the cavity. Holes were drilled as close to the un-bonded areas of the bar as possible to ensure epoxy resin covers most of bonded bar length to concrete.

Step 5: Holes are air pumped and brushed to remove dust particles from cavity walls (Fig. B.2(f)).

Step 6: Bar installation. The GFRP bar removed in **Step 1** is placed inside the beam segment again. This time, the bars have acrylic tubes placed 125 mm at end of segments to provide the same 225 mm embedment as CB beams described in Section B.1. Acrylic tubes should be flushed to the ends of segments to assure design bond length.

Step 7: Location of beam segments is shown in Fig. I(e). Each pair of segments were closely placed to each other and levelled so imperfections during fabrication process were minimized to avoid any undesired effects during tests. To do so, metallic shims and clamps were used as needed.

Step 8: Fig. B.2(g) shows epoxy injection. Epoxy resin is injected through the lateral holes drilled in **Step 4**. Epoxy nozzle is inserted in one cavity and resin pushed into the hole until it comes out from opposite lateral cavity. This pushes air out from the longitudinal hole and ensures that the hole is adequately filled. Excess epoxy was then cleaned off.

Step 8: Let resin cure according to manufacturer's recommendations (6.5 hours). In this case, at least 7-days were used to cure the resin and move to testing stage (Fig. B.2(h)).

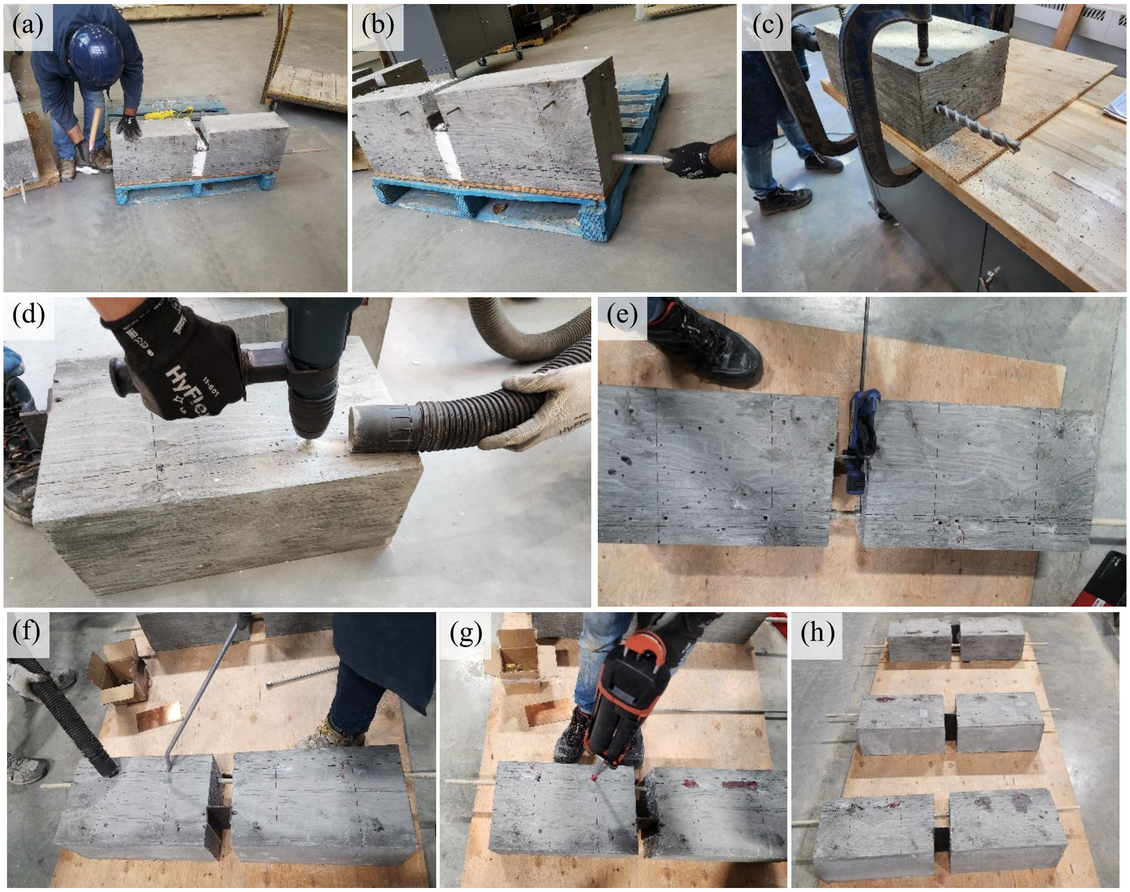

Figure B 2 (a) and (b) GFRP bar removal from hardened concrete, (c) hole wall roughening with rotary jack hammer, (d) lateral holes drilling, I beam segments positioning and levelling, (f) holes cleaned with pumped air, (g) epoxy resin injection into lateral cavities, and (h) specimens curing after epoxy injected.

B.3. Test Results for Remaining Beam Segments

Results shown are for those segments of each specimen that did not report first pullout failure (i.e., segments not reported in Chapter 4). Fig. B.3 shows bond-slip curves for CB and CE series, respectively. The same labelling for north and south sides is used as the plots in Subsection 4.3.5.3.

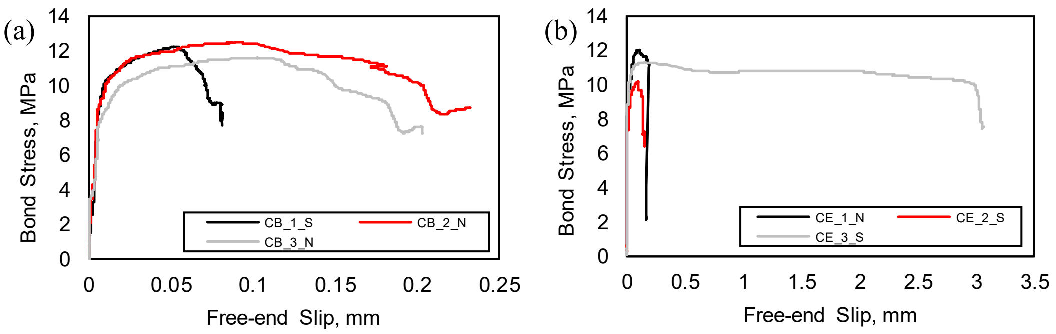

Figure B 3 Bond-slip curve for (a) CB beam series, and (b) CE beam series.

It is important to note the order of magnitude of slips recorded by these segments with respect to the side that first pulled out, where these segments reached 11 mm slip at the end of tests. This could be explained by equilibrium: as the bar pulls out from the segment that first experienced pullout, the bar in the opposing segment is unable to slip at the same rate to maintain force equilibrium of specimen during the test, preventing it to reach bond strength (τ_1). An interesting phenomenon occurred in CE_3, which had similar slips on each side of the specimen until slip equaled around 3.0 mm. At this point, the south side stopped slipping at the same rate with respect to north side, which continue slipping until test was terminated. Again, equilibrium could explain this behaviour.

The irregular behaviour recorded in these sides of specimens is unrepresentative of these tests and thus were not considered for model calibration in Subsection 4.3.5.4. Some aspects to highlight of tested specimens are shown in Fig. B.4 and explained in Subsection 4.3.5.3.

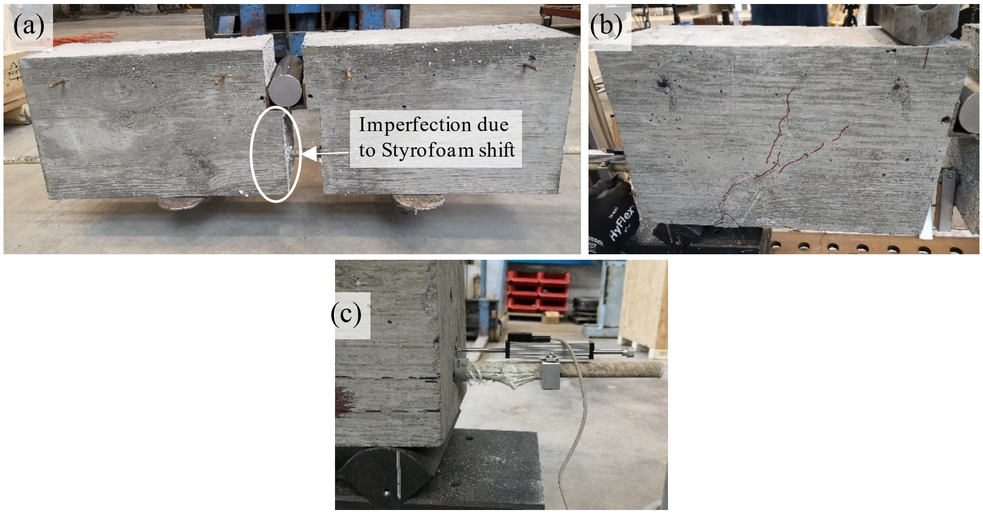

Figure B 4 Imperfection in one of the segments of CB_1 due to Styrofoam movement during concrete pouring, (b) Shear cracks observed in CE_1 after test terminated, and (c) GFRP bar ruptured after brittle failure of CE_1.

B.4. Notes on Demolition Performed to Tested Specimens.

Partial demolition was performed on both segments of specimens after testing to assess failure mechanisms and other effects (e.g., effects on epoxy resin on pullout failure, interaction with acrylic tube to slip recorded). A jackhammer with different tip sizes was used to crack concrete around the bars. Only the bottom section of the beams was demolished until the GFRP bar was reached to save time.

Pullout could occur under different circumstances. For instance, bars might had pulled out from concrete, showing sanded marks in concrete. Given the composite manufacturing process of FRP bars, bar sand coatings are adhered to resin matrix after pultrusion of the core bar which may form a failure plane between the core bar and coating. Thus, pullout may also be induced by peeling of the bar sand coating from the core of the bar. Finally, considering the use of epoxy for doweling, two more outcomes may be expected: (1) bar and epoxy resin pull out from concrete, or (2) bar pulling out of resin and concrete by peeling of its coating.

B.4.1. CB Series' Demolition Notes

Figure B.5 show a typical pullout failure mode of all three CB specimens after being demolished. The GFRP bar's outer coating peeled off and stuck in the concrete while the resin matrix pulled out. Beyond this, beams did not report any cracking in lateral faces, only in inner ones as described in Subsection 4.3.5.3. No concrete spalling was observed.

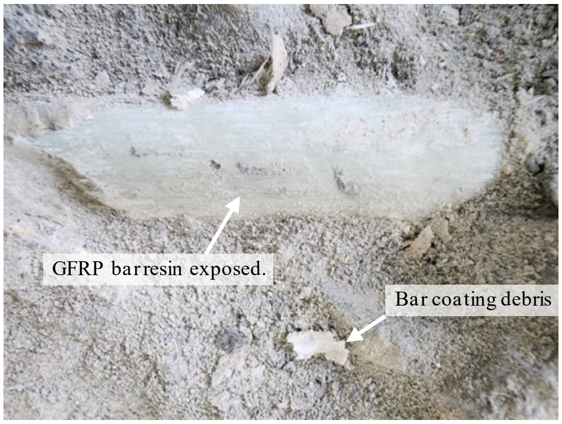

Figure B 5 Typical final state of CB beam series. Pullout failure due to bar coating peeling off from bar resin. Bar coat debris are shown.

B.4.2. CE Series' Demolition Notes

Figure. B.6 presents demolition photos from CE beams. As a reference, a trial beam segment was fabricated and demolished to compare features between a bar embedded into sound concrete with epoxy resin (Fig. B.6(a)) and bars registering pullout marks (e.g., smoothened surface of epoxy, bar surface peeled off from resin and concrete, concrete surrounding bar smoothened). Aside from CE_1 at its north side (which failed by shear after initial pullout; Fig. B.6(b) and (c)), beams showed localized signs of pullout (Fig. B.6(b)). Bar and epoxy formed a strong bond which led this system to slip as a unit as force was applied. This resulted in smoothened regions of epoxy in the segments that registered first pullout. The other segment in general recorded similar regions with smaller smoothened lengths (Fig. B.6(c)) and large portions of bars still with concrete surrounding it (Fig. B.6(d)).

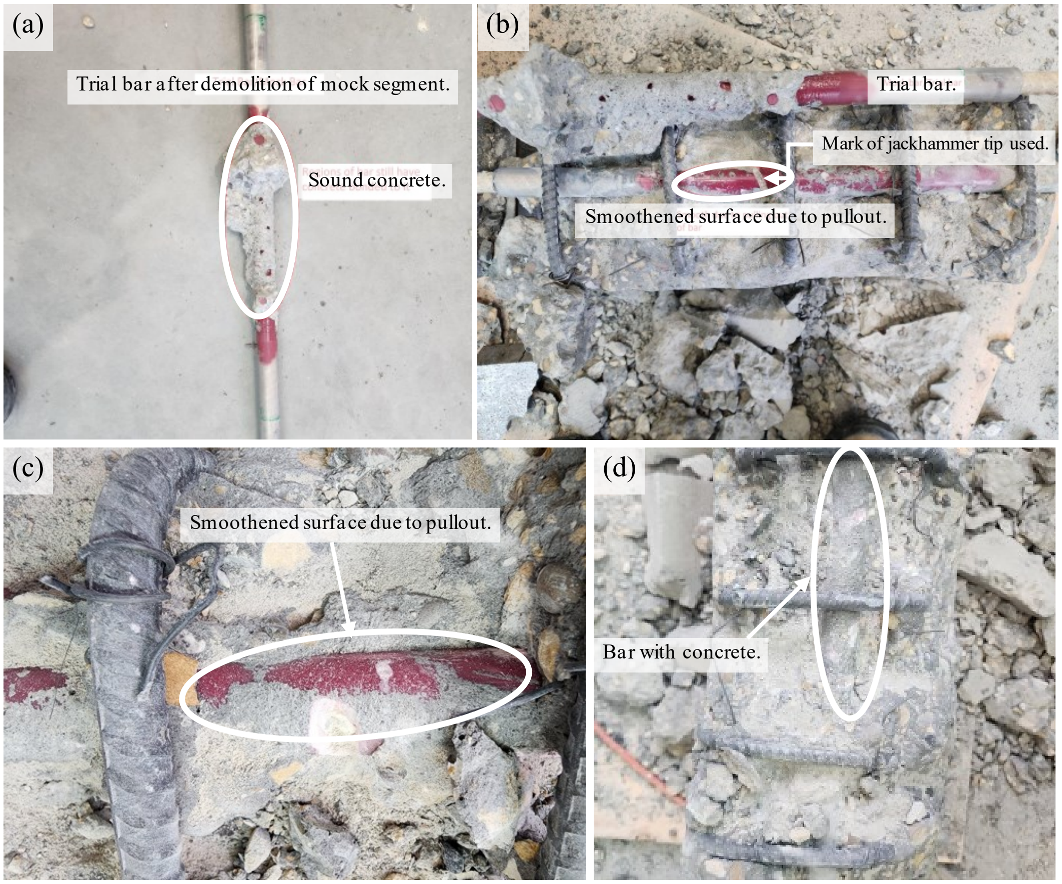

Figure B 6 (a) Trial bar used as reference, (b) Smoothened areas of bar in pical final state of CB beam series. (c) Pullout failure due to bar coating peeling off from bar resin. (d) Bar coat debris are shown.

APPENDIX C: TEST DETAILS

C.1. Additional Test Setup Details

$152 \times 152 \times 12.7\text{mm}$ HSS sections were placed below the PVC tubes in each specimen. Holes had same spacing as those from the strong floor (i.e., 2 ft or 610 mm in each direction). A 1500 mm-long overhang was attained with a 6 inch (152 mm) vertical gap that enabled specimens to deflect vertically. Four 31 mm-diameter rods were used to anchor the specimen's position and flushed to the face of holes by pushing structures longitudinally with a hydraulic jack, so relative displacement between floor and specimen was none or negligible. Each rod had a set of two nuts and plates that acted as washers which were used to bolt the structure to the strong floor. Concrete grout was used in contact areas between steel plates and concrete to ensure flush connections. Steel shims were used when gaps between HSS and deck were visibly large. Fig. C.1(a) shows SP-01 mounted on HSS profiles, and Fig. C.1(b) illustrates typical anchor treatment used for all specimens.

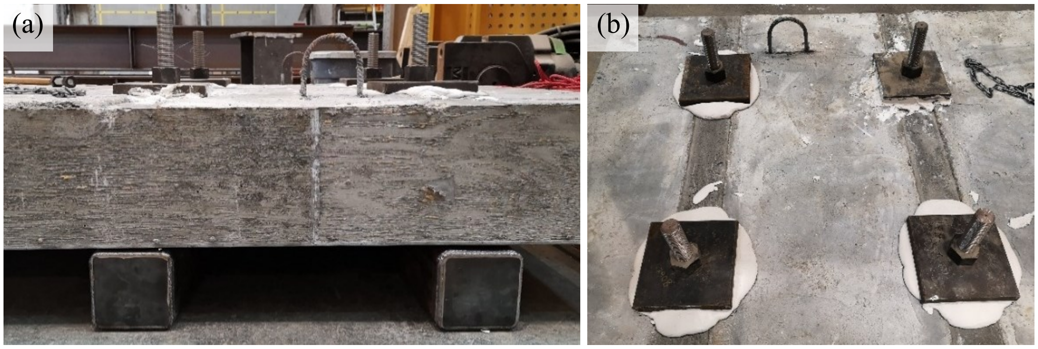

Figure C 1 (a) Structure mounted over HSS profiles, (b) typical treatment used to anchor specimens to strong floor.

The actuator was bolted to a set of rigid extensions connected to the face of the strong wall. The free end was connected to a plate. Both edges had pinned connections. This actuator is controlled by a hydraulic system composed of two hoses filled with oil that enables the extension / contraction of the ram's arm. Finally, a $\text{W}201 \times 201 \times 9.5$ mm profile was used as spreader beam with 9.5 mm thick stiffeners welded every 262.5 mm and 1050 mm width was bolted to the plate at the free end of the ram.

The position of the specimen was fixed by concrete anchors. To keep specimens and loading systems horizontal and plumbed prior to testing, chain hoists were used to adjust the actuator with a level. Fig. C.2(a) shows the final setup; Figs. C.2(b), and (c) shows relevant details. As observed in Fig. C.2(b), the actuator was not centred in the middle of the specimen width due to the strong floor's hole location relative to their position on each specimen. This resulted in the actuator centre being offset 3.5 in. (88.9 mm) towards the west side of each specimen.

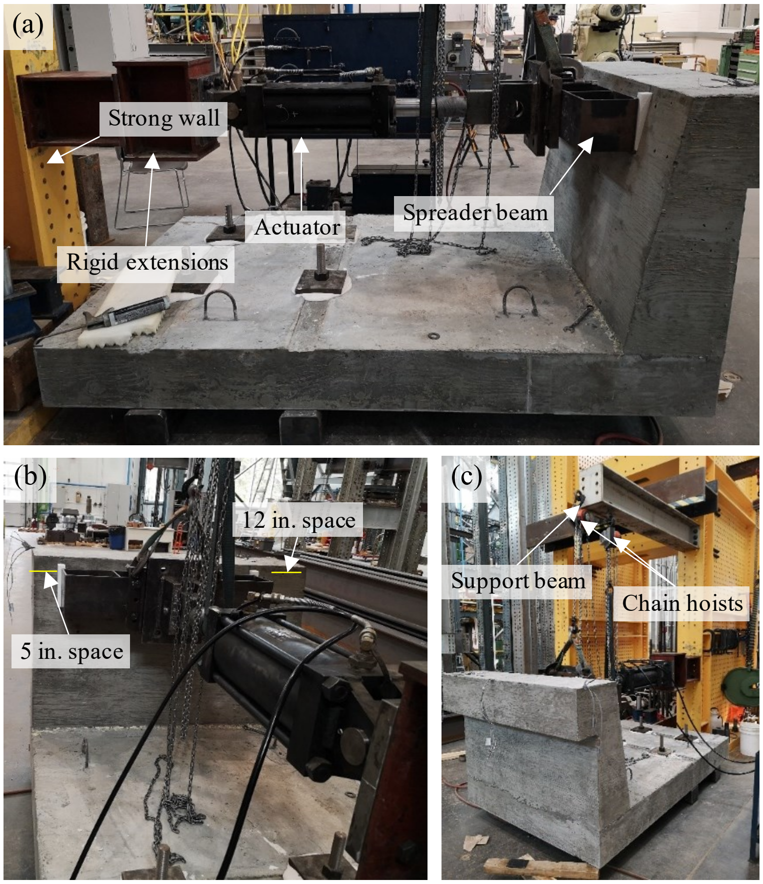

Figure C 2 Final test setup, (b) Spreader beam position along specimen's width, and (b) upper supporting structure composed of beam and chain hoists to maintain in a horizontal level the actuator.

The final position of all sensors used is shown in Fig. C.3. In the case of strain gauges labels, all gauges numbered from 1 to 3 were positioned at the west side of the specimen, while those with 4 – 6 labels were on the east side.

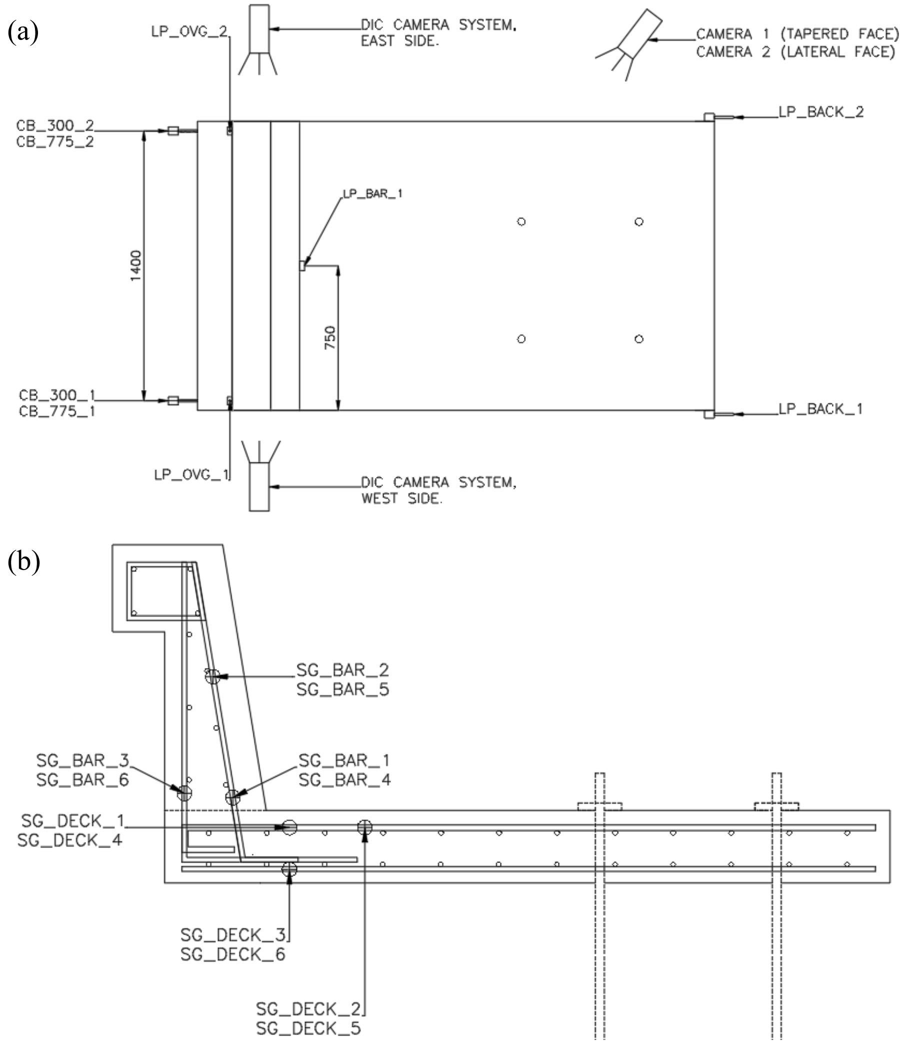

Figure C 3 Location and labelling of sensors used for specimen testing. (a) cameras and deflection sensors, and (b) strain gauges. All dimensions in mm.

C.2. Data Processing Methodology

As mentioned in Chapter 4, some structures had visible slips against the strong floor, particularly SP-01. Eq. C.1 was used to account for slip against the strong floor when reporting the final horizontal deflection exhibited in Fig. 4.13(a).

$$\delta_h = \delta_{775,avg} - \delta_{back,avg} \tag{C.1}$$

Here δ_h is the horizontal deflection plotted in load-deflection curves. $\delta_{775,avg}$ and $\delta_{back,avg}$ are the average deflection at any load step recorded by CB_775 and LP_BACK sensors, respectively.

In the case of computed rotations, average deflection from CB_300 sensors were used to process this information. As this sensor was referenced to the strong floor, this sensor had a vertical movement that shifted the original height of sensor and required adjustment to determine rotations. Equation C.2. express this; once height was adjusted, rotation was determined using C.3.

$$\delta_v = H_{300} - \delta_{ovg,avg} \tag{C.2}$$

$$\theta = \tan^{-1}\left(\frac{\delta_{300,avg}}{\delta_v}\right) \tag{C.3}$$

In expression C.2, H_{300} is the height at which CB_300 sensors were located (i.e., 300 mm above the top deck) and $\delta_{ovg,avg}$ is the deflection recorded by LP_OVG. Finally, for C.3 $\delta_{300,avg}$ is the deflection recorded by CB_300. All deflections used are the average values and at any load step recorded by sensors.

C.3. Load-Rotation Plots

Figure C.4 shows load-rotation curves corresponding to barrier rotation along test. Rotations were calculated using expressions C.2 and C.3.

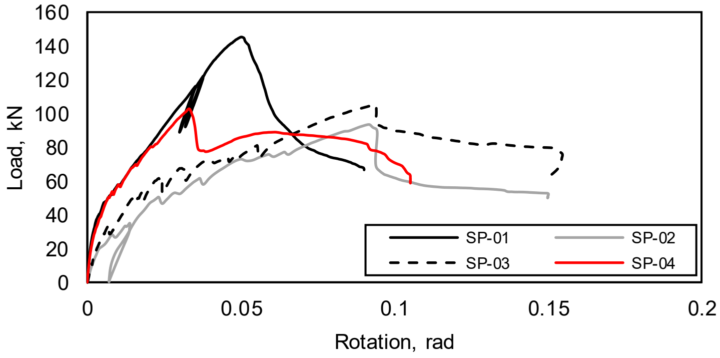

Figure C 4 Barrier load-rotation curves recorded for tested specimens.

APPENDIX D: ANCILLARY TESTS DATA

Ancillary test results were given in Subsection 4.3 for each material used for specimen fabrication. Details on concrete cylinder tests and steel reinforcement tensile tests are provided here. GFRP tensile bar tests are found elsewhere (Al-Jaaidi, 2021).

D.1. Concrete Cylinder Tests

Three concrete cylinders were tested at 28 days after each pour (Fig. D.1(a) and (b)) and 15 others were tested along the time span when barrier-deck specimens were tested. Results from these are not presented here.

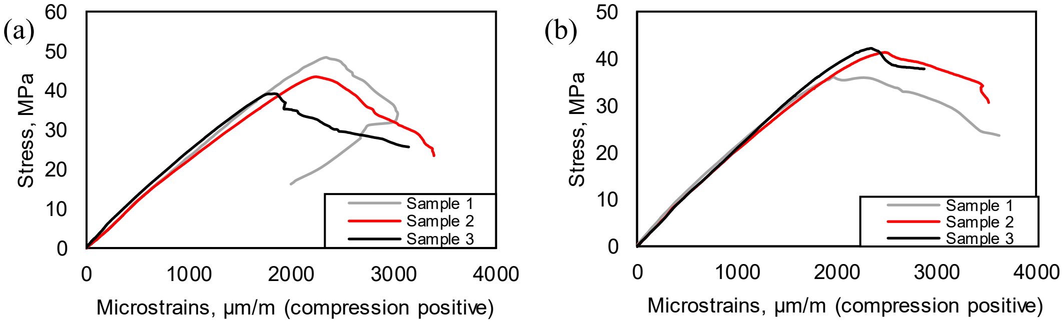

Figure D 1 Stress-strain curves of concrete cylinders at 28 days after pouring (a) deck slab samples, and (b) barrier samples.

D.2. Steel Reinforcement Bar Tensile Tests

Three bar coupons per diameter used in barrier-deck structures were tested to failure. Fig. D.3 presents stress-strain curves recorded.

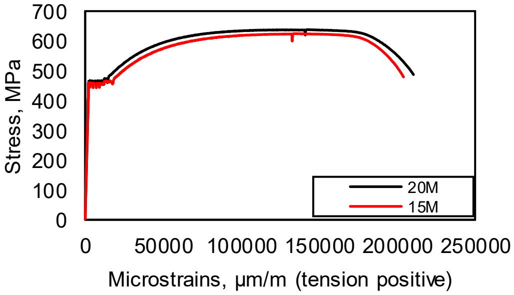

Figure D 2 Stress-strain curves of reinforcement tensile tests conducted on 20M and 15M bars.

APPENDIX E: FORMULATION OF PROPOSED MODIFICATION TO EL-METWALLY AND CHEN (2017) STRUT-AND TIE MODEL

Figure E.1 shows the additional width w_t to nodal zones from STM proposed by El-Metwally and Chen's (2017). This width contributes to the strut width, w_{cs}, in each nodal zone as tension, T, increases in the node. This force creates an opposite force N_d to maintain equilibrium in the node which is linked directly to w_t. This modification was proposed as the contribution of tensile forces to El-Metwally and Chen (2017) was not considered and CCT nodes in ACI 318R-19 show contributions of T to node size and force equilibrium.

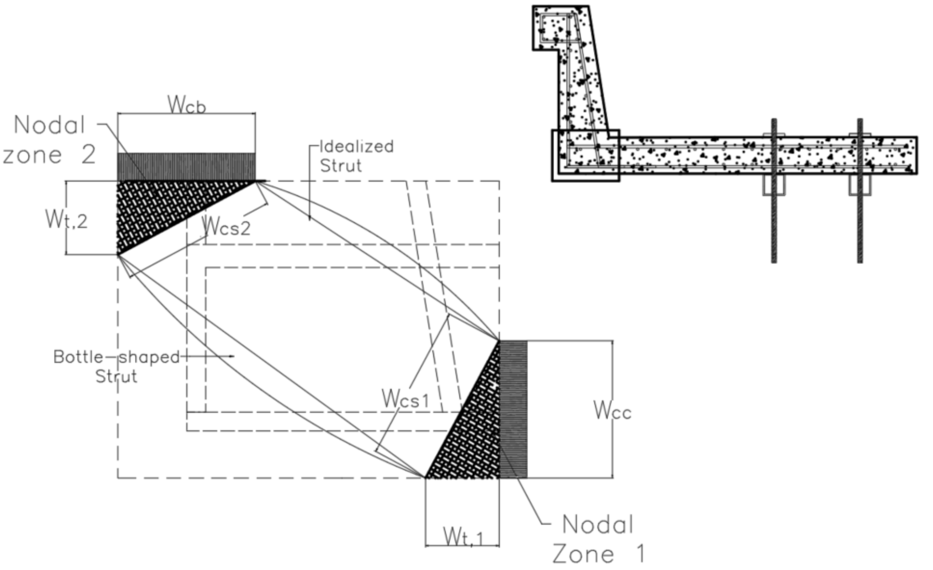

Figure E 1 Proposed STM modification to account tensile forces for a C-C-T node size.

Figure E.2 shows two free body diagrams used to determine w_t of Nodes 1 and 2 (deck and barrier nodes respectively). This analysis is based on the premise that STM is a lower-bound solution (El-Metwally and Chen, 2017) (i.e., equilibrium and failure criteria are only accounted to perform analysis using this methodology if element can always maintain force equilibrium) and since nodal zones should have at least three forces to be in equilibrium (ACI 318, 2019). N_d opposes T and linked to node capacity by Eq E.1. Equations E.2 and E.3 show the derivation of expressions for N_d using free body diagrams. Finally, Eqs. E.4 and E.5 are the final expressions for w_t obtained by merging E.1 into E.2 and E.3, respectively.

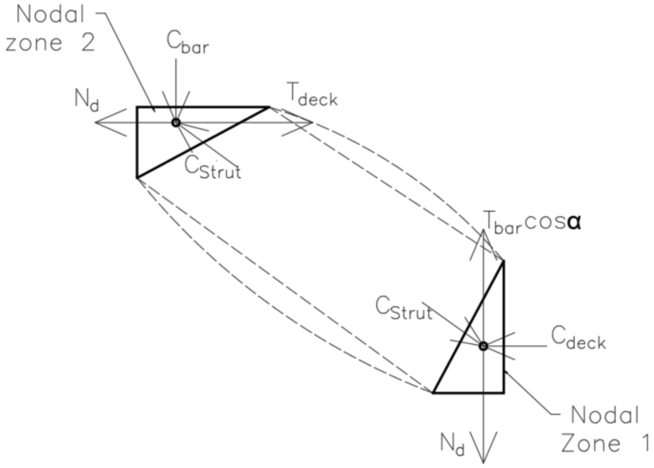

Figure E 2 Free body diagrams of nodal zones of STM.

$$N_d = f_{ce,n} w_t sp_{width} \tag{E.1}$$

$$\sum F_y = 0 \uparrow^{+} \quad \therefore T_{bar}\cos\alpha - N_{d1} - C_{strut}\cos\theta = 0$$

$$N_{d1} = T_{bar}\ cos\ \alpha\ -\ C_{strut}\ cos\ \theta \tag{E.2}$$

$$\sum F_x = 0 \rightarrow^{+} \quad \therefore\ T_{deck} - N_{d2} - C_{strut}\sin\theta = 0$$

$$N_{d2} = T_{deck}\ -\ C_{strut}\ sin\ \theta \tag{E.3}$$

$$w_{t1} = \frac{T_{bar}\ cos\ \alpha\ -\ C_{strut}\ cos\ \theta}{f_{ce,n}\ sp_{width}} \tag{E.4}$$

$$w_{t2} = \frac{T_{deck}\ -\ C_{strut}\ sin\ \theta}{f_{ce,n}\ sp_{width}} \tag{E.5}$$

Here, $f_{ce,n}$ is the nodal zone capacity shown in ACI 318R-19 for a CCT node (i.e., uses $\beta_n = 0.80$); sp_{width} is the total width of the specimen (~1500 mm; see Appendix A.3 for details); T is the tension coming from the node under analysis, related to force from reinforcement; C_{strut} is the acting compression force travelling through the diagonal strut. α and θ are angles from the inclined rebar assembly at the front of the barrier and diagonal strut relative to a vertical line, correspondingly. Final calculation to obtain the total length of diagonal face of nodal zone, w_{cs}, is done using expression E.6.

$$w_{cs} = w_t\cos\theta + W_c\sin\theta \tag{E.6}$$

With W_c defined as the length of the compression region in either barrier or deck along the test. This area may be obtained by running a cross-sectional analysis of the section (see Subsection 3.3.5.1) or experimentally using strain recorded in tests as explained is Subsection 4.5.3. w_{cs} is then used to compute the strut capacity using Eq. E.7.

$$C_{nd,srut} = w_{cs}\ sp_{width}\ f_{ce,s} \tag{E.7}$$

Variables used in expression have been previously defined except for $f_{ce,s}$, which is the limiting stress of the strut at the node – strut interface defined by ACI 318R-19 using a strut coefficient of $\beta_s = 0.4$ for tension members. Failure will occur when the acting compression force, C_{strut}, exceeds strut capacity, $C_{nd,strut}$, in either nodal zone. An example of how to apply this modification is presented in Table E.1 for all specimens at load when failure was recorded by using the proposed modification, except for SP-04 which did not register by this method failure. In this case, an arbitrary load equal to $1.06\ P_{max}$ was chosen to perform example calculations.

Table E 1 Example calculations for each tested specimen at subscribed force step using modified approach to compute diagonal strut width. Note: ΔB is the difference between major (bottom, 350 mm) and minor (top, 200 mm) bases of barrier.

Variable	**Equation used / Source**	**SP-01**	**SP-02**	**SP-03**	**SP-04**
Force level	$\frac{P_{fail}}{P_{max}}$	0.87	0.92	0.99	1.06
$W_{c,1}$, mm	Eq. 4.8	64	27.8	32.1	64.2
$W_{c,2}$, mm	Eq. 4.8	68	49	64.5	53.5
e	$\tan^{-1}\left(\frac{\Delta_B}{915}\right)$	80.1	80.9	80.9	80
α, deg	$90 - e$	9.9	9.1	9.1	9.
θ, deg	El-Metwally and Chen (2017)	53	51.8	50	52.5
T_{bar}, kN	Average strain gauge values recorded	431	336	269	115
T_{deck}, kN	Average strain gauge values recorded	929	318	401	579
C_{strut}, kN	El-Metwally and Chen (2017)	1320.3	513.3	660	853
$f_{ce,n}$, MPa	ACI 318-19	31.2	31.2	31.2	31.2
$f_{ce,s}$, MPa	ACI 318-19	15.6	15.6	15.6	15.6
$w_{t,1}$, mm	Eq. E.4	7.8	0.30	3.4	8.62
$w_{t,2}$, mm	Eq. E.5	2.7	1.82	2.23	1.3
$w_{cs,1}$, mm	Eq. E.6	55.8	22.1	27	56.2
$w_{cs,2}$, mm	Eq. E.6	55.9	40.3	51	43.2
$C_{nd1,srut}$, kN	Eq. E.7	1311	519	628	1321
$C_{nd2,srut}$, kN	Eq. E.7	1313	946	1193	1016

APPENDIX F: SOLVED EXAMPLE OF BARRIER-DECK JOINT STRENGTH CAPACITY USING EL-METWALLY AND CHEN (2017) STRUT-AND-TIE MODEL

Figure F.1 shows load and support conditions of SP-03 selected to explain joint strength analysis of the structure by STM using the analytical model proposed in Chapter 3. Relevant dimensions to perform joint strength analysis are given with material properties shown in Subsection 4.3. This example is done at a load when model reported failure (i.e., 96 kN).

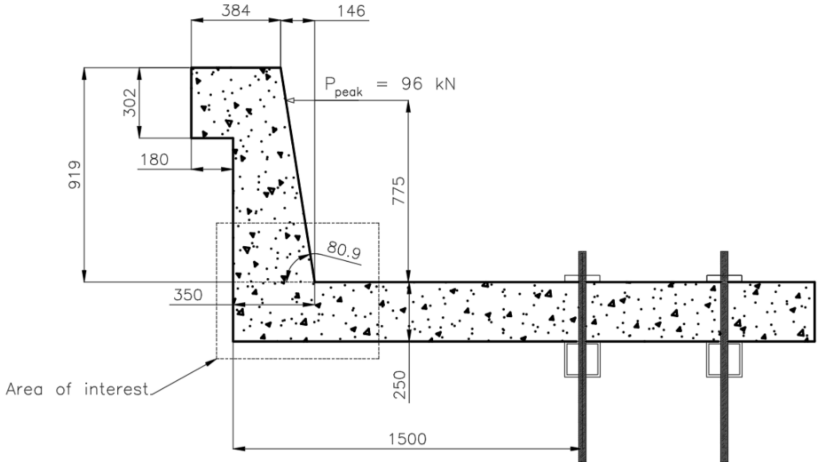

Figure F 1 Structure under analysis. All dimensions in mm.

The first step is determining the bending moment related to peak load at the barrier base barrier, M_{base}. This moment is resisted by both members (deck and barrier) on either side of the joint.

$$M_{base} = P_{peak}H_{load} = 96\ \text{kN}(0.775\ \text{m}) = 74.4\ \text{kNm} \qquad \text{(F.1)}$$

The second step is performing cross-sectional analysis for barrier and deck slab to find compression region widths and force related to M_{base}. Nuances of how the model conducts this type of analysis are given in Subsection 3.2.2.1. Fig. F.2 and F.3 show this analysis for barrier and deck respectively with corresponding results given below of each figure.

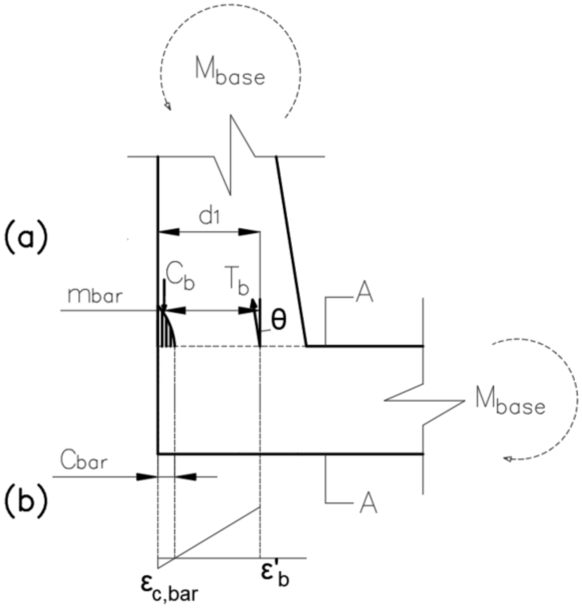

Figure F 2 Cross-sectional analysis of barrier at base. (a) force distribution and (b) strain profile at peak load.

For barrier,

$$\begin{gathered} H = 350\ \text{mm} \\ d_1 = 240.6\ \text{mm} \\ \theta = 90° - 80.9° = 9.06° \end{gathered} \tag{F.1}$$

For $M_r = M_{base} = 74.4$ kNm, force equilibrium was found at a strain level $\varepsilon_{c,bar} = -6.55 \times 10^{-4}$. Cross-section results obtained for this strain level are:

$$\begin{gathered} \varepsilon_{c,bar} = -6.55 \times 10^{-4} \\ c_{bar} = 39.8\ \text{mm} \\ T_b \cos\theta = 314.5\ \text{kN} \\ \therefore C_{bar} = T_b \cos\theta = -314.5\ \text{kN} \end{gathered} \tag{F.1}$$

Finally, moment arm is estimated between the centroid of compression region and the tensile force at d_1. For the compression region, it is assumed a parabolic stress distribution profile, as shown in Fig. F.2. Thus,

$$m_{bar} = d_1 - \frac{3}{8}\, c_{bar} = 225.6\ \text{mm}$$

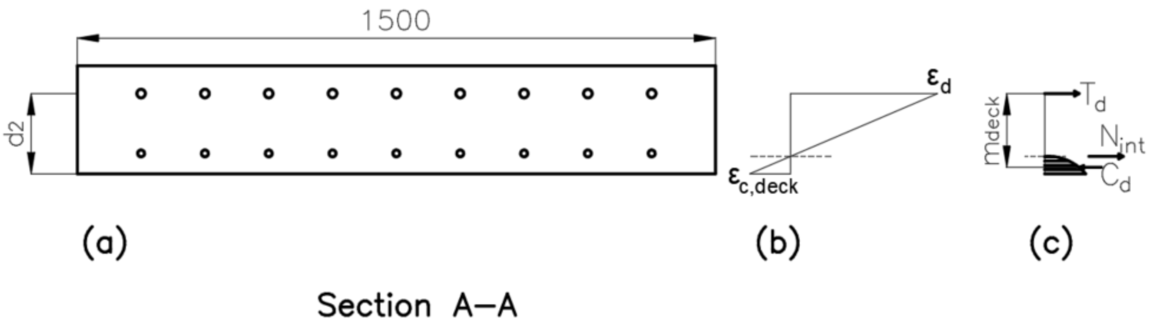

Figure F 3 Cross-sectional analysis of deck slab. (a) section cut dimensions, (b) strain profile at peak load, and (c) force distribution at peak load. All dimensions in mm.

For deck slab, cross section must resist combined action of $M_r = M_{base} = 74.4$ kNm and $N_{int} = -P_{peak} = -96$ kN. Hence,

$$\begin{gathered} H = 250 \text{ mm} \\ d_2 = 188.6 \text{ mm} \end{gathered} \tag{F.1}$$

In this case, force equilibrium was met at a strain level of $\varepsilon_{c,deck} = -9.02 \times 10^{-4}$. Cross-section results related to this strain are:

$$\begin{gathered} \varepsilon_{c,deck} = -9.02 \times 10^{-4} \\ c_{deck} = 41 \text{ mm} \\ C_{deck} = N_{int} - T = -96 - 446 = -542 \text{ kN} \end{gathered} \tag{F.1}$$

Finally, moment arm is estimated between the centroid of compression region and the tensile force at d_2. For the compression region, it is assumed a parabolic stress distribution profile, as shown in Fig. F.2. Thus,

$$m_{deck} = d_2 - \frac{3}{8}\, c_{deck} = 173.2 \text{ mm}$$

The third step is to build a STM (Fig. F.4) using compression region widths and forces determined from previous step. Given the low strain levels reported from gauges glued to bars, it was found that reinforcement was not close to rupture and thus the main objective of this STM is assessing compressive strut capacity.

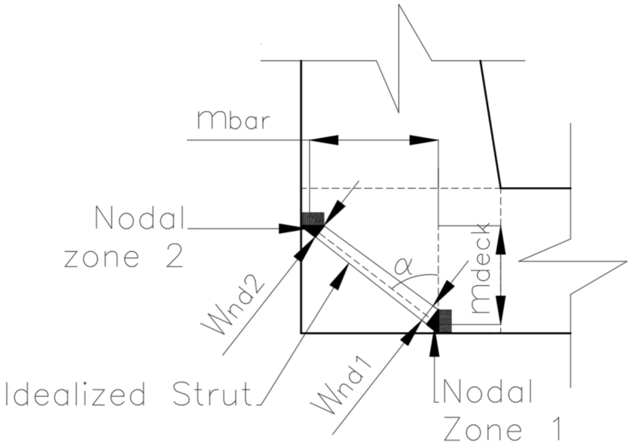

Figure F 4 STM implemented into barrier-deck joint with corresponding nodal zones, and compressive strut.

From step 2,

$$m_{bar} = 225.6 \text{ mm}$$

$$m_{deck} = 173.2 \text{ mm}$$

$$\therefore\ \alpha = \tan^{-1}\left(\frac{m_{bar}}{m_{deck}}\right) = 52.5°$$

The fourth step is to compute acting force travelling through compressive strut. This force will be then compared in step five to nodal zone capacities. To do this,

$$C_{bar} = -314.5 \text{ kN}$$

$$C_{deck} = -542 \text{ kN}$$

$$C_{critical} = \min(C_{bar};\ C_{deck}) = -542 \text{ kN}$$

$$\therefore C_{strut} = \frac{C_{critical}}{\sin(\alpha)} = -683.2 \text{ kN}$$

Step five consists in determine nodal zone dimensions at interface with strut.

For nodal zone 1,

$$c_{deck} = 41 \text{ mm}$$

$$W_{nd1} = c_{deck} \times \sin(\alpha) = 32.6 \text{ mm}$$

For nodal zone 2,

$$c_{bar} = 39.8 \text{ mm}$$

$$W_{nd2} = c_{bar} \times \cos(\alpha) = 25 \text{ mm}$$

Finally, **step six** uses nodal zone widths from previous step to determine their respective capacity. To do this, a limiting stress $f_{ce,s}$ of the strut at the node – strut interface is determined using a strut coefficient of $\beta_s = 0.4$ for tension members (ACI 318, 2019). Failure will occur when the acting compression force, C_{strut}, exceeds any nodal capacities, C_{nd1} or C_{nd2}.

For nodal zone 1,

$$W_{nd1} = 32.6\text{ mm}$$

$$Sp_{width} = 1500\text{ mm}$$

$$A_{nd1} = W_{nd1} \times Sp_{width} = 48900\text{ mm}^2$$

$$f_{ce,s} = \beta_s \times f'_c = 18.4\text{ MPa}$$

$$C_{nd1} = f_{ce,s} \times A_{nd1} = 897.8\text{ kN}$$

$$Cap = \frac{C_{critical}}{C_{nd1}} = 0.76 \ \therefore \text{ nodal zone 1 has not failed.}$$

For nodal zone 2,

$$W_{nd2} = 25\text{ mm}$$

$$Sp_{width} = 1500\text{ mm}$$

$$A_{nd1} = W_{nd2} \times Sp_{width} = 37500\text{ mm}^2$$

$$f_{ce,s} = \beta_s \times f'_c = 18.4\text{ MPa}$$

$$C_{nd2} = f_{ce,s} \times A_{nd1} = 688.5\text{ kN}$$

$$Cap = \frac{C_{critical}}{C_{nd2}} \cong 1.00 \ \therefore \text{ nodal zone 2 has failed.}$$